1-1-2006

Tribological properties of thin plasma electrolyte oxidation (PEO) coatings on aluminum alloys using electrolytic jet plasma process.

Peng Zhang
University of Windsor

Tribological Properties of Thin Plasma Electrolyte Oxidation (PEO) Coatings on Al Alloys using Electrolytic Jet Plasma Process

By

Peng Zhang

A Thesis

Submitted to the Faculty of Graduate Studies and Research

through Engineering Materials

in Partial Fulfillment of the Requirements for

the Degree of Master of Applied Science at the

University of Windsor

Windsor, Ontario, Canada

2006

Your file Votre référence
ISBN: 978-0-494-42326-4
Our file Notre référence
ISBN: 978-0-494-42326-4

ABSTRACT

In this research, a modified electrolytic jet plasma process (EJPP) was used to produce thin oxide coatings on Al390 and Al6061 in order to avoid high friction and large wear loss of their counterface materials caused by a thick oxide coating prepared by a conventional plasma electrolytic process. Effects of electrolyte concentration, treatment time and power mode on surface morphology of PEO coatings were systematically investigated and analyzed. Tribological properties of coatings against counter steel pins under different lubrication conditions were studied using a reciprocating sliding tester.

It was found that micro-pores formed on the thin PEO coating surface and surface morphology design for the favor of retaining oil would provide an advantage during the tribological tests. With proper process parameters, the coatings prepared by EJPP can exhibit high wear resistance, low friction and good compatibility for steel.

DEDICATION

To My Wife,

XiaoXia Xiao

and

My Parents,

Jicai Zhang and Yaling Yu,

for their endless support and encouragement

ACKNOWLEDGEMENTS

Great gratitude has to be expressed to Dr. Xueyuan Nie (Associated professor, Department of Mechanical, Automotive and Materials Engineering), for his animating and excellent supervision to the research, as well as his kindness and patience.

Mr. John Robinson and Mr. Andrew Jenner are acknowledged for their generous help in technical assistant, machine building, and sample preparation.

Sincere thanks are extended to the group members, Ms. Linlin Wang, Xia Li and Hua Xu for their help and advices. Thanks also to everyone in the MAME Dept. who has offered me encouragement and support during the course of my studies.

Last but not least, I would like to thank my beautiful wife, Xiaoxia Xiao, and my dear parents, Jicai Zhang and Yaling Yu, for their endless love, support and encouragement throughout my graduate studies.

TABLE OF CONTENTS

LIST OF TABLES

Chapter 6

LIST OF FIGURES

Chapter 2

Chapter 3

Chapter 4

Chapter 6

CHAPTER 1 INTRODUCTION

As the energy shortage and atmosphere pollution become more and more serious, it's very important for the automotive manufacturers to reduce vehicle weight so as to decrease the energy consumption and emission. Therefore, Al alloys, possessing a high strength over weight ratio, have been used in engine applications, such as pistons, cylinder heads and engine blocks. In order to improve wear resistance of Al alloys, silicon is added into the Al matrix to form a second phase. Hypoeutectic Al-Si alloy, with silicon content less than 12%, was used to produce engine block in the late of 1950s. Due to the low wear resistance, a cast-in steel cylinder liner was necessary to isolate Al from the piston contact and provided the cylinder bore with wear resistance [1]. However, elimination of cast iron cylinder liners will reduce more engine weight and avoid disadvantages caused by dissimilar materials. Thus, the focus of researchers shifted to hypereutectic Al-Si alloy (ALUSIL), containing a higher silicon (16 to 18% Si). To obtain a better wear resistant, the Al-Si alloy is usually electrochemically treated to etch away some aluminum matrix and expose primary silicon particles and eutectic silicon to avoid the Al-metal contact. Therefore, hypereutectic Al-Si alloy can be used to produce engine block without a cylinder liner [2]. There is also a trend to push Si content to higher and higher level (up to 35%) to increase the material's hardness and wear resistance as the PEAK spray forming method which does create Al-Si alloy materials for applications of the high-class car engine liners. However, the aluminum matrix is still soft, which may not be strong enough to hold the Si particles firmly. Additionally, Si is

hard but also brittle, and the broken Si particles have been observed in laboratory testing coupons, which may cause a worse abrasive wear [3].

In order to increase the wear resistance of Al alloys further, several techniques have been developed. Among them, Al-Matrix Composites (AMCs) have been demonstrated to have an enhanced anti-wear property. In AMCs, one of the constituents is the soft aluminum or aluminum alloy that forms percolating network structure as a matrix phase. The other constituent is the reinforcement fiber in forms of particle, whisker, continuous fiber and mono filament, which is embedded in the matrix [4]. The properties of AMCs can be tailored by adjusting the nature of constituents and their volume fraction. Primary fabrication processes of AMCs at industrial scale are classified into two groups, solid state processes and liquid state processes. Solid state processes include powder metallurgy (PM), diffusion bonding and vapor deposition technique. Stir casting, infiltration, spray casting and in-situ processing come under liquid state processes [5].

Surface coating is another approach to eliminate the tendency of severe wear by improving the mechanical property (hardness) and/or tribological properties (coefficient of friction and anti-wear resistance) of the contact surface. Various coating techniques have been developed to achieve the improvement. Nikasil, an electrodeposited nickel matrix silicon carbide coating, introduced by Mahle in1967 and popular in 1990s, exhibited low friction and wear when sliding against steel [6]. However, when it was used in an engine application, the sulfur compounds, existing in the low quality gasoline in the market, can damage the coating by forming sulfuric acid to destroy the coating's nickel base and free the silicon carbide, leading to disastrous cylinder bore wear [7, 8].

Thermal spaying technology can produce Fe-based or stainless steel-Ni-BN coatings. However, the coatings attach to the substrate only by mechanical adhesion that is highly dependent on a precise process control [7-9]. Hard anodizing can effectively produce hard ceramic coatings on low silicon content aluminum alloys (Si content less than 8%). For high silicon content aluminum alloys, since the silicon particles can not be anodized during the process, microscopic voids are formed in the coating, causing high friction coefficient and low peeling resistance [7, 8, 10].

Electrolytic plasma processing (EPP) is a plasma-assisted electrochemical treatment that is cost-effective and environmentally friendly. This versatile technique can be widely used in metal surface cleaning, metal-coating [11], carburizing, nitriding [12] and oxidizing [13-16]. When EPP comes to anodic oxidizing process, it is called plasma electrolytic oxidation (PEO). A hard ceramic coating with good adhesion and large thickness can be obtained by this technique. The coating formation mechanisms were studied [16-18]. Process characteristics and tribological properties of PEO coating on various low Si Al alloys (<1.5%) were investigated [15-18]. The silicon content effect on formation, morphology and composition of PEO coating on high Si Al alloys (7%~17%) was studied by L. Wang and X. Nie [19]. Compared with hard anodizing, PEO process can generate high temperature (up to 10^3~10^4 K) at Al-Si boundary, which is enough to melt silicon particles in Al alloys. Thus the melted Si particles can be mixed with the aluminum oxide to form Si-Al-O compounds. Most of those work studying tribological properties of PEO coatings focused on very thick PEO coatings (about 100 μm) that require high voltage (up to 600V~1000V) and long treatment time (over 60 mins), which

are challengeable to industrial application due to the production cost. Additionally, the hard and thick PEO coatings have high friction and cause large wear loss of counter part due to the rough surface and high hardness. Also, the thick coating needs polishing to meet roughness requirement for some cases, which also increases the production time. Therefore, it is necessary to study the tribological properties of thin PEO coatings that are smoother and softer than the thick ones but strong enough for load bearing and expected to exhibit lower COF and less counterface volume loss, especially under lubrication.

In this research, tribological properties of thin PEO coatings (0.3 ~ 20μm) on high Si content Al alloy (Al 390) substrates sliding against steels under residual oil lubrication were investigated. Effects of electrolytic concentration, power supply regime and treatment time on coating thickness, morphology, coefficient of friction (COF) and counterface wear loss were discussed. Also, thin PEO/graphite composite coatings on low Si content Al alloy (Al 6061) substrates were also produced. And their tribological properties against steels under different wear conditions were also investigated.

This thesis consists of seven chapters. Following the introduction, literature review mainly regarding PEO process characteristics, coating formation mechanism and coating properties on Al alloys are included in Chapter 2. Chapter 3 describes the experimental procedures. Chapter 4 demonstrates the tribological testing results of thin PEO coatings on Al 390 alloys treated with a DC power against steel balls under residual oil lubrication. Effects of process parameters, including electrolytic concentration and treatment time, on coating surface morphology, thickness and wear testing results have been particularly

studied. Chapter 5 presents the tribological testing results of thin PEO coatings on Al 390 alloys treated with a bipolar pulse DC power against steels under residual oil lubrication. The effects of process parameters, including bipolar pulse DC and treatment time, on coating morphology, thickness and wear testing results have also been investigated. Chapter 6 exhibits the tribological testing results of thin PEO/graphite composite coatings on Al 6061 alloys treated with the DC power against steel under different testing conditions. The effects of coating thickness, various reciprocating sliding frequency and different lubrication condition on wear testing results have been discussed. Chapter 7 summarizes the present study results and outlines recommendations of future research.

CHAPTER 2 LITERATURE REVIEW

The history of Micro-arc-oxidation process was introduced in Ref. [20]. In the mid 1970's, two Russian scientists, G.A. Markov and G.V. Markova, developed an advanced anodizing process on an aluminum anode [21, 22]. The wear resistant properties of the coatings on lightweight metal were investigated. The technology was later improved and named as 'micro-arc-oxidation' (MAO) process [23]. In the 1980's, Russia scientist, Snezhko [24-29], Markov [30-32], Fyedorov [33], Gordienko [34-36] and their coworkers attempted to apply the new oxidation technology on various metals. In Germany, Kurze and coworkers [37-45] researched the early industrial applications of MAO process. Due to the few information on the process phenomenology and mechanism, different terminology has been used for MAO in most of the above studies, such as 'micro-plasma oxidation', 'anode spark electrolysis', 'plasma electrolytic anode treatment' and 'plasma electrolytic oxidation (PEO)'. In nature, it is a process of plasma assisted electrochemical conversion of a metal surface to produce an oxide ceramic layer [20, 46]. In this thesis, the term PEO was used to name the process.

When applied to aluminum alloys, the PEO process can produce thick, hard and well-adhered alumina-based surface layers that have good wear resistance, thermal stability and dielectric properties, which make the process promising for several industrial applications.

In this chapter, previous works on the characteristic phenomenon, coating formation mechanism and coating tribological properties of PEO process are reviewed.

2.1 The equipment and electrolyte for PEO coating

Usually, PEO treatment of aluminum alloys is carried out in an alkaline silicate bath with a power supply that is able to output 300-1000V [47]. Figure 2.1 is the schematic of a typical treatment unit. The unit consists of an electrolyser and a powerful electrical source. The electrolyser is usually a water-cooling bath placed on a dielectric base and fixed in a grounded steel frame, which has an insulated current supply and a window to observe the process in operation. A stainless steel plate in the bath acts as the counter-electrode. Sometimes, an electrolyte mixing, recycling and gas exhausting arrangements, as well as some safety interlocks are also included.

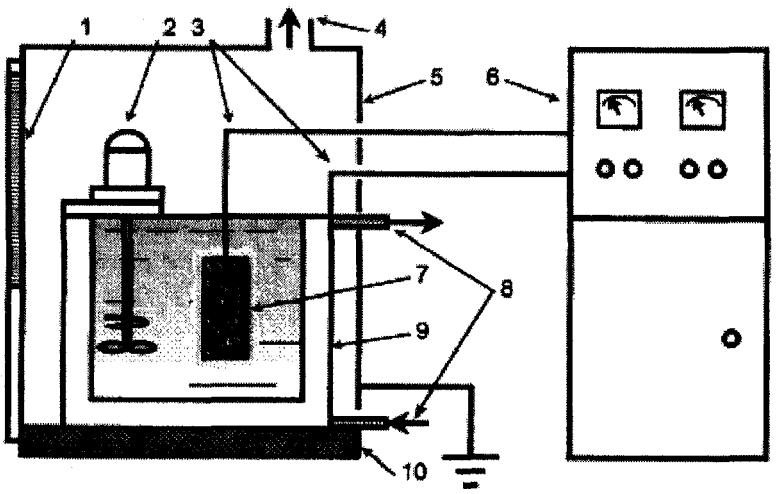

Fig. 2.1 Typical treatment unit for PEO process (1. window, 2. mixer, 3. connecting wires, 4. exhaust/ventilation system, 5, grounded case, 6. power supply unit, 7. workpiece, 8. cooling system, 9. bath, 10 insulating plate) [20]

Different types of power source can be used, including DC, unbalanced AC or pulsed DC source [20]. For a DC source, due to the difficulties for regulating the surface discharge

characteristics, it is only used for simple-shape components and thin coatings. For a pulsed DC source, since it allows adjusting the arc duration, the heat conditions during treatment and the coating composition and structure can be controlled. However, a pulse current can cause an additional polarization of the electrode surface. For an unbalanced AC source, besides the possibility of process control by means of arc interruption, it can also avoid the additional polarization of the electrode. Furthermore, the ability to independently change the amplitudes of both positive and negative components extends the controlled range of coating deposition. But the limitations in power (usually $\leq$ 10kW) and current frequency (main frequency only) constrain the range of its application.

To produce the PEO coatings on aluminum alloys, dilute alkaline electrolytes are widely used. Silicate, aluminates or polyphosphates are added into the electrolytes to promote strong metal passivation by forming near-surface gels or insoluble compounds.

2.2 Deposition procedure

After simple pretreatment, including cleaning and degreasing, the sample is connected to the anode of the power source unit and immersed into the bath, containing the electrolyte, at a depth of 30mm to 50mm beneath the solution surface. The cathode of the power source unit is attached to the stainless steel counter-electrode. After activating electrolyte cooling, mixing and gas exhaust systems, the working voltage up to 1000V is applied to the sample and the counter-electrode by the power supply for the selected treatment time, with the current density between 500 to 2000 A/cm^2. The treatment time is highly dependent on the application of the coating, ranging from a few minutes to several hours.

2.3 Current-voltage characteristics

The current-voltage characteristics of the electrochemical system during the process were studied in Ref. 20, and the current-voltage characteristics curve was shown in Figure 2.2. Initially, a conventional anodic oxidation of the surface of the alloys (anode) occurs with the current-voltage characteristics conforming to the Ohm's law, corresponding to the region '0-U_1' in type-a system and '0-U_4' in type-b system. However, for type-a system, beyond a critical voltage U_1, an increase in voltage results in current oscillation, followed by luminescence. The increased current causes local boiling of the electrolyte near the electrode. The consequent gas products (O_2 or H_2) over the electrode surface partially shield the electrode from the electrolyte, which limits the further current increment. With the voltage increase over another critical value U_2, the electrode is totally covered by a continuous gaseous vapor envelope of low electrical conductivity. Thus the electric field strength E within the envelope reaches a value over 10^6 V/m, which is adequate to initialize the ionization processes in the vapor envelope. A rapid sparking in scattered gaseous bubbles is observed as the result of ionization processes, followed by a uniform glow distributed throughout the vapor plasma envelope. Beyond voltage U_3, the glow discharge transforms into intensive arcing accompanied by a characteristic low-frequency acoustic emission.

As respect to type-b system, the process is more complicated. Initially, the passive film resulting from the anodic oxidation starts to dissolve when the voltage approximately approaches to the corrosion potential of the material U_4. Then a porous film forms as the result of a repassivation process from U_4 to U_5. At the point U_5, the electric field strength

in the oxide film is high enough to break through the film due to the impact or tunneling ionization. Upon that, small luminescent sparks are detected to move rapidly across the surface of the oxide film, which is favorable for film growth. At point U_6, the thermal ionization process is initialized and slower, larger arc-discharges arise. In the region U_6 to U_7, thermal ionization is partially limited by negative charge build-up in the bulk of the thickening oxide film. At this stage, micro-arc forms and causes the film fused and alloyed with elements contained in the electrolyte. Beyond the point U_7, the arc micro-discharges occurring throughout the film surface break through to the substrate, resulting in the failure of negative charge blocking, and transform into intensive arcs, which may cause destructive effects such as thermal cracking of the film.

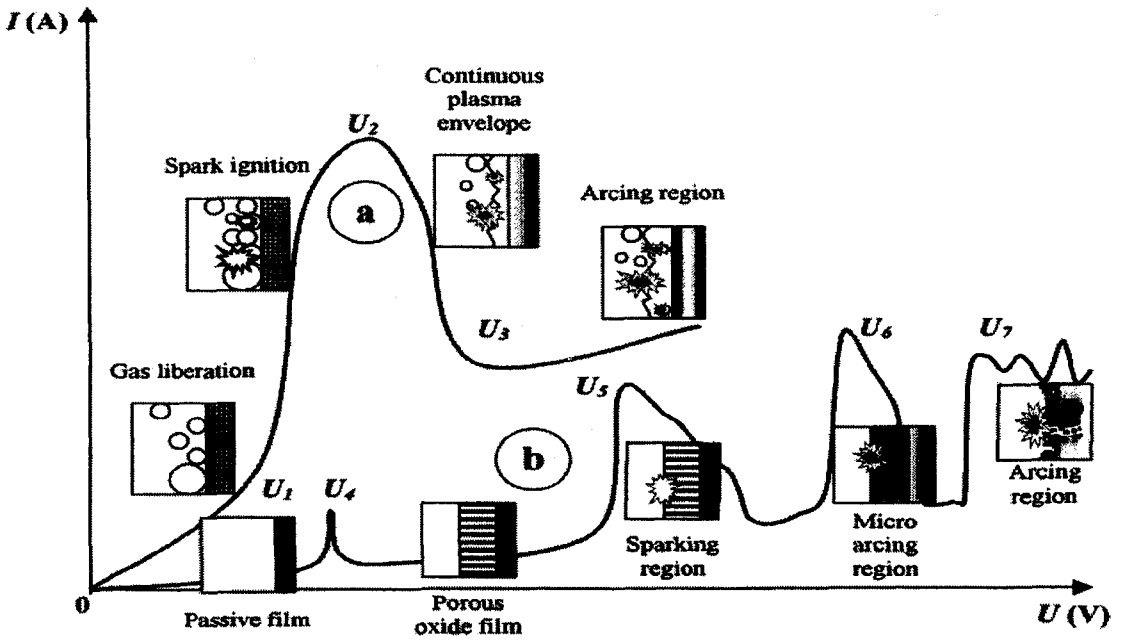

Fig. 2.2 Two kinds of current-voltage diagram for processes of plasma electrolysis; discharge phenomena are developed (a) in the near-electrode area and (b) in the dielectric film on the electrode surface [20].

2.4 Coating formation mechanism

With ionic current of the layer increase passing through oxide layer, there are two concurrent processes for PEO coating growth: the electrochemical and the plasma chemical mechanisms [17].

2.4.1Electrochemistry of plasma electrolytic oxidation (PEO)

The electrochemical formation of surface oxide layers can result from different mechanisms. If standard strong electrolytes, such as sulphuric, oxalic, salicylic acids and their salts, are used, then the alumina layer grows as a result of mutual diffusion of metal and oxygen ions through the oxide lattice [17]. However, these electrolytes are not widely used. Actually, aqueous solutions of inorganic polymers-silicates, aluminates, phosphates, etc, are more popular. Unfortunately, only little information about the electrochemical formation of surface oxide layers in such PEO electrolytes is available. The polycondensation of adsorbed anionic complexes of an electrolyte, due to dehydration under the action of an electric field, are proposed to explain the layer formation [48]. Consequently, ionic diffusion process has little effect on the layer formation, so the coating composition can only derive from the anionic complexes of an electrolyte in terms of the electrochemical formation of oxides in such electrolytes.

Recently, systematical studies [16-18] have been conducted to investigate the effects of process parameters on the growth kinetics, thermodynamics and associated changes in the structure, phase composition and mechanical properties of the oxide layers by the PEO

treatment. However, the controversial data of the current efficiency of PEO process in these literatures indicate that certain side processes take place but are not understood yet.

In order to reveal the basic electrochemical processes, A.L. Yerokhin et al. have conducted a series of experiments on plasma electrolytic oxidation. Initially aluminum titanate coatings were deposited on Ti using a PEO process [49]. The probable coating formation mechanisms, including electrochemical oxidation of Ti-electrode by OH^- anions, are discussed. However, the process parameters chosen in their research allowed only qualitative consideration of current distribution. According to the Fig. 2.3, oxide layer formation is induced both by the ionic component of the current which is transmitted via surface discharges and by the anodizing current passing across the surface which is free of discharges. Other components of the current cause secondary electrochemical processes which lead to liberation of electrode gases, accumulation of H_2O_2 in the electrolyte, anodic dissolution of the titanium metal and electrothermally induced metallurgical processes in the surface layer. The anodizing current is maintained by electrolyte anions mainly consisting of OH^- and AlO_2^- in alkaline aluminate solutions. Particularly, the relatively unstable aluminate ions can partly interact with water and /or create complex anions between themselves (in alkaline media) to form either mono- or poly-hydroxyanions, e.g. $Al(OH)_4^-$ or $Al_n(OH)_{4n+2}^{(n+2)-}$. On the surface of the Ti electrode, the above anions can be involved in the following anodic processes [49]:

$$Ti^{4+} + 2OH^- + 2H_2O = TiO_2 + 2H_3O^+$$
$$Ti^{4+} + 4AlO_2 = TiO_2 + 2Al_2O_3$$
$$Ti^{4+} + 4Al(OH)_4^- = TiO_2 + Al_2O_3 + 2Al(OH)_3 + 5H_2O$$

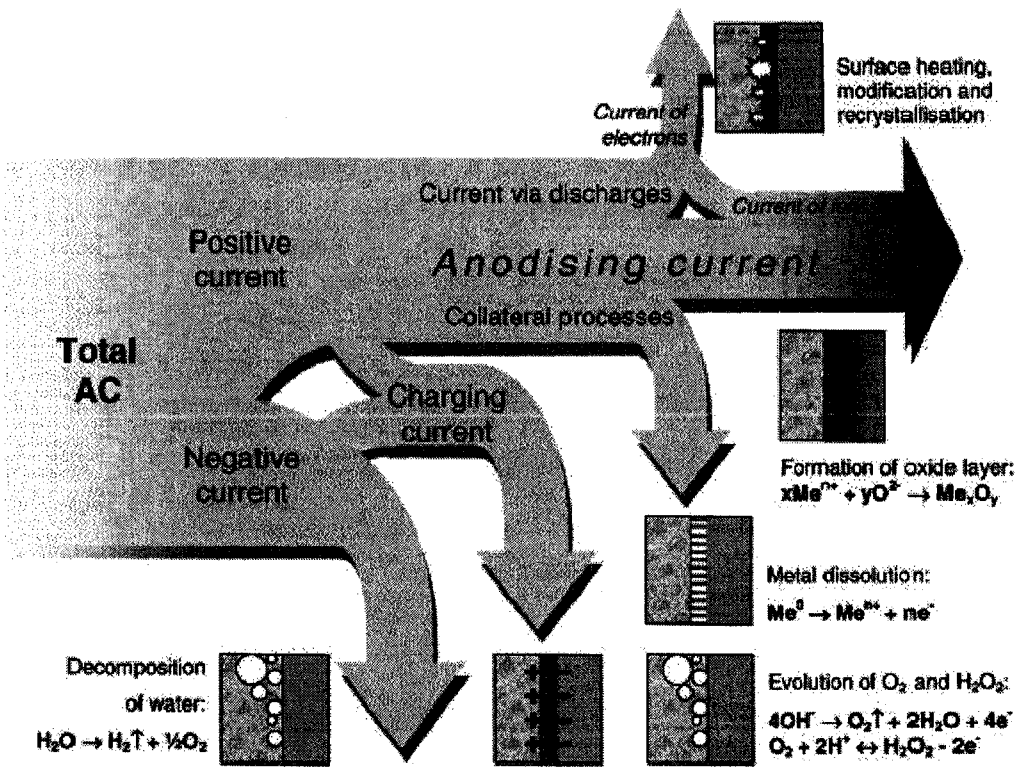

Fig. 2.3 Schematic diagram of current distribution during PEO treatment of metals in AC mode [49]

In their later works [18], a different approach was used to quantitatively evaluate the rates of the major anodic processes, in which a simplified model is considered for the rate evaluation of partial processes during PEO. The experimental facility designed for this purpose is used to determine the following characteristics: (i) evolution rate and composition of anodic gaseous products, (ii) rates of aluminum chemical and anodic dissolution in the electrolyte, (iii) oxide coating growth rate, structure and phase composition. The experiments were performed on aluminium anodes oxidized in a dilute alkaline solution (0.5 to 2 gl^- KOH) under conditions of galvanostatic DC PEO. Basic electrochemical processes were considered, such as oxide film growth, anodic dissolution

and oxygen liberation. Four different stages of the PEO processes were identified, characterized by various proportions of the partial anodic processes, i.e. (i) anodizing, (ii) anodizing with anodic dissolution, (iii) anodizing, dissolution and oxygen liberation and (iv) plasma electrolysis.

Dynamic equilibrium of partial processes of oxide formation, dissolution and oxygen evolution is quite common for aluminium anodizing in alkaline solutions, where the following general reactions normally occur:

(I) Metal-oxide interface
Anodic processes:

$$2Al + 3O^{2-}_{solid} -> Al_2O_3 + 6e^-$$

$$Al -> Al^{3+}_{solid} + 3e^-$$

(II) Oxide-electrolyte interface
(i) Anodic process:

$$4OH^- -> O_2 \uparrow + 2H_2O + 4e^-$$

(ii) Alumina chemical dissolution and oxidation of ejected Al:

$$Al_2O_3 + 2(x-3)OH^- + 3H_2O -> 2[Al(OH)_x]^{n-}_{gel}$$

$$Al^{3+}_{ejected} + xOH^- -> [Al(OH)_x]^{n-}_{gel}$$

$$[Al(OH)_x]^{n-}_{gel} -> Al(OH)_3 \downarrow + (x-3)OH^-$$

The overall current efficiency of the oxide film formation was estimated to be in the 10 to 30 % range (depending on the process conditions). It was also found that the film growth rate decreased sharply with increasing electrolyte concentration resulting in the increased rate of anodic dissolution. Oxygen evolution was shown to be the main electrochemical process at the potentials corresponding to the plasma stages of the electrolysis (oxygen current yields around 60 to 80 %). Estimations of the process efficiency were carried out, assuming that the Faraday's law governs the partial processes of oxide film growth,

dissolution and gas evolution on the surface. The overall rate of oxygen liberation at the anode exceeds the Faraday yield, which is probably due to the radiolytic effect of the plasma discharge on the adjacent electrolyte volume.

2.4.2 Plasma discharge models and plasma chemistry

Besides the electrochemical process, the plasma chemical processes were discussed [16, 17, 18, 48]. The plasma chemistry of the surface discharges is quite complex in nature, involving, on one hand, reactions among electrons, molecules of water and electrolyte anions, and one the other hand, atoms and ions of the metal electrode. An important consequence of the occurrence of surface discharges is the development of metallurgical processes in the growing oxide layer, which are induced by the heat liberated in discharge channels from electron avalanches. Cycles of instantaneous local heating and cooling of the areas of the oxide layer in close proximity to a discharge channel lead to the melting, quenching and recrystallisation of the substances deposited onto the surface. As a result, decomposition of aluminum hydroxide to alumina, formation of complex compounds based on the Al-O system, as well as high-temperature transformations of alumina, can occur. The direction and intensity of these processes depend on the density and power of the discharges which are known to be defined by thickness of the oxide layer, so that the thicker the layer the less frequent yet more powerful and extended the discharges become.

In the plasma reaction, the key is the formation of micordischarge. A.L. Yerokhin et al [46, 47] researched microdischarges using real time digital video to image the plasma electrolytic oxidation process. Both the spatial characteristics of microdischarges and

their collective behaviors during the PEO process of aluminum alloys using an AC power supply were analyzed. The typical evolution of microdischarge is shown in Fig 2.4, from which four consecutive stages of the PEO process can be distinguished. During stage I, intense gas evolution along with some luminescence at the surface is clearly observed, which is eventually replaced by the onset of a bluish glow discharge around the sample surface. In stage II, the discharge begins to shrink at the surface with maximum electric field intensity and transforms to the moving discrete white microdischarges, along with an occasional uniform glow. After about 10 to 12 minute of treatment, the process gradually reaches stage III, where the microdischarges phenomenon becomes more pronounced. Further PEO processing, stage IV, is characterized by some yellow, larger and slower moving microdischarges.

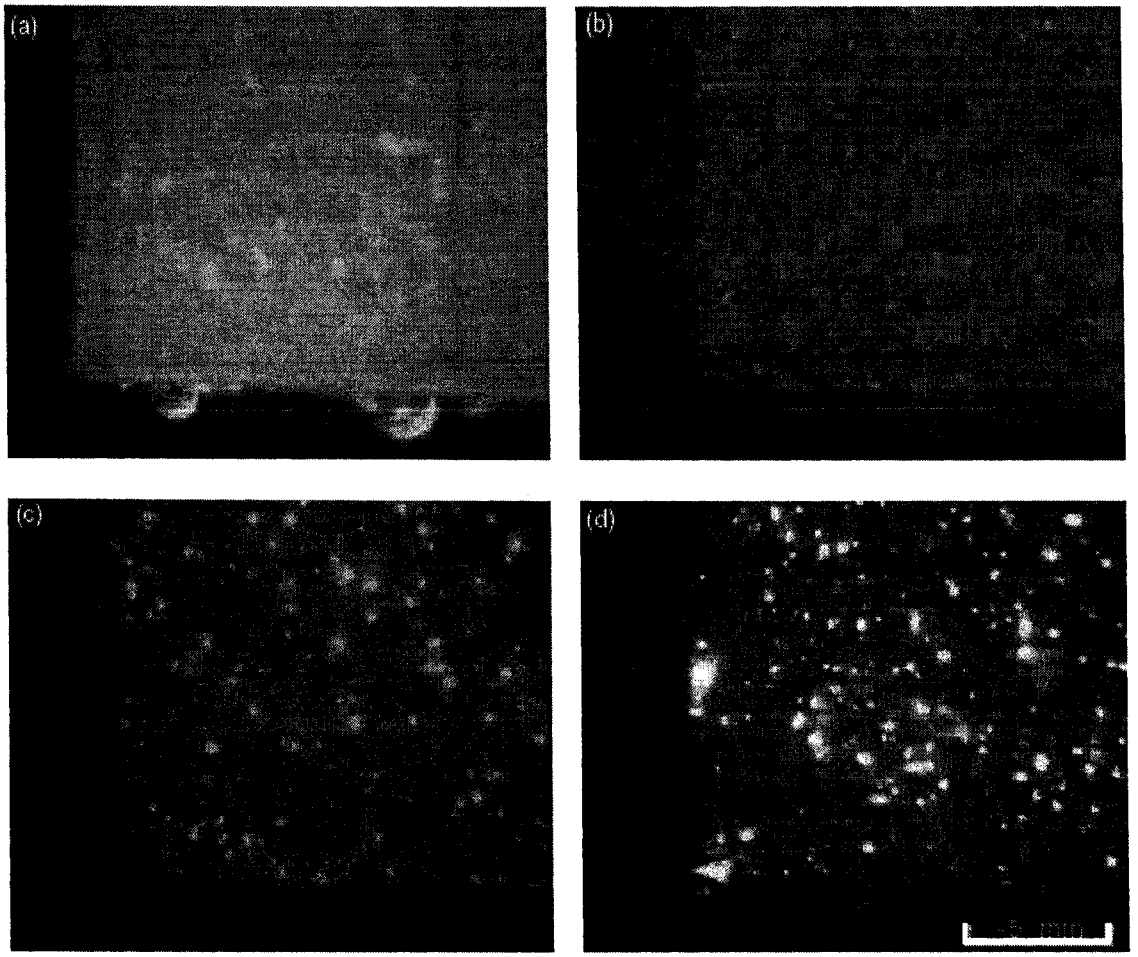

Fig. 2.4 Sample surface appearance at various stages of the coating formation process: (a) 0.5 min; (b) 10 min; (c) 35 min and (d) 65 min [47].

Several microdischarge formation models have been proposed. For the first model [17, 50, 51], the micordischarges appear as a result of the oxide film dielectric breakdown in a strong electric field, Fig. 2.5 (a). The breakdown is treated as "streamer propagation" due to the electron avalanche effects induced by film dopants and structural defects. Three main steps can be discerned in the breakdown process. In the first step, the discharge channel is formed in the oxide layer as a result of the loss of its dielectric stability in a region of elevated conductivity. This region is heated by generated electron avalanches

up to temperatures of ~10^4 K. Due to the strong electric field (of the order of ~10^6 Vm^{-1}), the anionic components of the electrolyte are drawn into channel. Concurrently, owing to the high temperature, aluminum and alloying elements are melted out of the substrate and enter the channel. Thus, a plasma column (plasmoid) is formed as a result of these processes. In the second step, plasma chemical reactions take place in the channel, which leads to an increase in pressure inside the channel. So the plasmoid expands to balance it. At the same time, separation of oppositely charged ions occurs in the channel due to the presence of the electric field. The cations are ejected from the channel into the electrolyte by electrostatic forces. In the last step, the discharge channel is cooled and the reaction products are deposited on to its wall.

The second group of models [46] considers each microdischarge as a gas discharge occurring in a micropore of the oxide film, Fig. 2.5 (b). The formation of a gas phase in the pore (and discharge ignition in it) is believed to be induced by an initial dielectric breakdown of a barrier layer in the bottom of the micropore.

An alternative model of microdischarge formation was proposed based on analogy with the contract glow discharge electrolysis [52], Fig. 2.5 (c). In their work, a glow discharge was observed at the interface of the electrolyte and a thin vapor sheath was formed at the surface of a platinum wire anode at $U^+ \cong 420V$. In the case of an aluminum anode, however, the gas bubbles accompanying the oxidation process and the discharge play the role of the vapor sheath; therefore, it seems as if it is disintegrated into a number of microdischarges. Nevertheless, it is important to recognize that the common condition of

discharge initiation in both cases appears to be electron emission from the electrolyte surface (partial cathode) into a gaseous phase, rather than dielectric breakdown of the growing oxide film. It should also be noted that free electrons might appear initially at the oxide-electrolyte interface in strong electric field, regardless of the presence of any gas/vapor phase, due to the ionization of anions and molecules of water. The free electrons would then immediately participate in a series of reactions with water, resulting in the formation of gaseous products (H_2 and O_2), thus providing the necessary conditions for maintenance of a stable plasma discharge environment.

Another model that considers the AC PEO discharge as the dielectric barrier discharge has recently been reviewed by Wagner et al [53]. Similar to PEO, the barrier discharge operates under AC polarization and atmospheric pressure conditions, with one electrode covered by a thin dielectric film. The barrier discharge usually operates in a filamentary mode, for which the phenomenology is similar in appearance to a microdischarge in PEO, except that the barrier discharge occurs during both positive and negative half-cycles. Furthermore, unlike the discharge in PEO, dielectric barrier discharges cannot be produced using simple DC polarization.

A.L. Yerokhin et al [47] found that the above models do not fit the spatial, temporal and electrical characteristics of microdischarge phenomena, which were observed in their investigation. A new model is suggested based on the analogy with contact glow discharge electrolysis. The model assumes the possibility of free electron generation and glow discharge ignition in the gaseous media at the oxide-electrolyte interface, which

leads to heating, melting and quenching of the underlying oxide layer. The estimated ranges of the microdischarge current density and duration time sufficient for initiating phase transitions in the surface oxide layer are in good consistence with the experimental data.

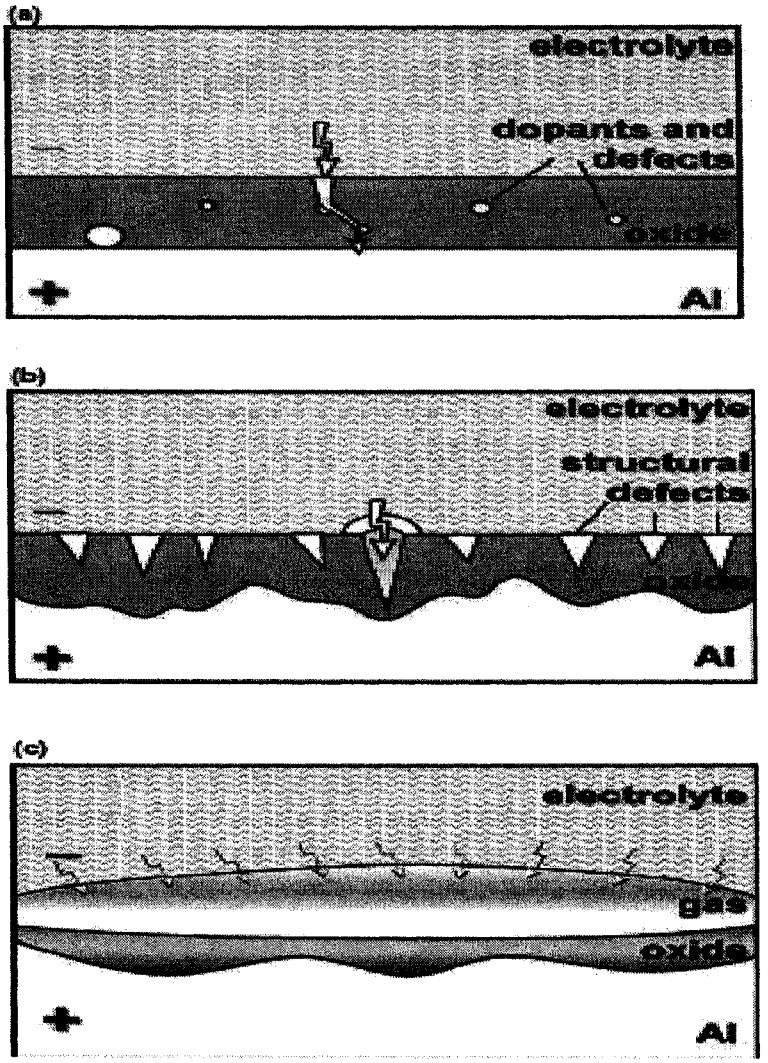

Fig. 2.5 Schematic illustration of model describing the appearance of surface discharge during anodic oxidationi of Al: (a) model of the oxide film dielectric breakdown; (b) discharge-in-pore model and (c) model of contact glow discharge electrolysis adapted for the presence of an oxide film on the metal surface [47].

2.5 PEO coating structure

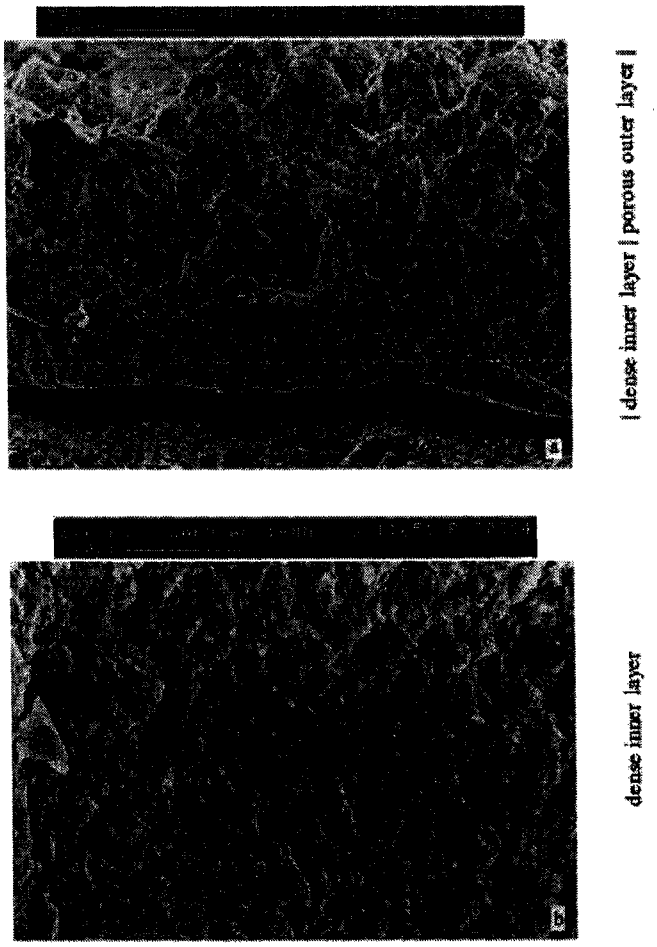

Fig. 2.6 SEM micrographs of PEO coating: (a) fracture section of the coating; (b) the dense (inner) layer [54].

Fig. 2.6 illustrates the structure of the PEO coating [54]. SEM investigations demonstrate that alumina coatings, produced on Al alloys by the PEO techniques, tend to consist of two layers, i.e. a porous outer layer, and thin inner dense layer. The porous outer region consists predominantly of the low temperature modification of Al_2O_3 (γ-Al_2O_3/η-Al_2O_3) and X-ray amorphous phase. A dense inner region is formed by mixture of high temperature α, γ-Al_2O_3 modifications of Al_2O_3 and complex Al-X-O phases (X is the

element from electrolytes), where complex phases of the substrate alloying elements are observed in a thin, interfacial region below the dense layer. The relative sizes of the regions, their structure and composition are substantially influenced by substrate composition, electrolyte composition and treatment regime. Comprehensive studies of these effects have been conducted to investigate the treatment process of Al alloys in silicate solution [13, 46, 55]. In these studies, different treatment time, current density and concentrations of Na_2SiO_3 (2-20 g/l) with addition of 2-3 g/l KOH solution were used to produce coatings with different ratios of Al_2O_3 and SiO_2 fractions. It has been observed that the increase of the silicon content in the electrolyte results in a higher growth rate by the formation of composite coatings and an extension of the inner dense layer. The relative proportion of the harder α-alumina is increased by raising the current density.

The microstructure in the inner layer of the coating was studied using cross-sectional TEM [14]. Fig. 2.7 shows cross-sectional TEM images of a representative microstructure near the coating/ structure interface. The thin inner layer of the coatings exhibits a number of (predominately amorphous) sublayers, whilst the lower portion of the intermediate layer has a nanoscaled polycrystalline microstructure. Some occluded porosity of nanoscale dimensions was observed in the inner and intermediate layers, but not adjacent to the interface between the coating and the substrate. The characteristics of the coating near the interface with the Al alloy substrate can be divided into three sublayers. Sublayer 1 shows a dense amorphous structure which has a thickness of ~140 nm constant over the entire sample, whereas the thickness of sublayer 2 varies, sublayer 2 shows a porous structure that is composed of amorphous and nanocrystalline regions with

porosity of a size in the range of approximately 10-100 nm. Fig. 2.7 (b) is an enlarged TEM image of the microstructure of sublayer 3. This layer was found to be composed of nanocrystalline structure whose grain size is in the range of 50-80 nm. According to the TEM investigations, no porosity was observed at the interface between the substrate and the coating and the porosity in sublayer 2 was occluded, rather than interconnected.

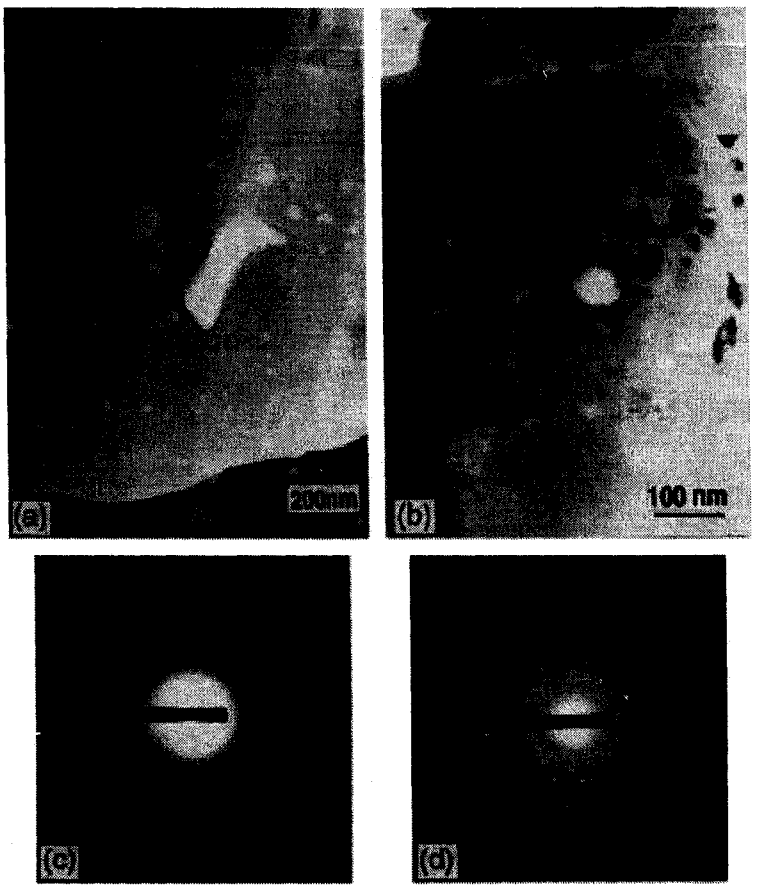

Fig. 2.7 Cross-section TEM images of (a) the inner layer near coating/substrate interface and (b) the intermediated layer, and SAED patterns taken from (c) sublayer 2 and (d) sublayer 3, respectively [14].

2.6 Tribological properties of the PEO coatings

The tribological properties of PEO coatings treated with different current density and electrolyte concentration on Al alloys were investigated using ball-on-disc sliding tests against 440C steel and sapphire balls under dry sliding [13]. The large thickness and high hardness endue the coatings with an excellent load bearing ability. Tests were conducted in air with relative humidity (RH) controlled in the range from 5~90%, and also in vacuum of 10^{-3} Pa. Wear resistance of the PEO coatings was measured according to ring-on-block sliding tests. The ambient environment where the tests were run was controlled with 30%~40% RH. Sliding speed of 0.2 m/s and normal load of 980N to provide contact pressure about 1GPa were chosen for the tests. In order to calculate the wear rates mg/rev. weight losses of friction pairs after 5000 ring revolutions were measured using microbalance and divided by revolutions. The tests results showed that the coating composition, the counterpart material, the relative humidity and the formation of the transfer film all had a great effect on the friction of Al-Si-O coatings. Coating $Al_{0.26}Si_{0.08}O_{0.66}$ exhibited the lowest friction coefficient, which varied from 0.15 to 0.25 for different RH, sliding against a sapphire ball. Also the coating reduced friction from 0.65 to 0.17, decreased wear rate by four orders of magnitude and avoid micro-cutting and/or adhesive wear of the friction pair at contact pressure of 1GPa.

The effect of coating thickness on tribological properties was explored [54]. Ball-on-plate reciprocating sliding tests, with a load of 10N over 5000 cycles at 2Hz frequency, were performed to coatings with different thickness from 100 μm to 250 μm. The sliding path for each cycle was 10 mm and ambient environment was controlled to 23±1 °C and 50±5

%. The friction coefficients of PEO coating against bearing steel (BS) and tungsten carbide (WC) balls were in the ranges of 0.64~0.68 and 0.68~0.86, individually, which were both higher than those of untreated substrate. However, all the coatings showed much lower wear rates, 10^{-8}~10^{-9} mm^3/Nm, than substrate, about 10^{-4} mm^3/Nm. The coatings with thickness of 150 μm were found to have poor wear resistance relative to their thicker and thinner counterparts.

Tribological characteristics of PEO coatings on Al 6061 and Al 4043 cylinder bores against Cr-plated steel piston rings under boundary lubrication were investigated [56]. A commercially-manufactured, ball-on-flat, reciprocating friction and wear testing machine was used. The normal force of 150N, the stroke length of 8.0mm, the oscillation frequency of 15Hz and total sliding distance of 865m were set for the testing. Engine oil was swabbed on the surfaces of all specimens prior to start-up. Grey cast-iron liners were used for comparison. Without diamond plateau honing process, the porous outer layer of PEO coatings fractured and caused three-body wear, which led to the higher friction coefficient and wear resistance than grey cast iron.

The friction properties of PEO coatings deposited on SAE6061 aluminum alloy cylinder liner against piston ring samples under the boundary lubrication were studied and compared with those of cast-iron liner, using a segmented Ring/Bore liner test apparatus to simulate the engine operation condition under low speed-maximum load [57]. The PEO coatings were honed before the wear testing, even smoother than the cast-iron liner,

which was attributable to the better friction properties and lower wear rate of PEO coatings.

Honing process is very important for PEO coating to remove the porous outer layer and expose the dense inner layer so as to reduce the risk of third-body wear contributing to high friction coefficient and wear rate.

The ceramic matrix-graphite particle composites structure is another approach to decrease the friction coefficient and increase wear resistance. Graphite particles embedded in the Al_2O_3-SiO_2 ceramic matrix as dry lubricant [58]. Without honing process, a low friction (~0.22) and good compatibility with the steel counterface were presented during dry tribological testing. In order to form a continuous graphite film at the interface between friction pairs, a rough and porous outer layer is necessary to sustain the graphite particles for the PEO coating. Therefore, for some industry applications, where there is a critical requirement on surface smoothness, the ceramic matrix-graphite particles composites coating can not effectively reduce the friction and wear after the porous outer layer as well as the graphite particles are removed by honing process.

A duplex treatment was developed to combine a load supporting PEO alumina layer with a low friction diamond-like carbon (DLC) coating, produced by a modified plasma-immersion ion implantation (PI^3) process [59]. The DLC layer can provide a low friction coefficient and the intermediate alumina layer is favorable for load supporting, essential to withstanding sliding wear at high contact loads.

2.7 Challenges on PEO coatings

Being environmentally friendly and cost-effective, PEO process is a very promising technique that can be widely applied to improve the wear resistance of aluminum alloys in industrial scale. However, some improvements in the following aspects are necessary.

Firstly, for the conventional PEO process, laborious masking process is necessary to isolate the region that needs no treatment before the working piece is immersed into the electrolyte. A modified electrolytic jet plasma process (EJPP) has been developed much far before this thesis to eliminate that extra process. Details about the process will be discussed in the following chapter.

Secondly, it is very inconvenient for the traditional PEO process to produce a ceramic matrix-graphite composites coating. The PEO process has to be paused in order to rub graphite on the coating surface. The new EJPP process can form the ceramic coating and rub graphite without interrupting the treatment.

Finally, the roughness of PEO coatings increases with the thickness of the coatings. And long treatment time is required to produce thick PEO coatings. Usually, the porous outer layer of PEO coatings needs removing to meet surface smoothness requirement and reduce abrasive wear for friction pairs. Therefore, thin PEO coatings with small surface roughness are preferable to large-scale production for less treatment time, energy consumption, counterface wear loss, and honing-free process. Although the thin PEO coatings have a less load-bearing ability than the thicker ones, they can withstand many applications, such as mild wear [60], where oil lubrication exists.

CHAPTER 3 EXPERIMENTAL PROCEDURES

This chapter describes all the experimental procedures in the thesis. Three main parts are included.

3.1 Part A. Effect of electrolyte concentration on the morphology and tribological properties of PEO coatings on Al 390

3.1.1 Preparation of substrates

Al-Si alloy 390 was chosen as substrate material. The composition of this alloy is shown in Table 3.1.

Table 3.1 Nominal composition of Al-Si alloy 390

Alloy	Composition, wt%						
	Si	Fe	Cu	Mg	Mn	Other	Al
Hypereutectic alloy 390	16-18	1.3	4.5	0.45-0.65	0.5	1.5 Zn	balance

A number of slices ($7\times1.5\times0.5$ cm^3) were cut from cast Al-Si 390 alloy. All the slice samples were polished to a similar surface roughness of 0.1 ± 0.05 μm, and then degreased with solvent, rinsed and cleaned with distilled water, finally dried. The metallurgical photograph of the polished Al390 substrate is displayed in Fig. 3.1. The photograph was taken using Buehler optical microscope (Fig. 3.2). The silicon particles are non-uniformly distributed in the Al matrix.

Fig. 3.1 Optical microscopic photograph of the polished Al 390 substrate

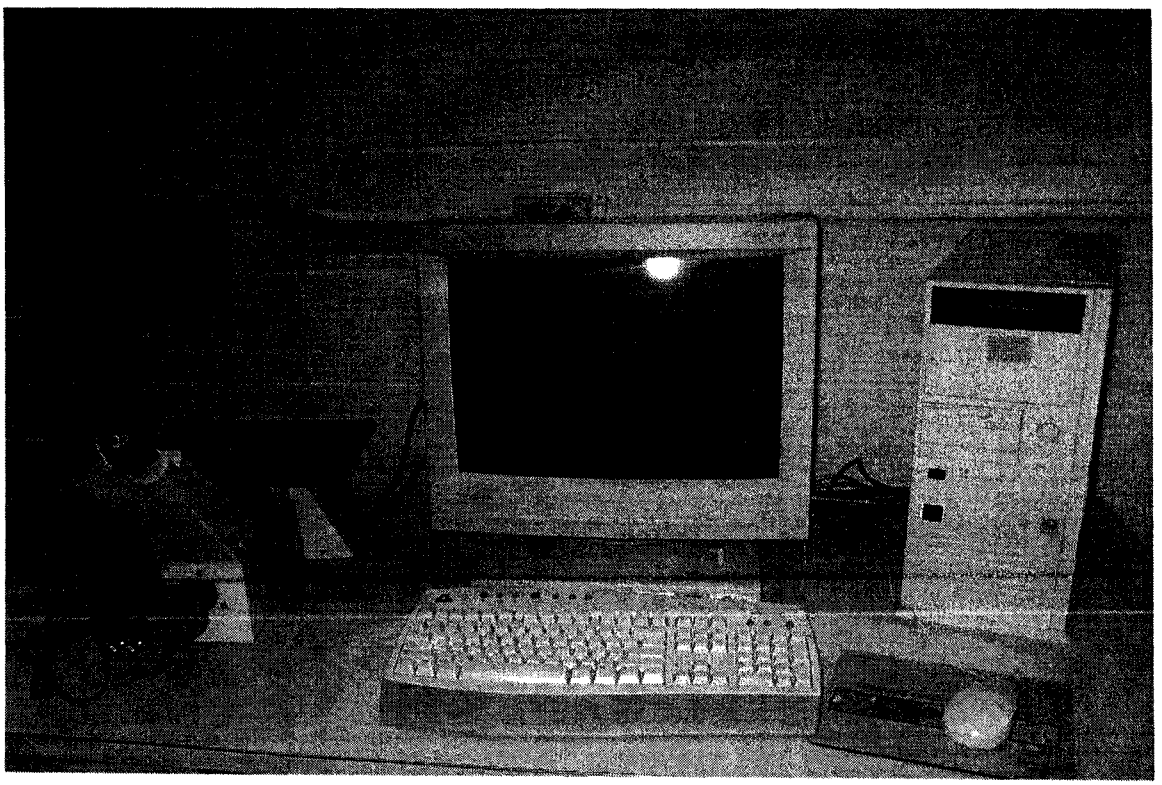

Fig. 3.2 Buehler optical microscope

3.1.2 Preparation of coatings

The PEO coating unit in this thesis consists of an electrolyser and a power electrical source. A DC power supply (Advanced Energy MDX 10K) was chosen (Fig. 3.3). The output voltage capacity is 0 to 1000V. 490V was the maximum output voltage used in this study to deposit thin coatings. The electrolyser is comprised of (i) an aluminum bath, with a plastic transparent window for observation, (ii) a plastic holder to fix the aluminum sample (anode) and insulate it from the bath, (iii) a circulating system to allow the electrolyte to circulate, and (iv) a stainless steel jet nozzle as a counter electrode (cathode), which can jet electrolyte toward the anode (i.e. the sample to be treated) to form an electrical circuit. The nozzle, which is connected to a rotatable shaft, can also spray and rotate at the same time. The schematic drawing of treatment cell for jet PEO coatings is shown in Fig. 3.4.

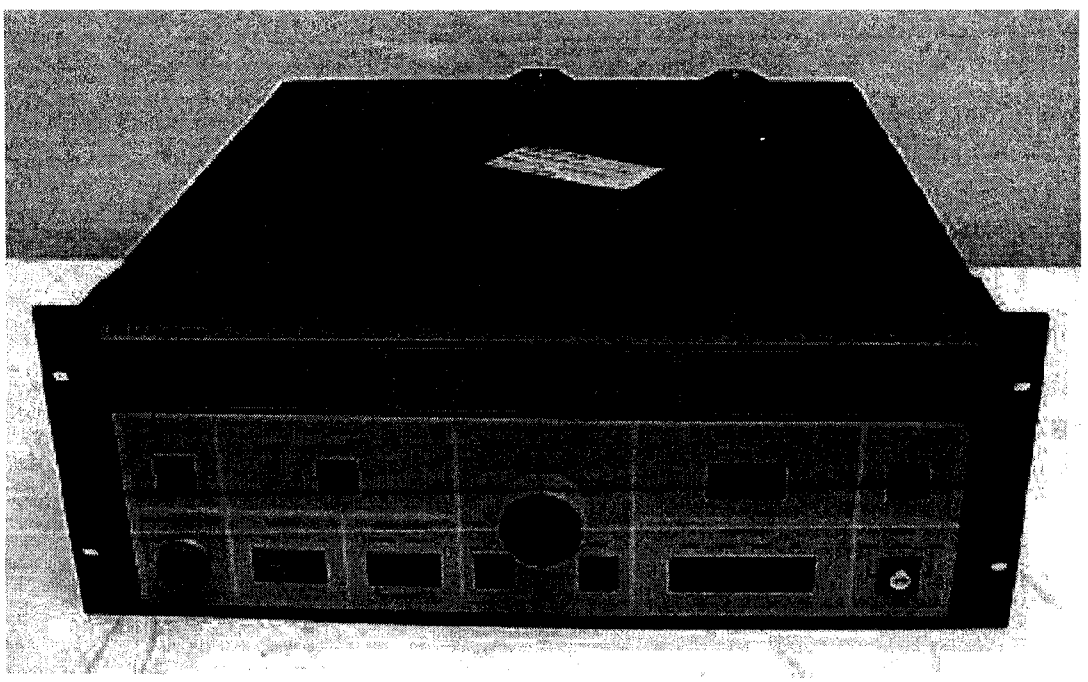

Fig. 3.3 Advanced energy MDX 10K

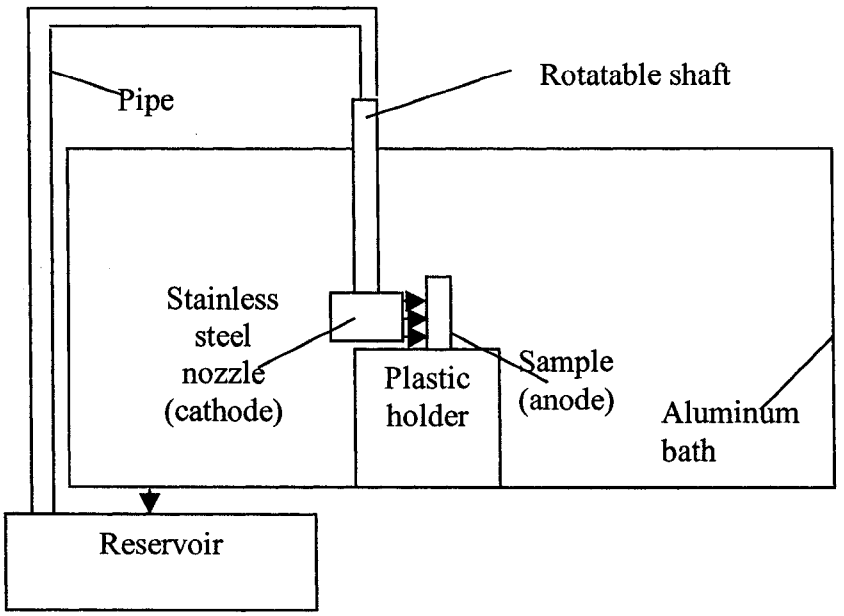

Fig. 3.4 Schematic diagram of the treatment cell for the EJPP PEO process

An alkali-silicate solution (Na_2SiO_3-KOH) was used as the electrolyte to produce PEO coatings on Al 390 substrates. A constant current density $0.3A/cm^2$ was set for all coatings. Since the conductivity of the oxide film decreases with the increase of coating thickness, the input voltage between anode and cathode has to increase gradually to maintain the current density. Voltage increment vs. treatment time was recorded for each sample. Two groups of PEO coatings were produced with two different alkali-silicate solution concentrations, 4g/l Na_2SiO_3 with 0.4g/l KOH and 8g/l Na_2SiO_3 with 0.8g/l KOH, listed in Table 3.2. Each group had three samples, of which the final voltages reached 410V, 450V and 490V, respectively. After treatment, all samples were taken out from the electrolyte, then flushed by distilled water and dried for the following tests.

Table 3.2 Sample codes for PEO coatings treated with different process parameters

Current density: 0.3A/cm^2 (constant)		Voltage (V)		
		410	450	490
Electrolyte concentration	4g/l Na_2SiO_3 0.4g/l KOH	X11	X12	X13
	8g/l Na_2SiO_3 0.8g/l KOH	X21	X22	X23

3.1.3 Characterization and tribological tests

(i) Surface morphology and coating thickness

A JEOL Scanning Electron Microscope (SEM) (Fig. 3.5) was employed for study on the coating surface morphology. A FEI SEM with Electron Dispersive X-ray (EDX) was used to identify the silicon particles in the substrate (Fig. 3.6). For coatings X13, X22, X23, the coating thickness was determined by the SEM observation on the cross-sections of the coatings. Cross-sections of samples were mounted with resin and polished with SiC abrasive paper of different grit size. Alumina suspension was used for the final polishing. All mounted samples were sputter-coated with gold before SEM observation. All SEM testing operated at an accelerating voltage 15KV. For coatings X12 and X22, the thickness was determined by F20 thin film measurement system (Filmetrics, Inc.), Fig. 3.7.

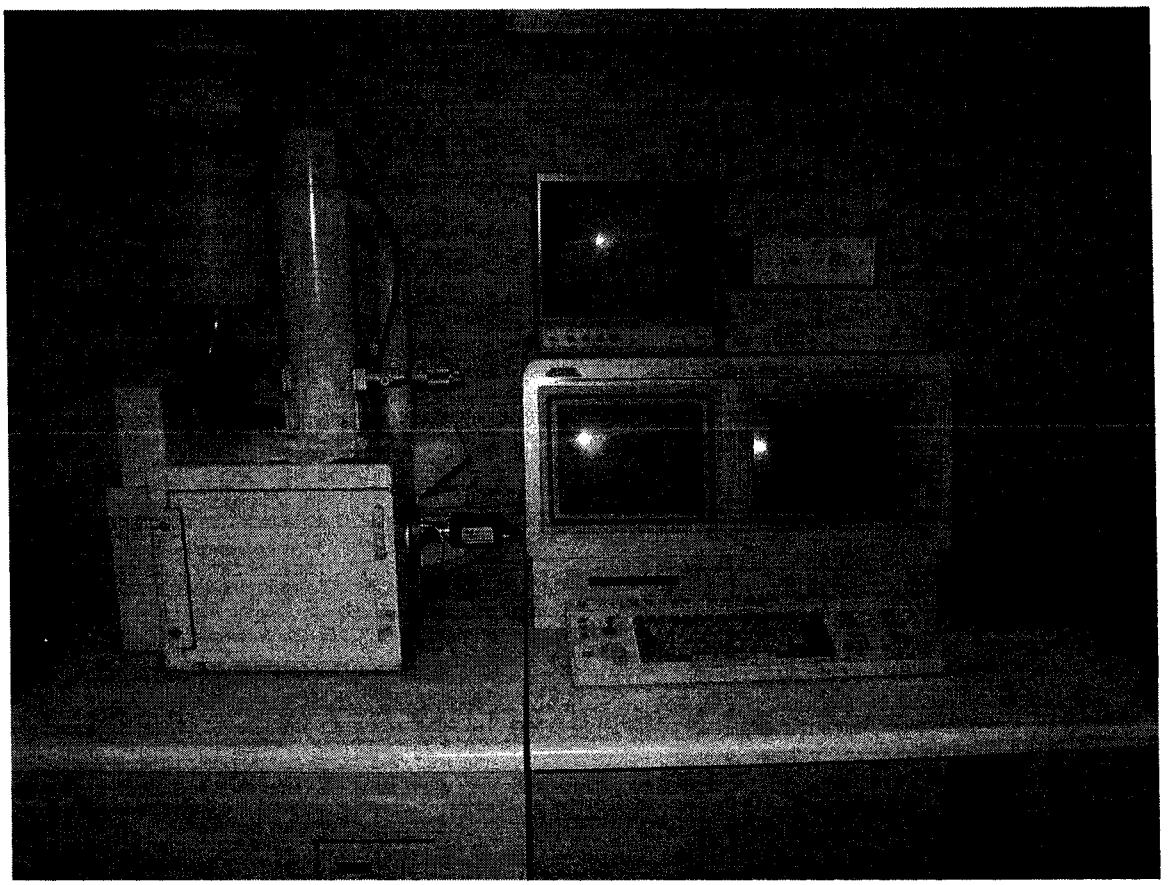

Fig. 3.5 JEOL Scanning Electron Microscope (SEM)

(ii) Surface roughness measurement

Mitutoyo SJ-201P surface profiler (Fig. 3.8) with a data acquisition system was used to measure the surface roughness of all testing samples, including Al substrates, PEO coatings and the etched Al samples.

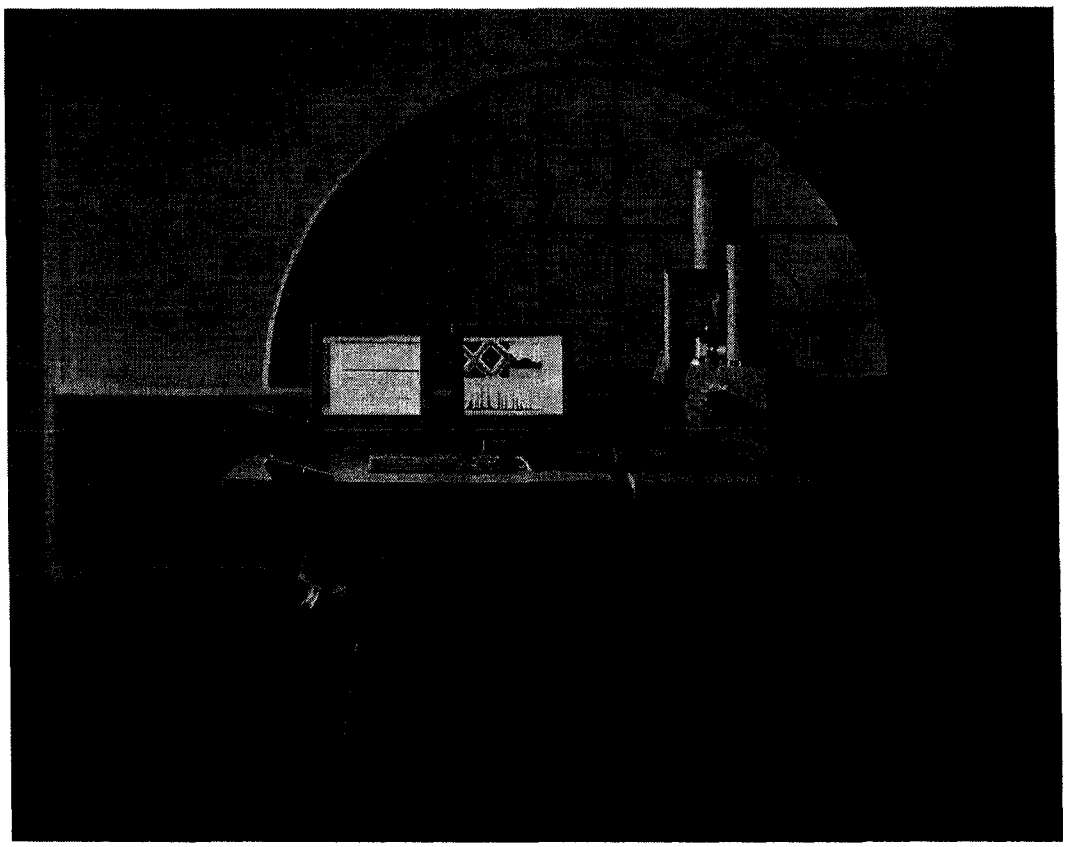

Fig. 3.6 FEI Scanning Electron Microscope (SEM)

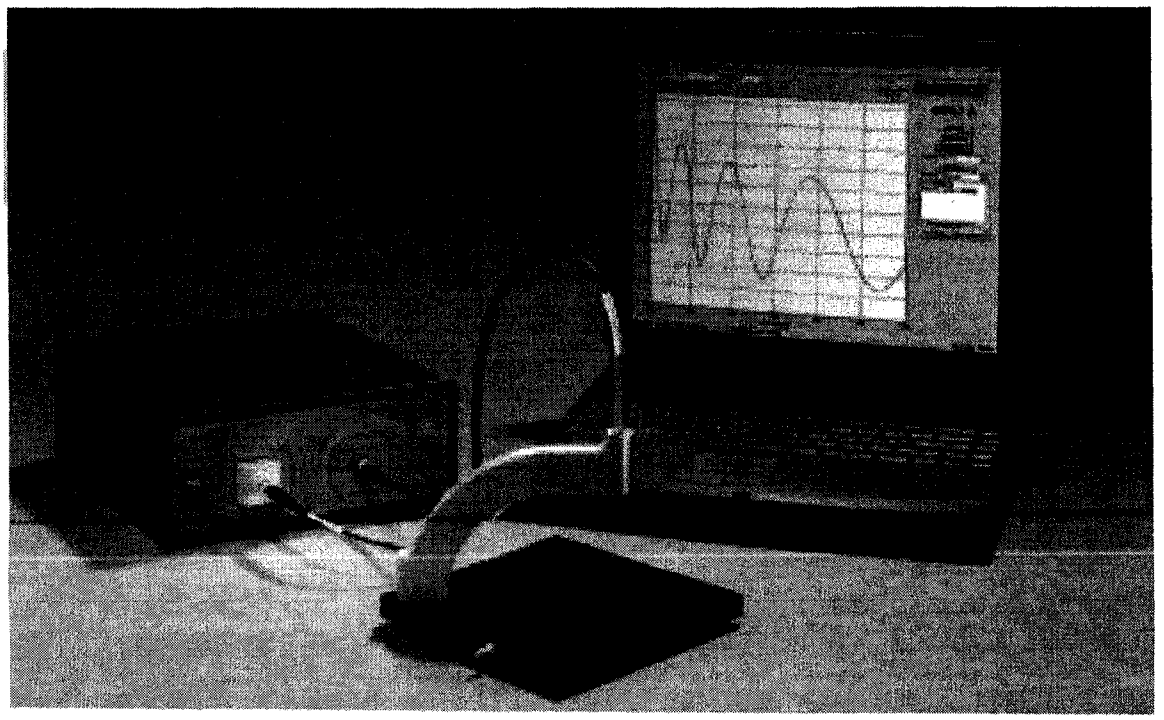

Fig. 3.7 Filmetrics F20 thin film measurement system

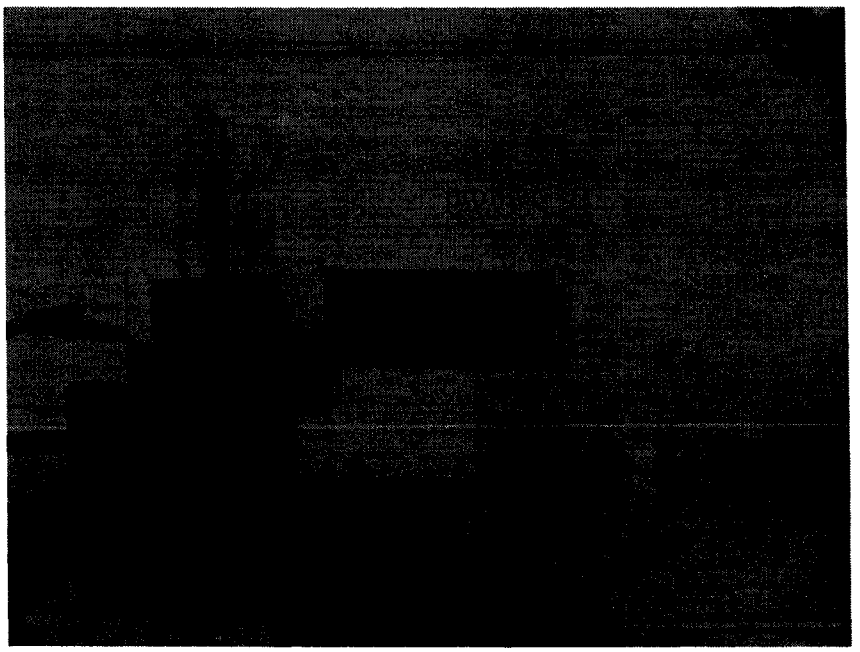

Fig. 3.8 Mitutoyo SJ-201P surface profiler

(iii) Tribological tests of Al 390 and PEO coatings

Tribological properties of Al390 were tested by use of a reciprocating sliding tester, attached to a pin-on-disc tribometer (Sciland Pin/Disc Tribometer PCD-300A), (shown in Figs. 3. 9 (a, b, c)) against 52100 Cr steel ball (5 mm diameter) under boundary oil lubrication and residual oil lubrication. 5W-30 engine oil was wiped on the sample surface to simulate boundary lubrication. The residual oil lubrication was generated by swabbing the oil on the sample surface. All the tests were performed under room temperature (20 ^{0}C), ~50% humidity, a 2N normal load, 0.04m/s sliding speed, 250m sliding distance and 2Hz reciprocating frequency. The sliding wear tests were also conducted to PEO coatings using the same instruments and parameters but only under residual oil lubrication. The tribometer recorded the coefficient of friction (COF) during the tests. The wear tracks of all samples were also investigated using SEM. And the worn

counterface steel balls were studied using the optical microscope (Fig. 3.2). The wear loss of counterface steel ball was represented by the average radius of the worn area.

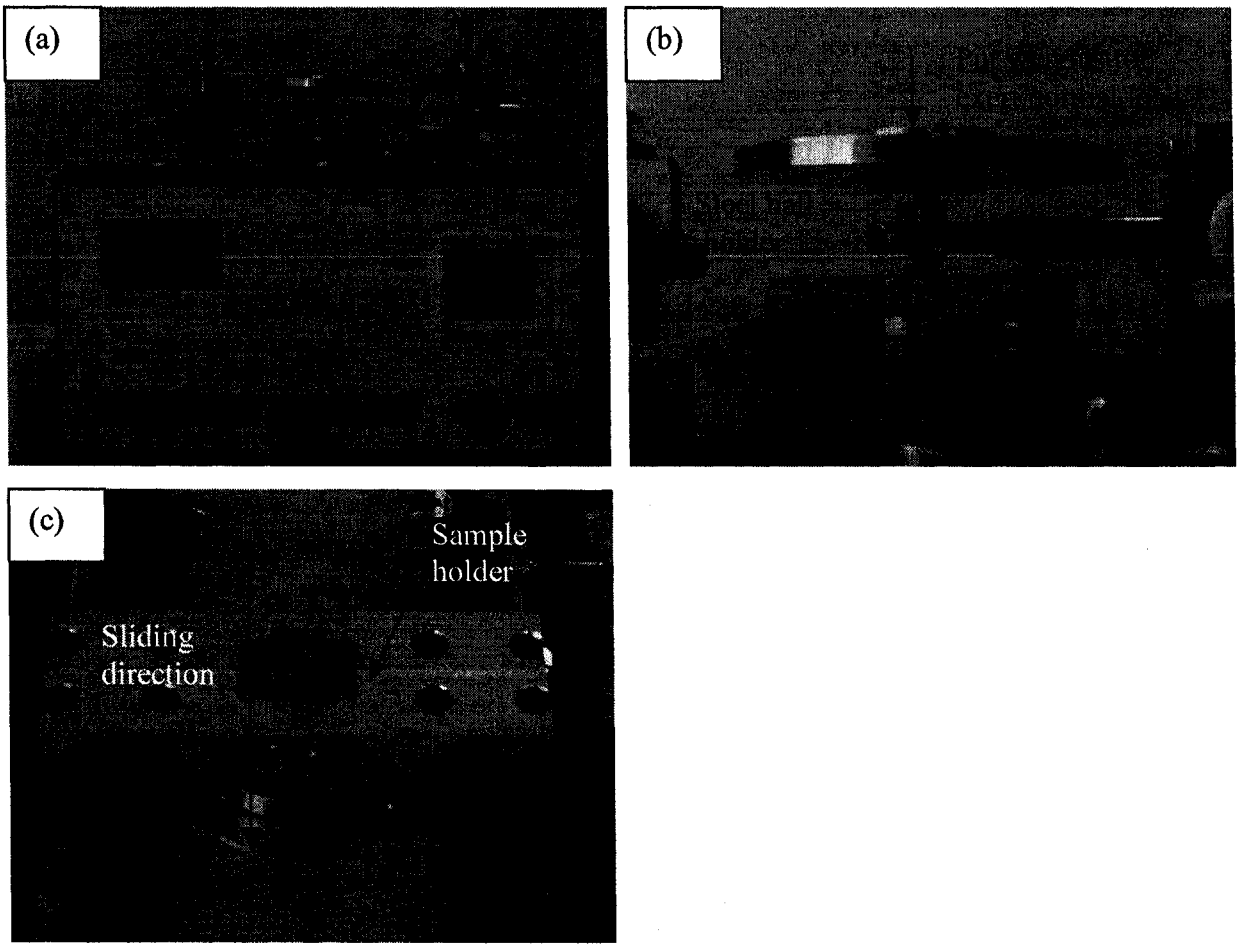

Fig. 3.9 Reciprocating sliding tester attached on (a) Sciland Pin/Disc Tribometer PCD-300A, (b) load cell and cantilever beam, (c) sample holder and sliding rails

3.2 Part B. Effect of pulsed bipolar DC on the PEO coatings

3.2.1 Preparation of coatings

A number of slices ($7\times1.5\times0.5$ cm^3) were also cut from cast Al-Si 390 alloy. The samples were prepared as the description in the section 3.1.1. Several polished Al390 samples

were etched with 10% KOH solution for 1 minute to expose the silicon particles. A SPIK 2000A bipolar pulse generator (Fig. 3.10) with the frequency varied in the 0.5 to 10kHz range was used to transform the DC current from the DC power supply used in the section 3.1.2 into the high frequency (3 kHz) pulsed bipolar DC, shown in Fig. 3.11. The positive pulse duration time was 80% of the period time of the pulse. 4g/l Na_2SiO_3 with 0.4g/l KOH silicate-alkali solution was used as the electrolyte. The current amplitude density was still 0.3 A/cm^2. Using the same electrolyser, four coatings, listed in Table3.3, were produced with their final voltages 350V, 370V, 390V, and 410V, respectively. The voltage change with the treatment time for each coating was also recorded.

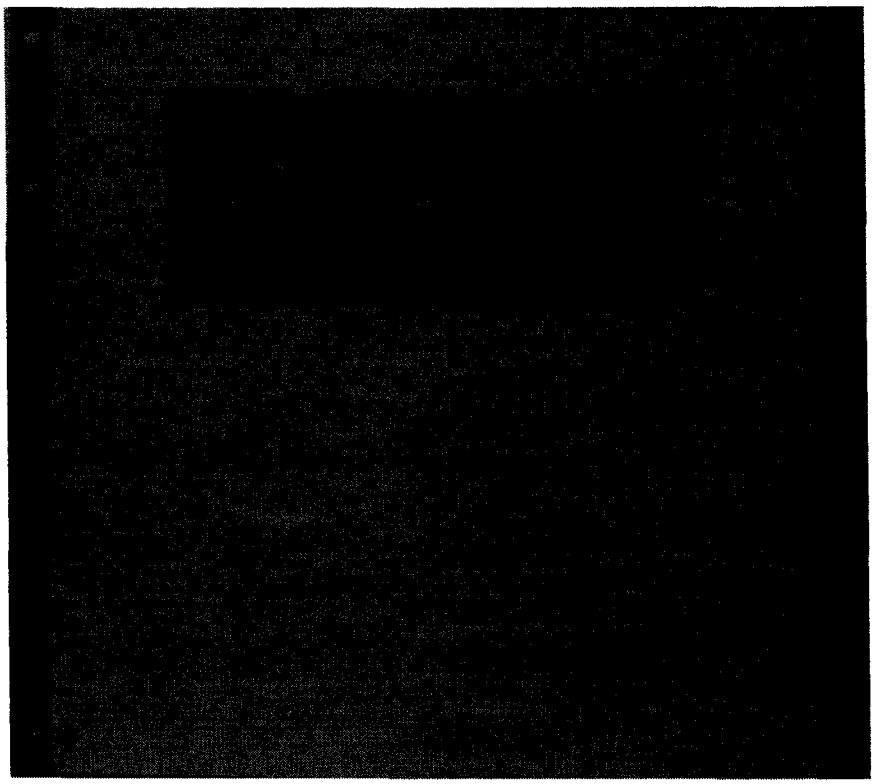

Fig. 3.10 SPIK 2000A bipolar pulse generator

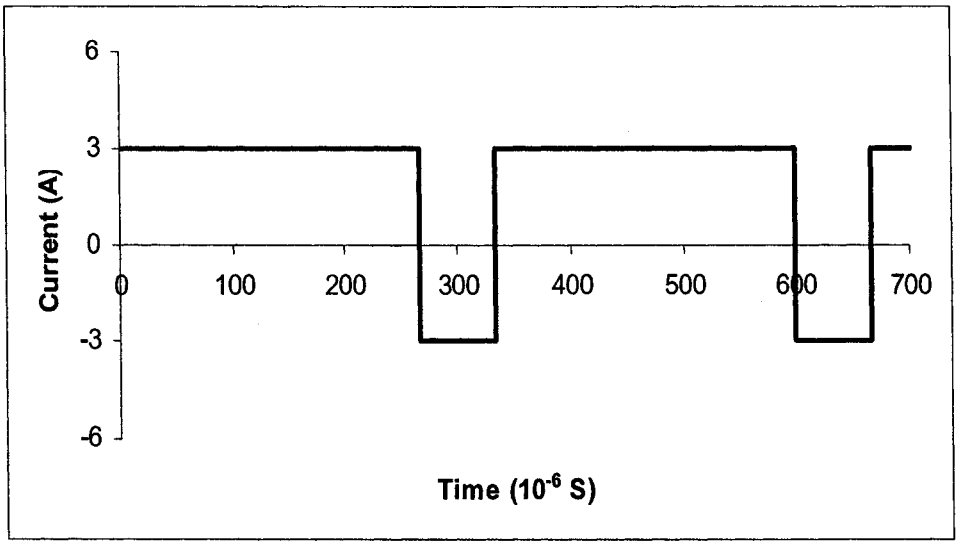

Fig. 3.11 Pulsed bipolar DC

Table 3.3 Sample codes for PEO coatings treated with different process parameters

Current density: 0.3A/cm^2 (bipolar pulsed current)	Voltage (V)			
Electrolyte concentration:	350	370	390	410
4g/l Na_2SiO_3 0.4g/l KOH	Y1	Y2	Y3	Y4

3.2.2 Characterization of coatings tribological tests

The morphology and surface roughness of coatings were investigated by SEM and surface profiler, described in section 3.1.3, individually. For coating Y1 and Y2, the coating thickness was also determined by F20 thin film measurement system. And the SEM observations for cross-section samples of coatings Y3 and Y4 were used to determine the coating thickness. The tribological tests were also conducted for coatings Y1, Y2, Y3 and Y4, using the reciprocating sliding tester with the same parameters as

those stated in section 3.1.3. For sample Y2 and the etched Al390, the tribological properties against steel balls with 2N normal load for 3600m sliding distance under residual lubrication were also investigated. The wear tracks and the counterface steel balls were studied using the same procedure as in section 3.1.3.

3.3 Part C. Effect of reciprocating sliding frequency on the tribological properties of PEO/graphite composite coatings on Al 6061

3.3.1 Preparation of Al6061 aluminum sample

Several aluminum cylinders ($\Phi 91 \times 6 \times 1.5$ cm^3) were cut from wrought Al 6061 alloy. The composition of this alloy is listed in Table 3.4. The internal faces of all cylinders were prepared just like the description in section 3.1.1.

Table 3.4 Nominal composition of Wrought Al alloy 6061

Alloy	Composition, wt%								
	Si	Fe	Cu	Mg	Mn	Zn	Ti	Cr	Al
Wrought Al alloy 6061	0.4-0.8	≤0.7	0.15-0.4	0.8-1.2	≤0.15	≤0.25	≤0.15	0.04-0.35	98

3.3.2 Preparation of coatings

4g/l Na_2SiO_3 with 0.4g/l KOH silicate-alkali solution was used as the electrolyte. The cylinder sample was fixed on the top of the plastic holder, and the jet nozzle was located inside the cylinder, shown in Fig. 3.12. During the PEO process, the jet nozzle sprayed

electrolyte toward the cylinder and rotated at 30rpm simultaneously to provide interruption to the established dielectric plasma discharges. Two carbon bars were also installed on the two side faces of the jet nozzle and pressed to the internal surface of the cylinder by springs. Rotating with the nozzle, the carbon bars rubbed against the formed oxide coating to form an oxide/graphite composite coating. The current density was set 0.3 A/cm^2. Two coatings with final voltages 380V and 430V, individually, were produced.

For another sample, 8g/l Na_2SiO_3 with 0.8g/l KOH silicate-alkali solution was used as the electrolyte. The final voltage for this composite coating was 460V. The variation of the voltage with the treatment time for each coating was still recorded.

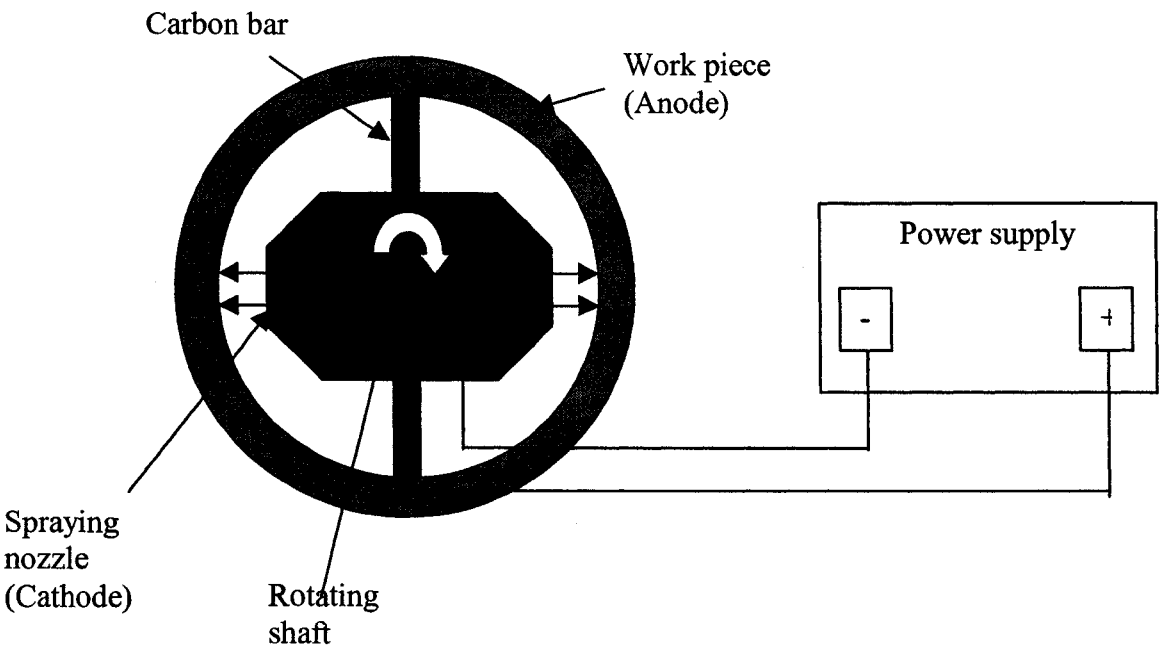

Fig. 3.12 Diagram of the coating unit to produce PEO/graphite composite coatings

3.3.3 Characterization of coatings and tribological tests

(i) Surface morphology and coating thickness

SEM was employed for study on the substrate and coating surface morphology using the same parameter as in section 3.1.3. F20 thin film measurement system was applied to determine the coating thickness of Z1. SEM observations for cross-section samples of Z2 and Z3 were used to measure the coating thickness.

(ii) Surface roughness measurement

Mitutoyo SJ-201P surface profiler was used to measure the surface roughness of the PEO coatings and the Al 6061 substrate.

(iii) Tribological tests of Al 6061 and coatings

The tribological properties of Al 6061 and coating Z1, Z2 and Z3 under residual oil lubrication were tested by use of the same reciprocating sliding tester with the following parameters listed in Table 3.5.

The tribological properties of Al 6061 and coating Z1, Z3 under mixture of boundary and hydrodynamic lubrication condition, where the steel balls were immersed into the lubricant (5W30 engine oil) and slid against the coating samples, Fig. 3.13, with the parameters listed in Table 3.6.

All wear tracks and counterface steel balls were also observed using the same procedure as in section 3.1.3.

Table 3.5 Tribological test parameters under residual oil lubrication condition

Samples	Reciprocating frequency	Normal load	Sliding distance (m)		
			50	250	3600
Al6061	2Hz	2N	√		
Z1			√	√	
Z2			√	√	
Z3			√	√	√

Table 3.6 Tribological test parameters under mixed lubrication condition

Samples	Normal load	Reciprocating frequency (Hz)		
		2	4	6
Al6061	1N	√	√	√
Z1		√	√	√
Z3		√	√	√

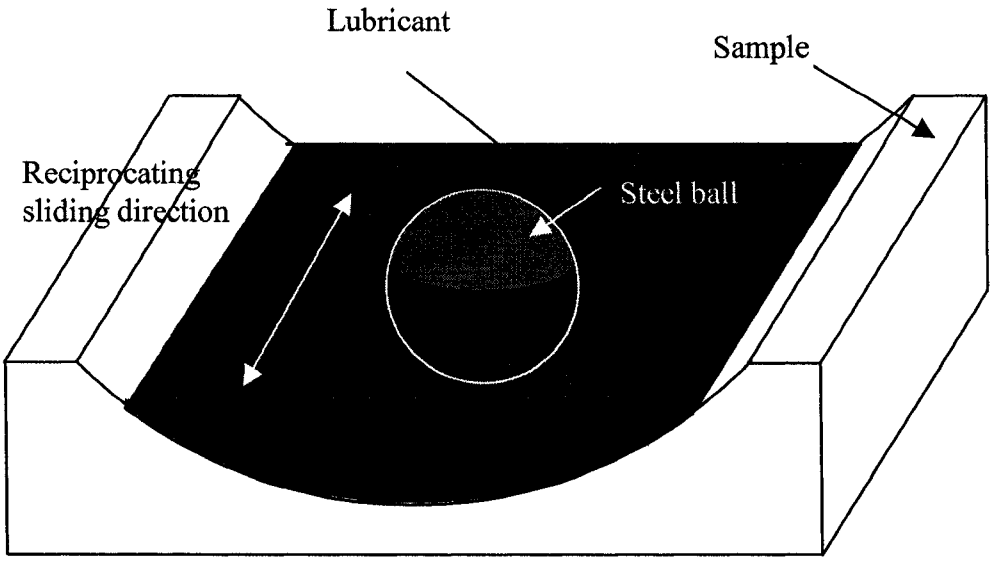

Fig. 3.13 Diagram of reciprocating sliding test under oil immersion lubrication

CHAPTER 4 EXPERIMENTAL RESULTS AND DISCUSSION I: SURFACE MORPHOLOGY AND TRIBOLOGICAL PROPERTIES OF PEO COATINGS ON AL390 SUBSTRATES TREATED WITH DC POWER

As mentioned in chapter 3, PEO coatings were deposited on the Al 390 alloys using the processing parameters listed in Table 3.2. In this chapter, the surface morphology and tribological properties of the coatings produced with DC power along with the Al 390 substrate are analyzed.

4.1 Tribological properties of Al 390 substrates

4.1.1 Morphology of Al 390 alloys before and after tribological testing

Figs. 4.1 (a) and (b) show the morphology of Al 390 alloys before tribological testing. Needle shaped silicon particles were observed, indicated by arrows in the figures. Due to the polishing process, the Al matrix was slightly etched, so that the silicon particles were a little protruding from the matrix. The average roughness of the unworn surface obtained using the surface profiler was 0.17 μm. From the surface profile (Fig. 4.2), the silicon particles were about 0.5μm higher than the matrix. According to the Hertz contact mechanism, of which the mechanism was illustrated in Fig. 4.3, the exposed hard silicon particles were expected to provide a good anti-wear contact surface, which is favorable to protect Al matrix from abrasive and adhesive wear.

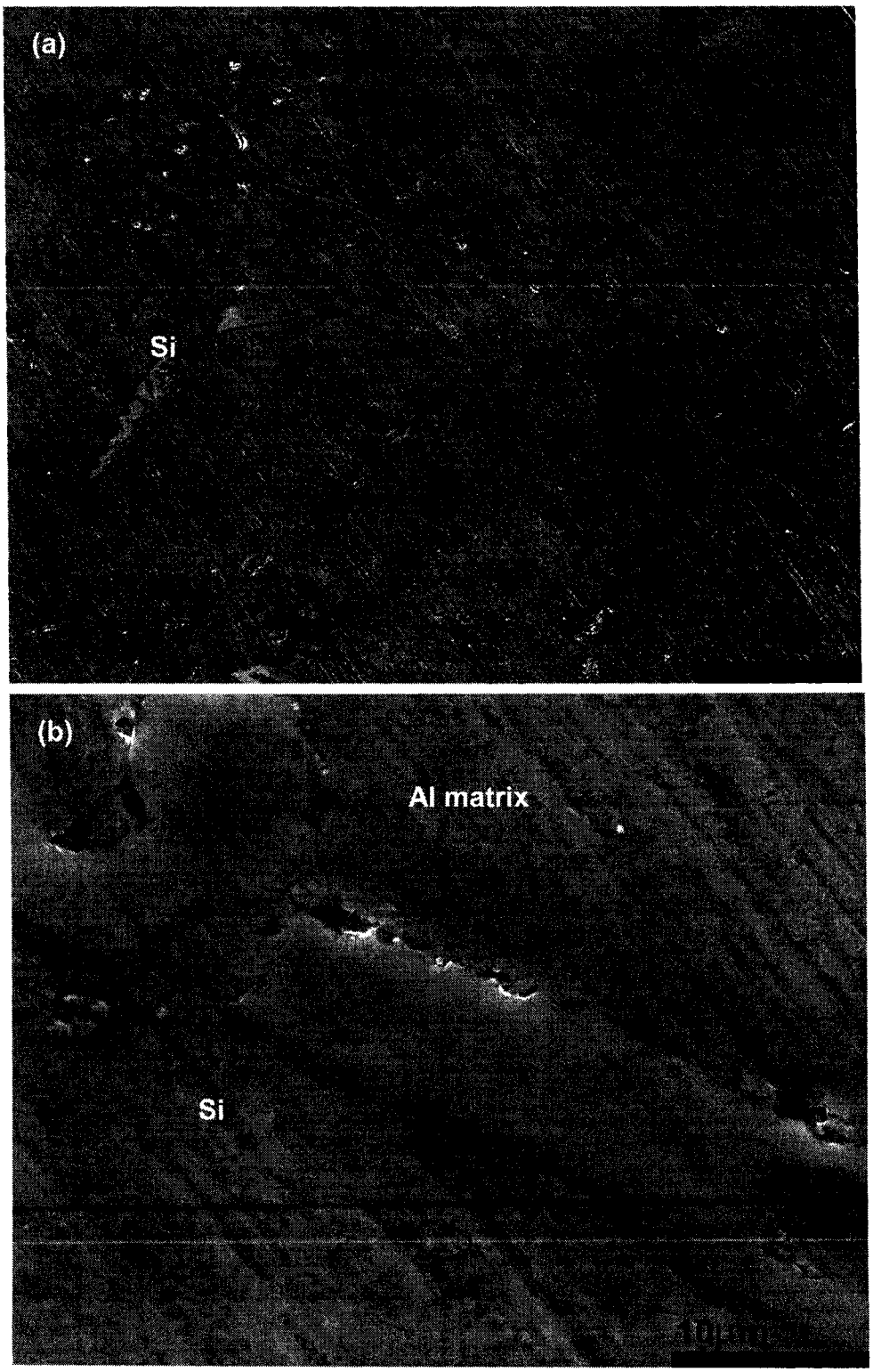

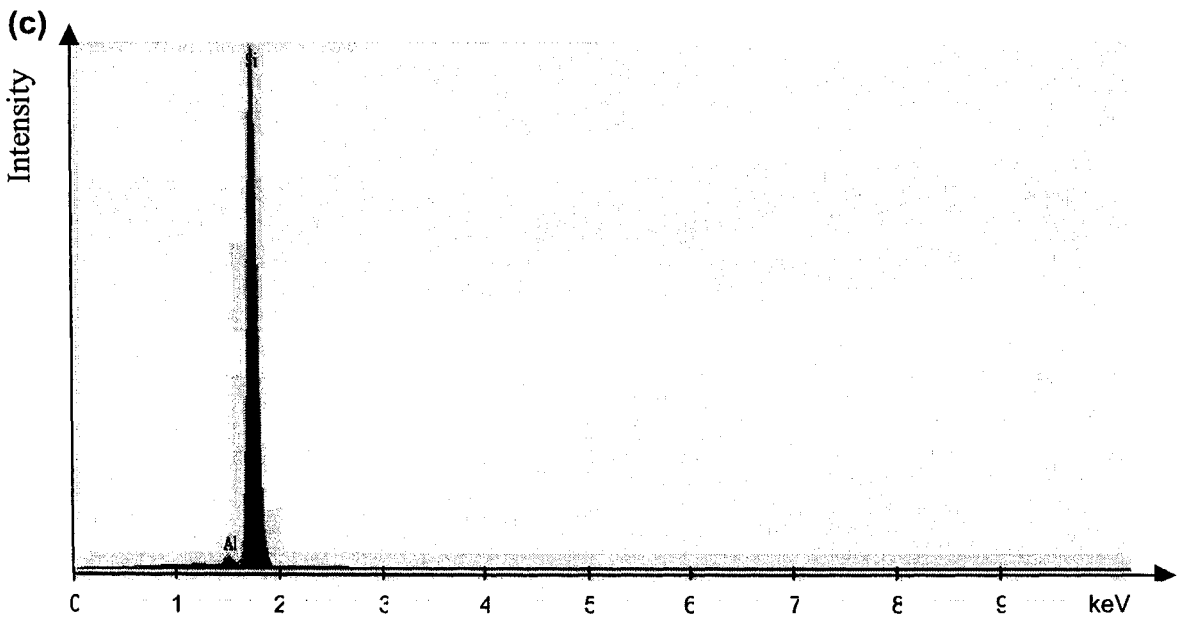

Figure 4.1 SEM micrographs of Al 390 (a) 200×, (b) 6000× and (c) EDX spectrum of the region of a needle shaped Si particle

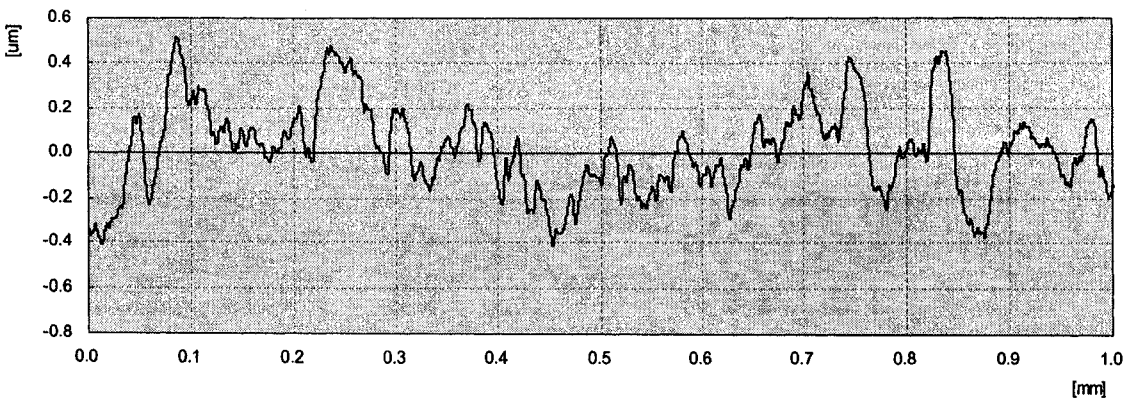

Fig. 4.2 Surface profile of the Al 390 sample

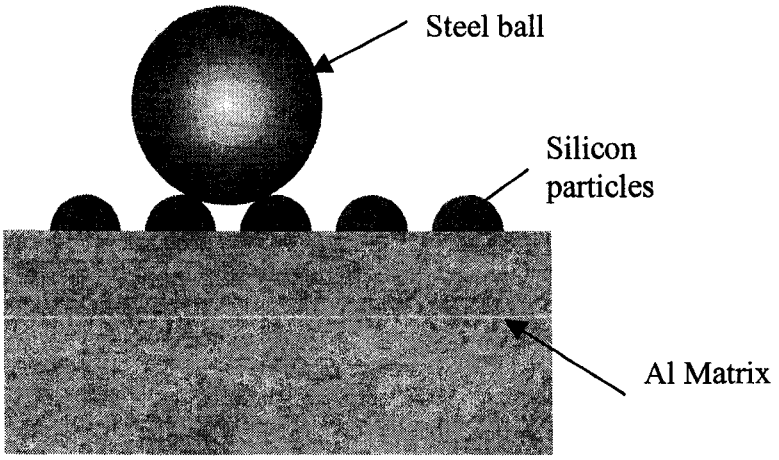

Fig. 4.3 Mechanism of Hertz contact

Figs 4.4 (a) and (b) show the wear track of Al 390 against a steel ball with residual oil lubrication under a 2N normal load for 250m sliding distance. Mild abrasive wear [60] occurs to Al matrix. At the interface between the Si particle and the Al matrix, cracks are observed. Also, there is fracture in the Si particle. Figure 4.4 (d) is the optical microscope photograph of the counterface steel ball, which experienced severe abrasive wear. The diameter of worn area is 400 μm.

Figures 4.5(a) and (b) illustrate the wear track of Al 390 against steel ball with boundary oil lubrication also under a 2N normal load for 250m sliding distance. No obvious abrasive wear is observed in the Al matrix. But, similar to the wear track of Al 390 against steel ball under residual oil lubrication, cracking at the interface between Si particles and Al matrix and fracturing of the brittle Si particle occur. Figure 4.5 (d) shows the optical microscope photograph of the counterface steel ball. Compared with the steel

ball sliding with residual lubrication, the steel ball sliding with boundary lubrication has a much smaller worn area, with the diameter of only 200 μm.

Figs. 4.6 (a, b) show Coefficient of Friction (COF) curves for the Al 390 sample sliding against steel ball with residual and boundary lubrication. With more lubrication added, the wear test under the boundary lubrication presents a smaller COF.

4.1.2 Discussion

During the polishing process, the aluminum matrix is etched to some extent, resulting in the protruding silicon particles. The hard silicon particles provide a hard contact face to protect the soft aluminum matrix during the sliding test. However, according the Hertz contact stress calculation, the stress, 800MPa, is much higher than the shear strength of the Al matrix, only 50MPa. Therefore, due to the softness of the Al matrix, the exposed Si particles, which increase the hardness of the contact surface, can not be supported by the Al matrix, causing a large plastic deformation by shearing occurred at the interface between the Si particle and the Al matrix. Also, the brittleness of the silicon particles results in the crack or fracture of the particles under impact (Fig. 4.4 (b) and Fig. 4.5 (b)). After that, aluminum matrix to steel contact occurs, resulting in the scratches in the soft Al matrix (Fig. 4.4 (a) and Fig. 4.5 (a)).

In both lubrication situations, where a complete fluid film does not develop between steel ball and Al substrate, momentary dry contacts between wear surface asperities occurs. For the counterface steel ball, the hard and sharp Si particles in the Al sample plough

across the steel ball surface during the sliding test, causing scratches in the worn area. However, for boundary lubrication, less dry contacts are involved, exhibiting less material removal of the counterface steel ball and a smaller COF.

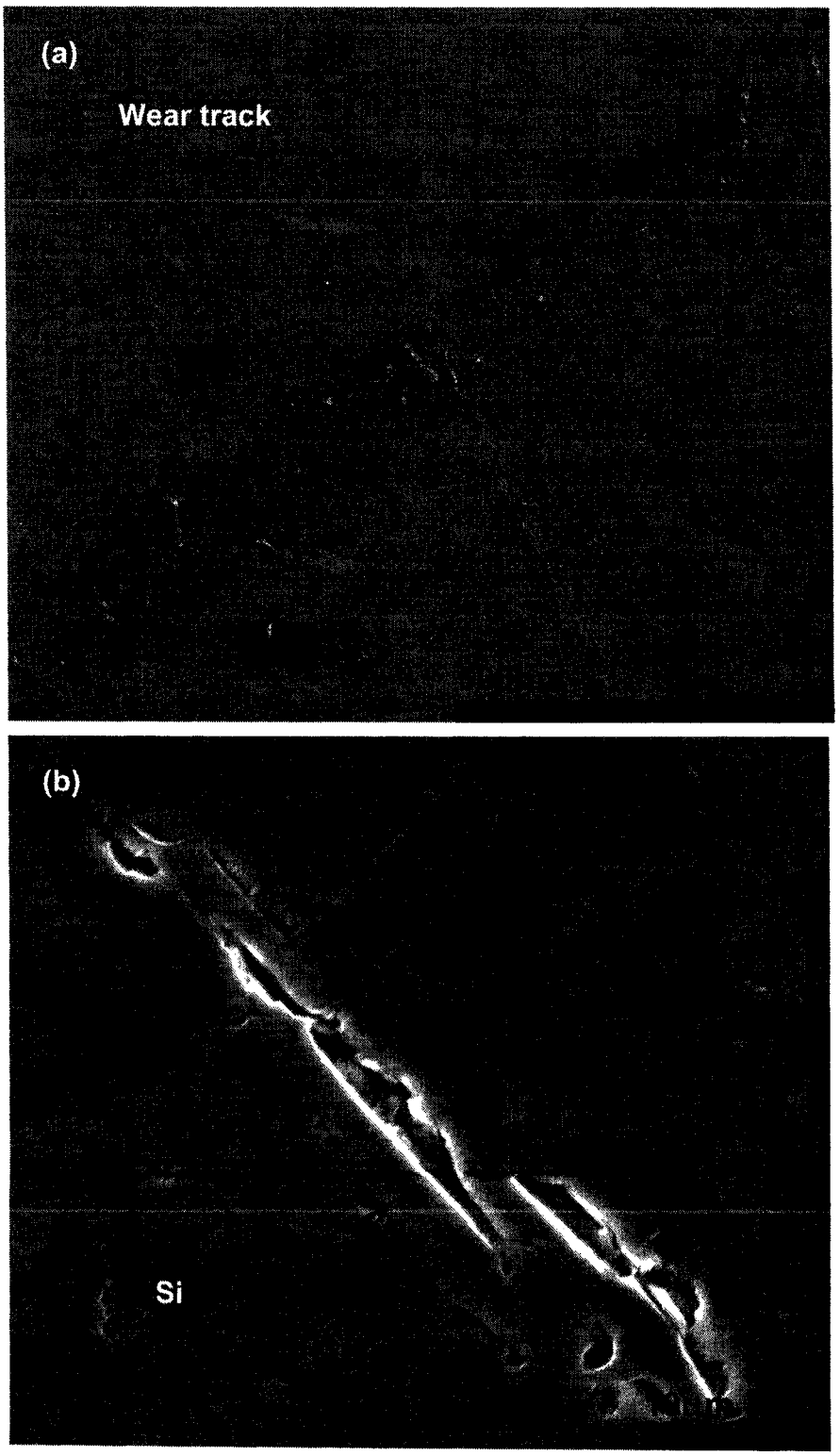

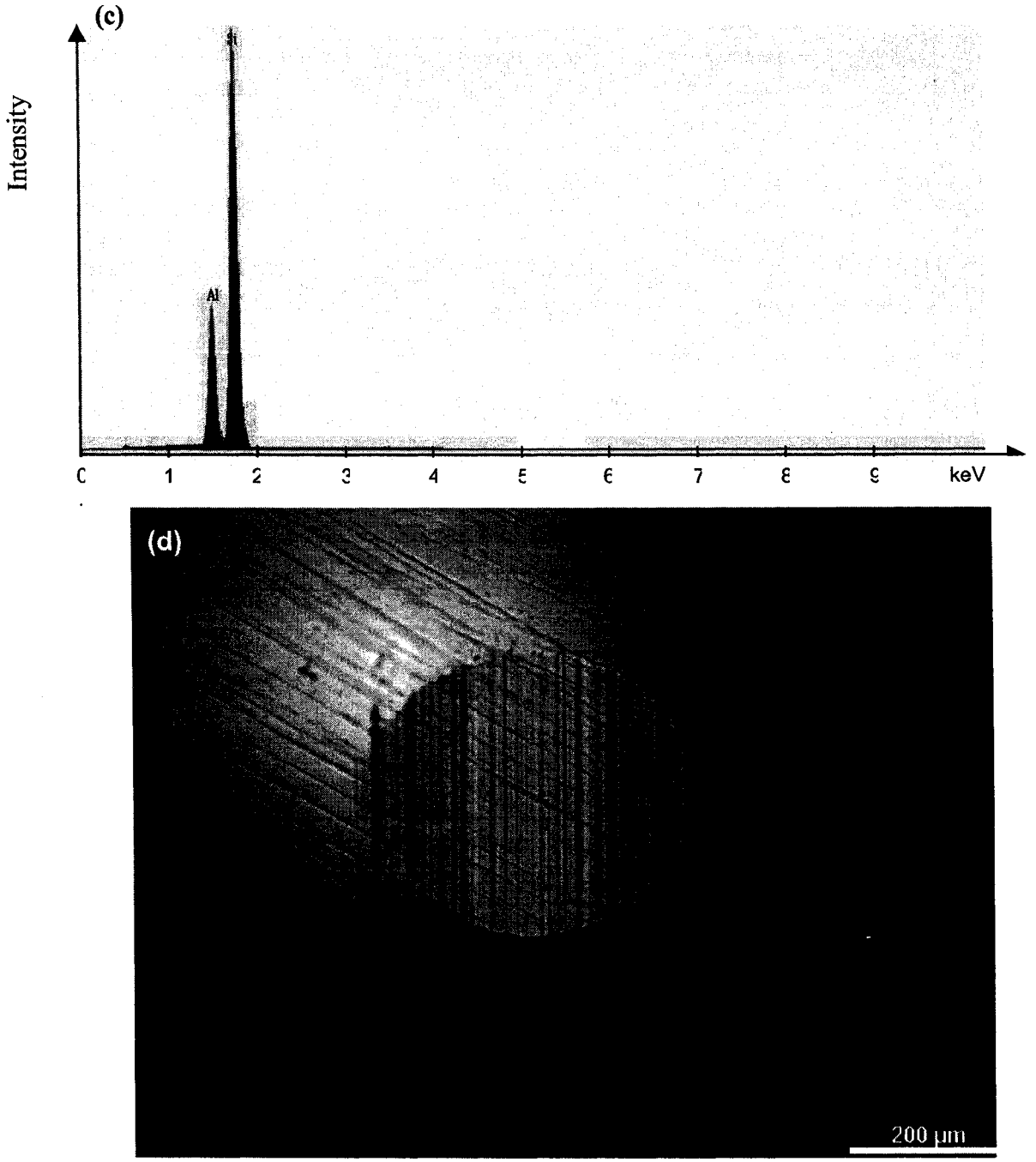

Fig. 4.4 SEM micrographs of wear track of Al 390 against steel ball with 2N normal load under residual oil lubrication for 250m sliding distance. (a) 200×, (b) 6000× , (c) EDX spectrum of needle shaped Si particle area and (d) the optical microscopic photograph of the corresponding worn steel ball

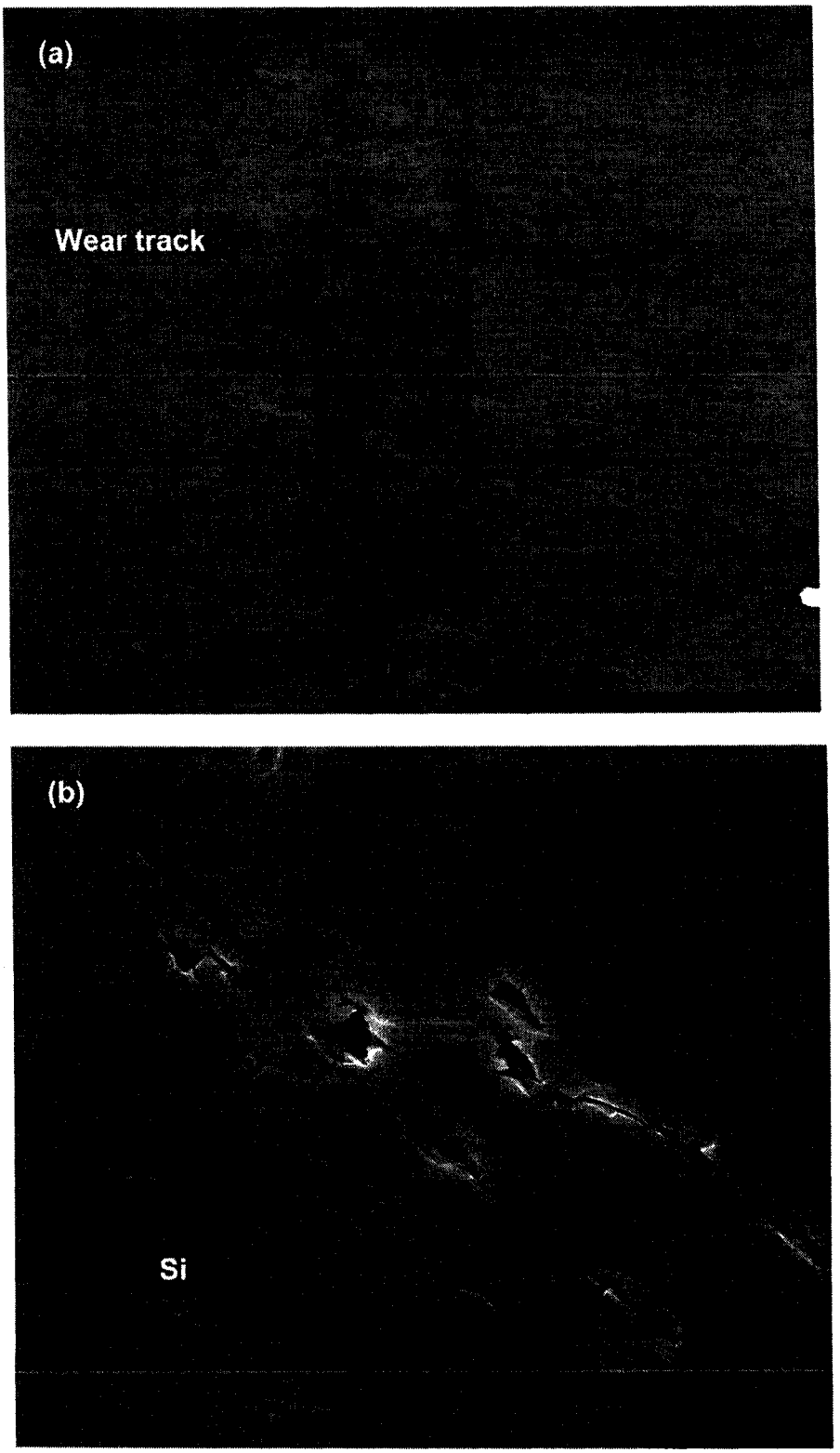

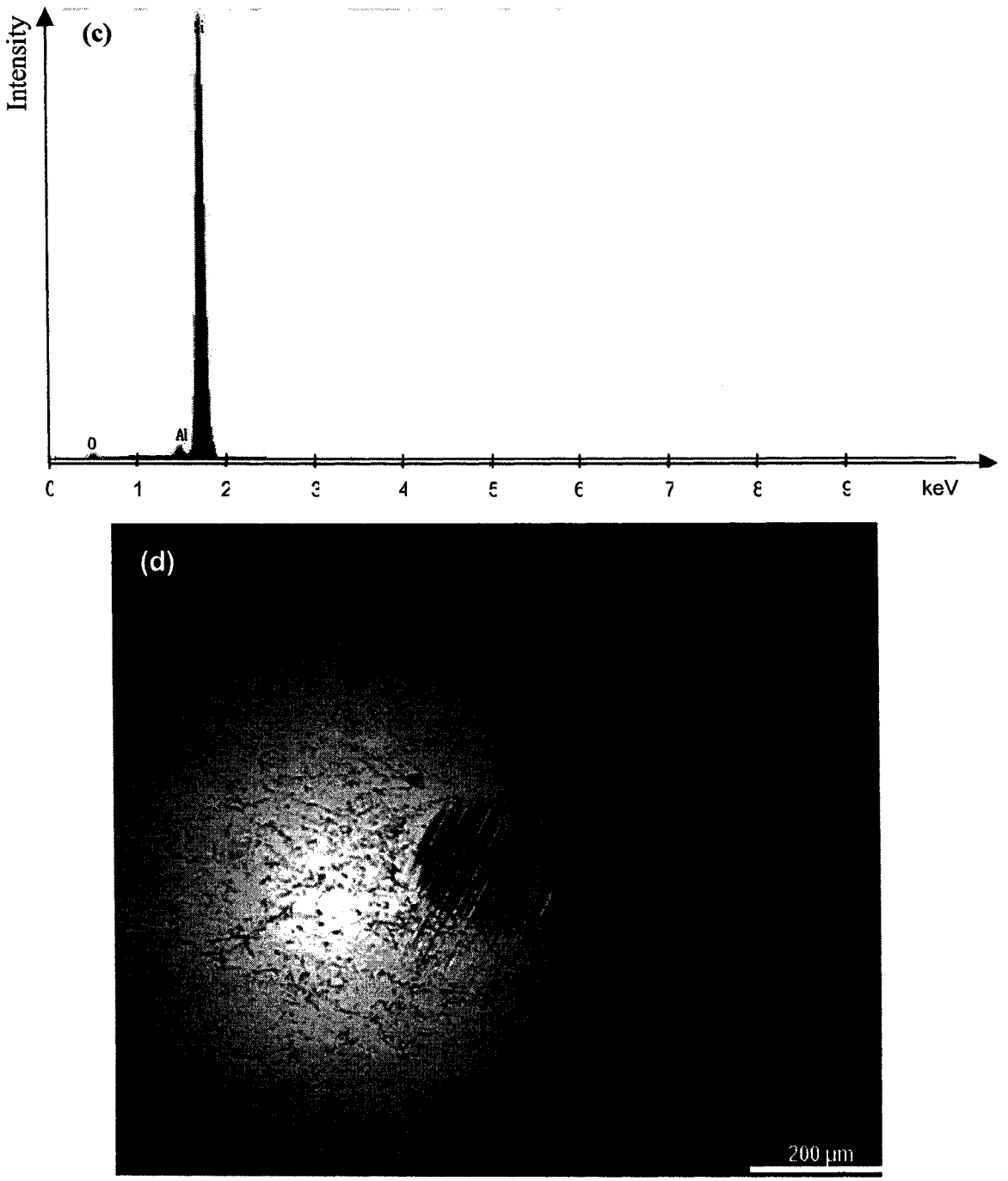

Fig. 4.5 SEM micrographs of wear track of Al 390 against steel ball with 2N normal load under boundary oil lubrication for 250m sliding distance. (a) 250×, (b) 6000× , (c) EDX spectrum of needle shaped Si particle area and (d) the optical microscopic photograph of the corresponding worn steel ball

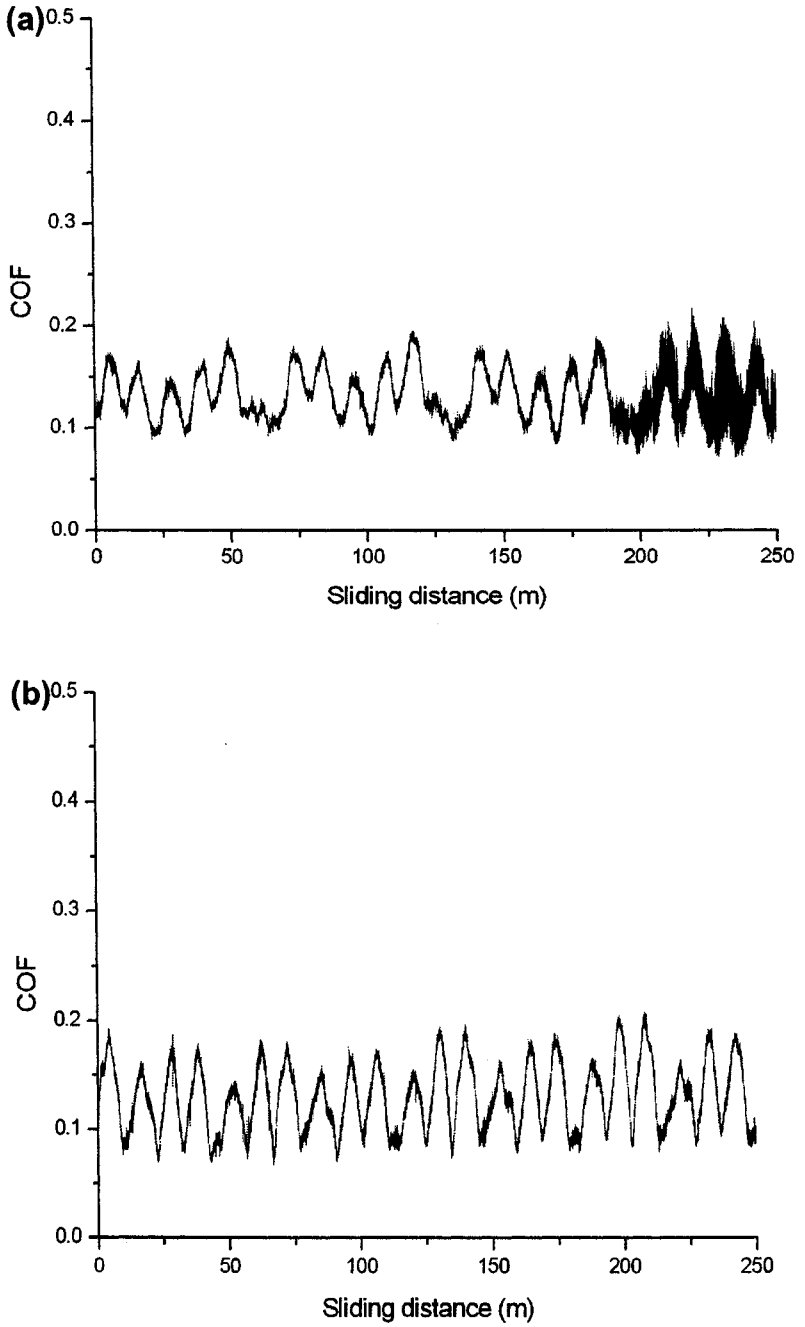

Fig. 4.6 Coefficient of Friction (COF) curves of Al 390 against steel ball with 2N normal load under (a) residual and (b) boundary oil lubrication for 250m sliding distance

4.2 Characterization of DC PEO coatings on Al 390

4.2.1 Voltage variation during the PEO process

Figs 4.7 (a) and (b) show the voltage increment of two groups of PEO coatings, which were treated with different electrolyte concentration, 4g/l and 8g/l, respectively, during the PEO treatment on Al 390. For each group, the voltage increment curves of all samples are very similar. Therefore, the curves of coating X13 and X23 can be used to represent the voltage variation of each group during the PEO process, shown in Fig. 4.7 (c) and (d) individually. For coating X23, in order to demonstrate the voltage change at the beginning of the PEO process and compare with coating X13, only the initial part of the curve is plotted. Several distinct stages can be identified in terms of the voltage growth rate in each figure. According to the two figures, the voltage range of each stage for two groups and how many stages each sample experienced during the PEO process can be determined and listed in Table 4.1. Obviously, the treatment for coating X11, of which the process stops at 410V, only goes through two stages, and the treating processes for the other coatings X12 and X13 undergo three and four stages, individually. Also, the voltage growth rate in each stage for two groups is calculated and shown in Table 4.2. Clearly, the voltage always grows faster in the first group than in the second group.

Table 4.1 Voltage range of each stage for different electrolyte concentration

		Samples	Voltage range of each stage				Treatment time (min)
			Stage I	Stage II	Stage III	Stage IV	
			0-325V	325V-440V	440V-475V	≥475V	
Electrolyte concentration	4g/l	X11(410V)	•	•			0.4
		X12(450V)	•	•	•		0.7
		X13(490V)	•	•	•	•	2.4
			0-260V	260V-400V	400V-425V	≥425V	
	8g/l	X21(410V)	•	•	•		1.5
		X22(450V)	•	•	•	•	5.3
		X23(490V)	•	•	•	•	26.8

Table 4.2 Voltage growth rate of each stage for different electrolyte concentration

		Voltage growth rate (V/S)			
		Stage I	Stage II	Stage III	Stage IV
Electrolyte concentration	4g/l	24.3	7.2	0.98	0.15
	8g/l	11.8	5.8	0.6	0.04

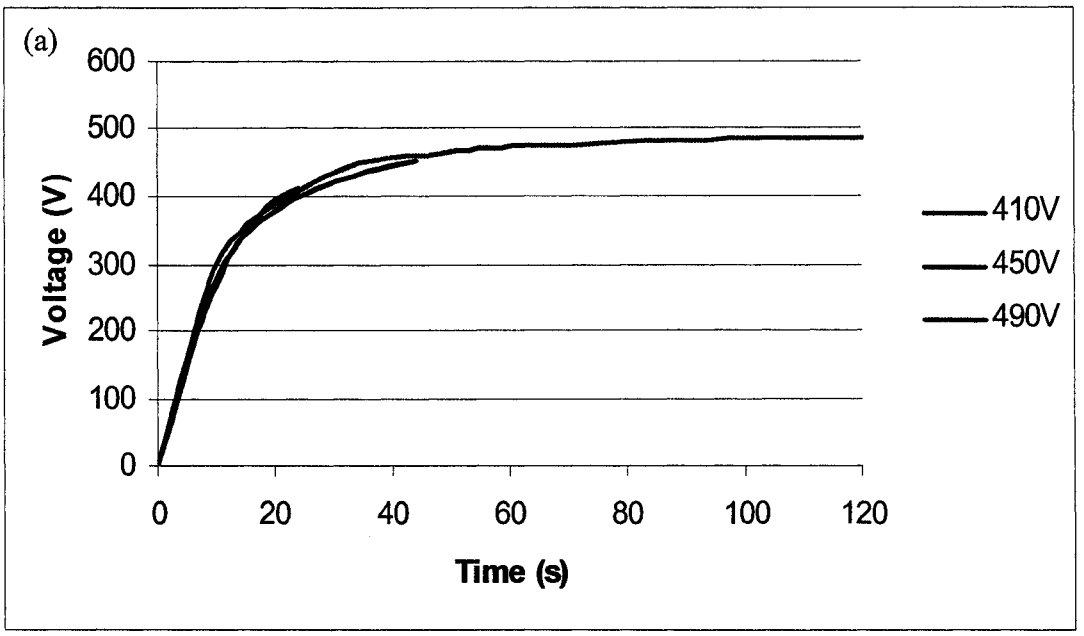

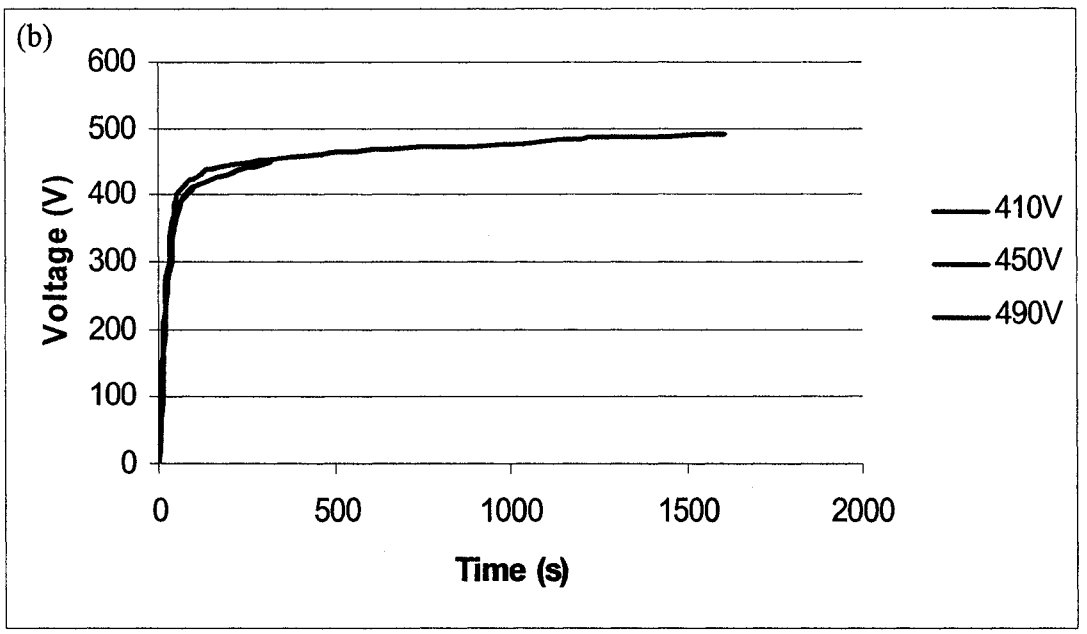

Fig. 4.7 to be continued

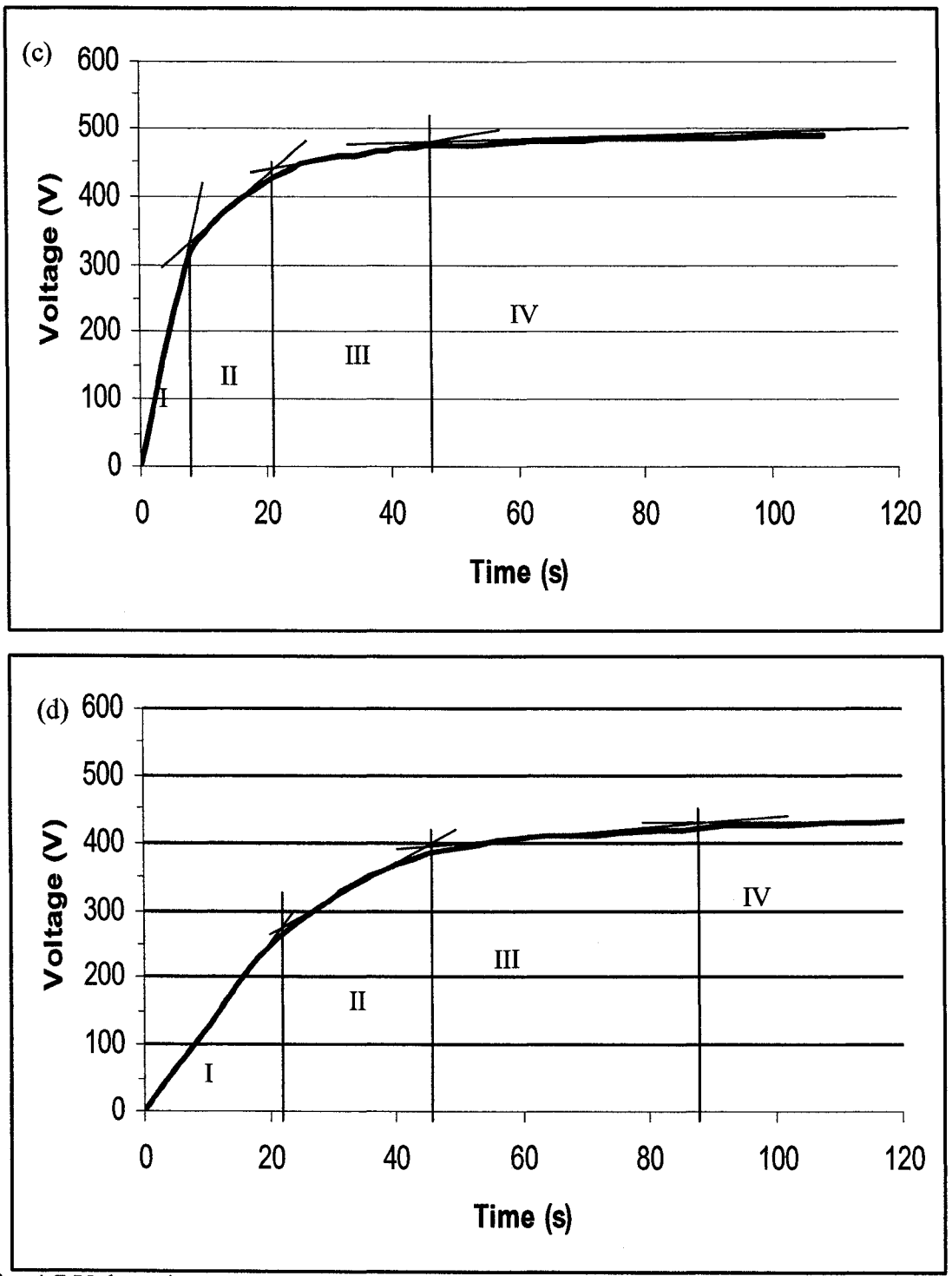

Fig. 4.7 Voltage increase Vs. Treatment time curves for two groups of the PEO coatings treated with (a) 4g/l electrolyte, (b) 8g/l electrolyte, and the magnified graph of the curves for samples (c) X13 and (d) X23

4.2.2 Surface morphology and thickness of DC PEO coatings on Al 390

Figures 4.8 (a, c, e) show the low magnification SEM micrographs of the morphology of DC PEO coatings treated with 4g/l electrolyte. Figs. 4.8 (b, d, f) illustrate the corresponding high magnification micrographs. Coatings X11 and X12 consist of aluminum matrix region and piling-up silicon phase regions (Fig. 4.8 (a) and (c)). For coating X11, discharge channels appearing as small dark pores mainly exist in the silicon rich regions, forming a small bubble-like surface, (Fig. 4.8 (b)). But the boundaries of most Si particles are still distinct. Also, there are some core parts in the large silicon rich content particles. In the Al matrix region, the smooth and dense aluminum oxide film starts to form, where some tiny pores are observed.

For coating X12 (Figs. 4.8 (c) and (d)), compared with coating X11, the silicon regions are rougher, due to the increase in the amount and diameter of the porosity. And the silicon regions mix with the aluminum oxide further, leading to a blurred Al-Si boundary. The aluminum oxide film was relatively rougher than that of coating X11, because more small porosities exist in the coating X12. The silicon phase rich regions are still protruding from the matrix. For coating X13 (Figs. 4.8 (e) and (f)), the porous silicon particles are mixed with the aluminum oxide to a great extent, such that the boundaries are almost indiscernible. And more and larger cavities are observed at the whole coating surface.

Figures 4.9 (a, c, e) are the low magnification micrographs of DC PEO coatings treated with 8g/l electrolyte. Figs. 4.9 (b, d, f) illustrate the corresponding micrographs at a high

magnification. The protruding silicon phase regions in coating X21 are characterized by a lot of cavities and partially mix with aluminum oxide regions [19], which have less and smaller cavities, shown in Figs. 4.9 (a) and (b). However, the aluminum oxide regions on coating X22 (Figs. 4.9 (c, d)) are more mixed with the porous silicon phase regions and the Al-Si boundaries are less obvious. Additionally, the aluminum oxide film is rougher and possesses more cavities than coating X21 in general, but is relatively denser than its porous silicon phase region. For coating X23 (Figs. 4.9 (e) and (f)), the silicon phase regions and the aluminum oxide region mix together and can be hardly distinguished. Large spherically shaped projections arise at the surface. In comparison with coating X22, coating X23 presents more and larger pores on the whole coating surface, indicating that stronger micro-arc discharges occur.

Figs. 4.10 (a, b) show the reflectance spectra as a function of wavelength for coatings X12 and X22, respectively. According to the spectra, film thickness can be determined accurately. Figs. 4.10 (c, d, e) display the SEM cross-section images of coating X13, X22 and X23. The coating layer is between the bright nickel coating and the Al-Si 390 substrate. During the nickel electroless plating process, the nickel flew inside the discharge channel and filled up the voids in the coating. Compared with coating X13 and X22, coating X23 possesses more large porosities. All thickness measurement results are listed in Table 4.3. For coating X22, the measurement results from two methods are very close, indicating good consistency.

Fig. 4.11 exhibits the surface profiles of all coatings. The highest peaks in Figs. 4.11 (a, b, d) are believed as the positions of the piling-up silicon phase regions in coatings X11,

X12 and X21. Clearly, coating X11 presents the largest peak height, about 2.5 μm, whilst the other two have the similar value, around 2 μm. For the rest coatings, due to the mixture of aluminum oxide region and silicon phase regions, the projections in the profiles would be the combinations of aluminum oxides and Al-Si-O compounds.

Fig. 4.12 displays the surface roughness measurement results of all coatings. In each concentration group, the surface roughness increases with the treatment time, represented by the final voltage. Also, the electrolyte concentration has a great effect on the surface roughness. For the same final voltage, the coating treated with high concentration electrolyte is rougher.

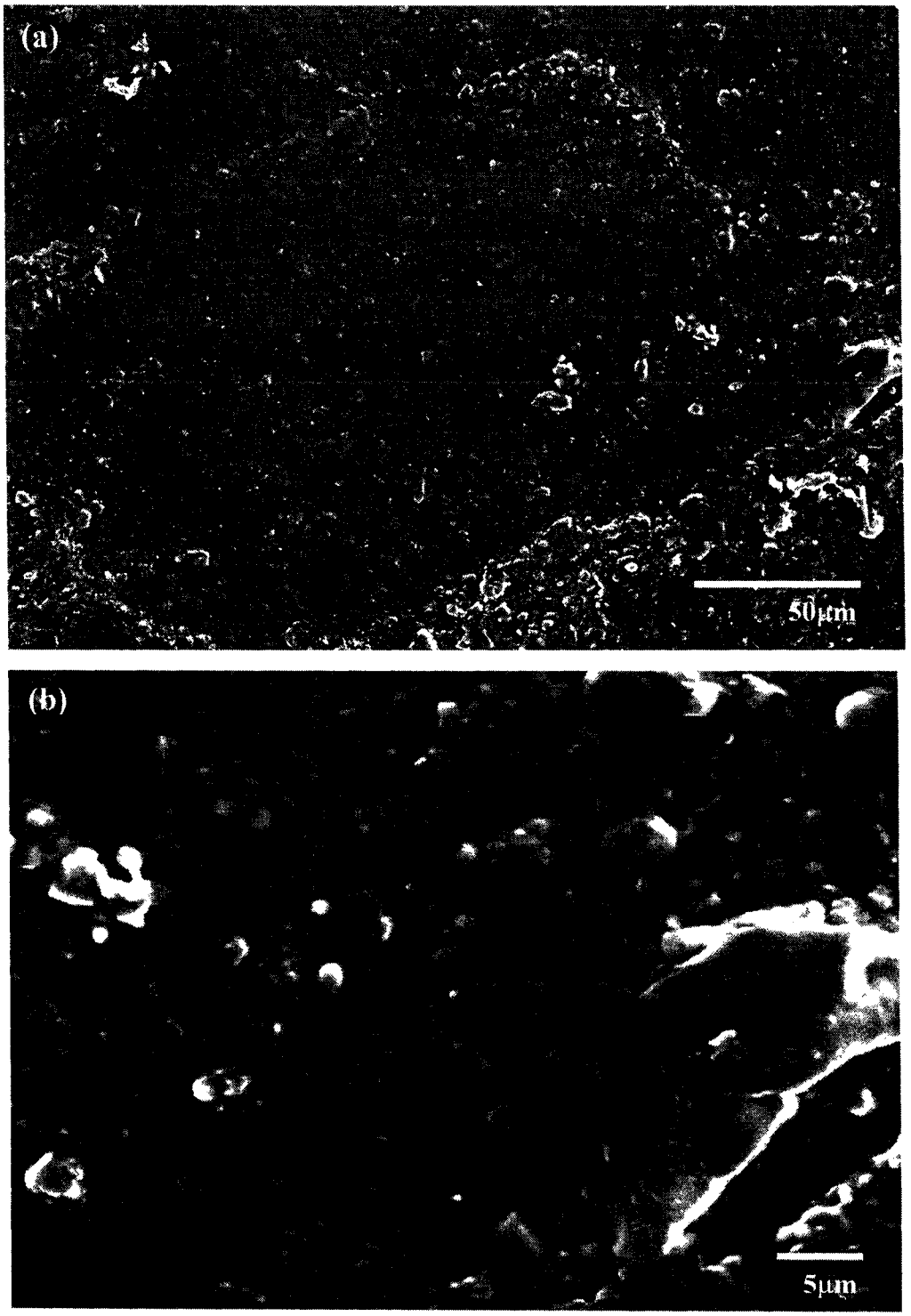

Fig. 4.8 to be continued

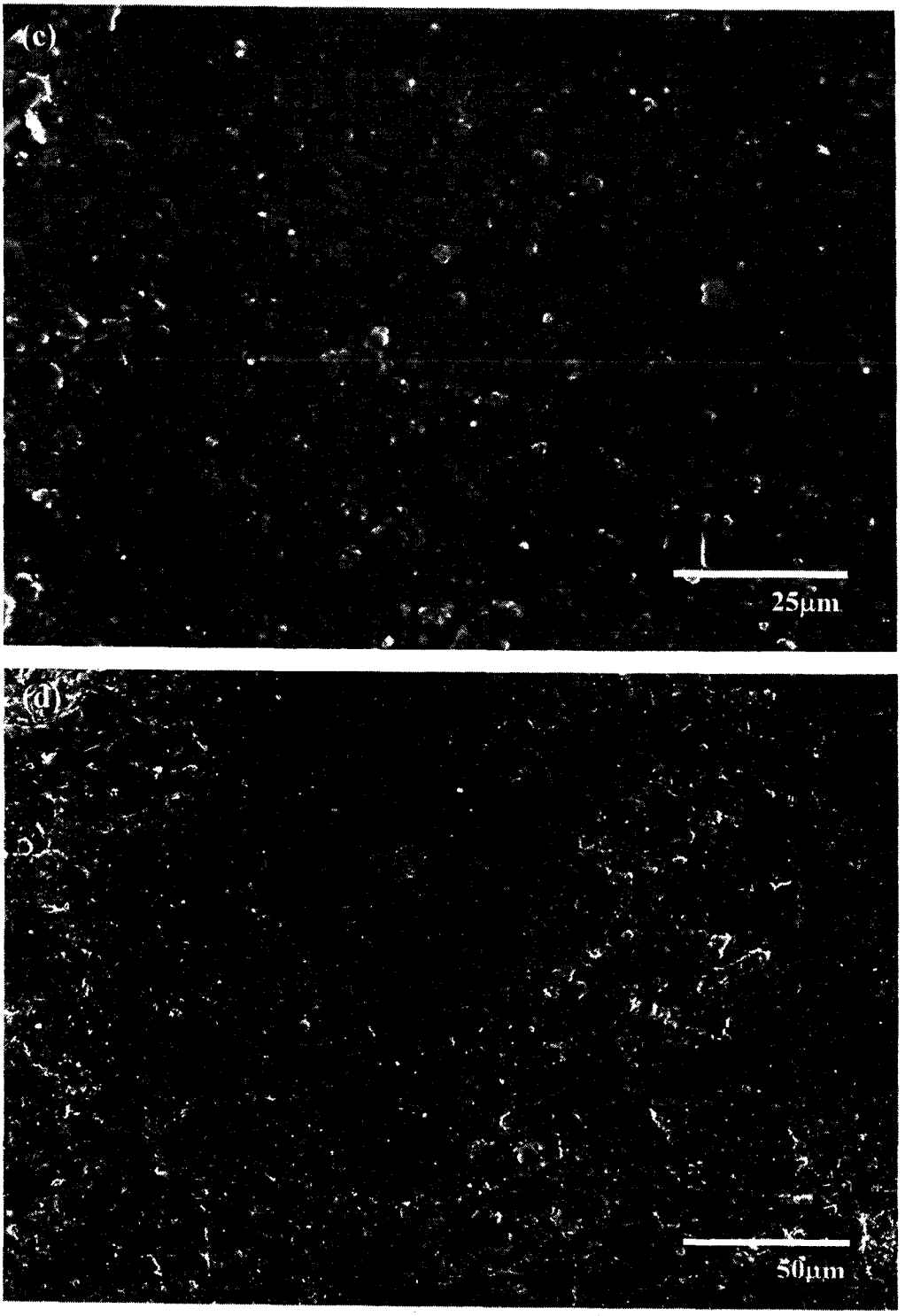

Fig. 4.8 to be continued

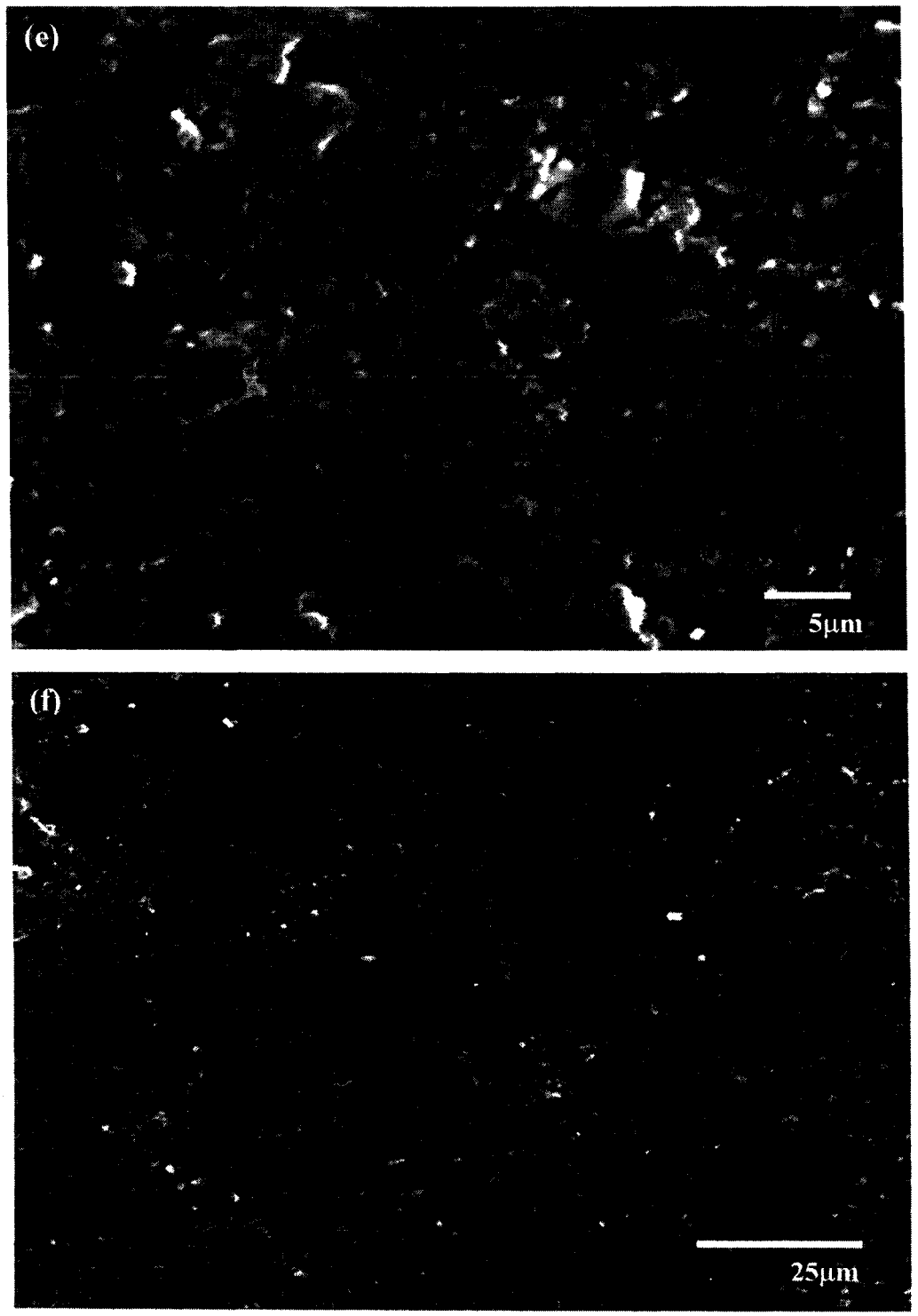

Fig. 4.8 to be continued

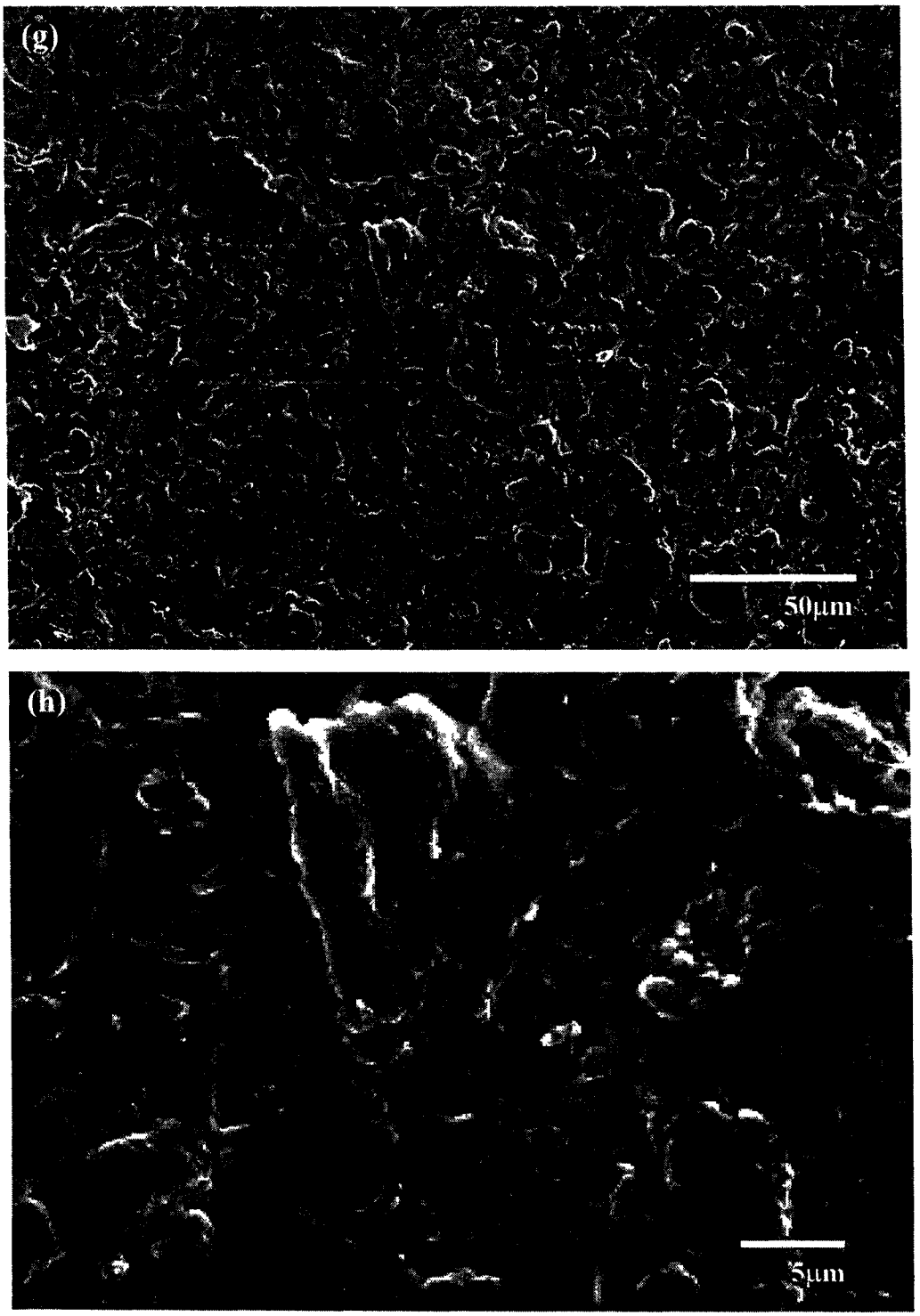

Fig. 4.8 SEM micrographs of PEO coatings of (a) X11, (d) X12 and (g) X13, and the corresponding high magnification micrographs for the silicon phase regions of (b) X11 and (e) X12; for the aluminum oxide regions of (c) X11 and (f) X12; and for the whole region of (h) X13

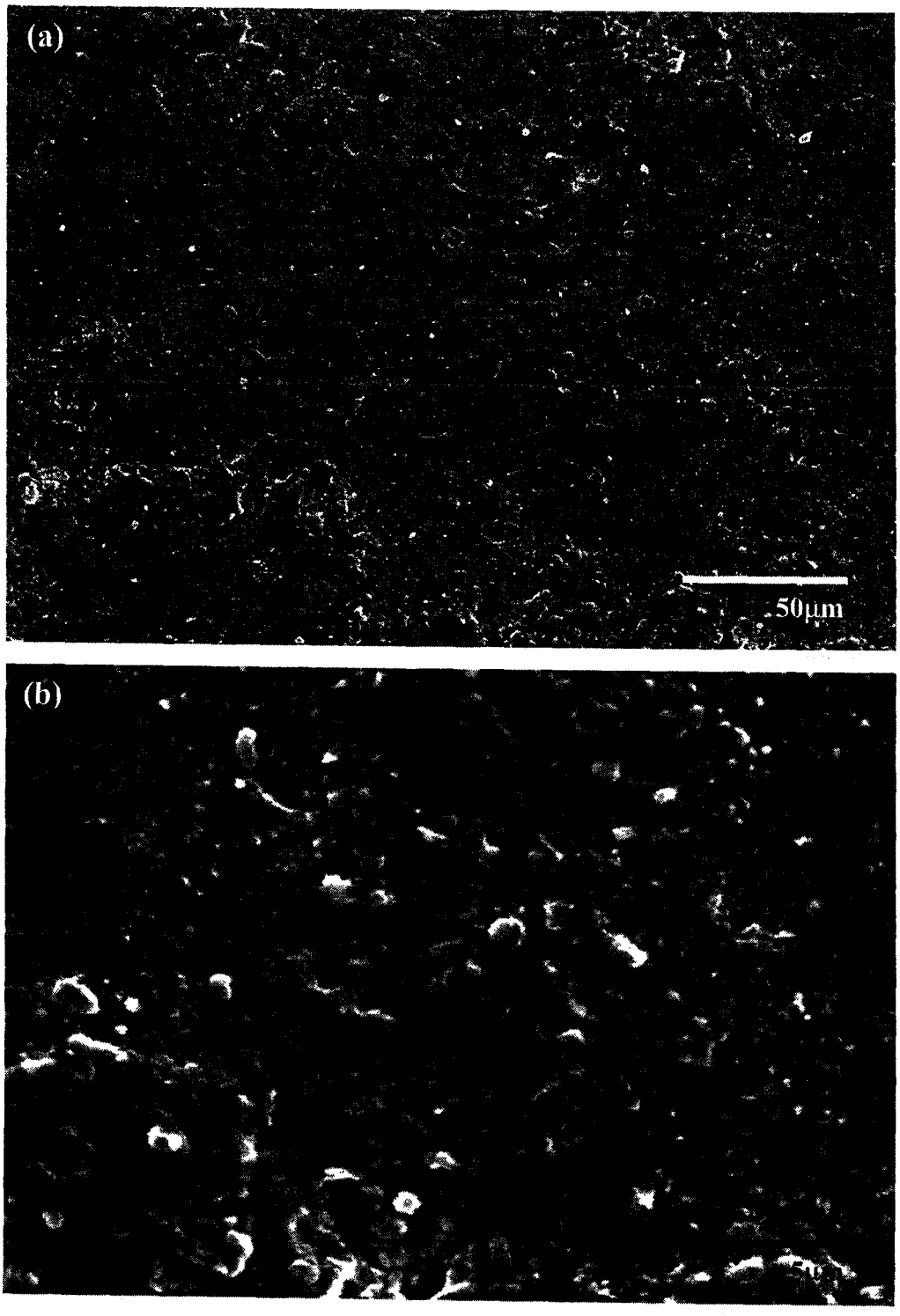

Fig. 4.9 to be continued

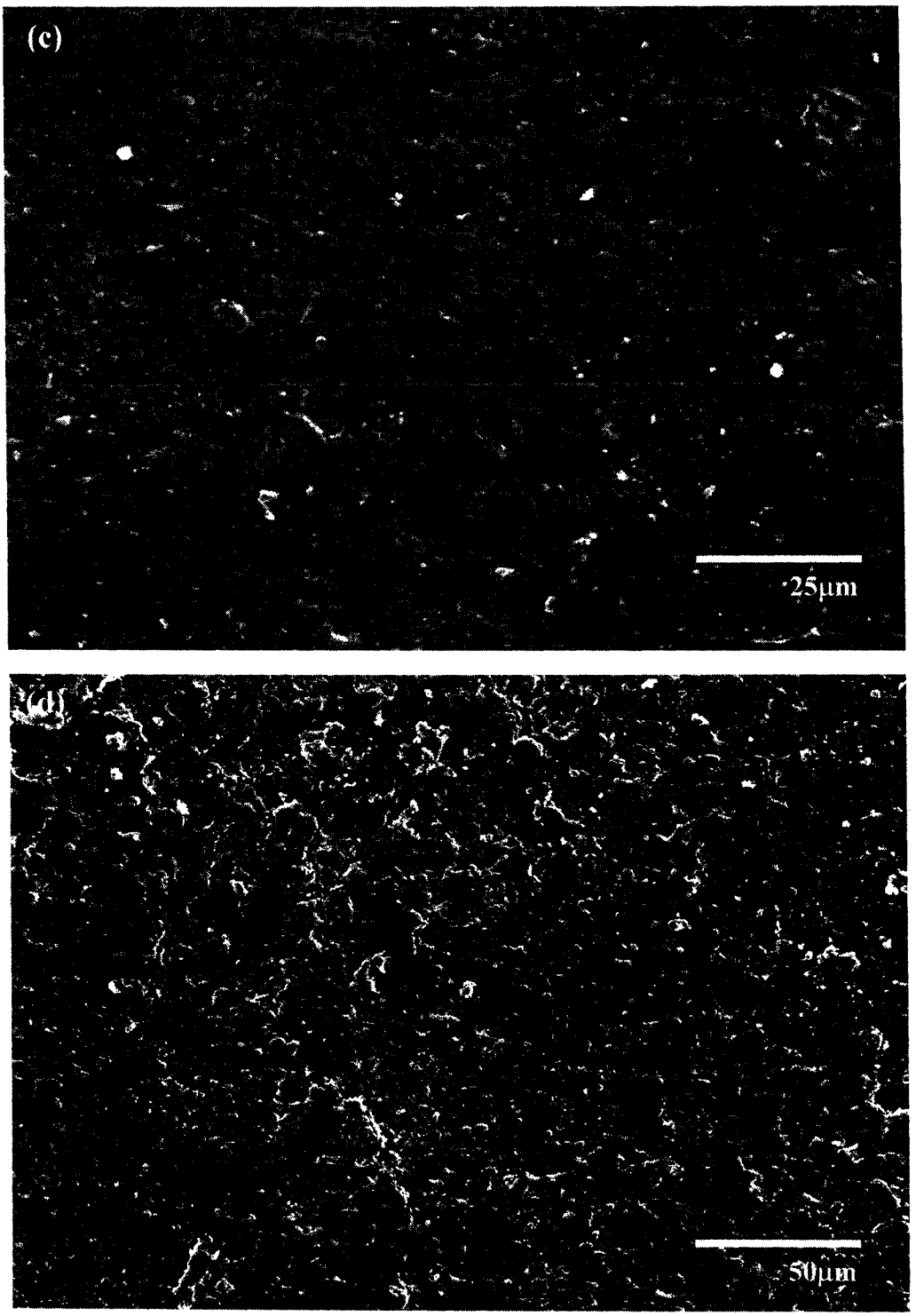

Fig. 4.9 to be continued

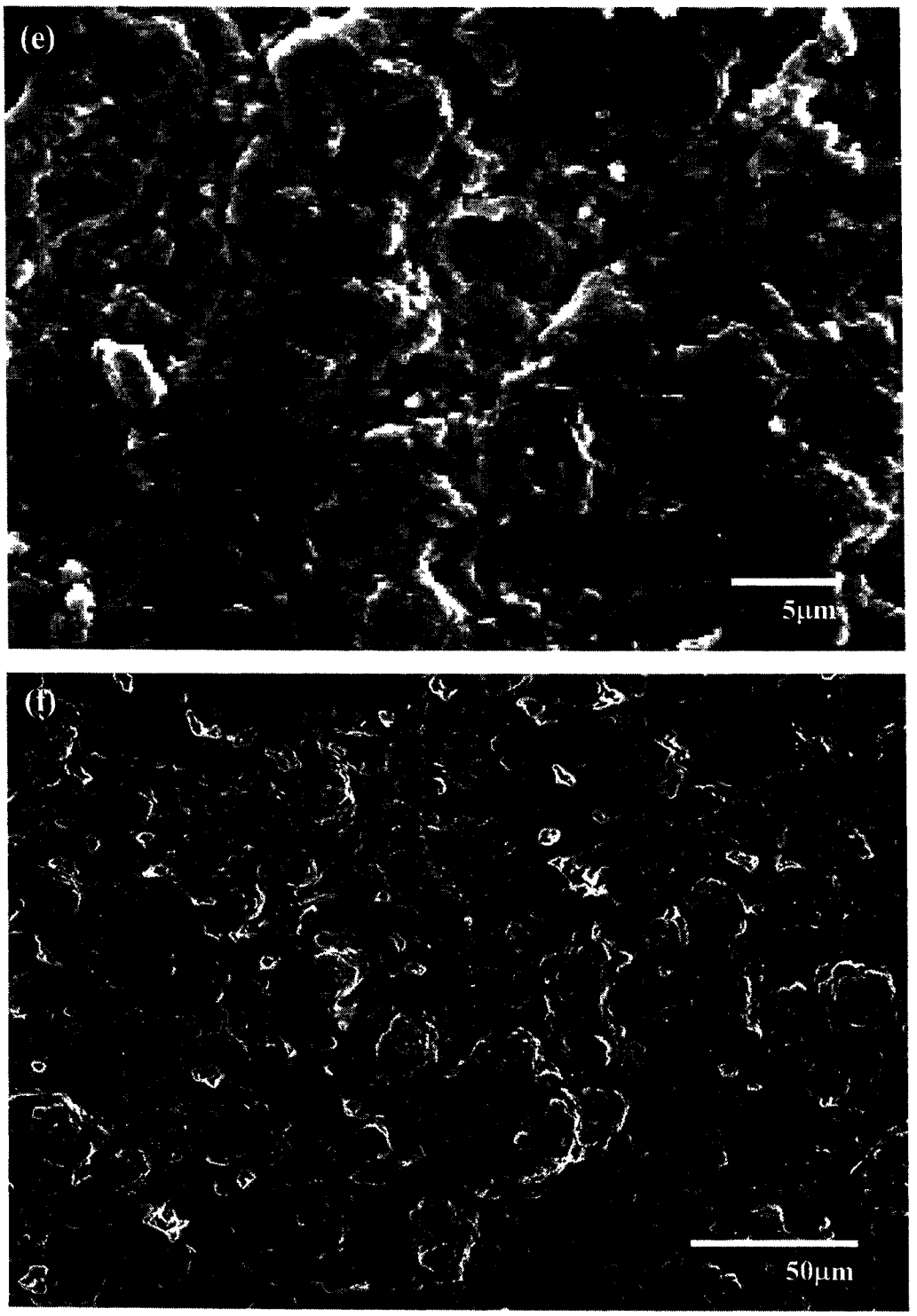

Fig. 4.9 to be continued

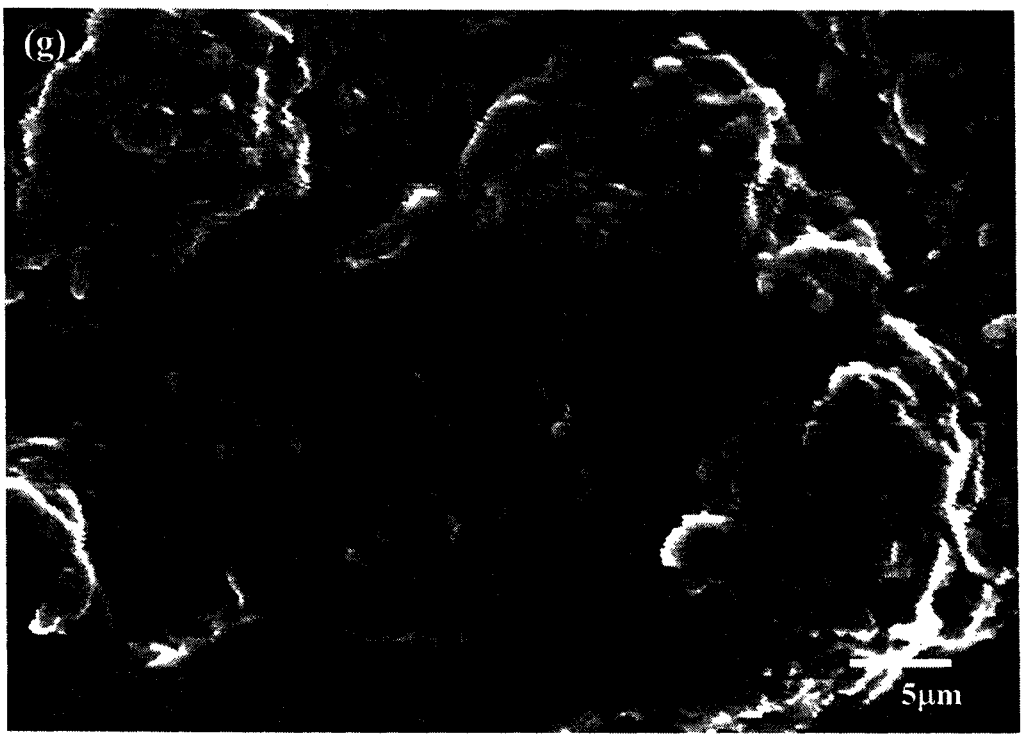

Fig. 4.9 SEM micrographs of PEO coatings of (a) X21, (d) X22 and (f) X23, and the corresponding high magnification images for (b) the silicon phase regions of X21, and (c) the aluminum oxide regions of X21, and the whole region of (e) X22 and (g) X23

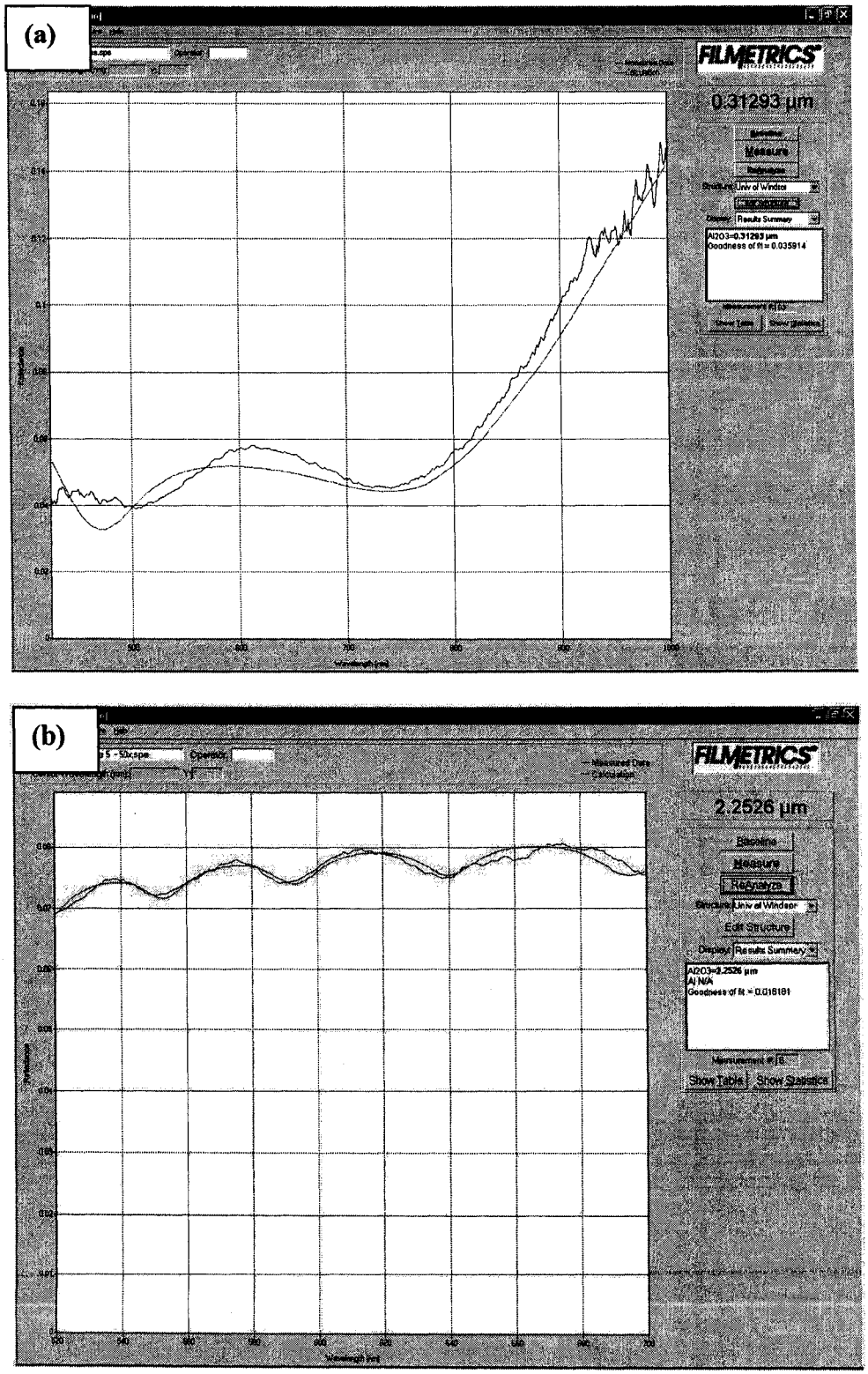

Fig. 4.10 to be continued

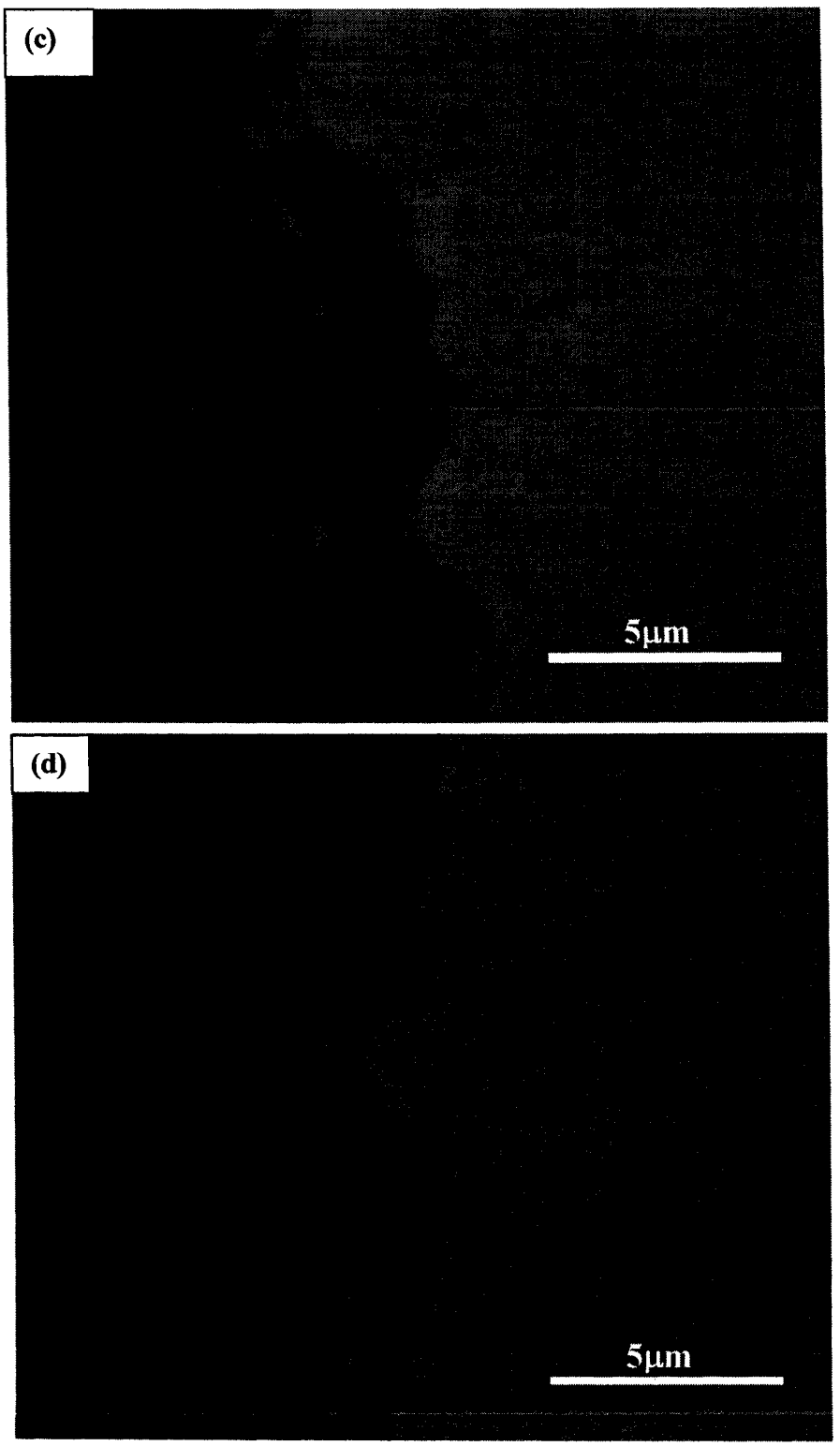

Fig. 4.10 to be continued

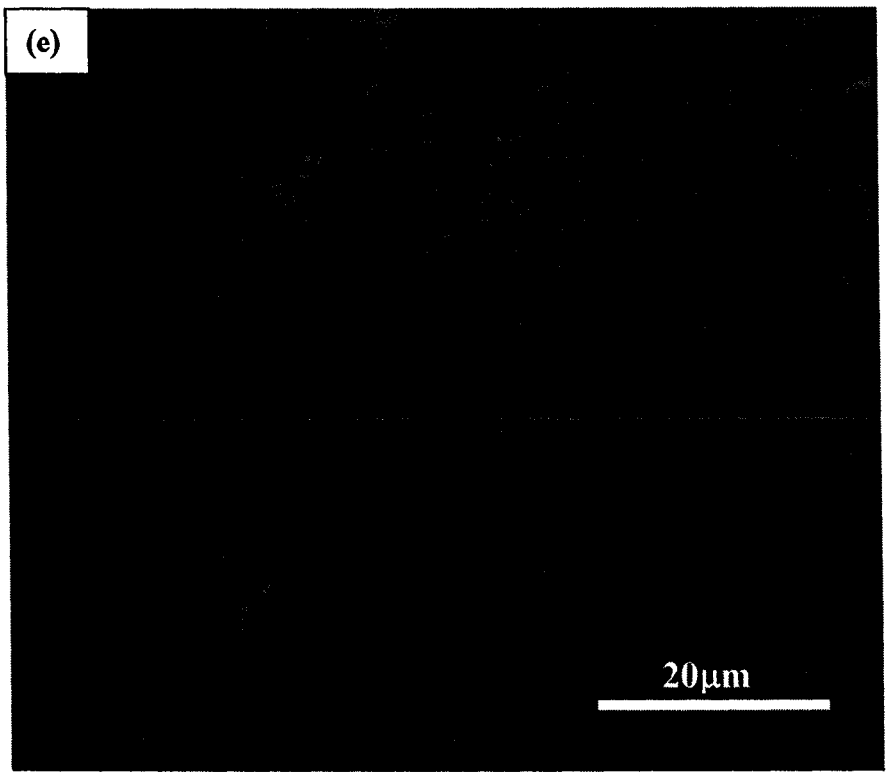

Fig. 4.10 Reflection spectra for (a) X12 and (b) X22, and SEM cross-section micrographs for (c) X13, (d) X22, and (e) X23

Table 4.3 Thickness measurement results

Method	Reflection spectrum		SEM cross-section image		
Coating	X12	X22	X13	X22	X23
Coating Thickness (μm)	0.31	2.25	2.45	2.12	15

(a)

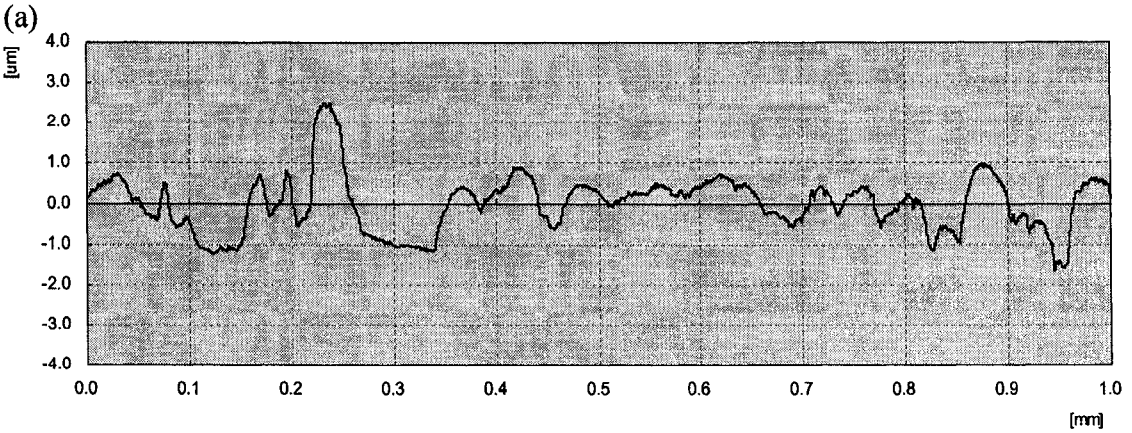

(b)

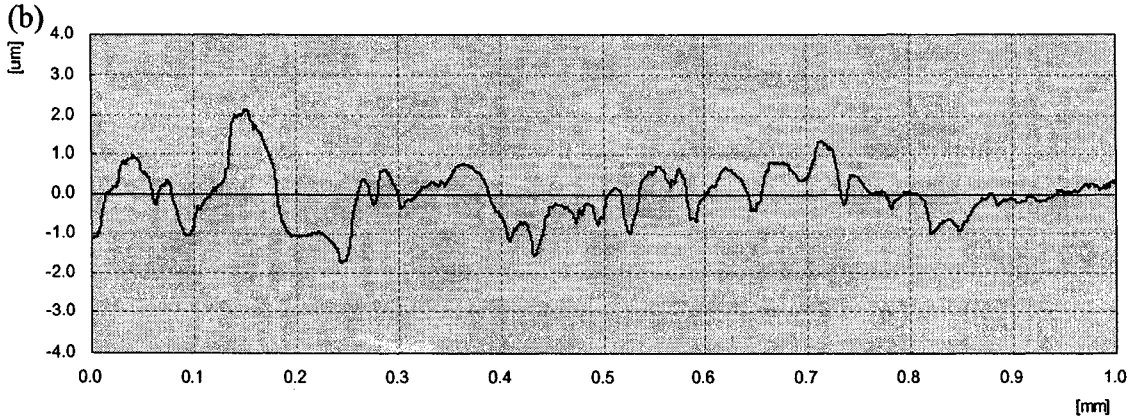

(c)

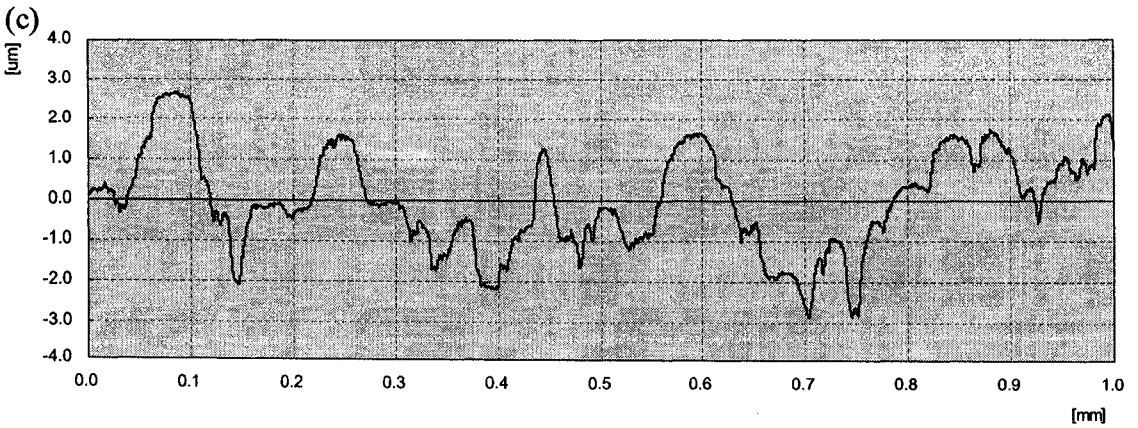

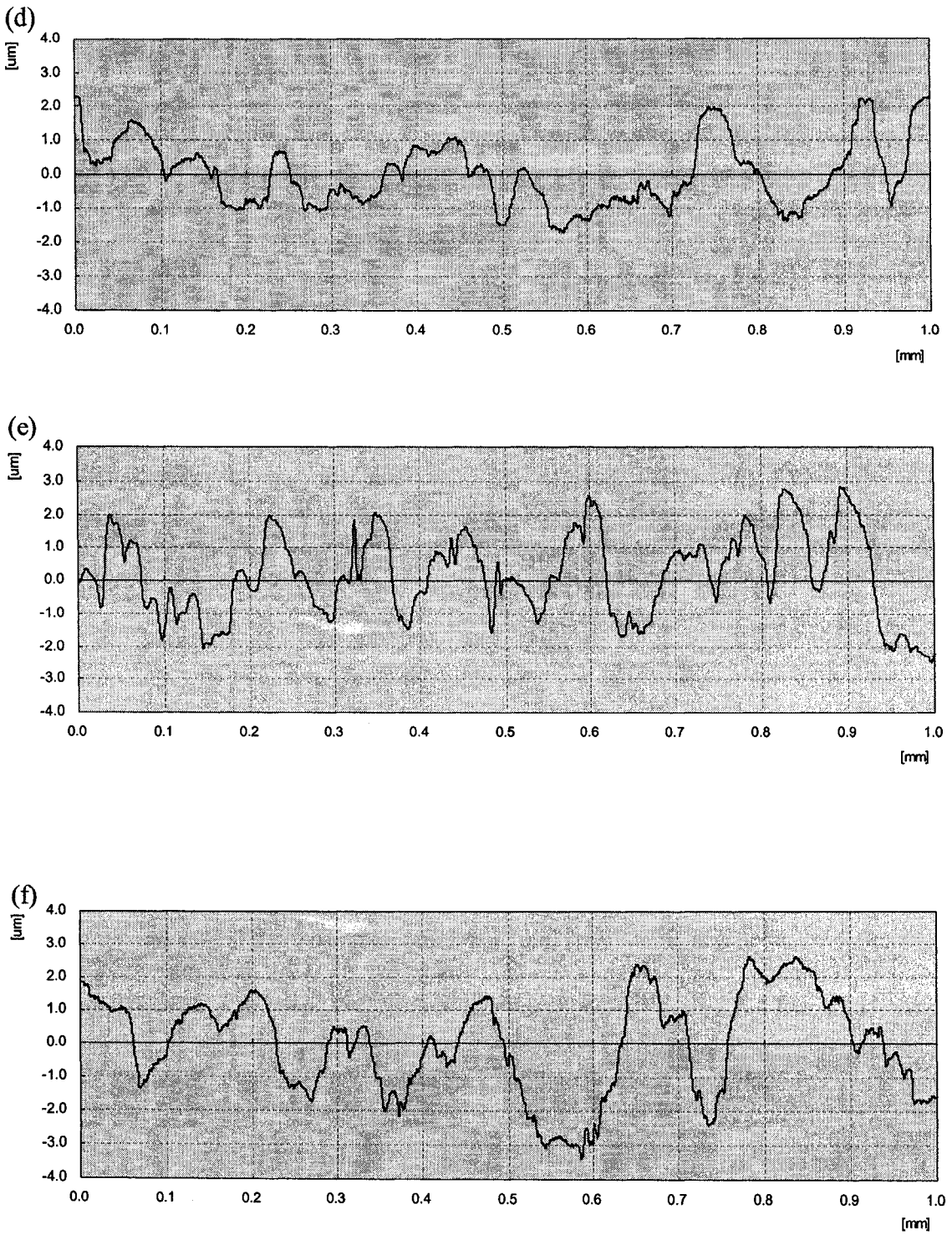

Fig. 4.11 Surface profiles for coatings (a) X11, (b) X12, (c) X13, (d) X21, (e) X22, and (f) X23

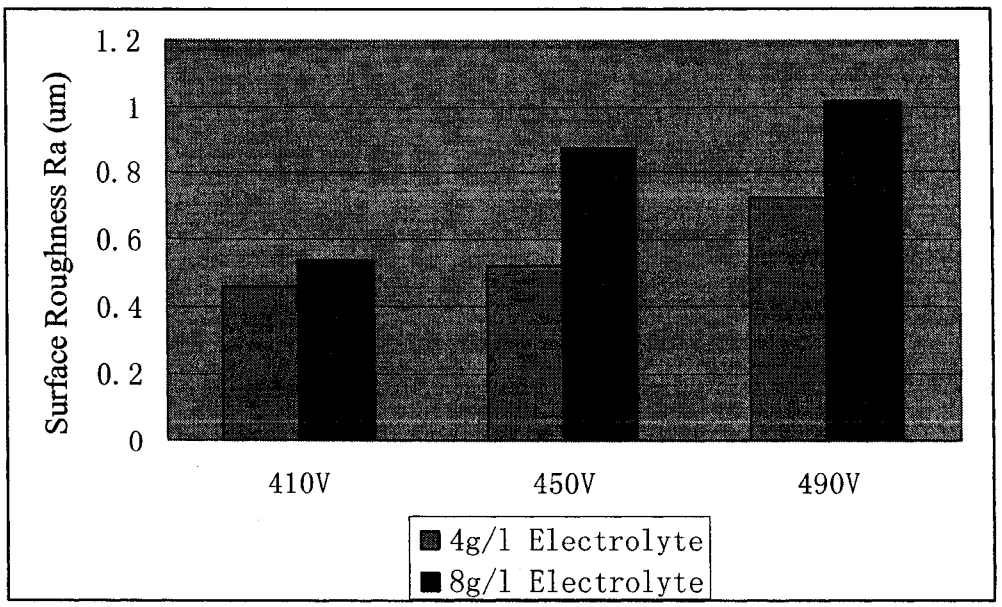

Fig. 4.12 Surface roughness Ra for all coatings

4.2.3 Discussion

During the PEO process, an anodizing process mainly occurs at the aluminum matrix region in stage I, characterized by a rapid linear voltage increase. Due to the low conductivity of silicon (~10^{-4} $(\Omega \cdot m)^{-1}$), only a passivation layer (about 6-20nm thick) forms on the silicon particle surface via chemisorption process in stage I [19]. In stage II, with the voltage increasing, the electrical field at the Al-Si boundary increases dramatically due to the tip/corner effect of electrical field concentration. When the voltage reaches a critical value, the electrical strength at the boundary is beyond the dielectric strength of the oxide (~10^4 V/m), leading to breakdown of the oxide film and initialization of the micro-discharges at the boundary. Thus the voltage growth rate decreases. Due to the electron avalanches, the discharge region is heated up to 10^3~10^4 K [17, 18], higher than the melting point of Si (1410 ^{0}C) and SiO_x (<1800 ^{0}C) [61], causing the silicon crystal surface to melt and mix with the aluminum oxide to form Al-Si-O

compounds [19]. Thus, the compounds firstly form at the boundary of silicon phase region. Since the addition of Si into alumina reduces the melting temperature of the oxide compound, the Al-Si-O compound is easy to form and cover the whole silicon phase region. And the melt compound rapidly solidified around the discharge channel, resulting in a porous structure of silicon phase region, shown in Figs. 4.8 (a, b). At the same time, a number of small sparks could also be observed at the aluminum oxide region. Thus, the voltage increase rate slackens. In stage III, since the coating is still thin and the Al-Si-O compounds have a lower melting point and more porosity than the aluminum oxide region, more discharge spots occur at the silicon rich regions, resulting in piling up of the Al-Si-O compounds, shown in Figs. 4.8 (c, d) and Figs. 4.9 (a, b). In stage IV, the silicon phase region is mixed with the aluminum oxide region further, causing a uniform mixture. With the oxide film thickness increasing, the electrical field reaches a critical value of 10^6 V/m, which is high enough to break down the oxide film and lead to the formation of micro-discharge at the aluminum oxide rich region. The high temperature of 10^4K generated by electrical discharge can melt the aluminum oxide as well as the Al-Si-O compound. And the melted oxide is quickly quenched by the electrolyte and solidifies around the discharge channel, forming a porous structure at the whole area of the coating, shown in Figs. 4.8 (e, f) and Figs. 4.9 (c, d). As treatment time goes on, the discharges contract to form stronger micro-arc discharges, increasing the diameters of discharge channels but decreasing the discharge channel amounts. The mass flow of the melted oxide adjacent to each channel increases, forming a larger projection around the channel.

With the electrolyte concentration increasing, the electrical resistance of the solution decreases, causing a lower voltage for a given current. Moreover, the high concentration electrolyte supplies more Si and O, which accelerates the combination of Al-O in coatings with Si-O in the electrolyte to form the Al-Si-O compound. Compared with Al_2O_3, the Al-Si-O compound has a low electrical resistance and low breakdown voltage. Thus, the micro-discharge can occur at relatively low voltage in high concentration electrolyte. For example, coating X22 possesses more discharge channels than coating X12, although the voltages applied to the two coatings are the same. And the micro-discharge will enhance the compound formation by heating the discharged region. Therefore, the critical voltage of the coatings treated with the higher electrolyte concentration for each stage is lower and so is the voltage growth rate.

4.3 Tribological properties of DC PEO coatings on Al 390 sliding against steel balls under residual oil lubrication

4.3.1 Tribological test results of DC PEO coatings on Al 390 sliding against steel balls under residual oil lubrication.

Figs. 4.13 (a, c, e) show the low magnified SEM images of the wear tracks for PEO coatings X11, X12, and X13. Figs. 4.13 (b, d, f) are the corresponding high magnification images for X11, X12, X13, respectively. For coating X11, abrasive wear is clearly observed. Scratches exist at the aluminum oxide region. And the piling up part of the porous silicon particles is removed, leading to a sunken area. Also, wear debris presents in the wear track. For coating X12 and X13, no obvious abrasive wear presents in the aluminum oxide region. But for coating X12, the extrusive porous silicon particles are also worn away. For coating X13, no material removal is detected.

Figs. 4.14 (a, c, e) show the low magnified SEM images of the wear tracks for PEO coatings X21, X22, and X23. Figs. 4.14 (b, d, f) are the corresponding high magnification images for X21, X22, X23, respectively. For coating X21, material removal is observed at aluminum oxide region. Also, the piling-up porous silicon particles are removed. For coating X22, no abrasive wear is found at aluminum oxide region. Again, the piling-up porous silicon particles are worn away. For coating X23, the wear track can not be discerned.

Figs. 4.15 (a, b, c) exhibit the optical microscope photographs of the counter steel balls sliding against the PEO coatings X11, X12 and X13, individually. The worn area of the counter steel ball against coating X11 is the smallest. The other two have almost the same size of the worn areas. Abrasive wear occurs to all steel balls.

The optical microscope photographs of the counter steel balls sliding against the PEO coatings X21, X22 and X23, are shown in Figs. 4.15 (d, e, f), individually. Coating X22 exhibits a slightly better compatibility for steel ball with a smaller worn area of the counterface than the other coatings, which have a similar worn area size. All steel balls present abrasive wear.

Figs. 4.16 (a, b, c) show COF curves for PEO coatings X11, X12 and X13. The COF curve of coating X11 fluctuates widely, Fig. 4.16 (a). Coating X12 and X13 present similar COF curves. The average COF for three coatings are listed in Table 4.4. Coating X12 exhibits the lowest COF, while the COF of X11 is the highest.

Table 4.4 Average COF for PEO coatings treated with 4g/l electrolyte

Sample	X11	X12	X13
COF	0.149	0.145	0.146

Figs. 4.16 (d, e, f) presents the COF curves of PEO coatings X21, X22 and X23. Coating X21 has a more fluctuated COF with a higher average, listed in Table 4.5, than the other

two coatings. Coating X23 presents the lowest average COF among the coatings treated with high electrolyte concentration.

Table 4.5 Average COF for PEO coatings treated with 8g/l electrolyte

Sample	X21	X22	X23
COF	0.171	0.155	0.148

4.3.2 Discussion

Coatings X11, X12, X21 and X22 are all comprised of relative dense aluminum oxide region and porous silicon oxide regions. And coatings X13 and X23 consist of aluminum oxide and Al-Si-O compounds, the latter resulting from the mixture of the two regions, caused by the high temperature generated from the micro-discharge. For coating X11, according to Fig. 4.11 (a), the isolated silicon particles extend from the matrix. Due to the shortest treatment time, the aluminum oxide film is too thin to hold the silicon particles and can not provide enough load- bearing ability. Therefore, just like the Al substrate, when coating X11 slides against steel ball under residual lubrication, where silicon oxide-metal contact firstly happens at most of the asperities, the protruding parts of the porous silicon oxide particles are worn away owing to the stress concentration at the asperities, possibly forming third-body particles. After that, ceramic coating-metal contact comes into being, causing mild abrasive wear to the aluminum oxide region, Fig. 4.13 (b). Therefore, the COF of X11 is the highest among the first group, Table 4.4. Since the hardness of the aluminum oxide film increases with the treatment time, owing to the phase transformation from soft γ-Al_2O_3 to hard α-Al_2O_3, the hardness of coating X11 is lower than those of coating X12 and X13. Therefore, coating X11 provides a less

aggressive wear to the steel ball. The same worn area on the counterface steel ball is almost the same as that of ball against the Al substrate, (Fig. 4.4 (d) and Fig. 4.15 (a)). For coating X12, the piling up silicon phase regions are also removed due to the stress concentration. Comparatively, the dense aluminum oxide layer is hard and thick enough to bear the normal load and provide good wear resistance, so no abrasive wear occurs to that region. Therefore, coating X12 presents a lower COF than coating X11, although higher than Al substrate. But the high hardness results in a larger worn area of counterface. Coating X13 mainly consists of the Al-Si-O compounds, resulting from the mixture of the aluminum oxide region and the porous silicon oxide regions. Different from the morphologies of coating X11 and X12, the surface of coating X13 has a large number of porosities, Figs. 4.8 (g, h), which is good for oil retaining. But the oil exists in the porosities can not effectively provide a lubrication film at the projections, because most porosities lie among the projections rather than on top of them. Also, the coating becomes rougher and harder. Therefore, the COF is lower than that of coating X11, but a little higher than that of coating X12.

Coating X21 also comprises of dense aluminum oxide region and porous piling up silicon phase regions, Fig. 4.9 (a). The aluminum oxide region is relatively looser than that of coating X12, Fig. 4.8 (f), resulting in poor support for the silicon phase regions and wear resistance. Thus, after the porous silicon phase regions are worn away, material removal occurs to the aluminum oxide region, Fig. 4.14 (b). The delaminated particles might lead to the third-body wear. As a result, coating X21 presents the highest COF and largest worn area of the counterface steel. Similar to coating X13, coatings X22 also exhibits a

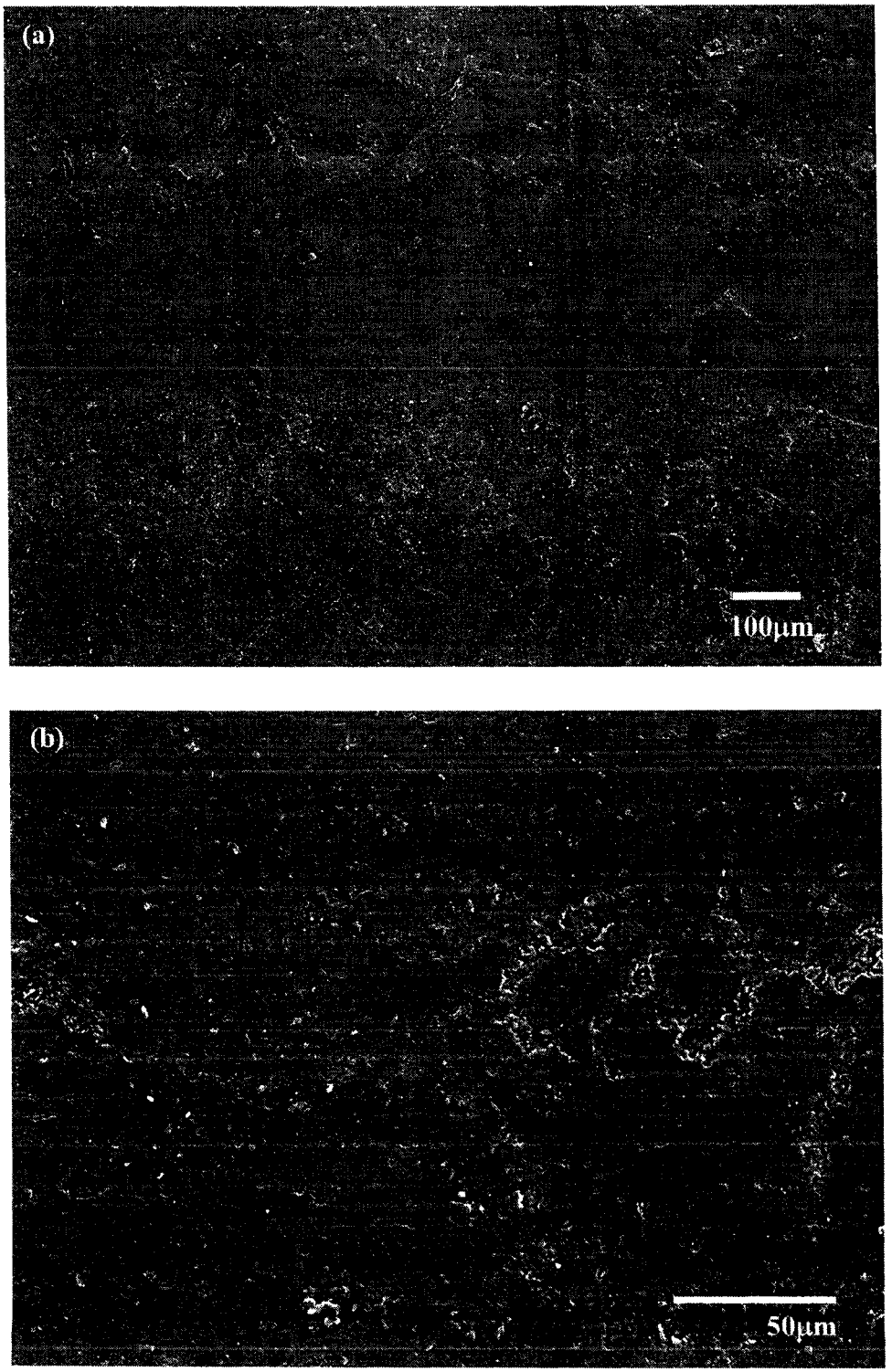

Fig. 4.13 to be continued

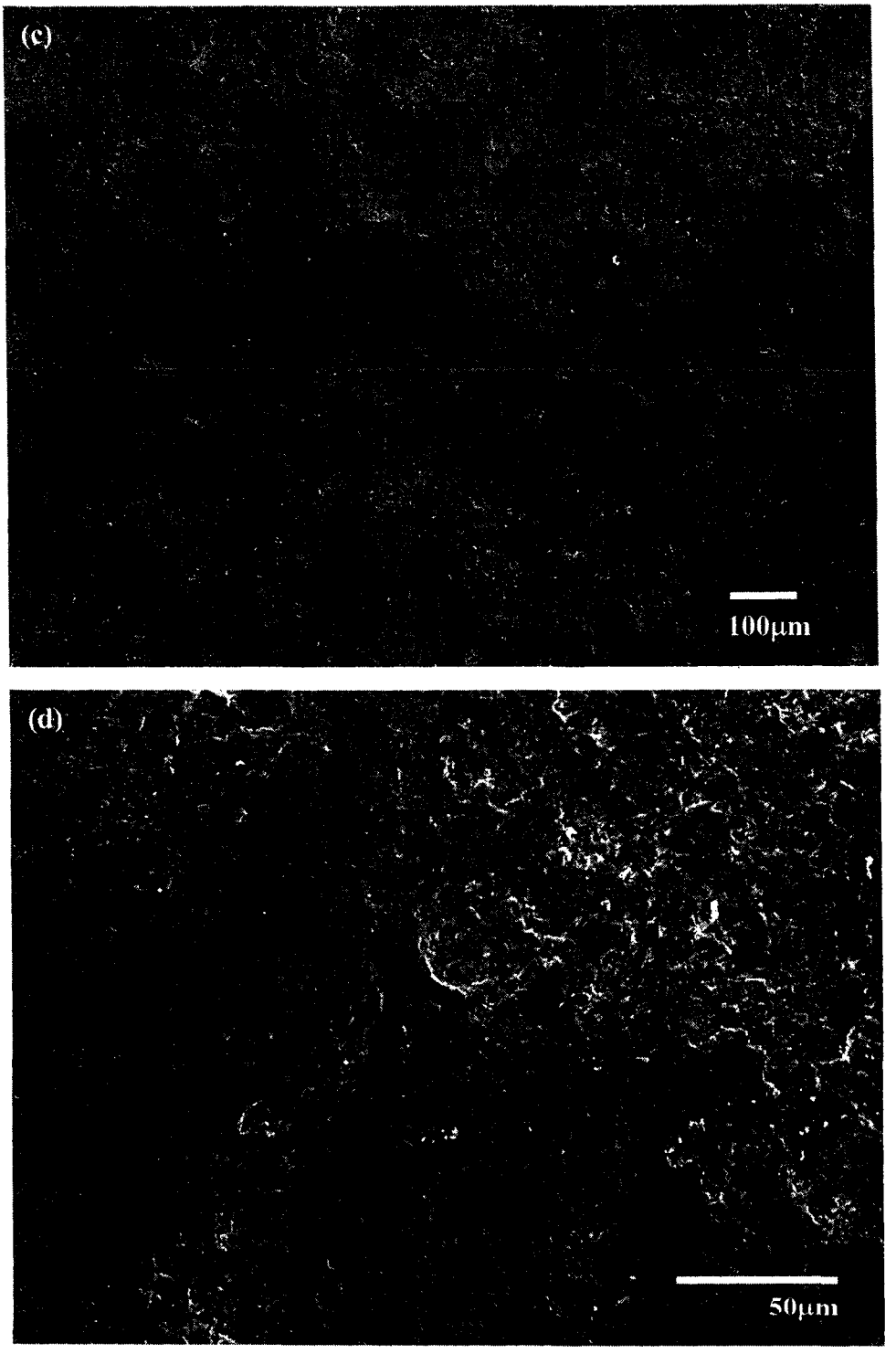

Fig. 4.13 to be continued

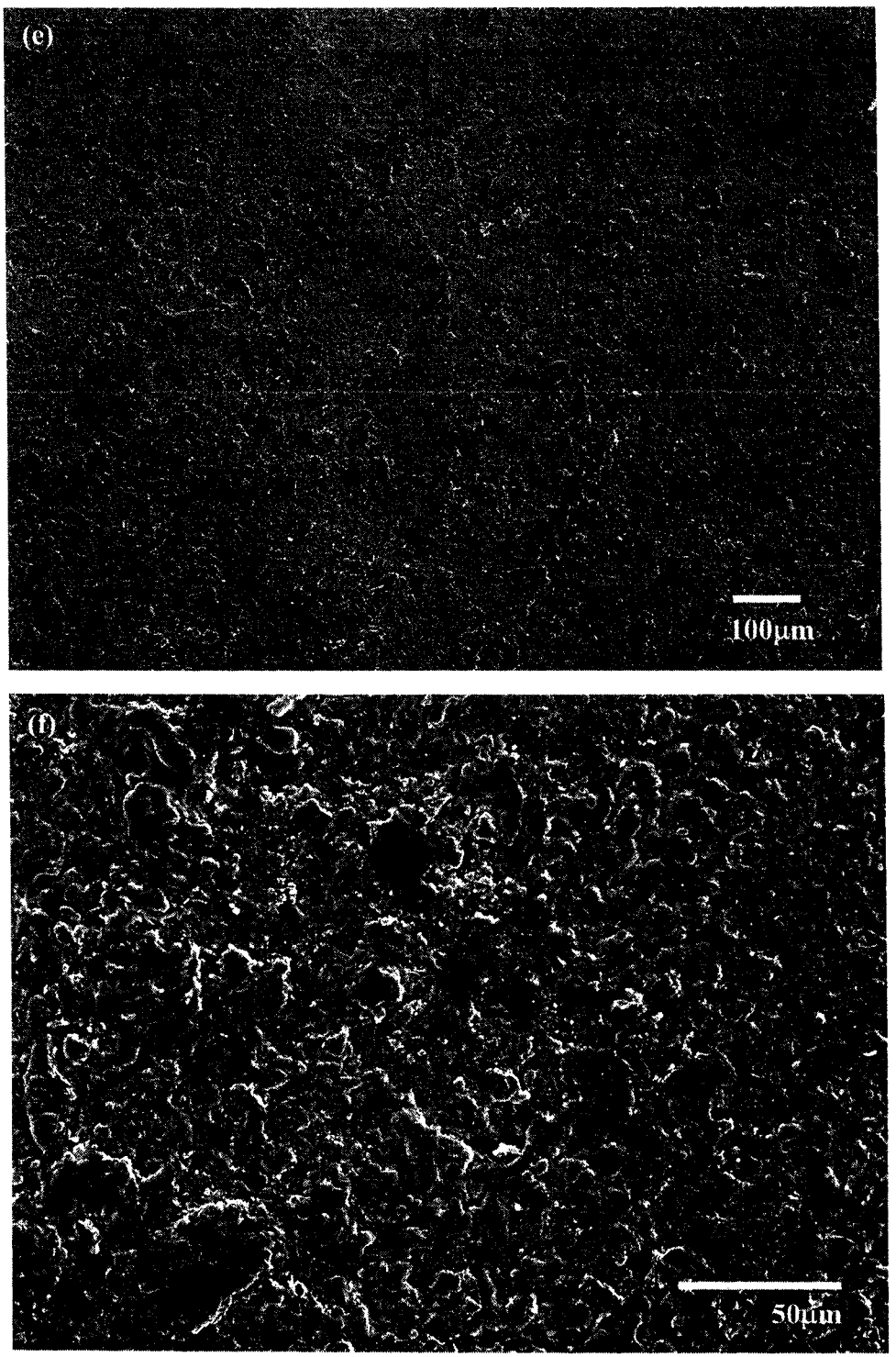

Fig. 4.13 SEM micrographs of the wear tracks for PEO coatings sliding against steel ball with 2N normal load under residual oil lubrication, (a) X11, (c) X12, and (e) X13, and the corresponding high magnification micrographs (b), (d) and (f)

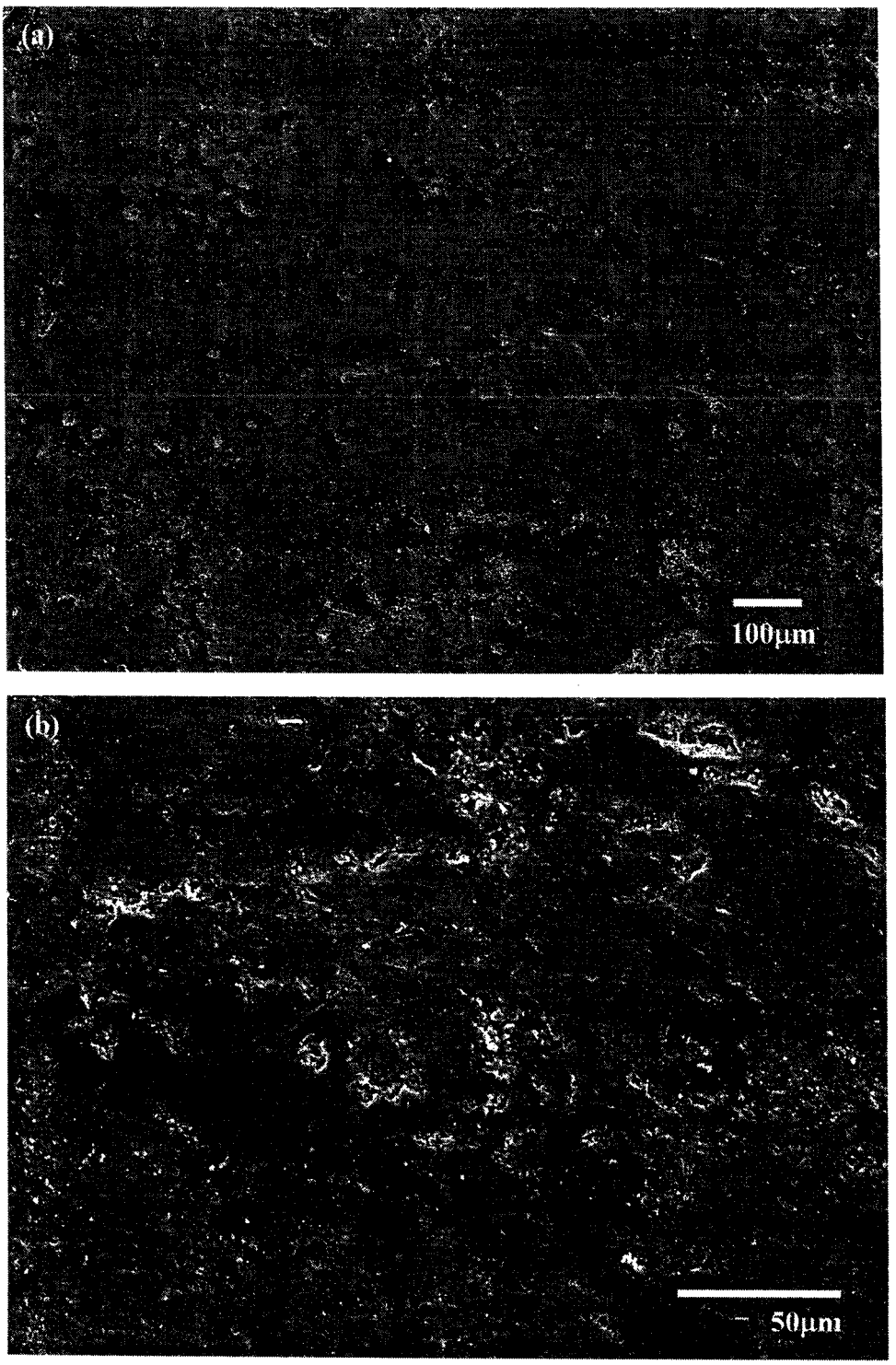

Fig. 4.14 to be continued

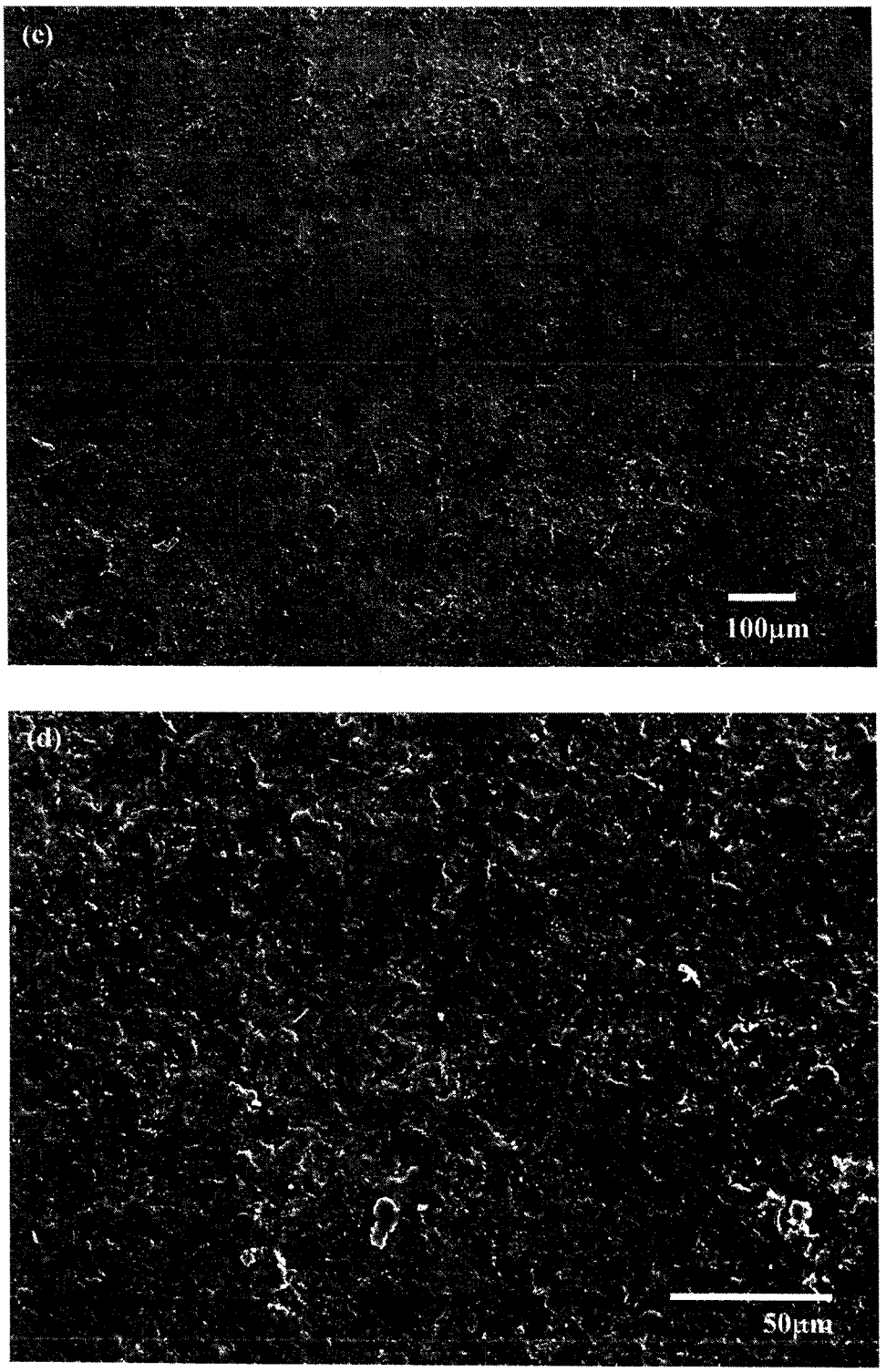

Fig. 4.14 to be continued

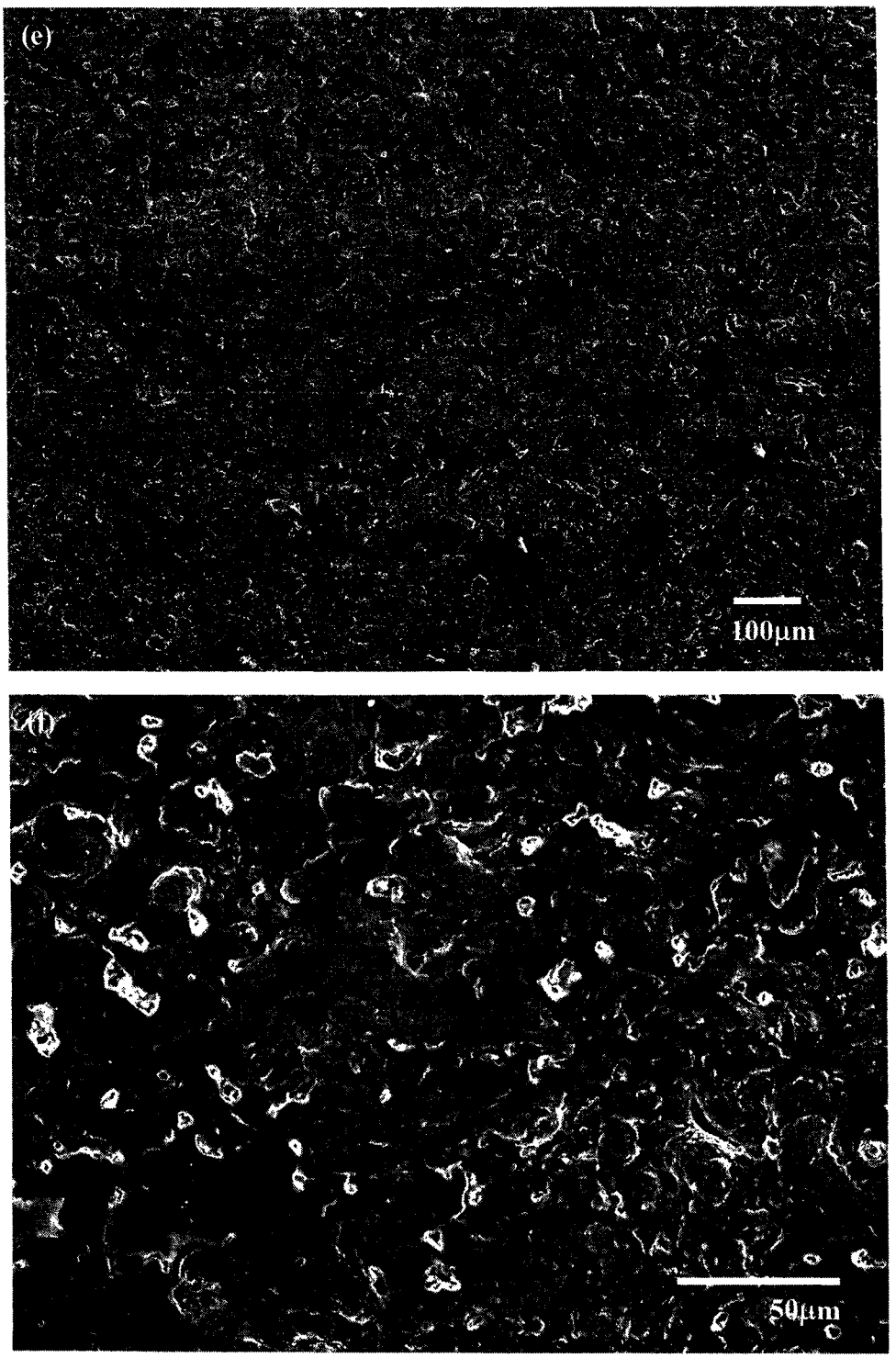

Fig. 4.14 SEM micrographs of the wear tracks for PEO coatings sliding against steel ball with 2N normal load under residual oil lubrication, (a) X21, (c) X22, and (e) X23, and the corresponding high magnification micrographs (b), (d) and (f)

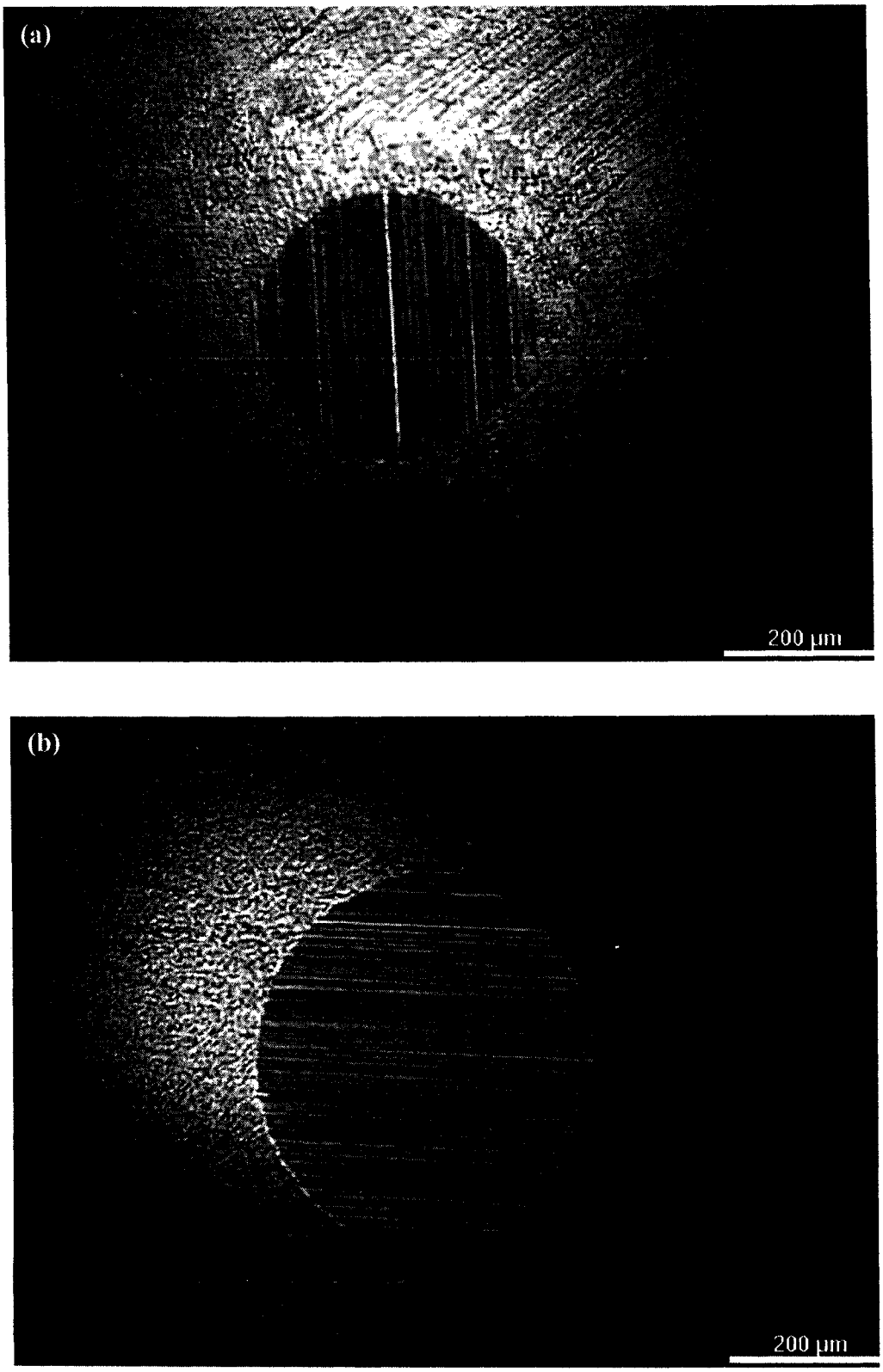

Fig. 4.15 to be continued

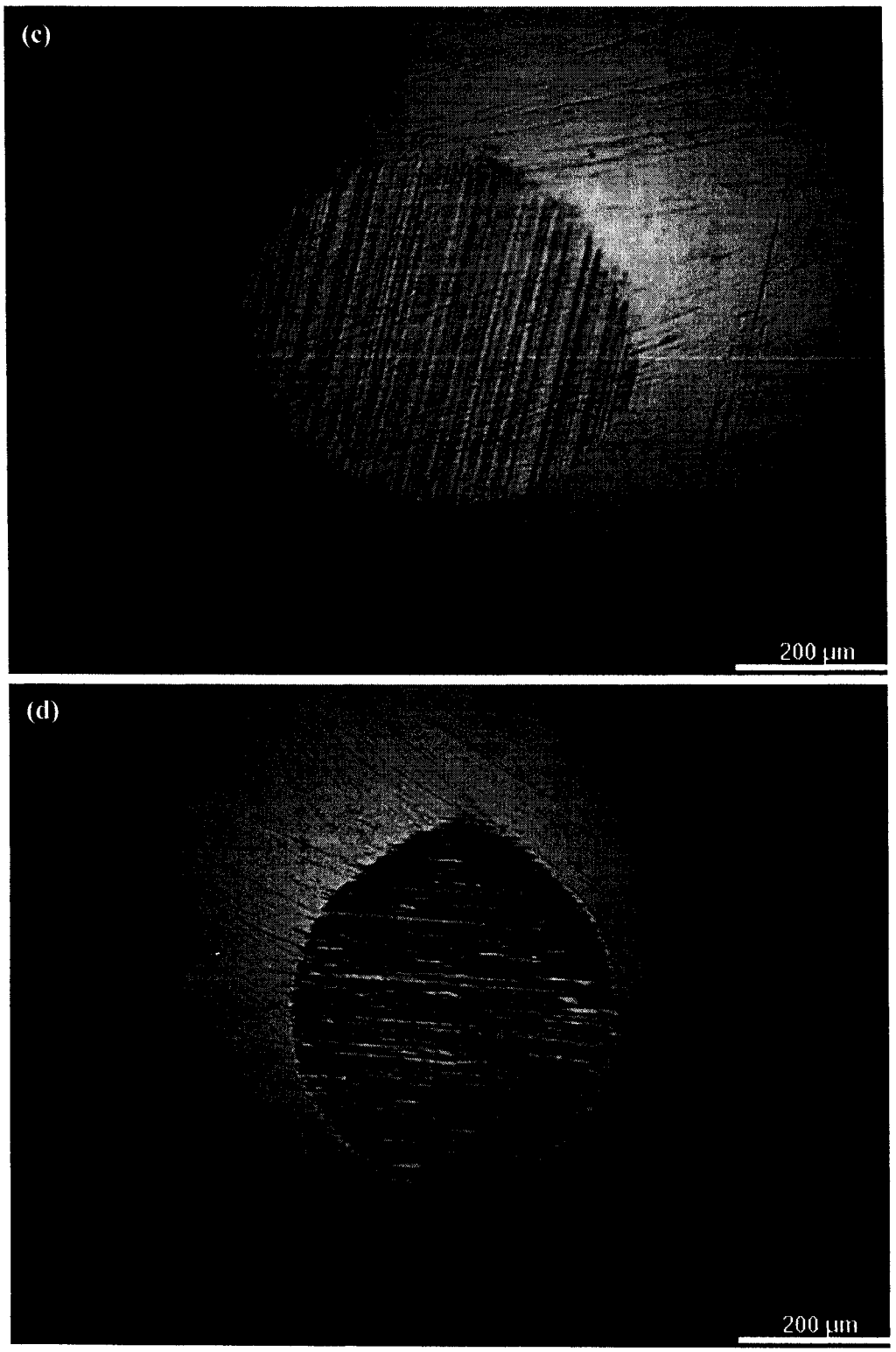

Fig. 4.15 to be continued

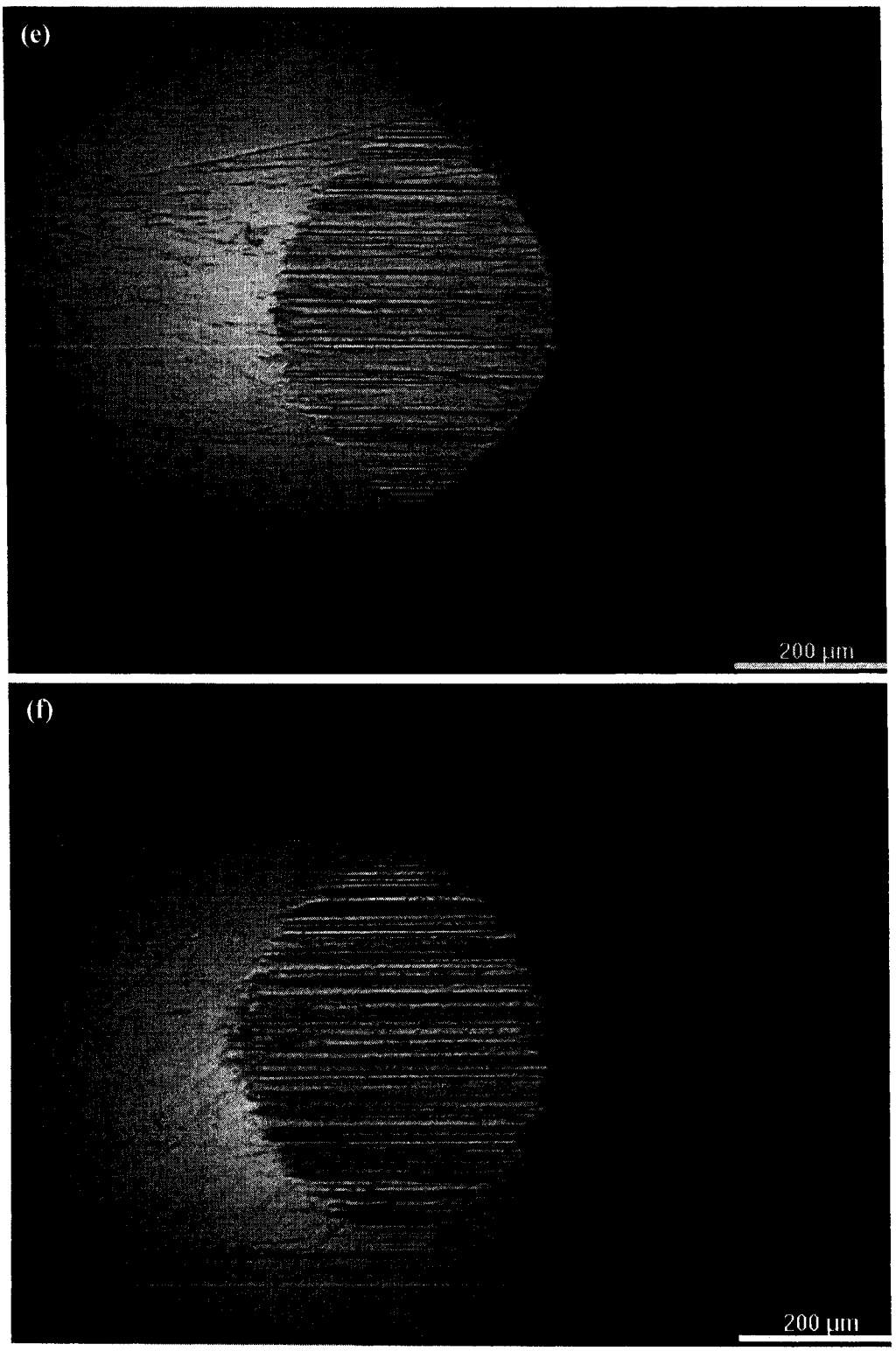

Fig. 4.15 Optical microscope photographs of the counterface steel balls sliding against the PEO coatings (a) X11, (b) X12, (c) X13, (d) X21, (e) X22 and (f) X23

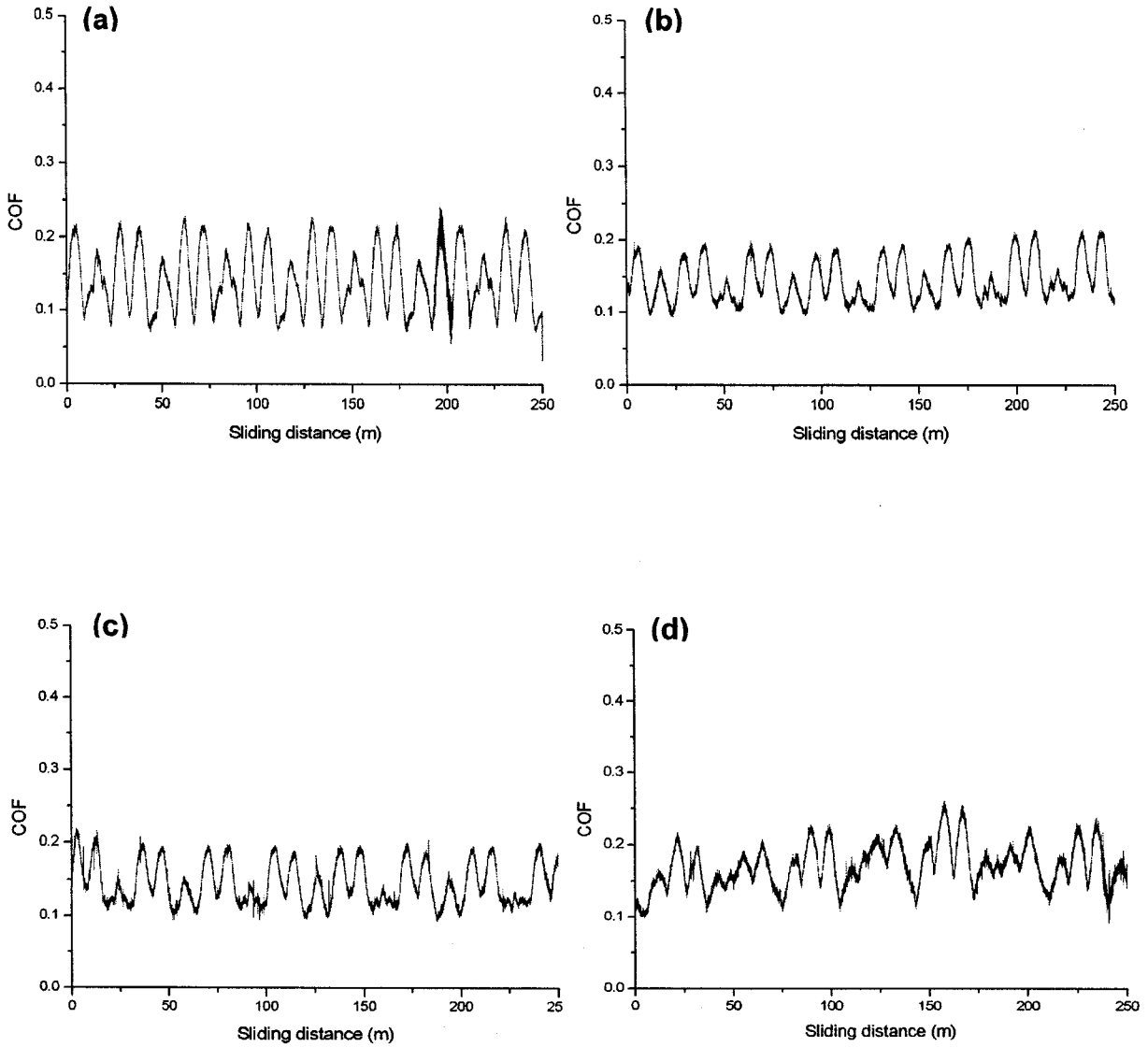

Fig. 4.16 to be continued

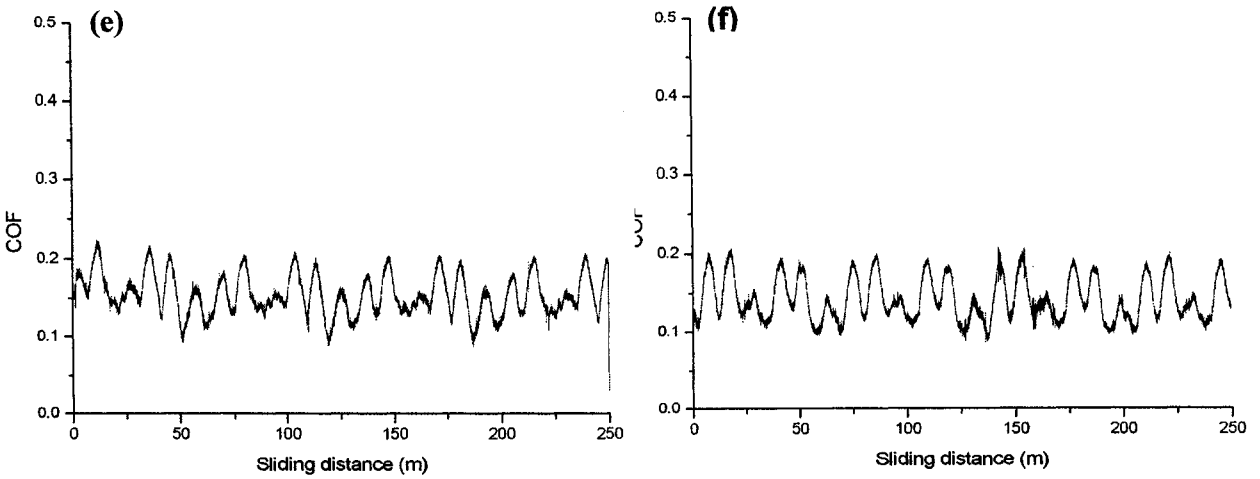

Fig. 4.16 COF curves of PEO coatings (a) X11, (b) X12, (c) X13, (d) X21, (e) X22 and (f) X23, against steel ball with 2N normal load under residual oil lubrication for 250m sliding distance

mixture surface. But, compared with coating X13, coating X22 is rougher due to the stronger discharge and the longer treatment time. The porous projections of the coating are subjected to be removed during the sliding test, possibly also leading to the third-body wear. However, the cavities distributed at the whole surface can provide oil during the test. Thus the COF is lower than that of coating X21, but higher than X13. Unlike the porous projections of coating X22, the projections of coating X23 are larger and denser. Thus, no obvious material removal is detected. Additionally, cavities in the surface also can provide lubricant oil during the test. Thus the COF is lower than that of coating X22.

But the coating surface is harder and rougher than those of coating X22, contributing to a slightly larger worn area of counterface steel.

4.4 Summary

In this chapter, two series of EJPP PEO coatings were produced on Al 319 substrates with two different electrolyte concentrations, using a DC power supply. At the beginning of the process, an anodizing process occurs at the aluminum matrix to form a thin and smooth aluminum oxide layer. Then, micro-discharges appear, which mainly concentrate on the silicon phase regions. The smooth aluminum oxide region has a poor oil retaining ability during the wear tests. After the protruding silicon phase regions in the thin coatings are worn away, the abrasive wear occurs to the smooth film. With the treatment time increasing, micro-discharges also form at the aluminum oxide region and promote the film growth. However, only a few of porosities exist at that region, which also results in the oil starvation during the wear test. But for the thin coating treated with the dilute solution, the smooth surface of aluminum oxide region is hard enough to avoid material removal. Therefore, a slightly higher COF and larger worn area of the counter pin are exhibited, compared with the pin counterpart sliding on Al390 substrate. Due to the high temperature produced by the discharges, mixture of silicon phase region and aluminum oxide region starts at the boundaries. Finally, large Si-Al-O compound projections scatter at the whole coating surface. Also, the coating roughness and hardness increase with the treatment time, which incline to increase the friction. However, the rough coating surface is good for oil retaining, although the oil can barely exist at the top surfaces of the imperforate projections under the residual oil lubrication condition. The combination effect makes the coatings have different tribological behavior, i.e., low friction and high

wear resistance. The coating X12 has the lowest COF, whilst the coating X23 has the highest wear resistance. Further increasing the coating thickness will result in a loose coating surface, leading to a severe third body wear if the surface is not polished. Therefore, the thick coatings do not guarantee a desired tribological property.

CHAPTER 5 EXPERIMENTAL RESULTS AND DISCUSSION II: SURFACE MORPHOLOGY AND TRIBOLOGICAL PROPERTIES OF PEO COATINGS ON AL390 SUBSTRATES TREATED WITH PULSED BIPOLAR DC POWER

As mentioned in chapter 3, a PEO process using bipolar DC power (PDC PEO) was used to deposit PEO coatings on the Al 390 alloys with the processing parameters listed in Table 3.3. In this chapter, the surface and tribological properties of the coatings are analyzed.

5.1 Characterization of PDC PEO coatings on Al 390

5.1.1 Voltage variation during the PDC PEO process

Fig 5.1 (a) shows voltage increment during the PDC PEO coating process for different treatment time on the Al 390 substrate. Since the voltage increment curves of all samples are almost overlapped and could be represented by the curve of coating Y4, shown in Fig. 5.1 (b). According to the curve, four distinct stages can be discerned in terms of the voltage growth rate. The voltage range of each stage and how many stages each sample experienced during the PDC PEO process, as well as the voltage growth rate of each stage, are determined and listed in Tables 5.1, and 5.2. In stage I, the voltage increasing

rate is the highest. Then, the voltage growth remains almost static in stage II. In stage III, the voltage increasing rate rises. After that, in stage IV, the growth rate becomes sluggish.

Table 5.1 Voltage range of each stage for different treatment time

Samples	Voltage range of each stage				Treatment time (min)
	Stage I	Stage II	Stage III	Stage IV	
	0-280V	280V-280V	280V-360V	≥360V	
Y1(350V)	•	•	•		0.9
Y2(370V)	•	•	•	•	1
Y3(390V)	•	•	•	•	1.5
Y4(410V)	•	•	•	•	3

Table 5.2 Voltage growth rate of each stage

Voltage growth rate of each stage (V/s)			
Stage I	Stage II	Stage III	Stage IV
18. 7	0	2. 7	0. 5

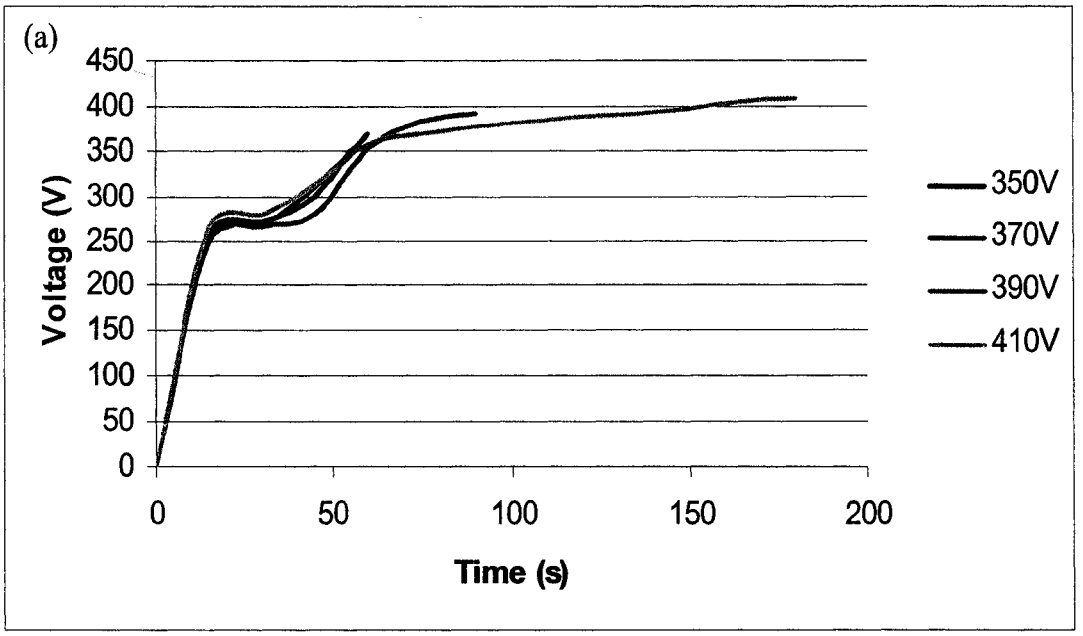

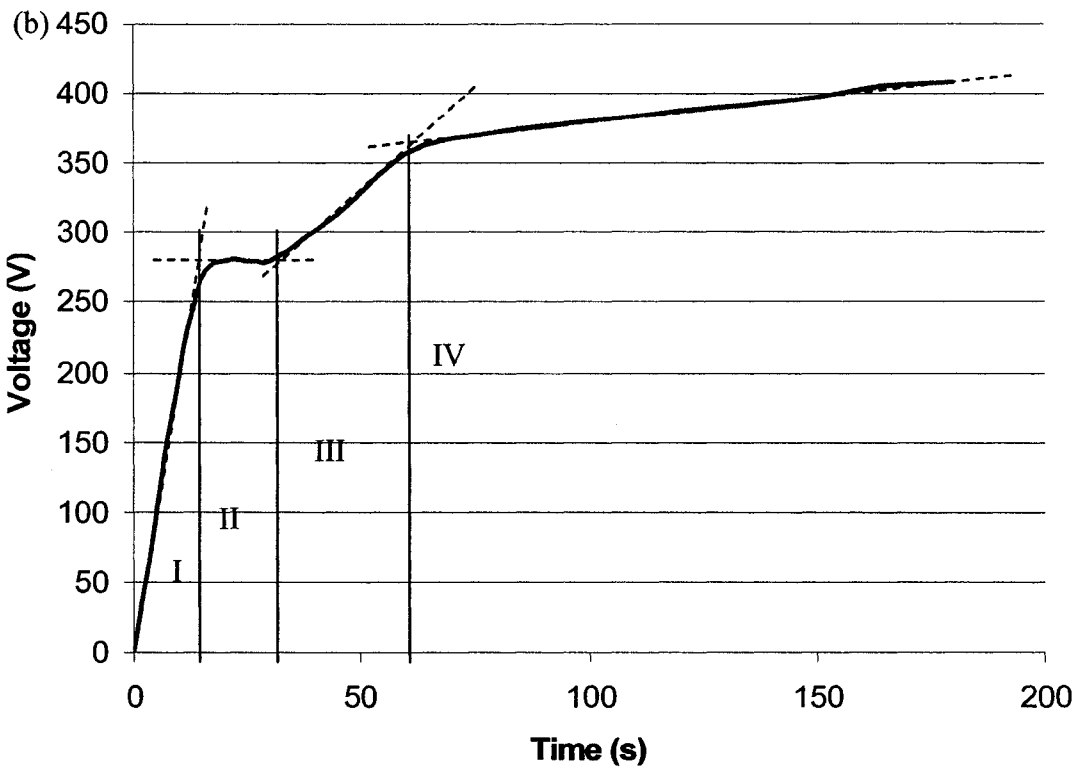

Fig. 5.1 (a) Voltage increment curves of PDC PEO coatings for different treatment time on Al 390 substrates and (b) classification of the stages for coating Y4

5.1.2 Surface morphology of PDC PEO coatings on Al 390

Figs. 5.2 (a, c, e, g) show the low magnification SEM micrographs of PDC PEO coatings. Figs. 5.2 (b, d, f, h) illustrate the corresponding high magnification micrographs. Both the aluminum matrix region and silicon phase rich regions can be identified in the coating surfaces of Y1, Y2 and Y3. For coating Y1, most discharge channels, indicated by the cavities, concentrate on the silicon phase rich regions (Figs. 5.2 (a, b)), where moving discrete white microdischarges are observed. The porous silicon rich regions are piling up from the aluminum matrix. Some tiny discharge channels exist at the smooth and dense aluminum oxide film, forming on the surface of aluminum matrix region, where luminescence and small sparks are observed. Similar to coating Y1, the silicon rich regions of coating Y2 are also piling up and porous. However, more discharge channels present at the aluminum oxide film of coating Y2, forming volcano-shape aluminum oxide projections (Figs. 5.2 (c, d)). Compared with coating Y1 and Y2, the silicon rich regions of coating Y3 are rougher and more aluminum oxide projections come into being, (Figs. 5.2 (e, f)). However, most projections have no porosities. For coating Y4, the silicon rich regions are mixed with the aluminum oxide film completely. A semi-sphere kind of structure is observed (Figs. 5.2 (g, h)). Furthermore, coating Y4 has less but larger discharge channels than the other coatings.

Figs. 5.3 (a, b) show the reflectance spectrums as a function of wavelength for coatings Y1 and Y2, individually. According to the spectra, film thickness can be determined accurately. Figs. 5.3 (c, d, e) display the SEM cross-section images of coating Y2, Y3 and Y4. The coating lies between the bright nickel coating and the dark Al-Si 390

substrate. The nickel flew inside the discharge channel and filled up the voids in the coating during the electroless plating process. Compared with coating Y3 and Y4, coating Y2 is much denser and smoother due to its smaller discharge channels. All thickness measurement results are listed in Table 5.3. For coating Y2, the measurement results from two methods are very close, indicating good consistency. For coating Y1, the thin layer makes it too difficult to get a good cross-section image.

Figs. 5.4 (a, b, c, d) display the surface profiles of coatings Y1, Y2, Y3 and Y4, respectively. The highest peaks in Figs. 5.4 (a, b, d) are corresponding to the positions of the piling-up silicon phase regions in coating Y1, Y2 and Y3. Coating Y1 and Y2 present almost the same peak height (about 1.5 μm). Coating Y3 exhibits a little higher peak value. For coating Y4, due to the mixture of aluminum oxide region and silicon phase regions, the projections in the profiles indicate the positions of Al-Si-O compounds.

Fig. 5.5 displays the surface roughness measurement results of all coatings. The surface roughness increases with the treatment time.

Table 5.3 Thickness measurement results

Method	Reflection spectrum		SEM cross-section image		
Coating	Y1	Y2	Y2	Y3	Y4
Coating Thickness (μm)	0.3	0.59	0.55	1.25	4.21

5.1.3 Discussion

Same as the PEO process with DC mode discussed in Chapter 4, the PDC PEO process, in stage I, also experiences a rapid linear voltage increase as a result of an anodizing process that mainly occurring at the aluminum matrix region. Microdischarge, starting at stage II, firstly concentrates on Al-Si boundary. The silicon particles are oxidized in the discharge channels and melted with Al, Figs. 5.2 (a, b, c, d). With the coating growth, discharges occurs at all coating surface. Due to the high temperature generated by the discharge, aluminum oxide region and the silicon phase region are melted and mix with each other. With the treatment time increasing, the diameters of the discharge channels increase, while the amount of the channels decrease.

However, compared with DC PEO process, the high frequency PDC PEO process has the following characteristics. Firstly, the reversal of sample polarity promotes the hydrogen liberation [62], providing a plasma-supporting gas medium in the vicinity of the oxide-electrolyte interface from the very beginning of the oxidation process, unlike the DC mode of PEO. A consequent acoustic emission can be heard for each coating after the beginning of the treatment about several seconds. A gas phase discharge at the oxide surface can be easily established when the voltage drop across the gas bubble reaches the critical breakdown value during the positive biasing. Therefore, the critical breakdown voltage, indicating the beginnings of the second stage is lower than the counterpart in DC mode PEO process. However, the oxidation reaction of the anode, resulting in the formation of the anodizing film, is restrained by the reversal of sample polarity.

Therefore, the voltage increasing rate of the first stage is lower than the counterpart in DC PEO process.

Secondly, the overall positive current density is less than that of DC PEO process for the same current amplitude. As a result, the voltage growth in stage II is almost stagnant, which is also observed in the DC PEO process with low current densities and the duration of stage II can diminishes with increasing the current density, shown in Fig. 5.6 [18].

Thirdly, in PDC PEO process, the sharp rising edge of each pulse current produces a high initial current peak, which triggers the ignition of short and intense plasma microdischarges at the sample surface due to the electron impact ionization. Different from the long-lived, large microdischarges initiated by thermal ionization in DC PEO process, the short and intense plasma discharges have lower thermal impact to the sample surface and higher rate of mass transfer directed toward the substrate through the channels. Therefore, the voltage growth rates of stage III and IV are higher than those of DC PEO process.

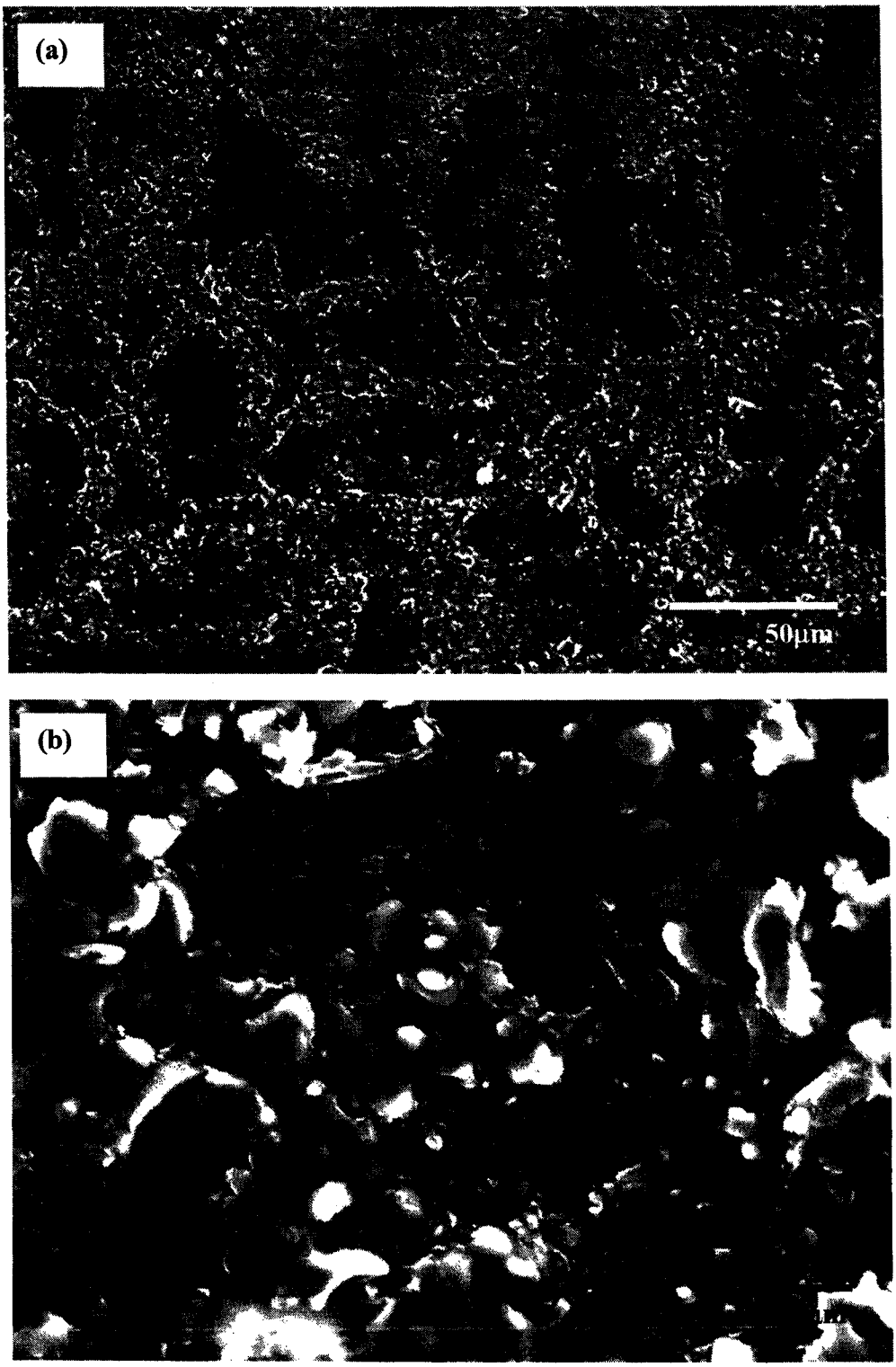

Fig. 5.2 to be continued

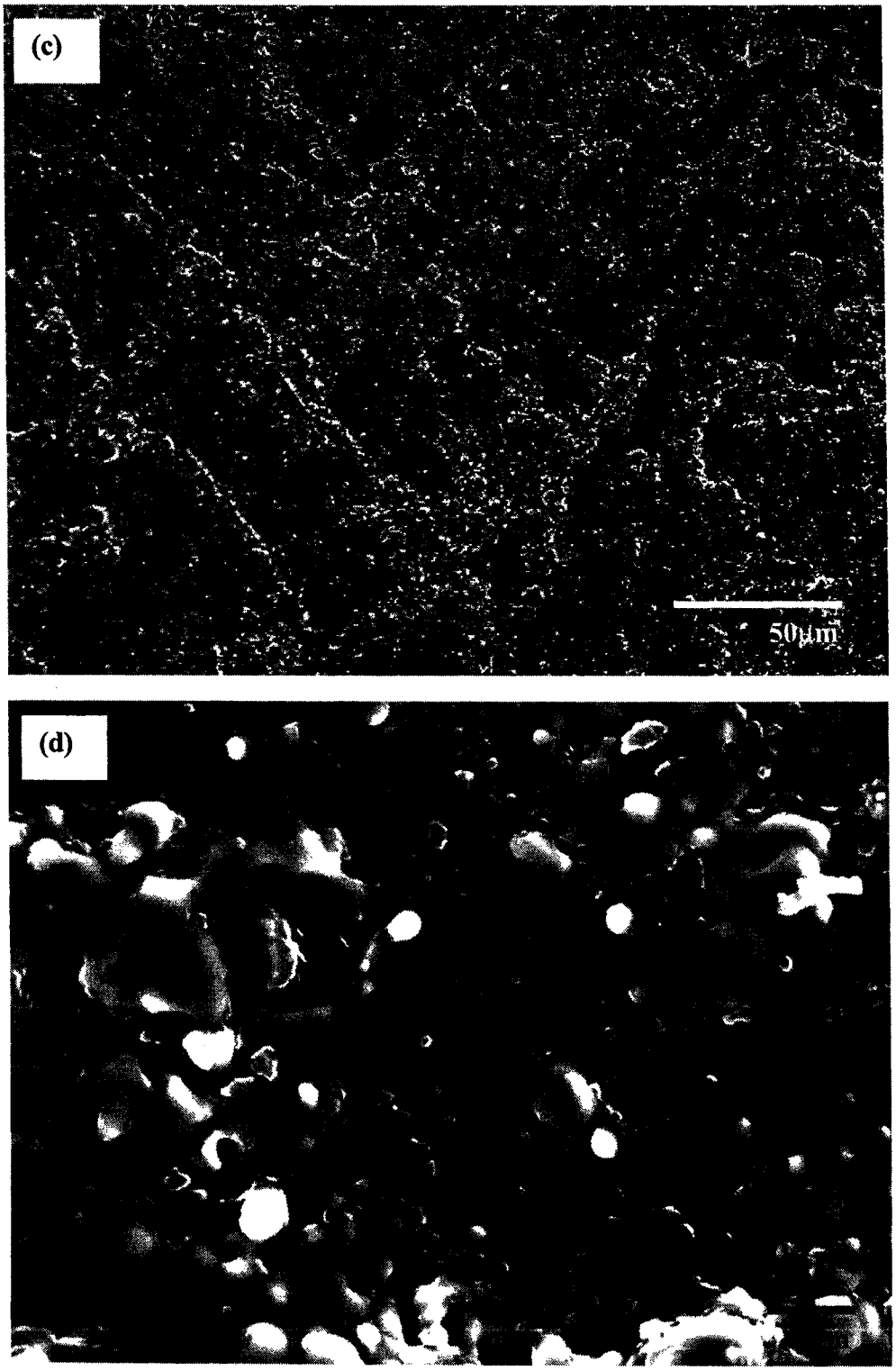

Fig. 5.2 to be continued

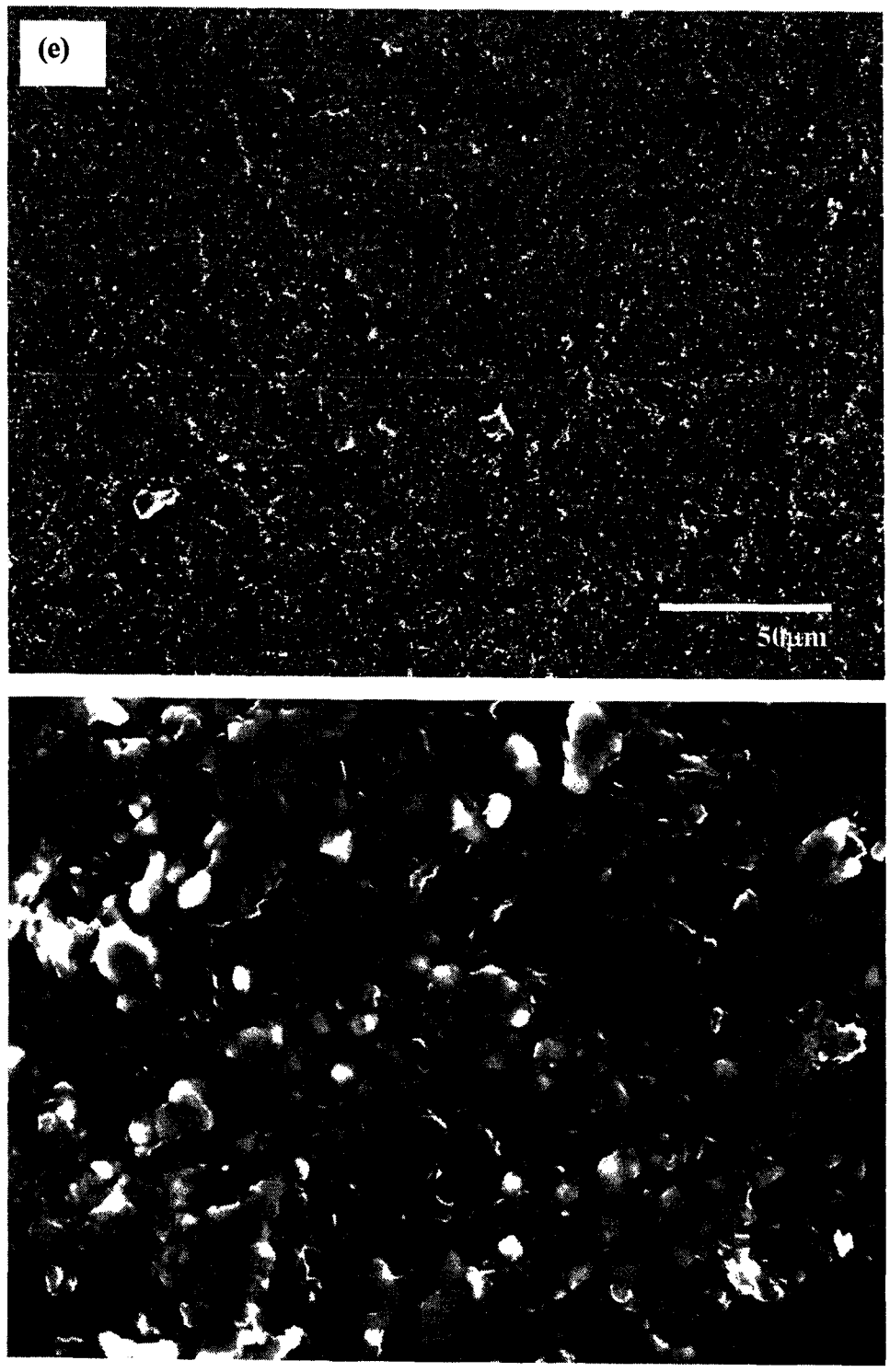

Fig. 5.2 to be continued

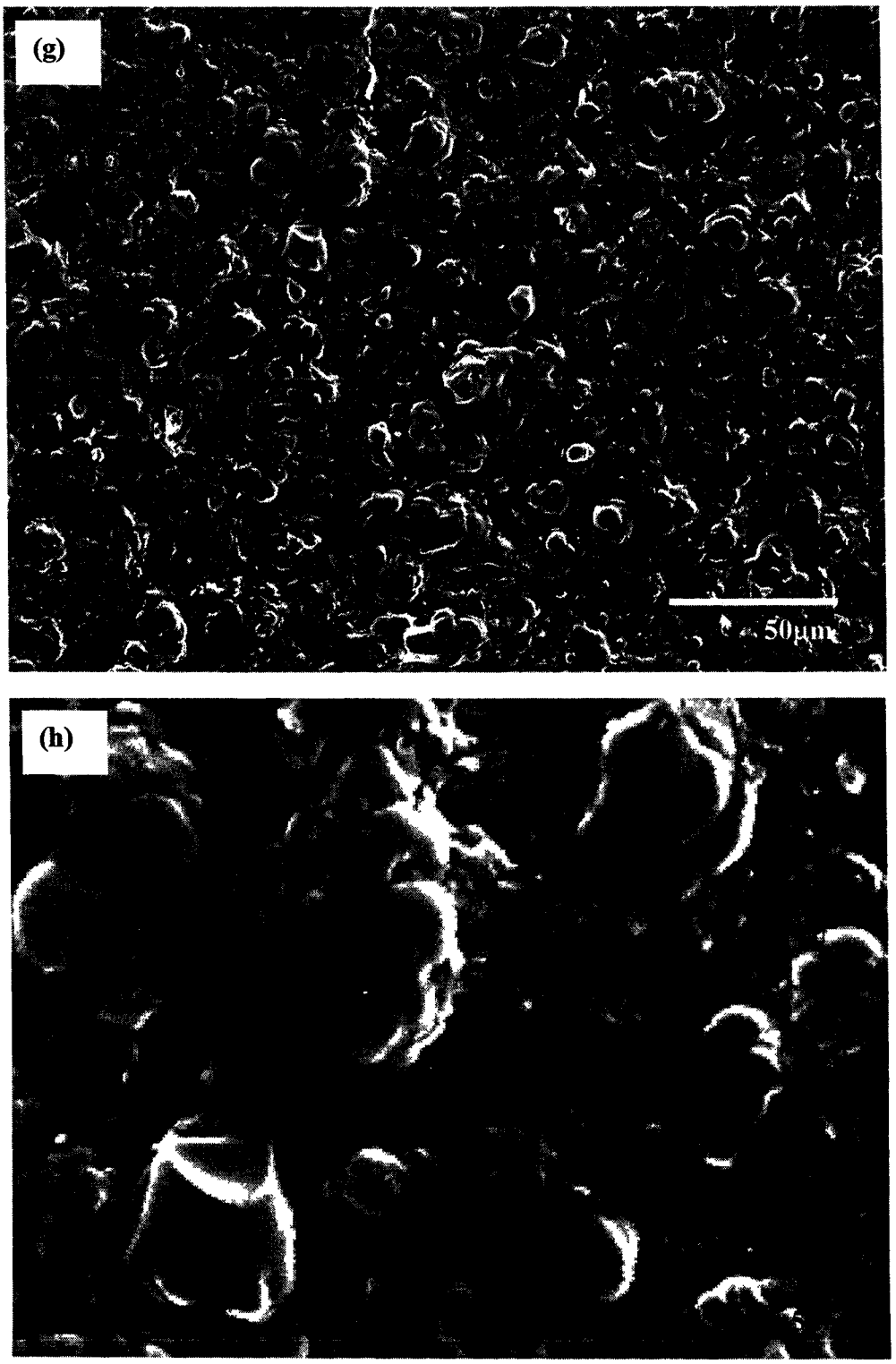

Fig. 5.2 SEM images of PEO coatings of (a) Y1, (c) Y2, (e) Y3 and (g) Y4, and the corresponding high magnification images (b), (d), (f), and (h)

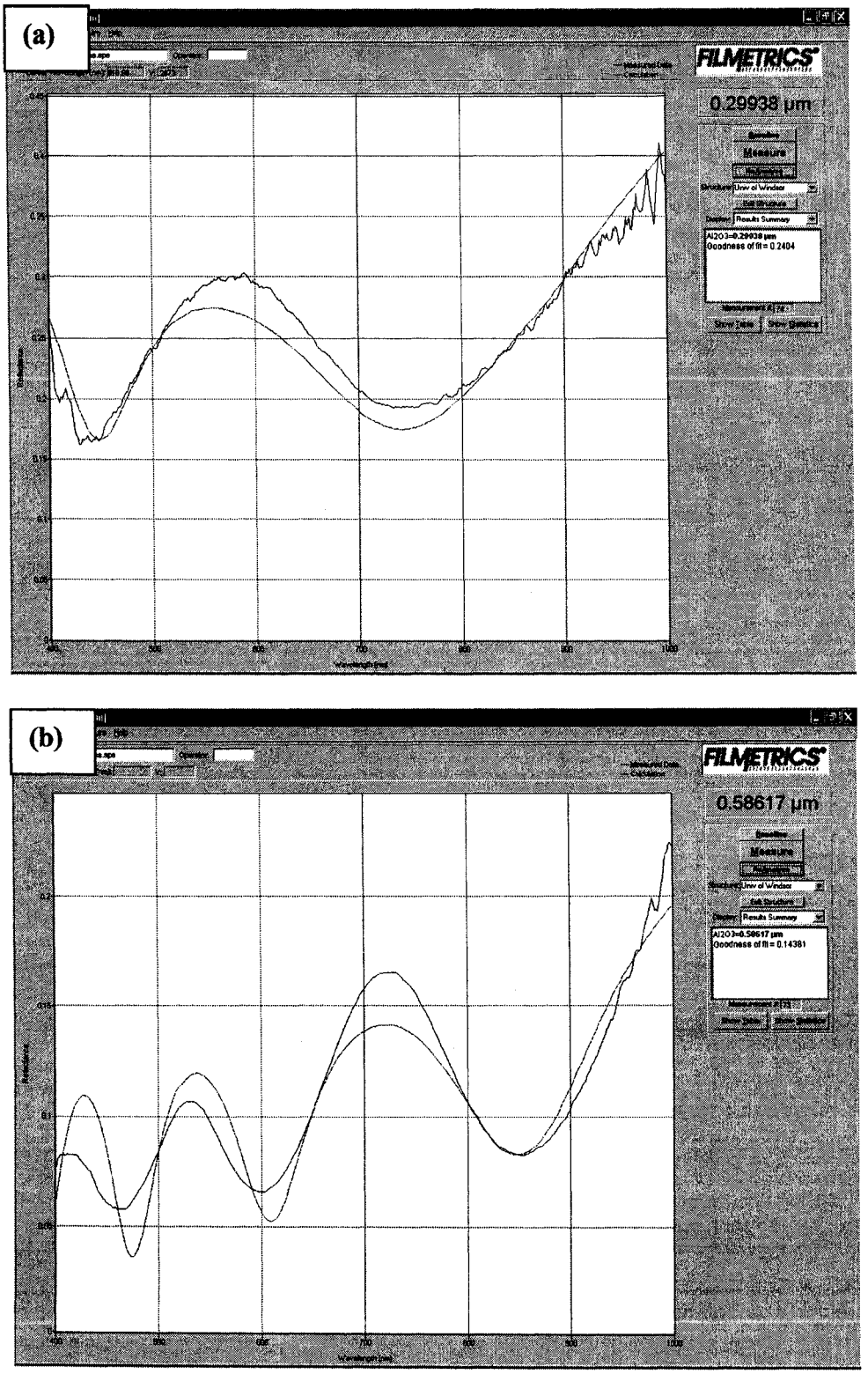

Fig. 5.3 to be continued

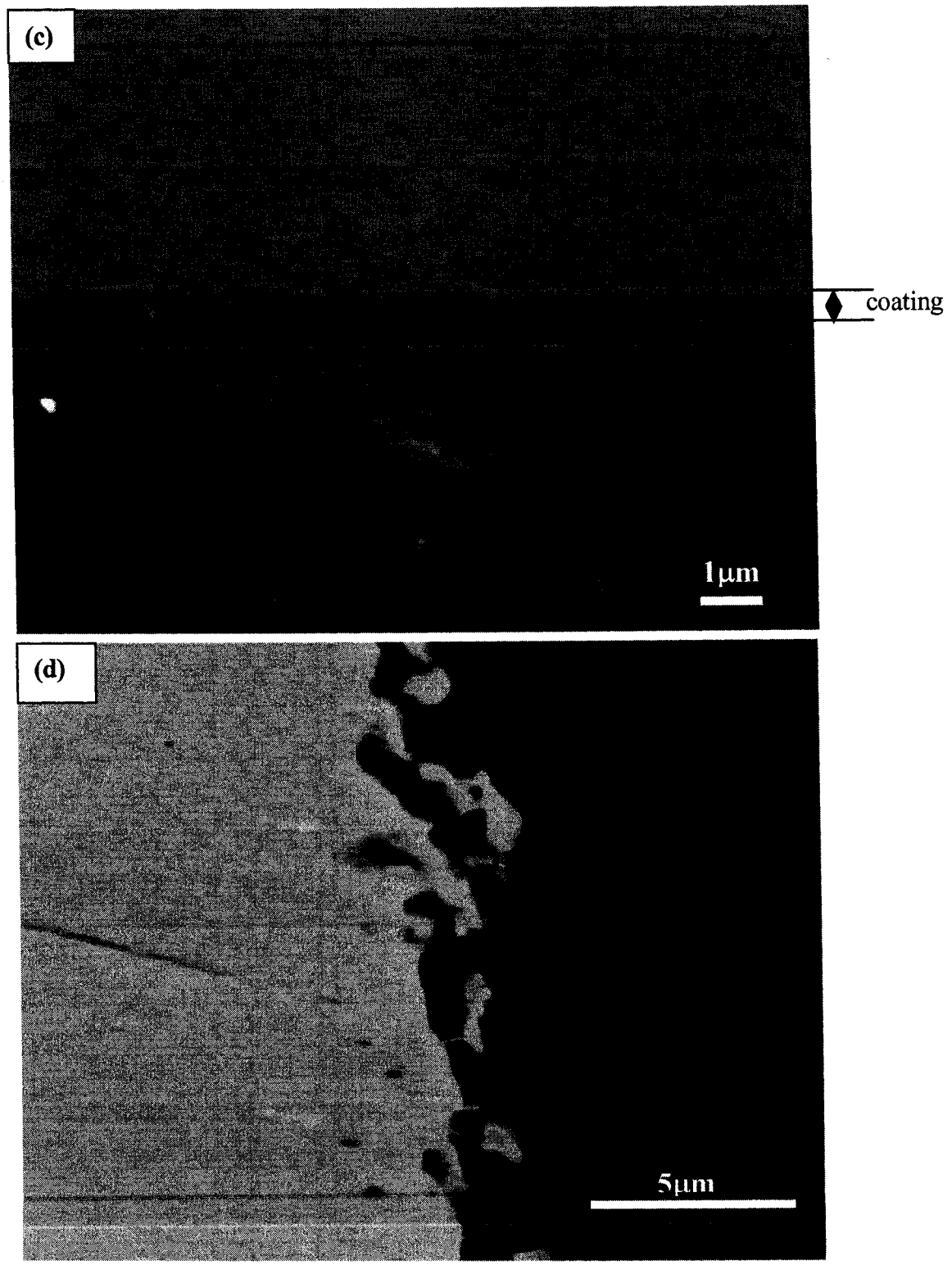

Fig. 5.3 to be continued

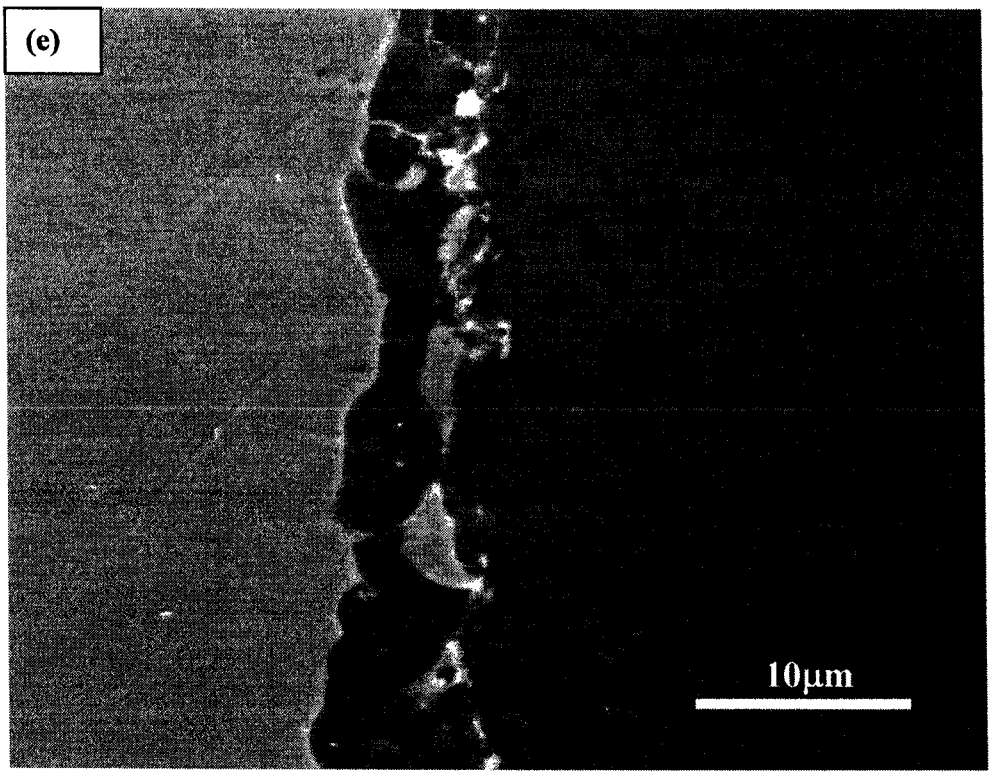

Fig. 5.3 Reflection spectra for (a) Y1, (b) Y2, and SEM cross-section images for (c) Y2, (d) Y3, and (e) Y4

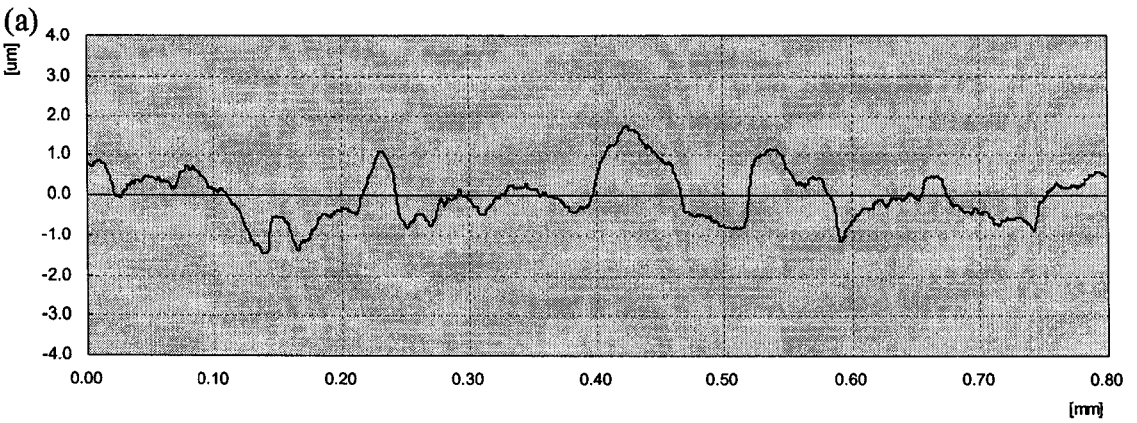

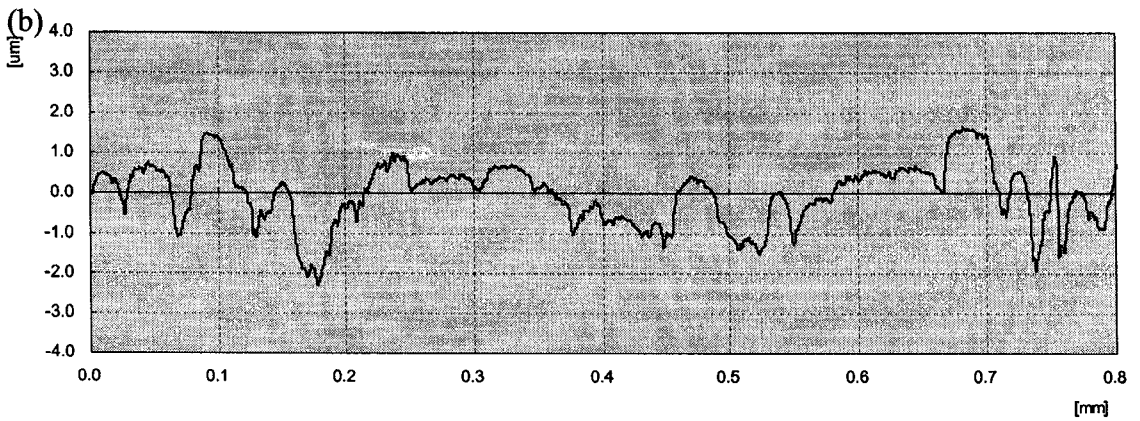

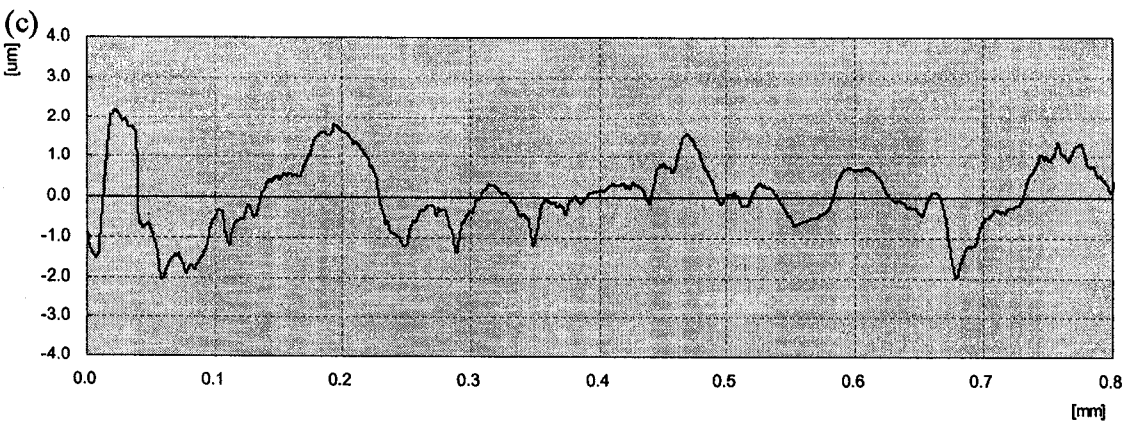

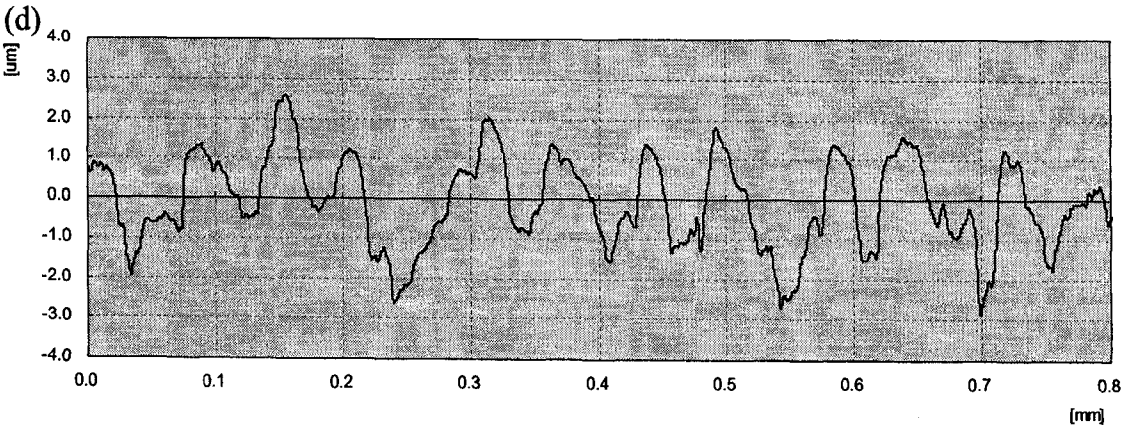

Fig. 5.4 Surface profiles for coatings (a)Y1, (b) Y2, (c)Y3, and (d) Y4

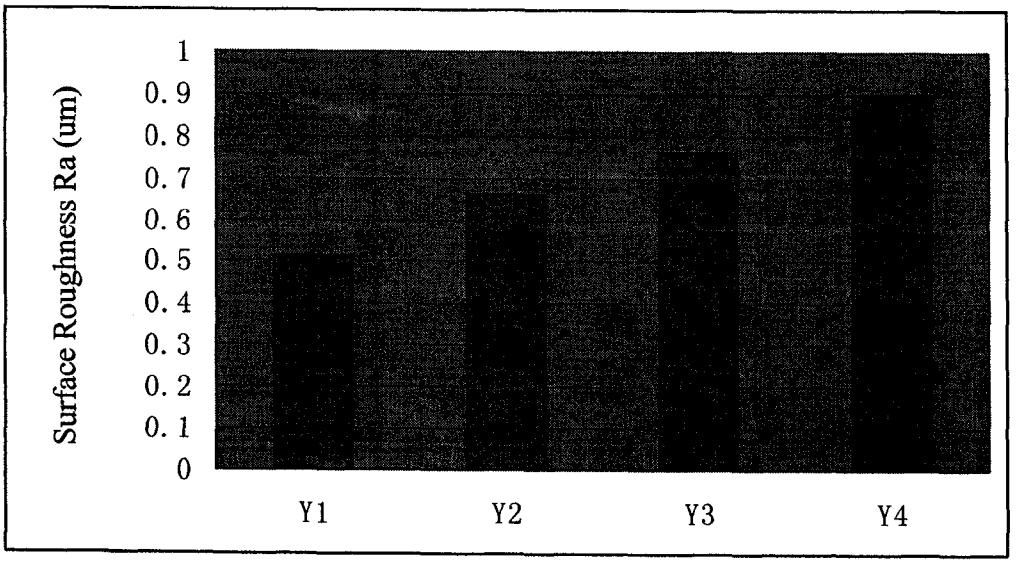

Fig. 5.5 Surface roughness Ra of all coatings

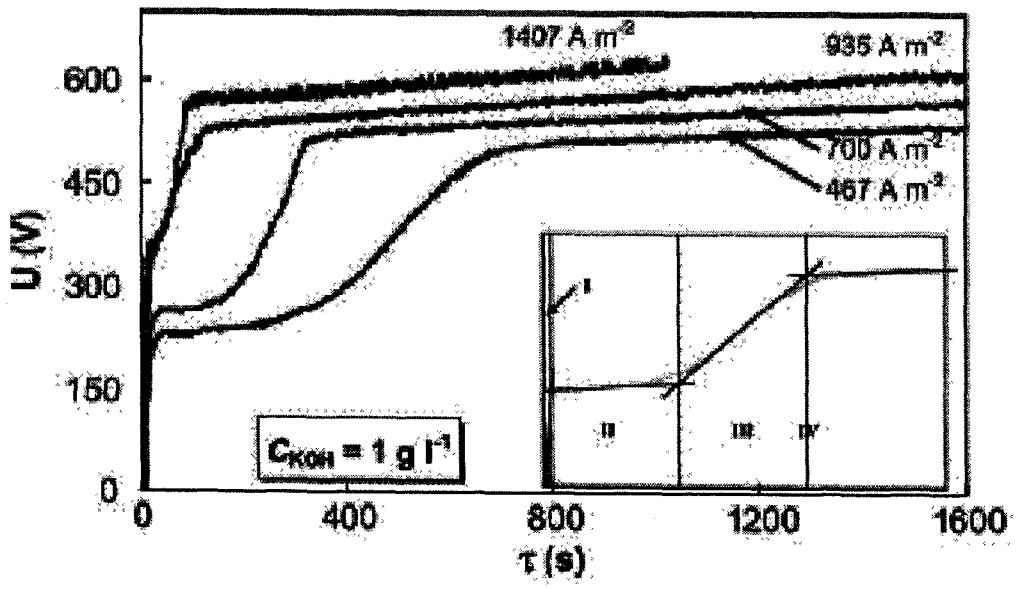

Fig. 5.6 Voltage vs. time plots of DC PEO process, under different current density [18]

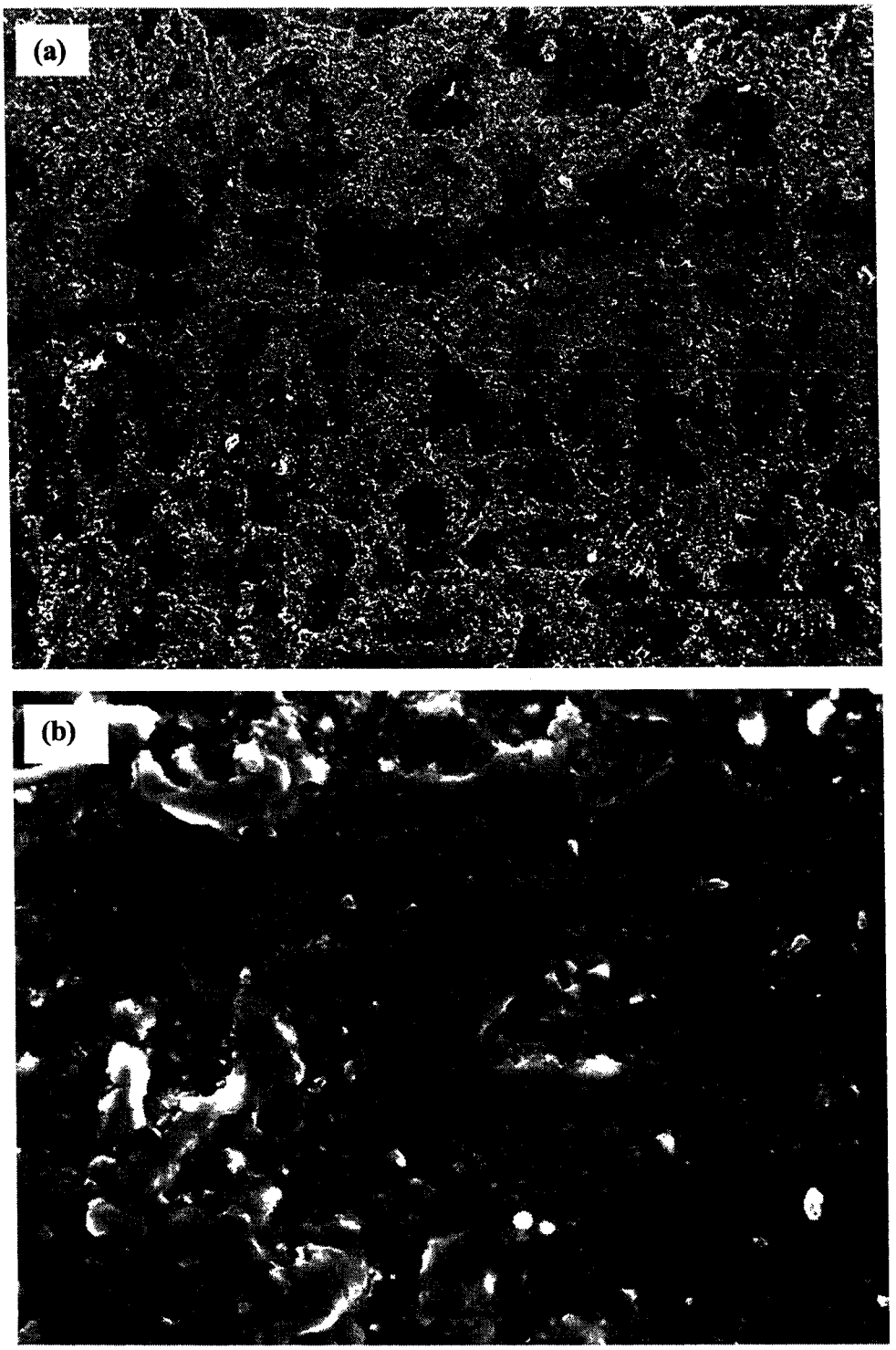

Fig. 5.7 to be continued

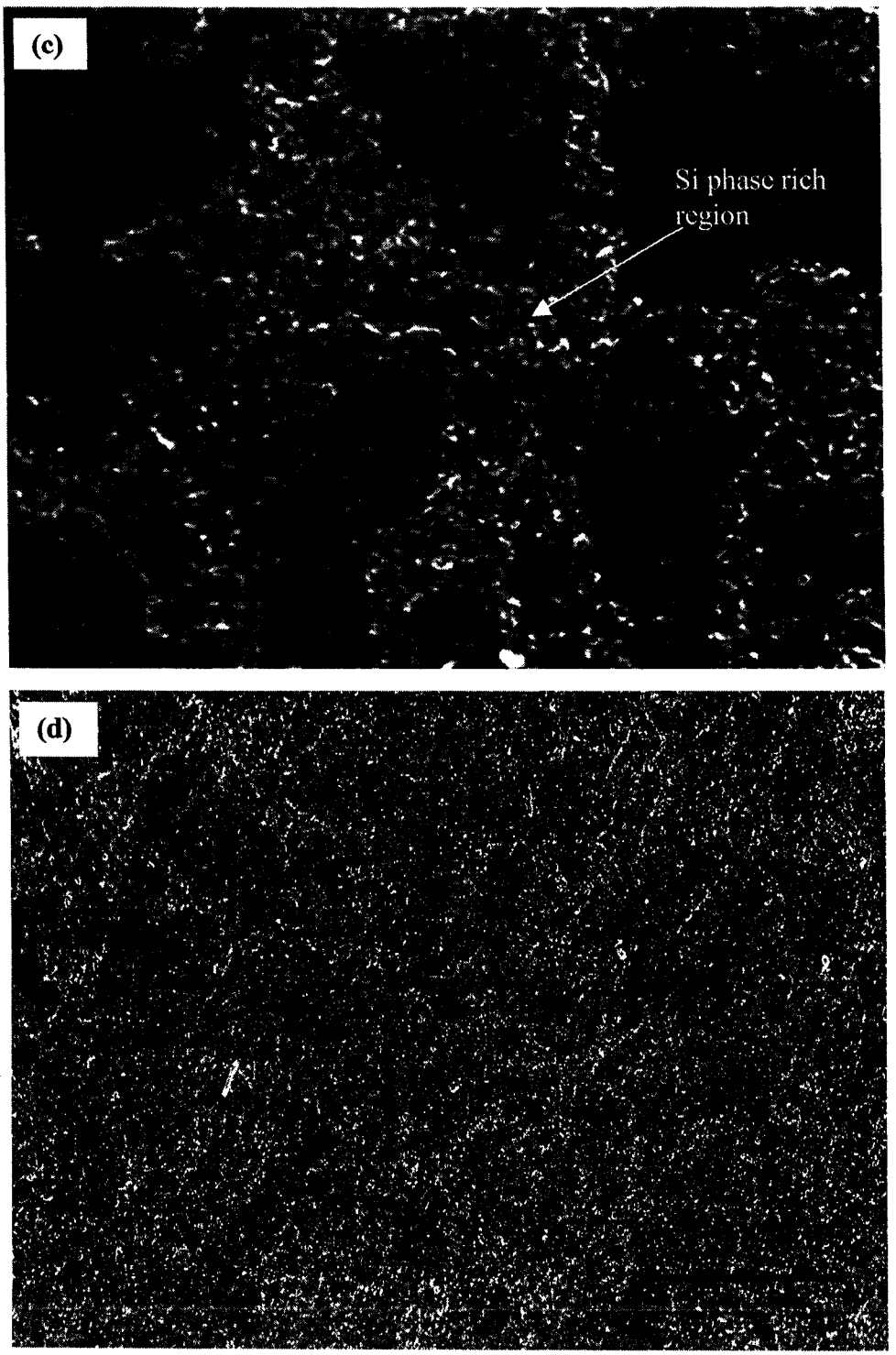

Fig. 5.7 to be continued

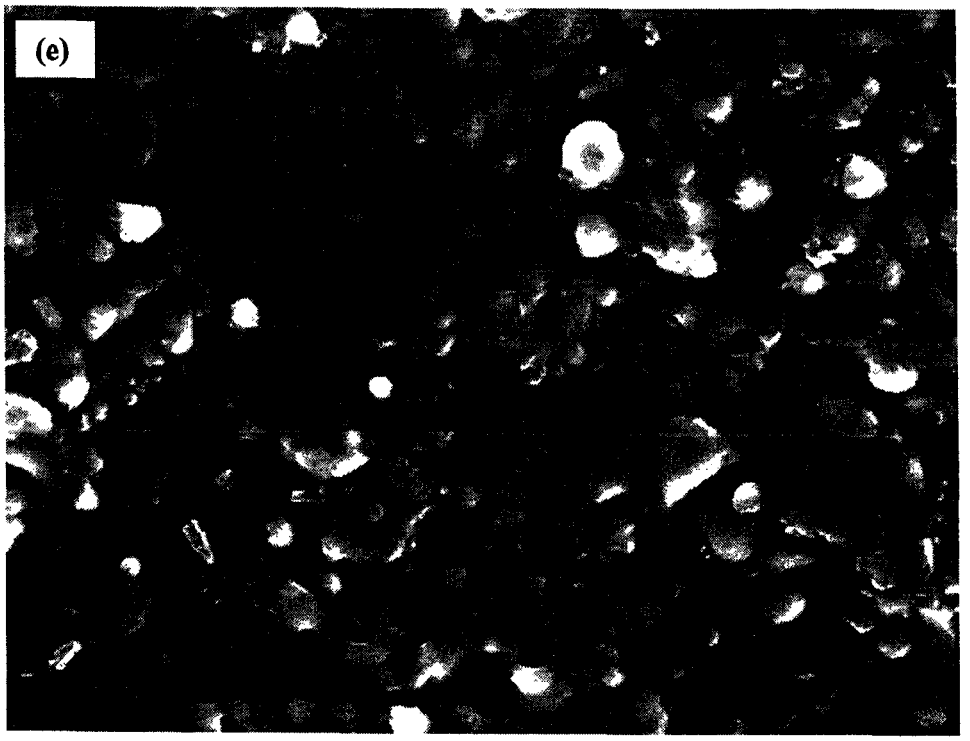

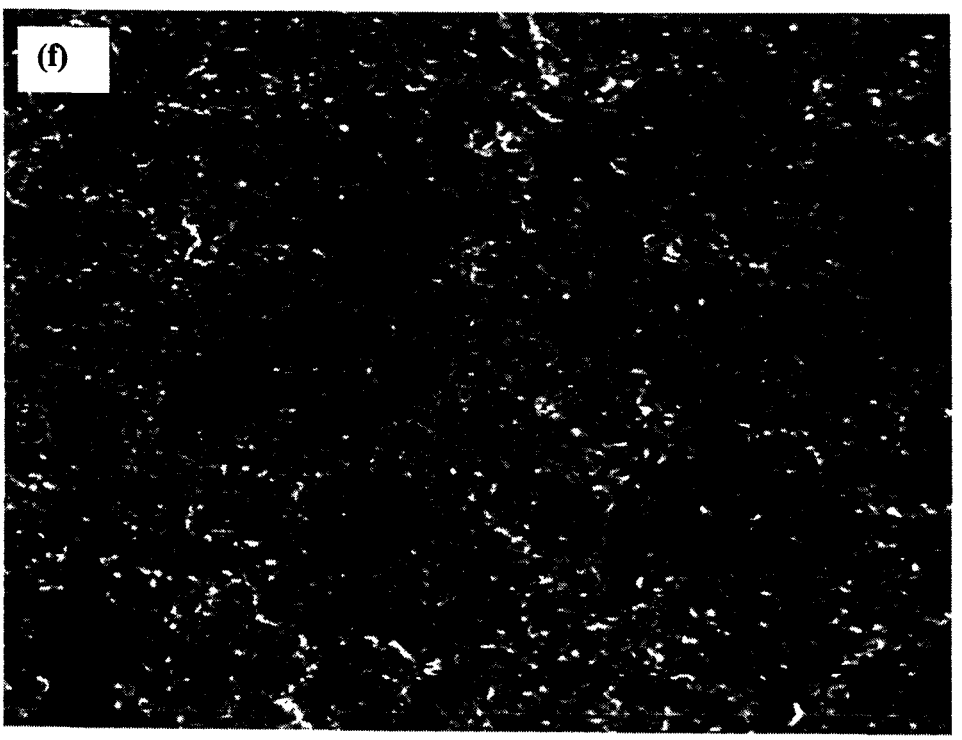

Fig. 5.7 to be continued

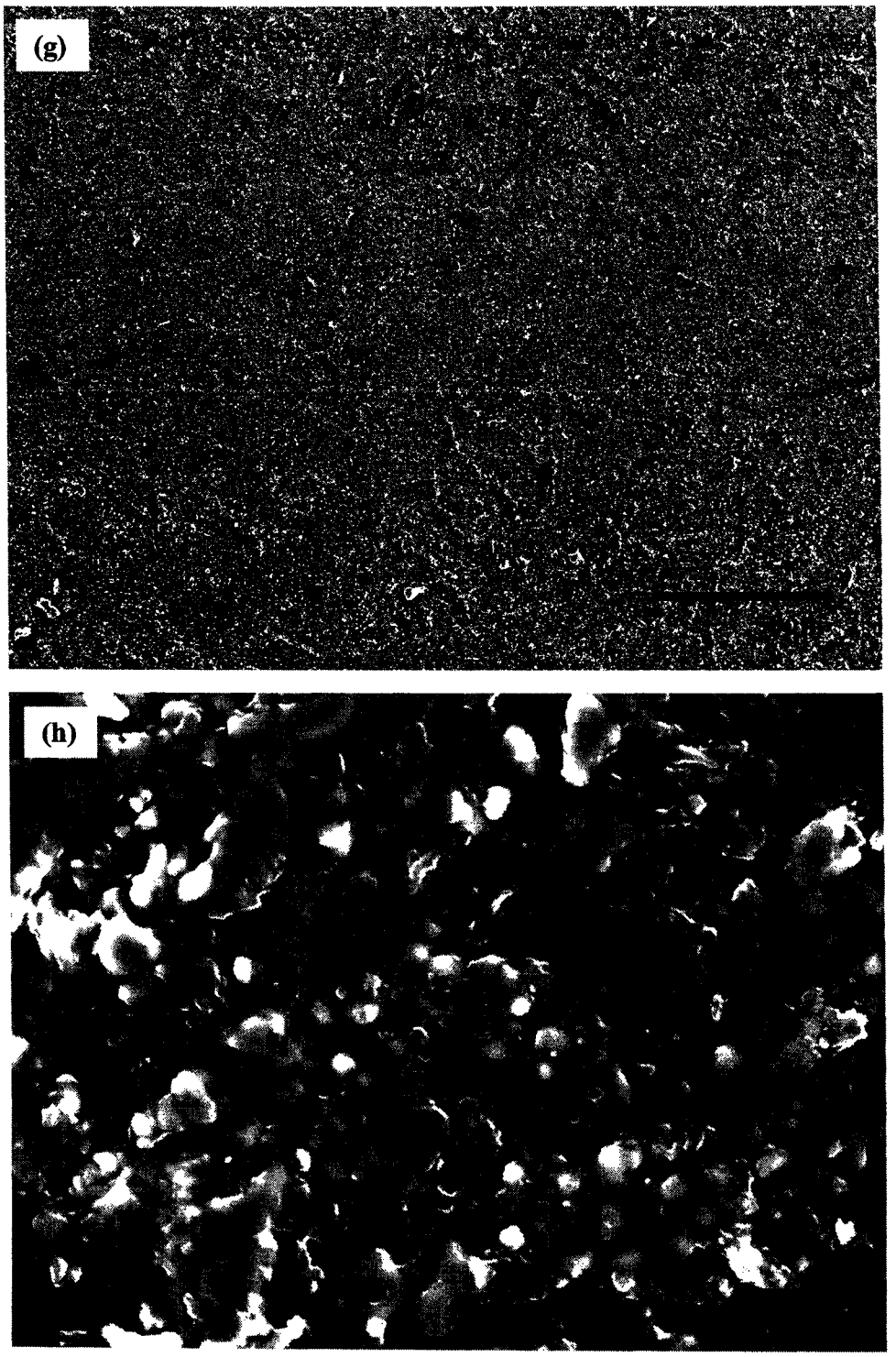

Fig. 5.7 to be continued

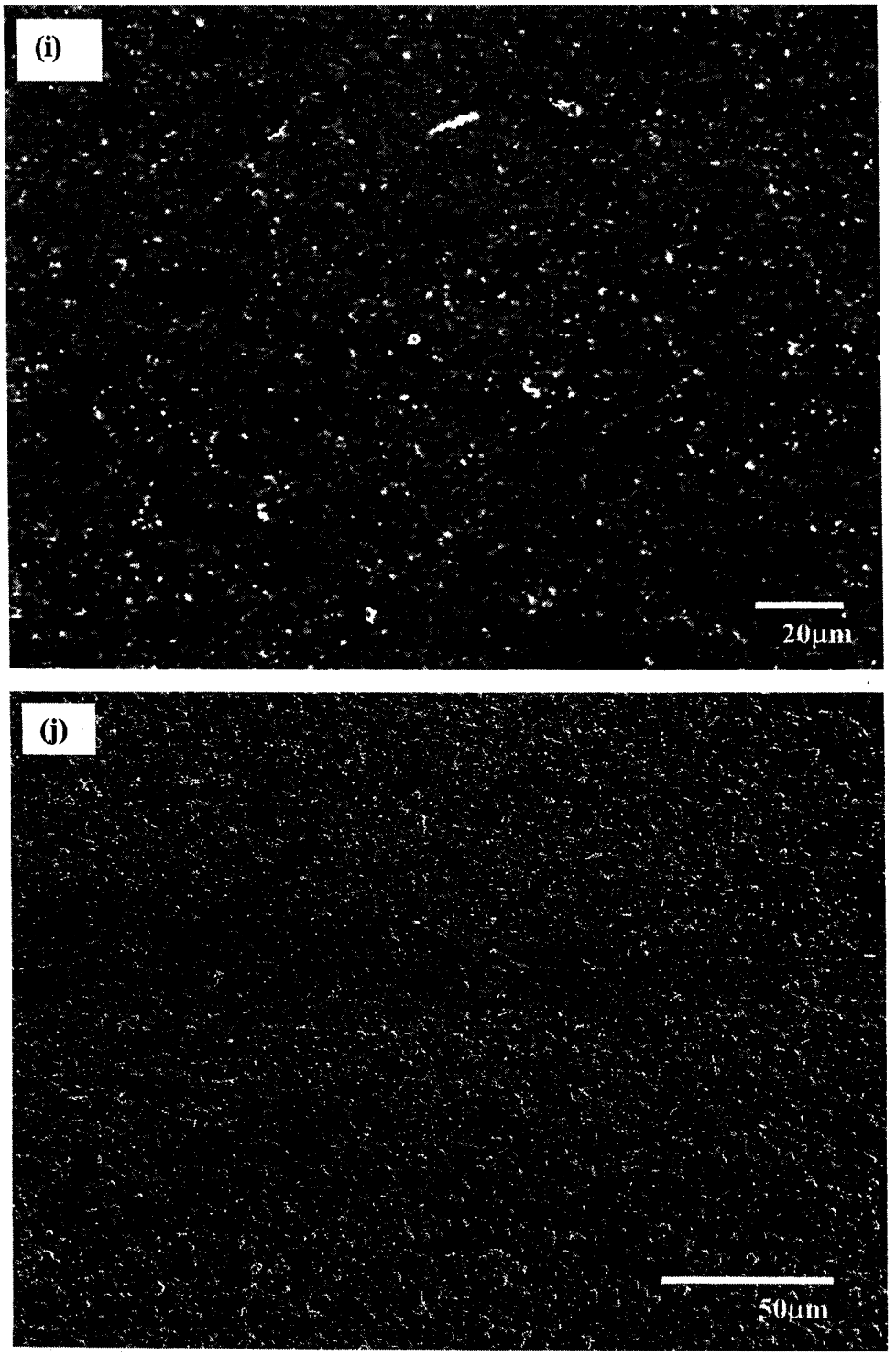

Fig. 5.7 to be continued

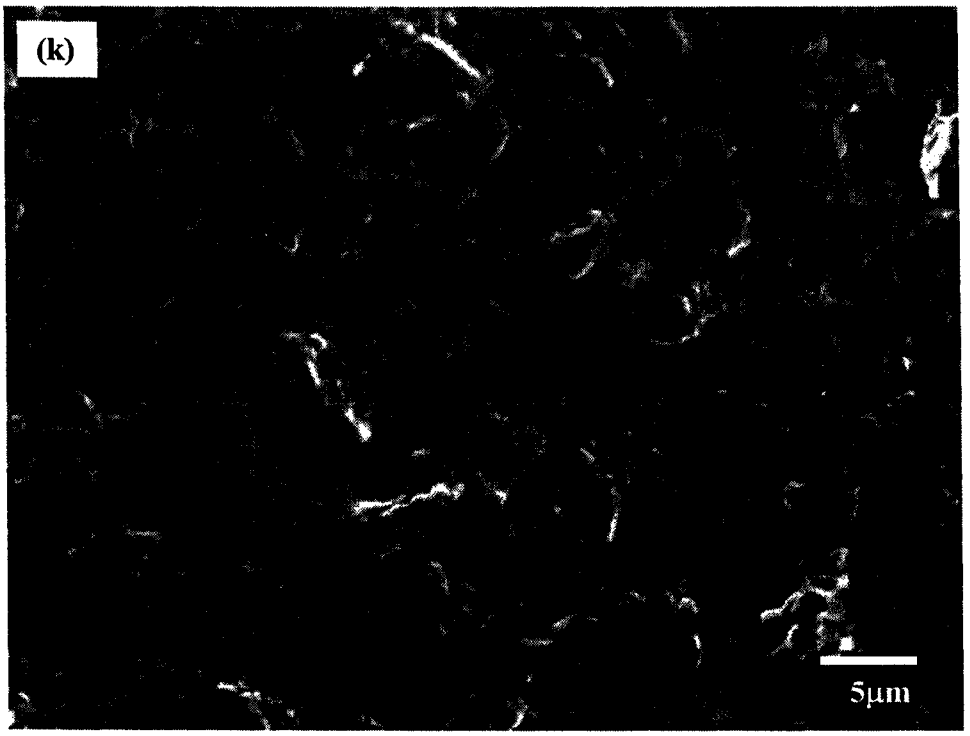

Fig. 5.7 SEM micrographs of the wear tracks on PEO coatings sliding against steel ball with 2N normal load under residual oil lubrication for 250m, (a) Y1, (d) Y2, (g) Y3 and (j) Y4, and the corresponding high magnification micrographs for aluminum oxide regions of (b) Y1, (e) Y2, (h) Y3, for silicon phase regions of (c) Y1, (f) Y2, (i) Y3, and for the whole coating surface of (k) Y4

5.2 Tribological properties of PDC PEO coatings on Al 390 sliding against steel balls under residual oil lubrication

5.2.1 Tribological test results of PDC PEO coatings on Al 390 sliding against steel balls under residual oil lubrication

Figs. 5.7 (a, d, g, j) show the low magnified SEM micrographs of the wear tracks for PEO coatings Y1, Y2, Y3 and Y4. Figs. 5.7 (b, e, h) are the corresponding high magnification micrographs for aluminum oxide regions of Y1, Y2, and Y3, respectively. Figs. 5.7 (c, f, i) display the corresponding high magnification micrographs for silicon phase rich regions of Y1, Y2, and Y3, individually. Fig. 5.7 (k) is the high magnification one for Y4. On coating Y1, the piling up porous silicon regions are removed, shown in Figs 5.7 (a, c). No scratch is clearly observed at the aluminum oxide region, Fig 5.7 (b). Also, wear debris presents in the wear track, Fig 5.7 (a). For coatings Y2 and Y3, the protruding porous silicon regions are slightly or partially removed, whilst the aluminum oxide region remains intact, Figs 5.7 (d, e, f) and Figs 5.7 (g, h, i). For coating Y4, the abrasive wear is clearly observed, indicated by the scraped protruding particle, Fig. 5.7 (j). Compared with the unworn area, shown in Figs. 5.2 (g, h), a lot of small holes are exposed in the wear track area. And the dense and smooth pancake-shape structure does not exist any more, replaced by a relatively loose and more porous structure, Fig. 5.7 (k).

Figs. 5.8 (a, b, c, d) show the optical microscope photographs of the counter steel balls, sliding against the PEO coatings Y1, Y2, Y3 and Y4, individually. Abrasive wear is

observed for all counter pins. However, coating Y2 exhibits the best compatibility for steel ball with the smallest worn area of the counterface, almost equal to the worn area of counter steel ball sliding against Al substrate under the same conditions. Coating Y4 shows the worst compatibility for steel.

Figs 5.9 (a, b, c, d) display the Coefficient of Friction curves for coatings Y1, Y2, Y3 and Y4. The average values of COF curves for all coatings are listed in Table 5.4. It is very clear that coating Y2 presents the lowest average COF, and coatings Y1 and Y4 exhibit the highest ones, whilst the average COF of coating Y3 is in the middle.

Table 5.4 Average values of COF curves for all coatings sliding against steel ball with 2N normal load under residual oil lubrication for 250m.

Coatings	Y1	Y2	Y3	Y4
COF	0.195	0.133	0.153	0.192

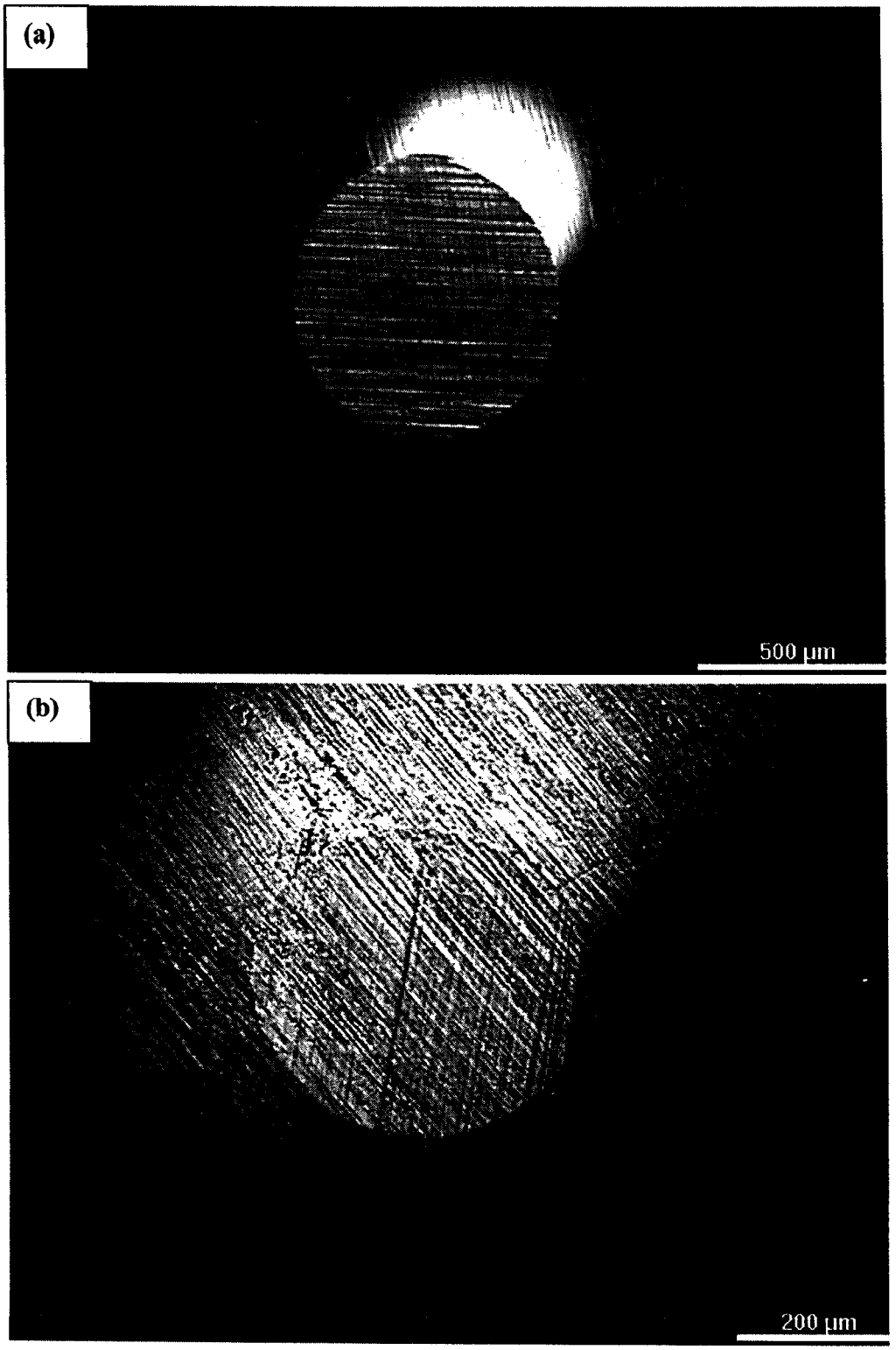

Fig. 5.8 to be continued

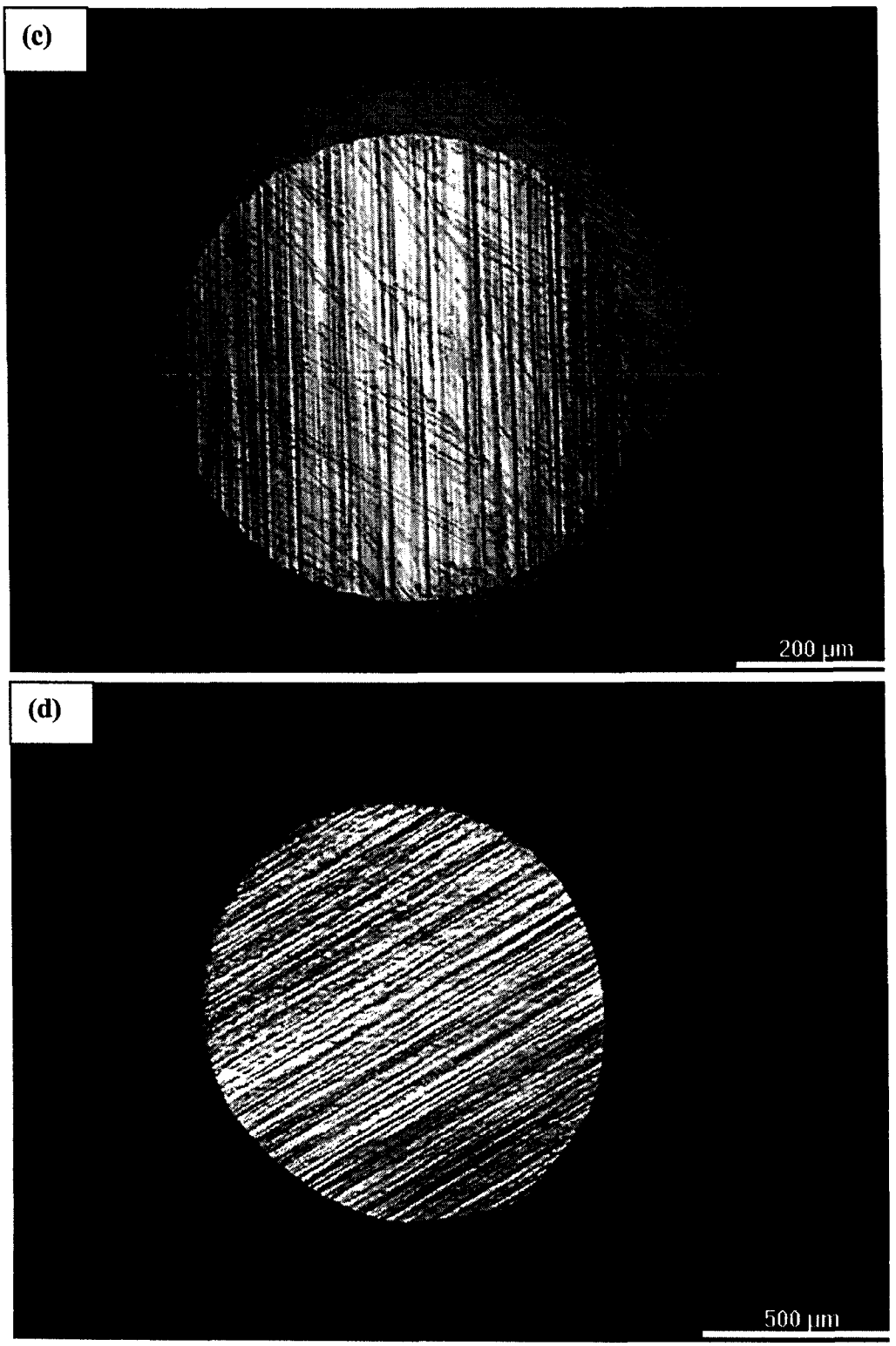

Fig. 5.8 Optical microscope photographs of the counterface steel balls sliding against the PEO coatings (a) Y1, (b) Y2, (c) Y3 and (d) Y4, with 2N normal load under residual oil lubrication

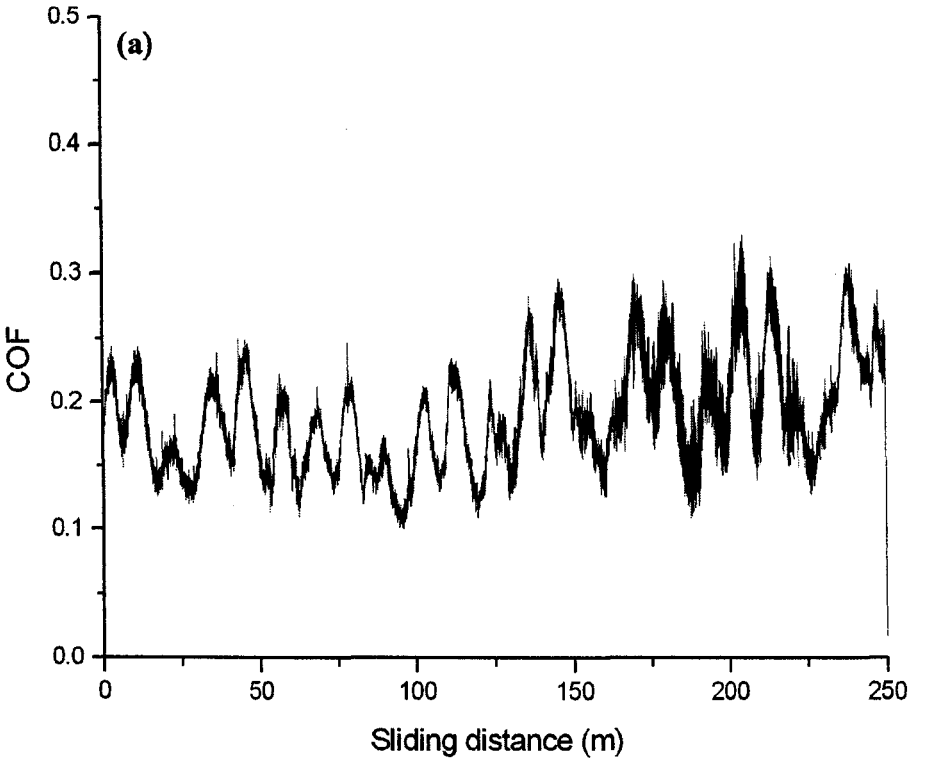

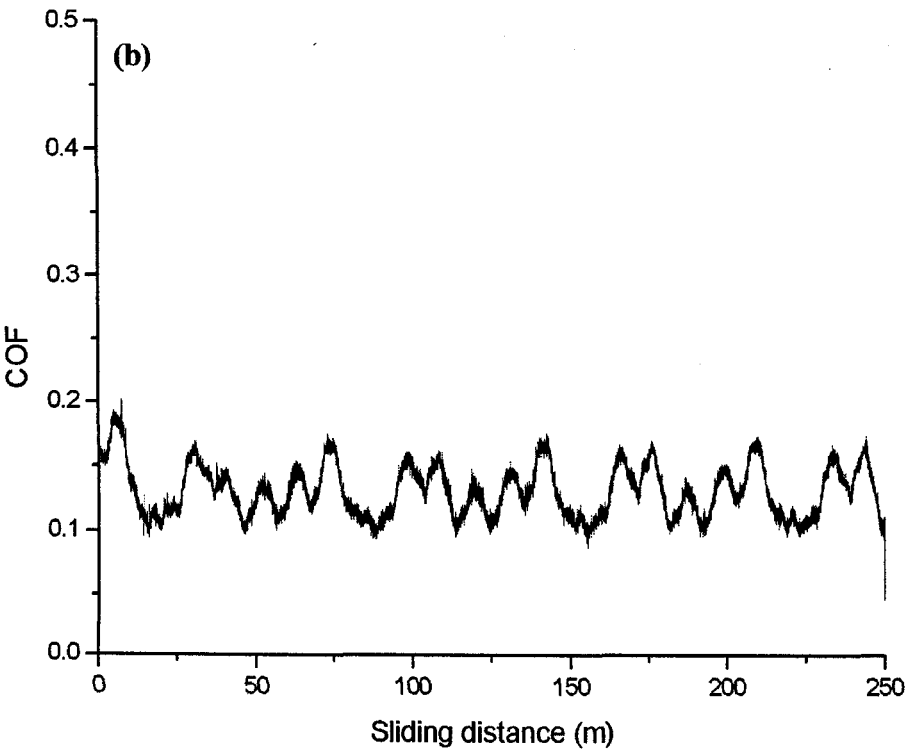

Fig. 5.9 to be continued

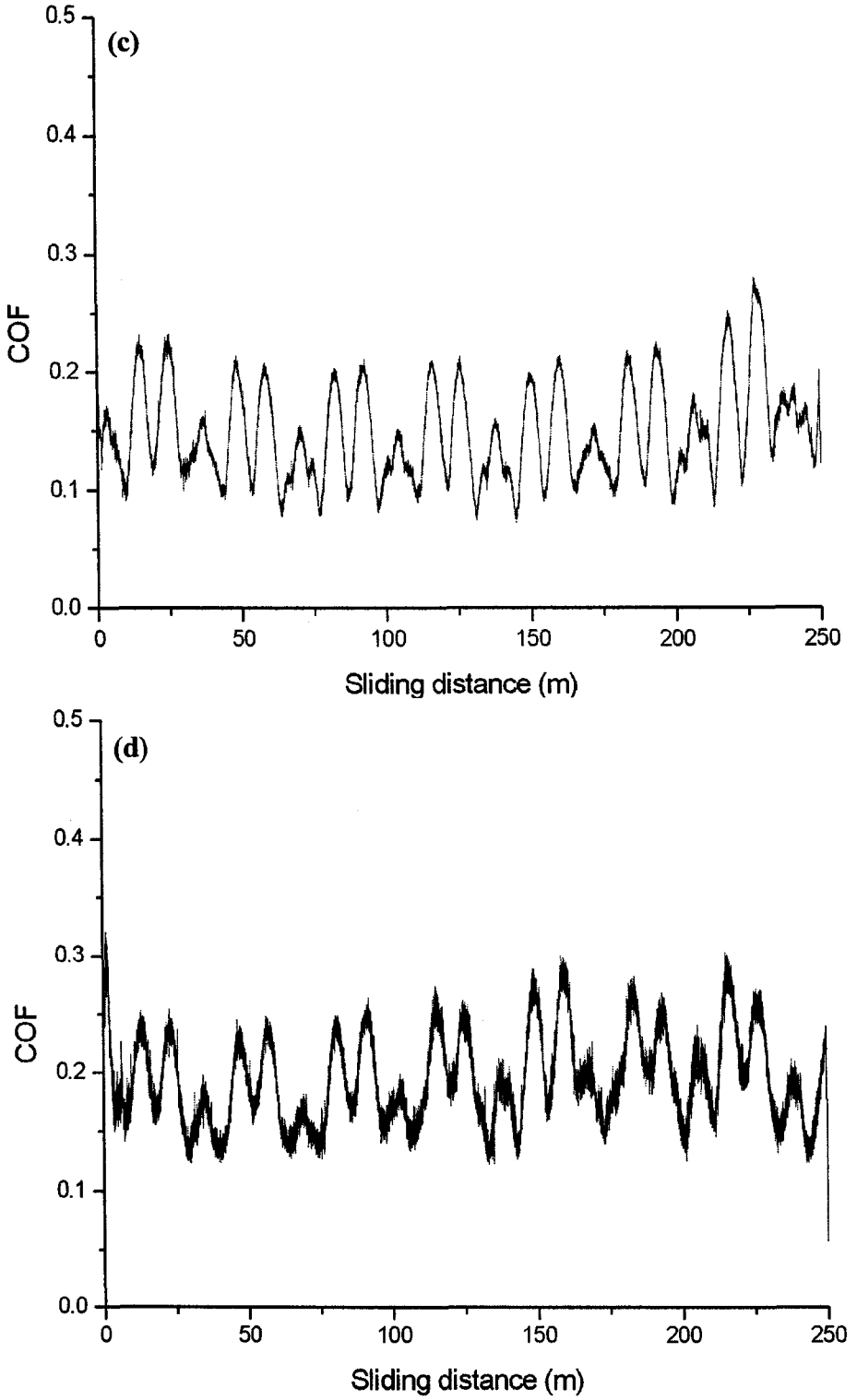

Fig. 5.9 COF curves of PEO coatings (a) Y1, (b) Y2, (c) Y3 and (d) Y4 against steel ball with 2N normal load under residual oil lubrication for 250m sliding distance

5.2.2 Tribological test result of PDC PEO coating Y2 on Al 390 sliding against the steel ball under residual oil lubrication for long distance

Fig. 5.10 (a) shows the low magnified SEM micrographs of the wear tracks on PEO coating Y2 sliding against steel ball for 3600m under residual lubrication. Figs. 5.10 (b, c) are the corresponding high magnification micrographs for aluminum oxide region and porous silicon phase regions, respectively. The wear track is barely observed, Fig 5.10 (a). Slightly material removal occurs to the piling up silicon particles, Fig. 5.10 (b), and the no abrasive wear presents at aluminum oxide region, Fig. 5.10 (c).

Fig. 5.10 (d) shows an optical microscope photograph of the counter steel ball. The worn area is almost the same as that tested in a shorter distance (250m), Fig. 5.8 (b). Abrasive wear on the ball is clearly observed, however, the worn area increases very little after sliding of a certain distance. Fig. 5.10 (e) exhibits the corresponding Coefficient of Friction curve, with the average COF of 0.135.

5.2.3 Tribological test result of etched Al 390 sliding against the steel balls under residual oil lubrication for long distance

To compare the wear behavior of PDC PEO coating with uncoated Al 390 substrate, the same long distance testing condition is applied to the etched Al 390. The etched Al 390 has a better anti-wear performance than bare Al 390 as shown in section 4.1, chapter 4. Fig 5.11 (a) shows the morphology of etched Al 390. The needle shaped silicon particles

are protruding from the Al matrix. The SEM micrograph of the wear track of etched Al390 sliding against steel ball under residual lubrication for long distance is shown in Fig. 5.11 (b). The projecting part of hard silicon particles are worn away. Fractures of silicon particles and cracks at the particle boundaries are obviously present. Consequently, abrasive wear to the soft Al matrix occurs. Furthermore, within the wear track, the roughened Al matrix due to the previous etching process is scratched, causing a plastic deformation on it. Fig 5.11 (c) is the optical microscope photograph of the worn steel ball. The worn area is a little larger than that of steel ball sliding against coating Y2 under the same conditions, shown in Fig. 5.10 (d). A much higher COF, 0.385, is presented at the initial stage of the test, after then, the COF reduces to 0.175, shown in Fig. 5.11 (d).

5.2.4 Discussion

Aluminum oxide region and protruding silicon phase regions can be recognized on coating Y1, Y2 and Y3 surfaces. For coating Y1, due to the short treatment time, most discharges concentrated on the silicon phase regions, thus the aluminum oxide region is quite smooth, which is not in favor for oil retaining during the wear test. Therefore, the projecting silicon oxide or Si-Al-O compound particles are removed due to the lack of oil lubrication. After that, the steel ball slides against the aluminum oxide region, which is thick and hard enough to bear the normal load. Therefore no obvious abrasive wear is detected at that region. However, the hard aluminum oxide layer has a poor compatibility for steel due to the high hardness, causing the large worn area of counterface steel ball. Finally, the deficient lubrication, third body wear and hard contact face (aluminum oxide layer) lead to a high COF. For coating Y2, more discharge channels appear at aluminum

oxide region. The melted aluminum oxide, being ejected from the discharge channels, is quenched by the electrolyte and solidifies around the channels, forming volcano-shape projections. Since the projections are still lower than the protruding silicon phase region, during the wear test, the contact between SiOx or Si-Al-O compound and steel ball occurs at most asperities. After the silicon phase regions are partially removed, those aluminum oxide projections, as well as the remaining parts of the silicon phase regions, serve as the contact surfaces. The porosities in both regions, acting as lubricant oil reservoirs, can reduce the COF and wear loss of the counterface. Additionally, compared with the thick coating, which has a high ratio of hard α-Al_2O_3 [16], the thinner coating has a lower hardness, also contributing to the smallest worn area of counterface steel ball and the lowest COF. For coating Y3, with the treatment time increasing, more aluminum oxide projections come into being. Consequently, the coating becomes rougher and harder. However, most projections are imperforate, reducing the oil retaining ability. Therefore, the COF is higher and the worn area of counterface steel ball is larger than the corresponding ones of coating Y2. For coating Y4, the aluminum oxide region and the silicon phase regions are alloyed together. Unlike coating Y2 and Y3, where the projections are supported by the relative dense aluminum oxide region, the large spherical projections forming at the coating Y4 surface are hold by the loose porous base, Fig. 5.2 (h). Therefore, although there is lubricant oil existing in the channels, the spherical particles are removed due to the weak backbone, which contributes to the high COF. Additionally, the increased coating hardness and roughness result in the worst compatibility of steel.

When coating Y2 slides against steel ball under residual oil lubrication for long distance, most material removal of the counterface steel ball occurs at the first 250m, which is suggested by the fact that the worn area in Fig. 5.8 (b) is almost the same as the one in Fig. 5.10 (d). Due to the increase in contact surface, the morphology of wear track and COF remain unchanged after 250m sliding. Comparatively, for the etched Al390, where the silicon particles are also protruding from the Al matrix to form Si asperities so as to protect the soft Al matrix, the lack of locations for oil retaining and the very soft Al matrix that can not firmly hold the hard Si particles during the wear test result in a dramatically increase in COF after the removal of the projecting Si particles. Therefore, coating Y2 exhibits better tribological properties and anti-wear resistance than substrate for a long distance test.

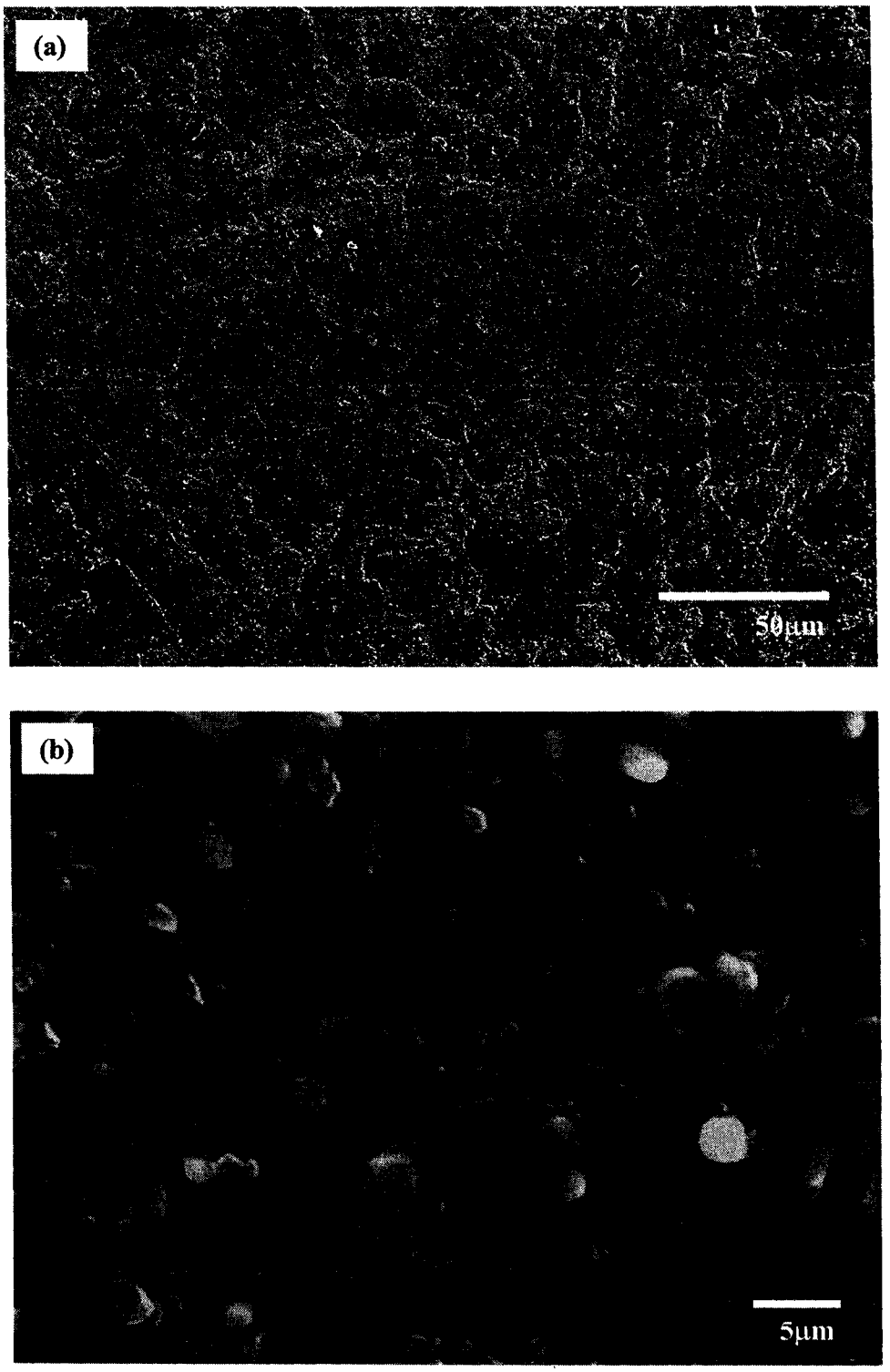

Fig. 5.10 to be continued

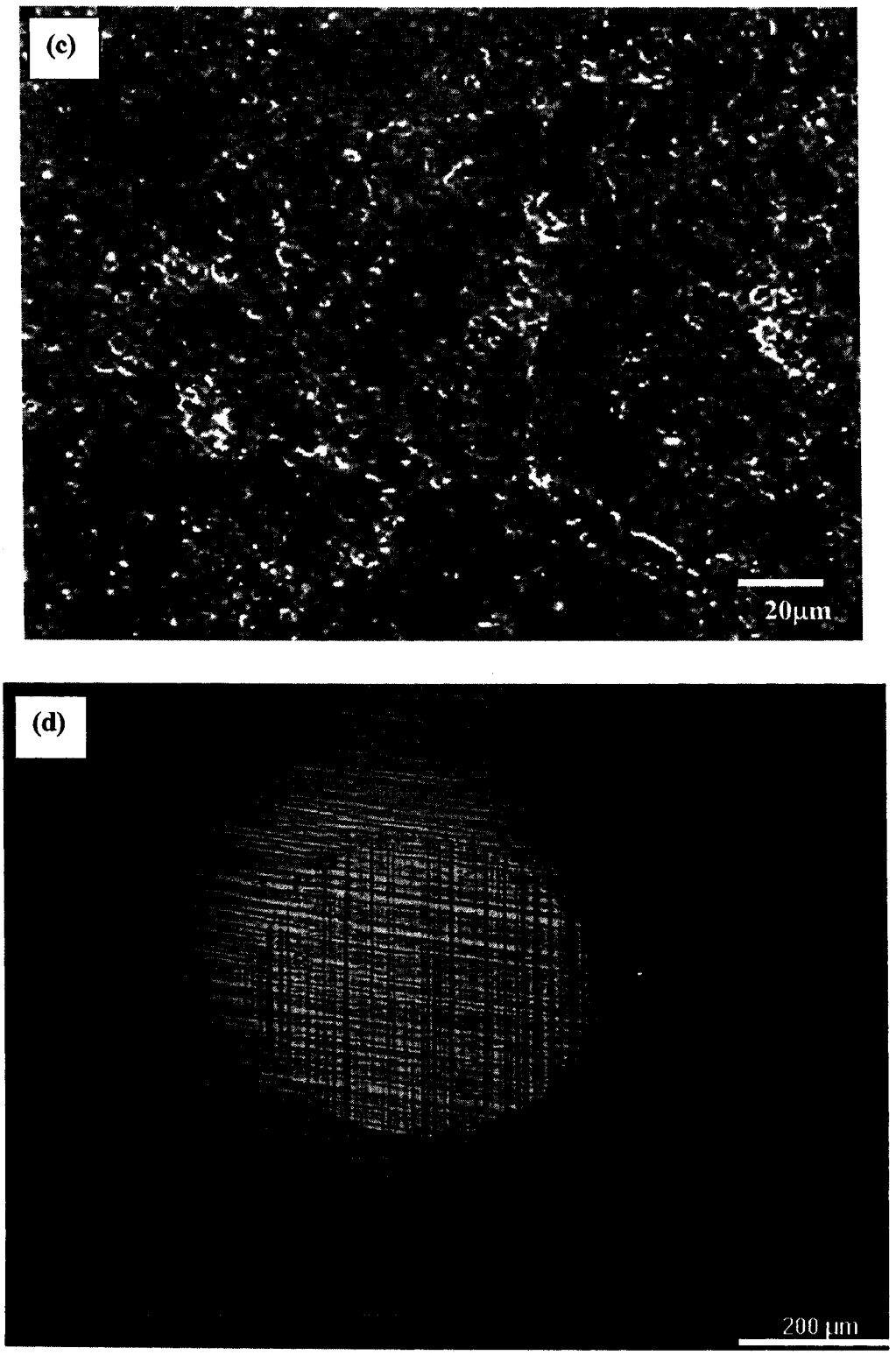

Fig. 5.10 to be continued

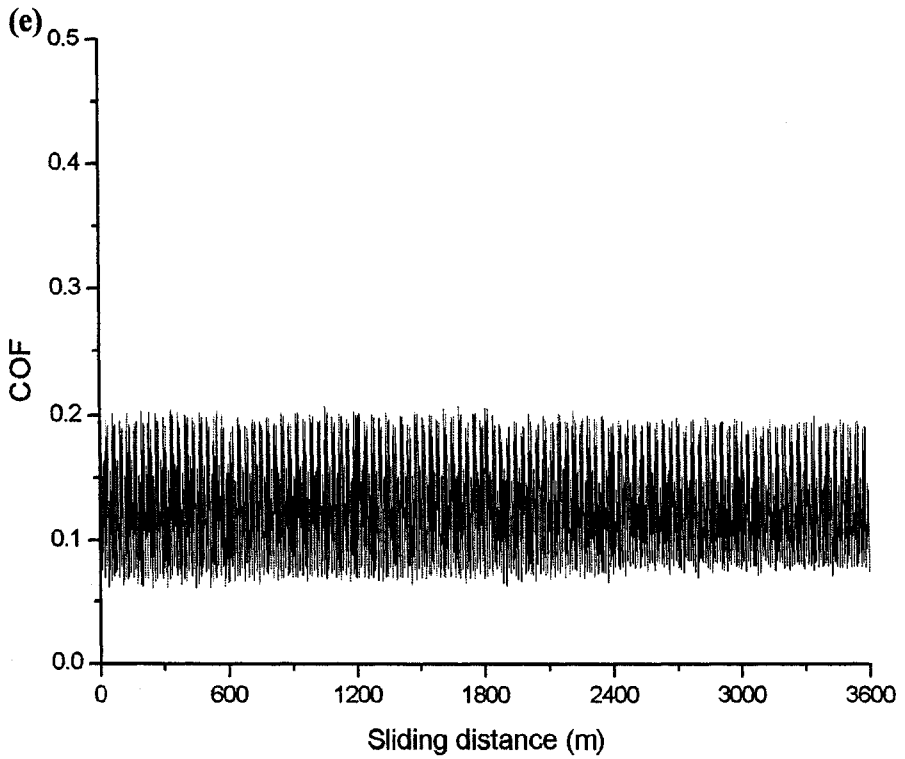

Fig. 5.10 SEM micrographs of the wear tracks on PEO coating Y2 sliding against steel ball with 2N normal load under residual oil lubrication for 3600m, (a) low magnification, (b) high magnification for aluminum oxide region, and (c) high magnification for silicon phase region, (d) optical microscope photograph of the counterface steel balls and (e) the corresponding COF curve

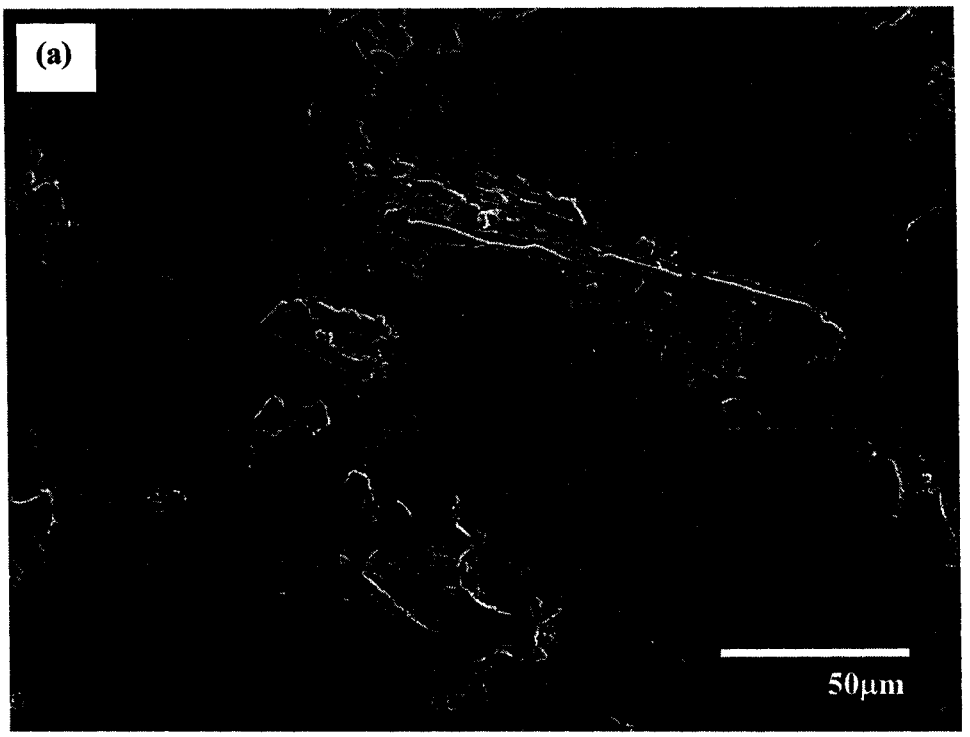

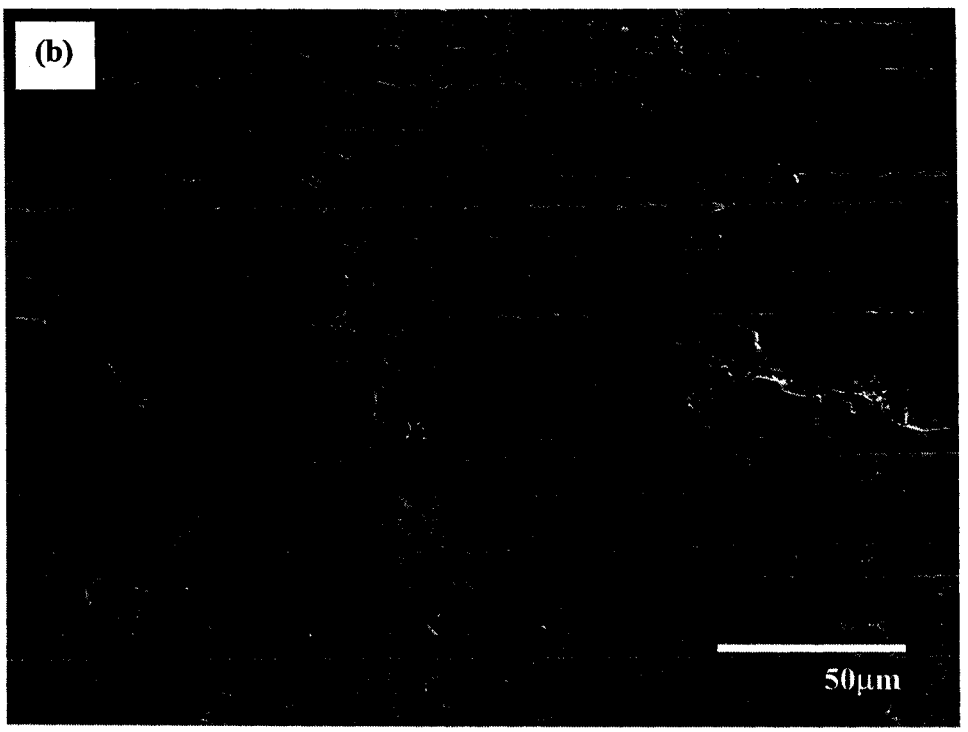

Fig. 5.11 to be continued

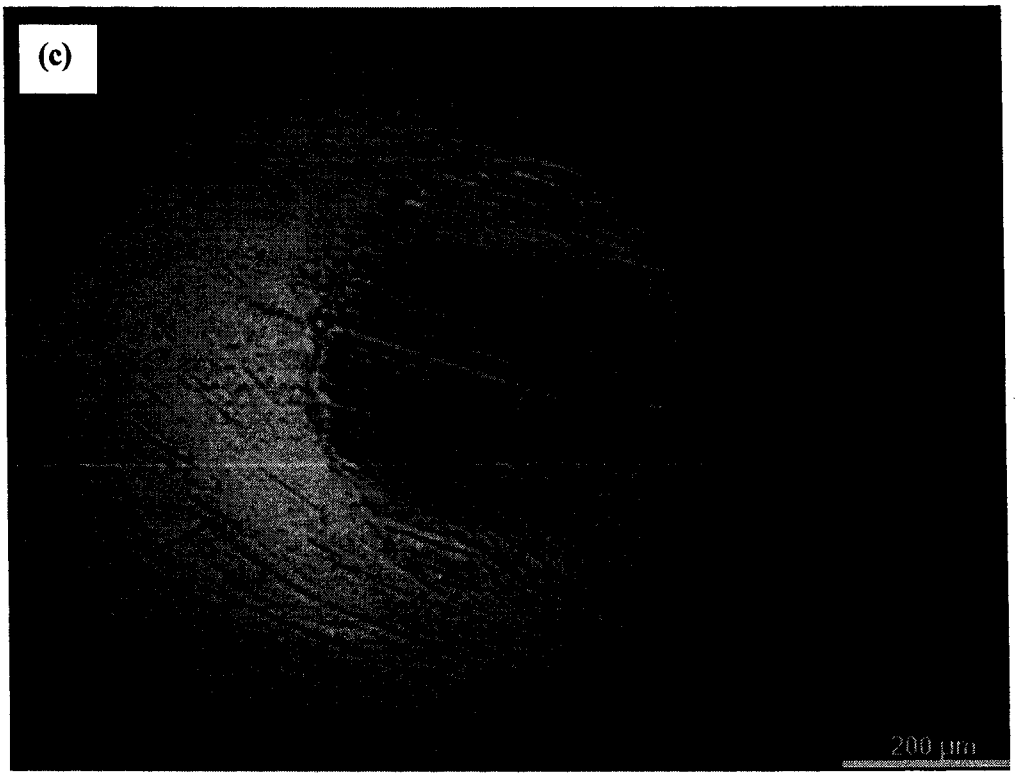

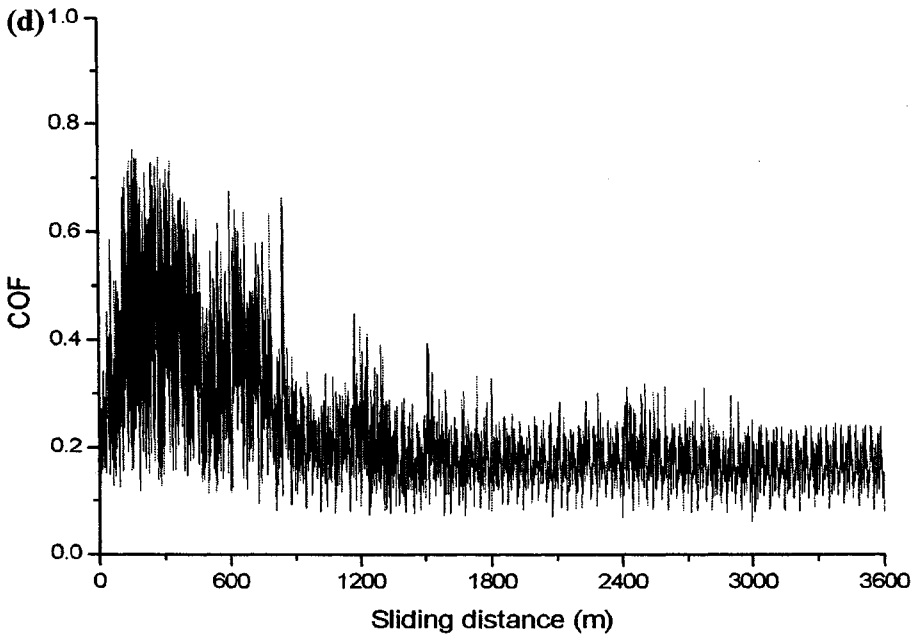

Fig. 5.11 SEM micrographs of (a) etched Al 390, (b) the wear tracks for etched Al390 sliding against steel ball with 2N normal load under residual oil lubrication for 3600m, (c) optical microscope photograph of the counterface steel balls and (d) the corresponding COF curve

5.3 Summary

In this chapter, a series of EJPP PEO coatings were produced on Al 319 substrates using a pulsed bipolar DC power supply. Similar to the PEO process in Chapter 4, an anodizing process occurs at the aluminum matrix to form a thin aluminum oxide layer at the initial stage. Then, micro-discharges occur at the silicon phase regions and the aluminum oxide region, in turn. As the treatment time goes by, the silicon phase regions gradually mix with the aluminum oxide region. However, different from the thin coatings (X11, X12 and X21) produced using DC power, where few discharge channels form at the aluminum oxide region, the thin coating treated with pulsed bipolar DC power exhibits the dissimilar morphology of aluminum oxide regions, which is characterized by the volcano-shape projections. Compared with the piling-up silicon particles, existing in the etched Al 390 surface, the aluminum oxide projections with porosities are harder and bonded with the aluminum oxide matrix more firmly, even lasting for the long distance sliding wear test. What's more important, the oil retained in the porosities can reduce the COF and worn area of counterface. Oppositely, the broken silicon particles results in the high friction for Al390 at the early stage of wear test. Also, after the protruding silicon particles are removed, the steel pin contacts with Al matrix directly and scratches the latter. However, for the coating, with the treatment time increasing, most volcano-shape projections are formed, but late on are replaced by the imperforate ones after a longer treatment time, causing the reduction of the oil retaining ability. Also, the coatings become rougher and harder. Therefore, the increase in COF and the worn area of the counter pin is caused. With the treatment time increasing more, the large semi-spherical

projections, the most of which are also not perforated, are distributed at the whole coating surface, leading to a high COF and poor compatibility of counter pin.

CHAPTER 6 EXPERIMENTAL RESULTS AND DISCUSSION III: SURFACE MORPHOLOGY AND TRIBOLOGICAL PROPERTIES OF PEO/GRAPHITE COMPOSITE COATINGS ON AL 6061 ALLOYS TREATED WITH DC POWER

As mentioned in Chapter 3, PEO/graphite composite coatings were deposited on the Al 6061 alloys with the parameters mentioned in section 3.3.2. In this chapter, the morphology and tribological properties of the coatings are analyzed.

6.1 Characterization of EJPP PEO/graphite composite coatings on Al 6061 with DC power supply

6.1.1 Voltage variation during the PEO process

Fig 6.1 (a) shows the voltage increment of EJPP PEO/graphite composite coatings, Z1 and Z2, treated with 4g/l electrolyte for different treatment time on Al 6061 substrates. The insert in the figure displays the detail about the beginning of the process. It is clear that the voltage increment curves of two coatings are almost overlapped, so they could be represented by the curve of coating Z2. Fig. 6.1 (b) shows the voltage increment of EJPP PEO/graphite composite coating Z3, treated with 8g/l electrolyte on Al 6061 substrate. The voltage change at the beginning of the process is magnified in the insert. The voltage

range of each stage and how many stages each sample experienced during the PEO process, as well as the voltage growth rate of each stage, are determined and listed in Table 6.1, and 6.2. The voltage growth rate decreases with the stages and the electrolyte concentration. Since only two segments of the cylinder inner surface that directly face the two spraying nozzles, each with the width of 1cm, are treated in each moment, the actual treatment time on each segment is equal to the total treatment time divided by the inner perimeter of the cylinder sample (28.6 cm) and multiplied with the double width of the nozzle. The treatment time on each segment for each sample is also listed in Table 6.1.

Table 6.1 Voltage range of each stage for different process parameters

Samples		Voltage range of each stage				Treatment time on each segment (s)
		Stage I	Stage II	Stage III		
		0-220V	220V-385V	≥385V		
4g/l	Z1(380V)	•	•			1.2
	Z2(430V)	•	•	•		3.6
		Stage I	Stage II	Stage III	Stage IV	
		0-290V	290V-410V	410V-460V	≥460V	
8g/l	Z3(460V)	•	•	•	•	125

Table 6.2 Voltage growth rate of each stage

	Voltage growth rate of each stage (V/s)			
	Stage I	Stage II	Stage III	Stage IV
4g/l	240	10. 1	1. 3	
8g/l	22	5. 3	0. 6	0. 3

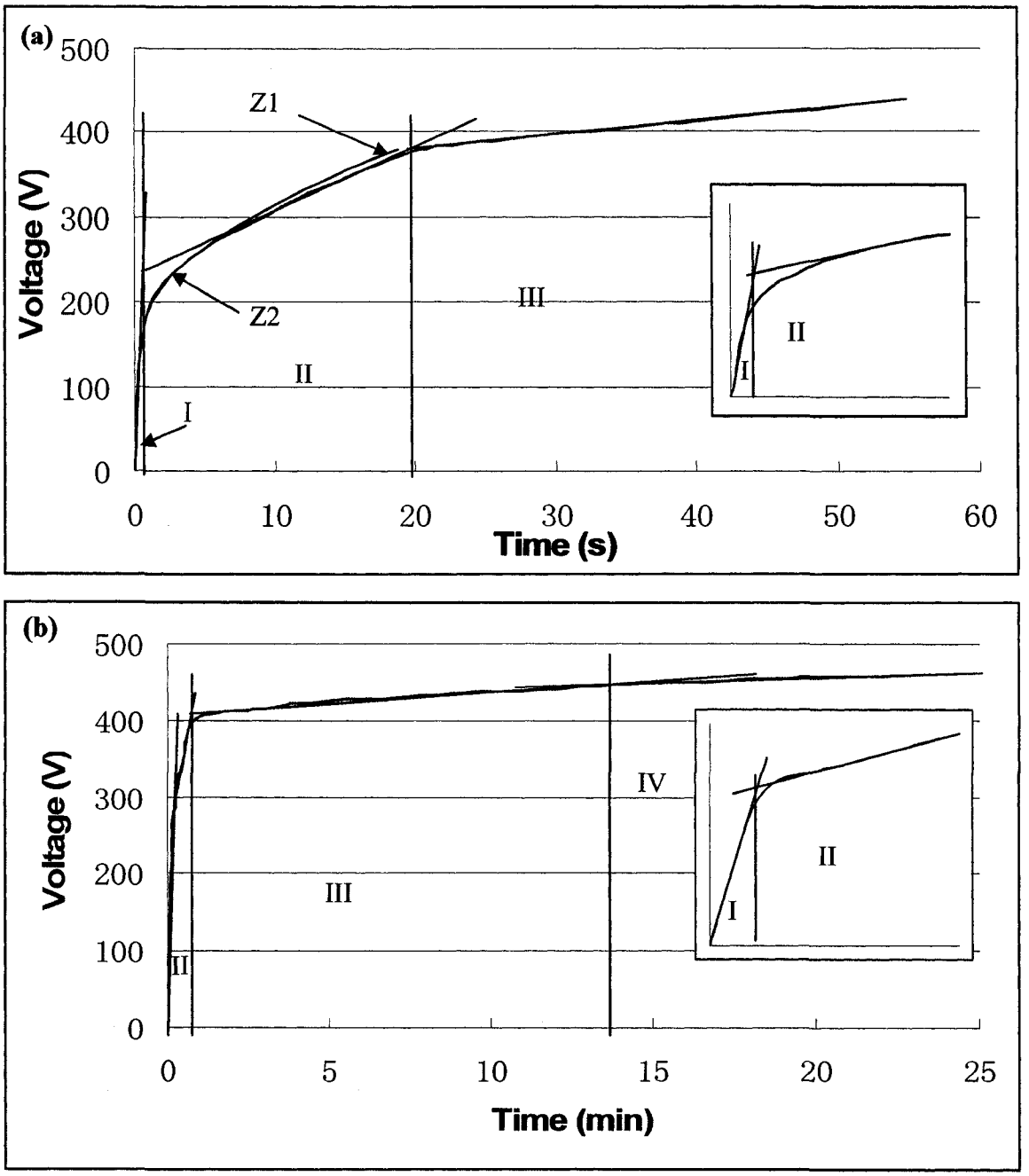

Fig. 6.1 (a) Voltage increment curves of EJPP PEO/graphite composite coatings (a) Z1 and Z2, treated with 4g/l electrolyte, (b) Z3 treated with 8g/l electrolyte, for different treatment time on Al 6061 substrates, the insert in each figure shows the voltage increase in the early stages

6.1.2 Morphology and thickness of PEO/graphite composite coatings on Al 6061

Figs. 6.2 (a, c, e) show the low magnification SEM micrographs of the morphology of PEO/graphite composite coatings Z1, Z2 and Z3. Figs. 6.2 (b, d, f) illustrate the corresponding high magnification micrographs. For coating Z1, a few of porosities, indicating the discharge channels, appear at the smooth aluminum oxide region, Figs. 6.2 (a, b). For coating Z2, small curly and dense projections appear at the whole coating surface. Among them lie valleys and cavities, Fig. 6.2 (d). Also, relatively larger cavities, indicating strong and intense micro-discharge, scatter evenly at the whole surface, Fig. 6.2 (c). Comparatively, the larger smooth curly projections form at the surface of coating Z3, among which valleys and cavities exist. Strong discharges are observed.

Fig. 6.3 (a) shows the reflectance spectrum as a function of wavelength for coating Z1. The measured and calculated reflection spectra match with each other very well. Fig. 6.3 (b) is the SEM cross-section micrographs of coating Z2. The coating lies between the bright nickel coating and the dark Al6061 substrate. The voids in the coating were filled with nickel during the electroless plating process. Fig. 6.3 (c) exhibits SEM cross-section micrograph of coating Z3. All thickness measurement results are listed in Table 6.3.

Table 6.3 Thickness measurement results

Method	Reflection spectrum	SEM cross-section image	
Coating	Z1	Z2	Z3
Coating Thickness (μm)	0.3	2.1	5.2

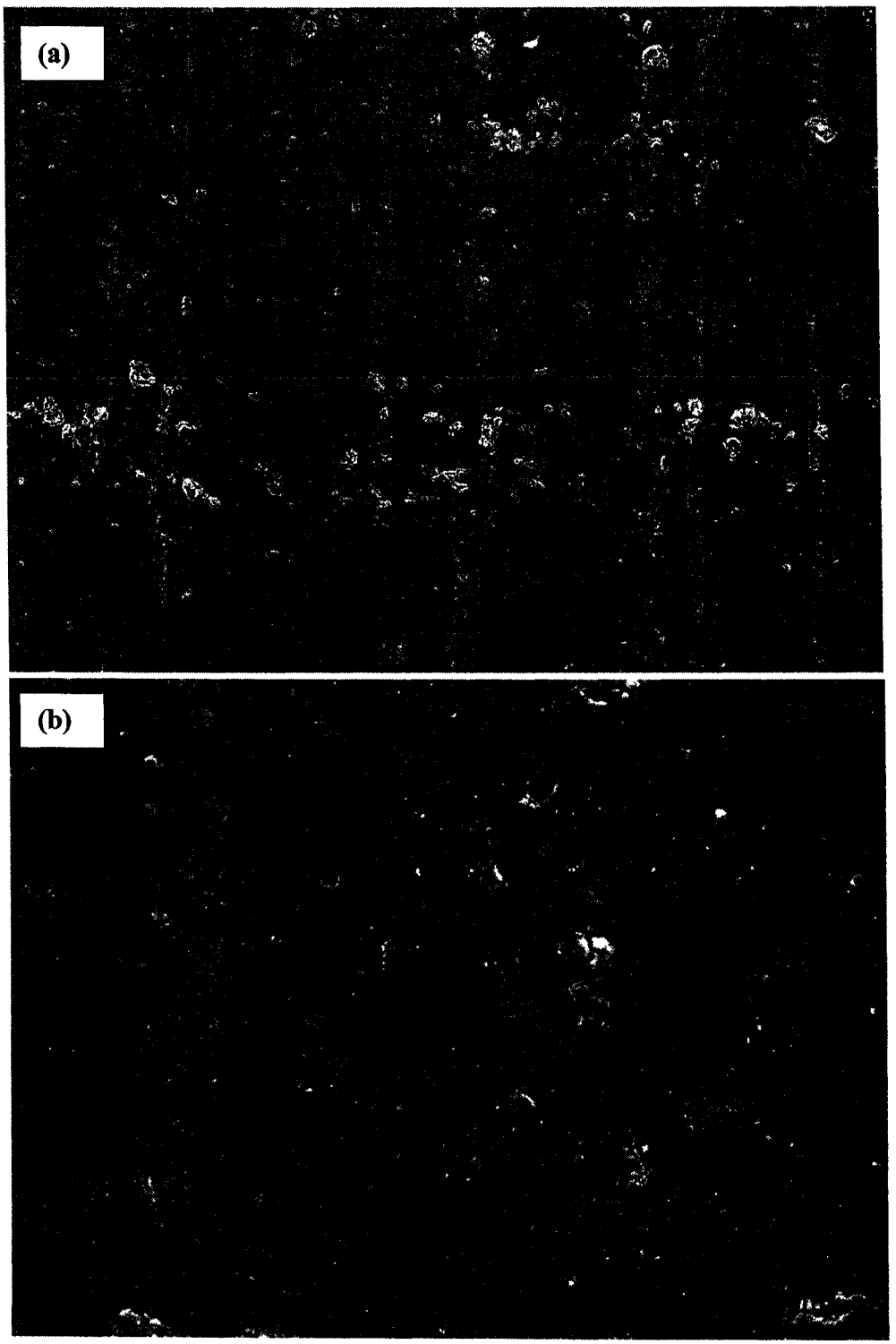

Fig. 6.2 to be continued

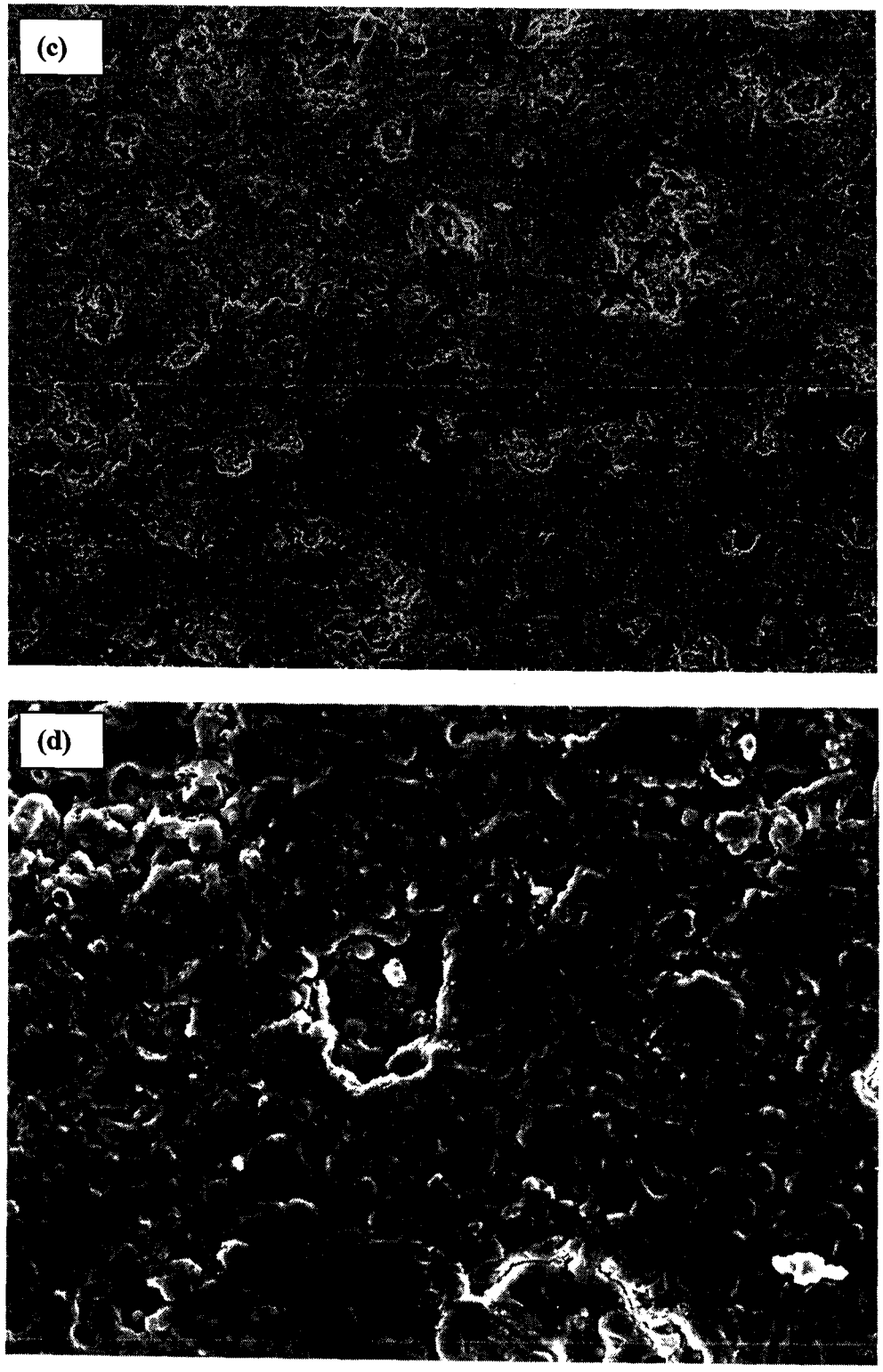

Fig. 6.2 to be continued

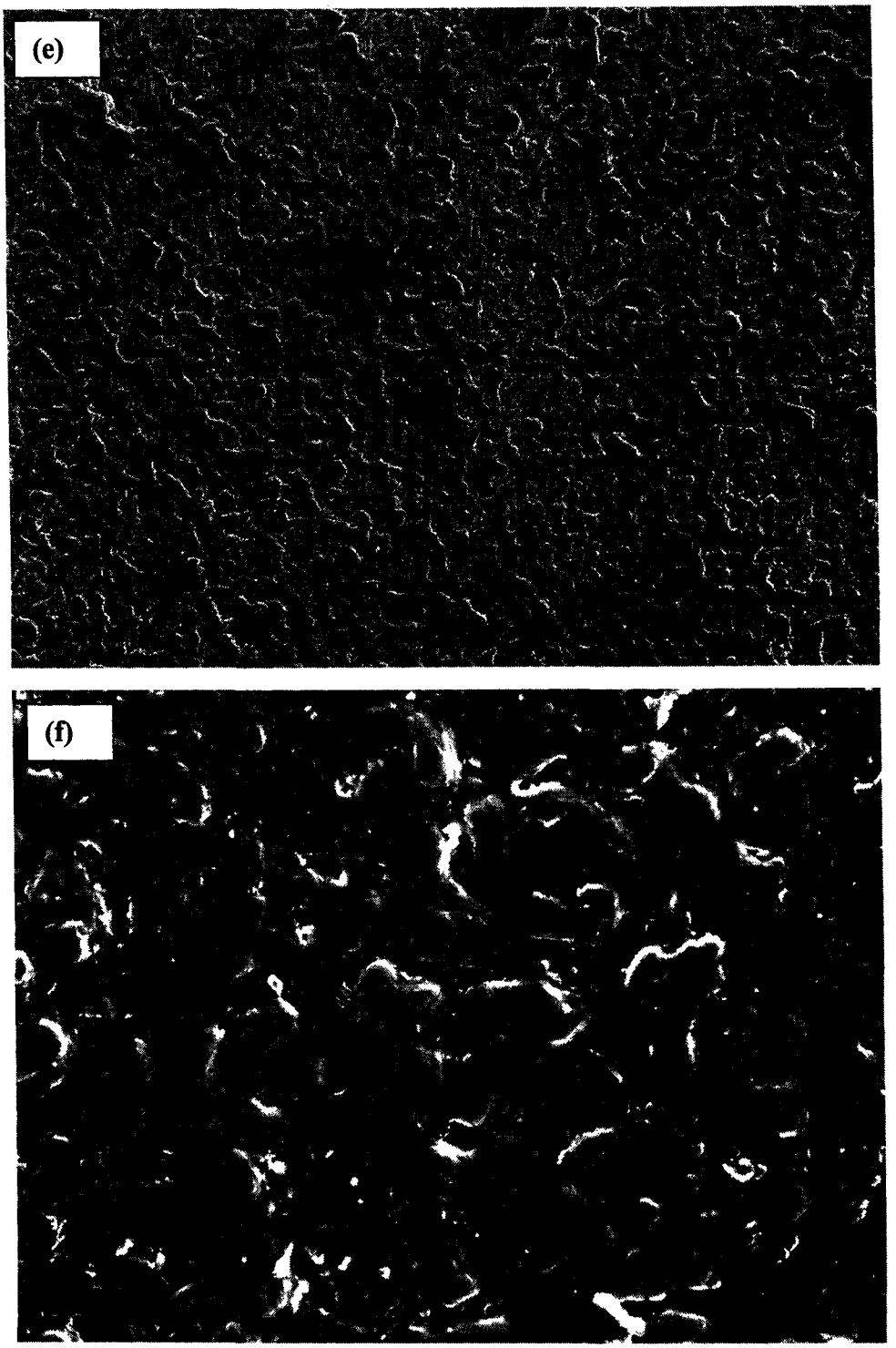

Fig. 6.2 SEM micrographs of the morphology of PEO/graphite composite coatings of (a) Z1, (c) Z2, and (e) Z3, and the corresponding high magnification micrographs (b), (d), and (f)

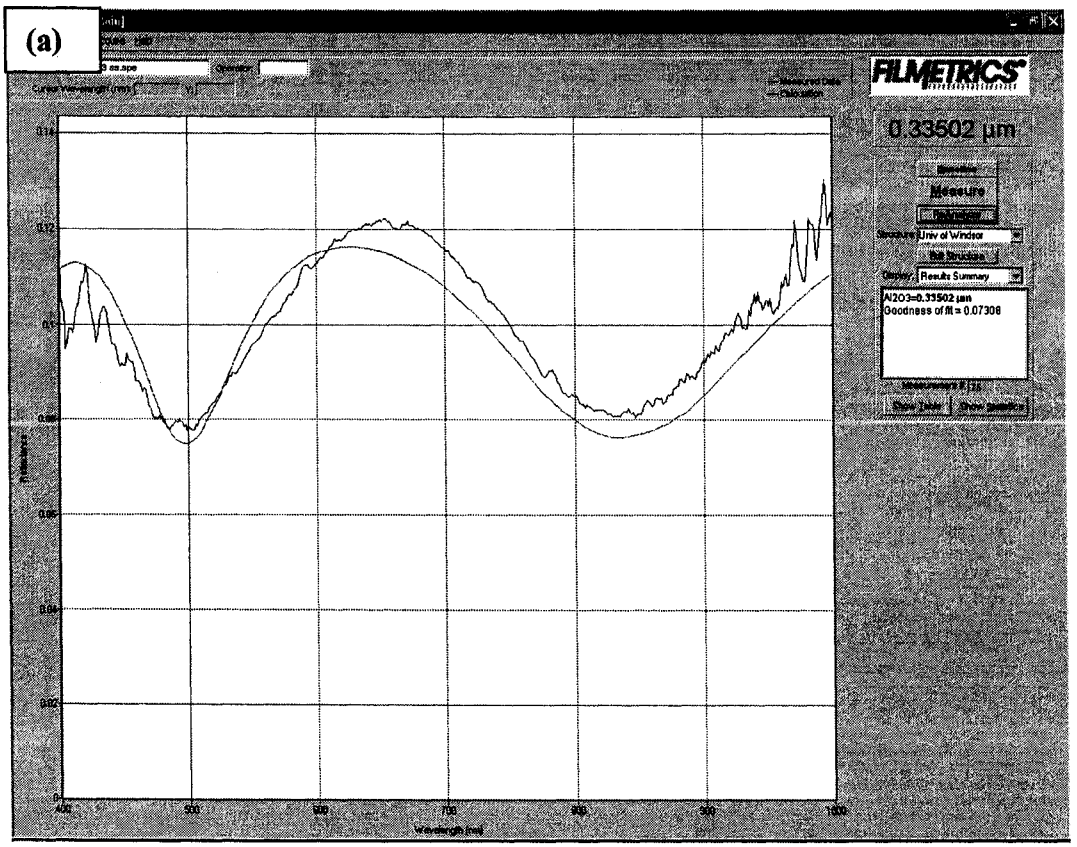

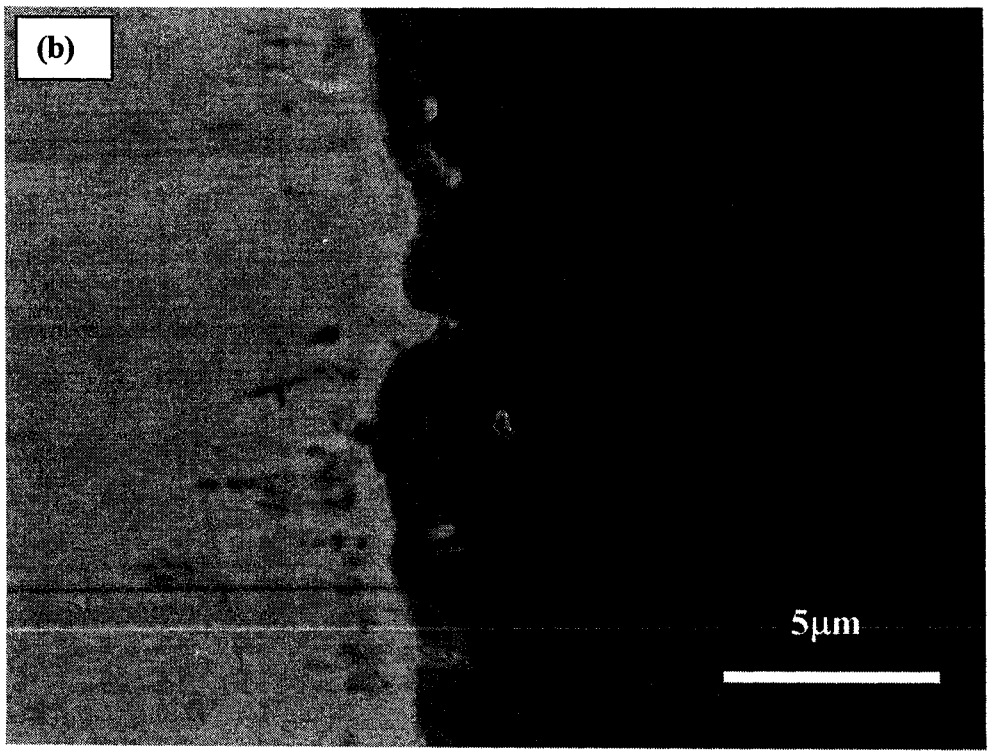

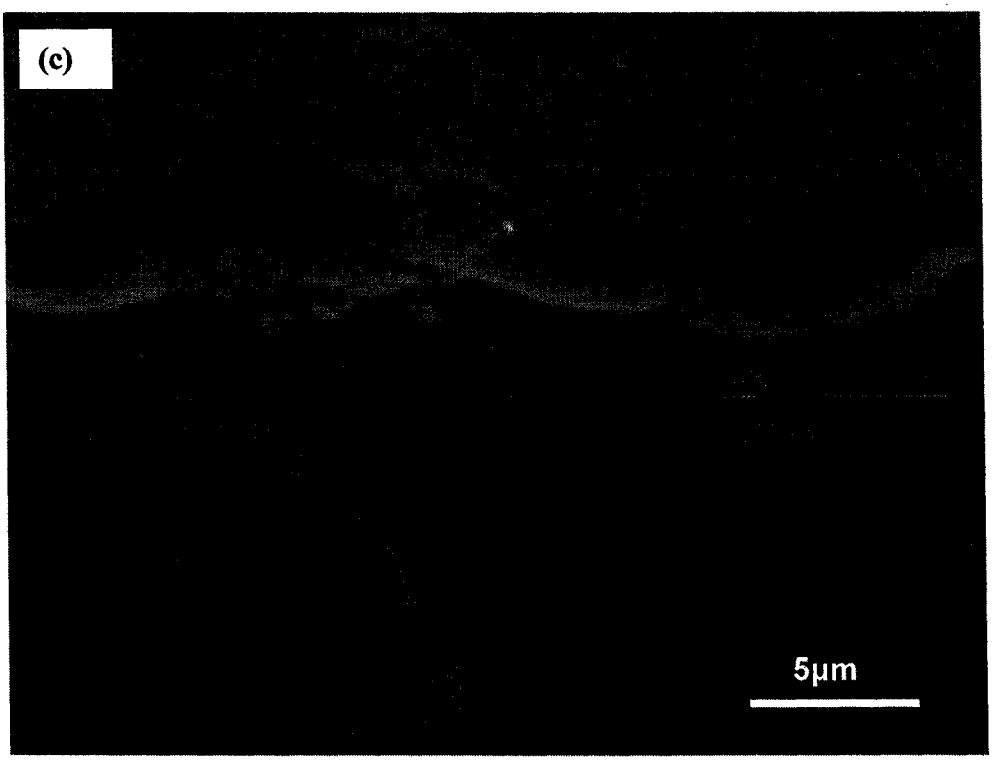

Fig. 6.3 Reflection spectrum for (a) Z1 and SEM cross-section micrographs for (b) Z2, and (c) Z3

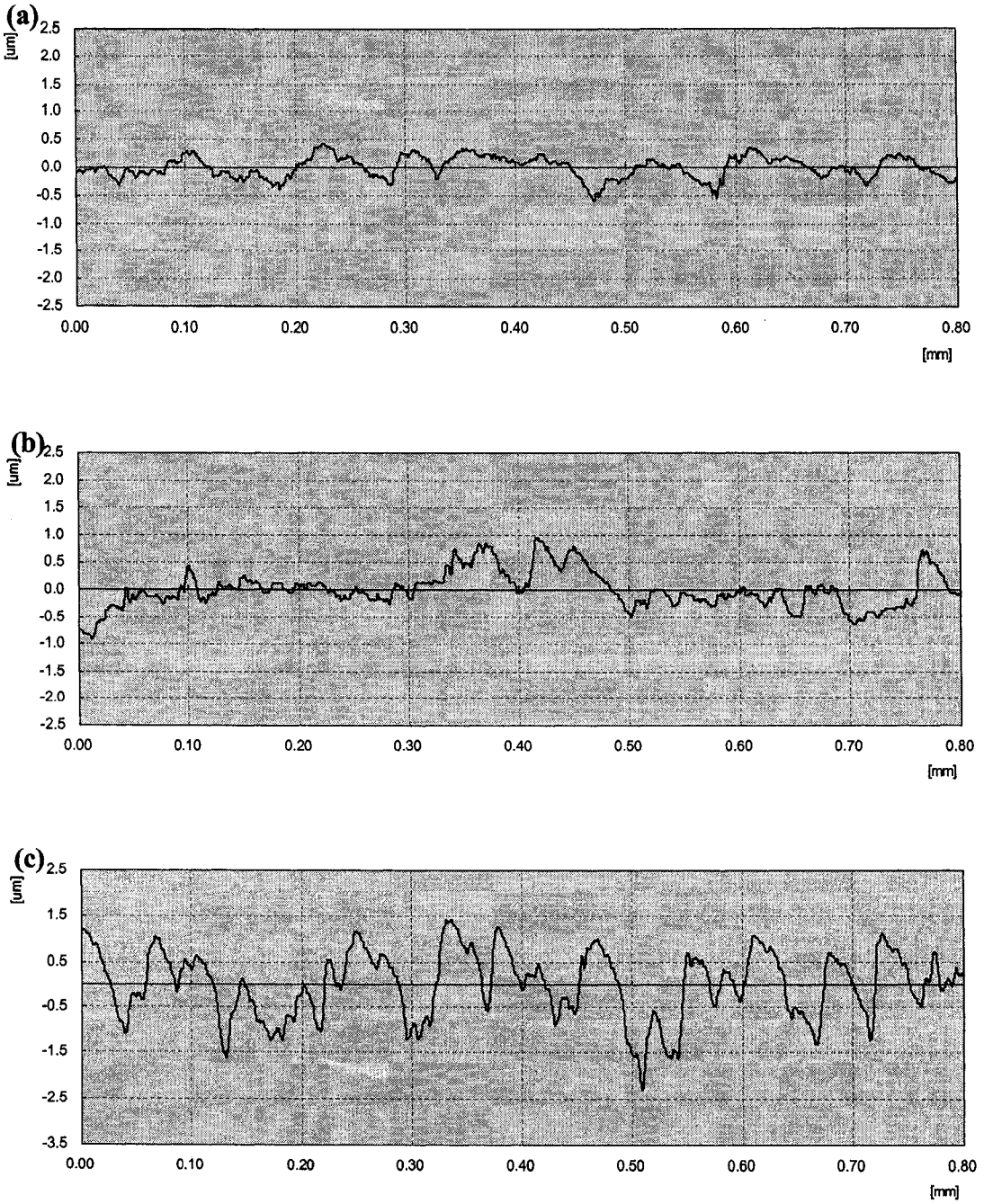

Fig. 6.4 to be continued

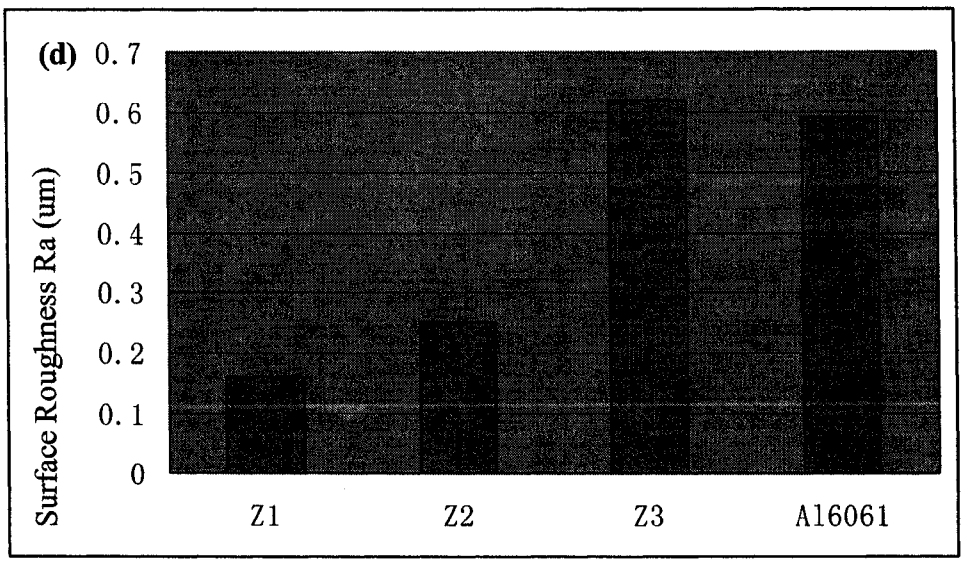

Fig. 6.4 Surface profiles for coatings, (a) Z1, (b) Z2, and (c) Z3, and (d) Surface roughness Ra for all coatings

Figs. 6.4 (a, b, c) display the surface profiles of coatings Z1, Z2, and Z3, individually. Fig. 6.4 (d) is the surface roughness measurement results for all samples. The surface roughness increases with the treatment time. The Al6061 with cross hatch has the similar roughness to coating Z3.

6.2 Tribological properties of PEO/graphite composite coatings on Al 6061 treated with DC power supply under residual oil lubrication

Figs. 6.5 (a, c, e, g) show the low magnification SEM micrographs of the wear track of Z1, Z2, Z3 and Al 6061, individually, sliding against steel ball with 2N normal load under residual oil lubrication for 50m. Figs. 6.5 (b, d, f, h) are the corresponding high

magnification micrographs of Z1, Z2, Z3 and Al 6061, respectively. Coating Z1 peeled off at the center of the wear track. Porous regions are exposed. The projections of coating Z2 and Z3 almost remain intact.

Figs. 6.6 (a, b, c, d) show the optical microscope photographs of the counter steel balls, sliding against PEO/graphite composite coatings Z1, Z2, and Z3, and Al6061 individually, for 50m. Abrasive wear is observed for all counter pins. However, Al6061 exhibits the best compatibility for steel ball with the smallest worn area of the counterface. Coating Z2 and Z3 show the worst compatibility for steel.

Figs. 6.7 (a, b, c, d) display the corresponding COF curves of Z1, Z2 and Z3 and Al6061. The average values of COF for all samples are listed in Table 6.4. Coating Z3 presents the lowest average COF. Coating Z1 displays the higher values.

Table 6.4 Average value of COF for Al6061, Z1, Z2 and Z3, sliding against steel balls for 50m

	Al6061	Z1	Z2	Z3
COF	0.155	0.197	0.186	0.154

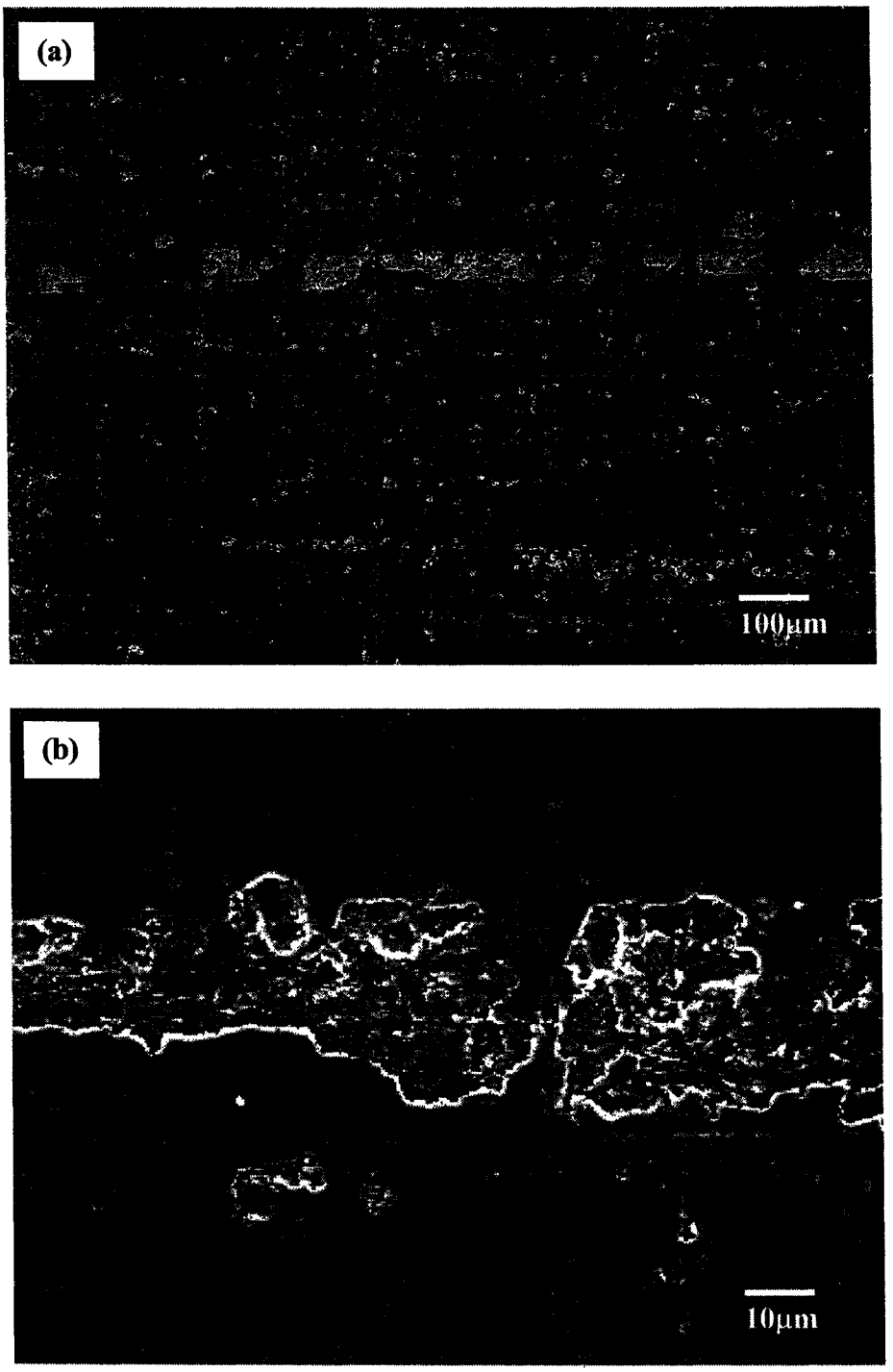

Fig. 6.5 to be continued

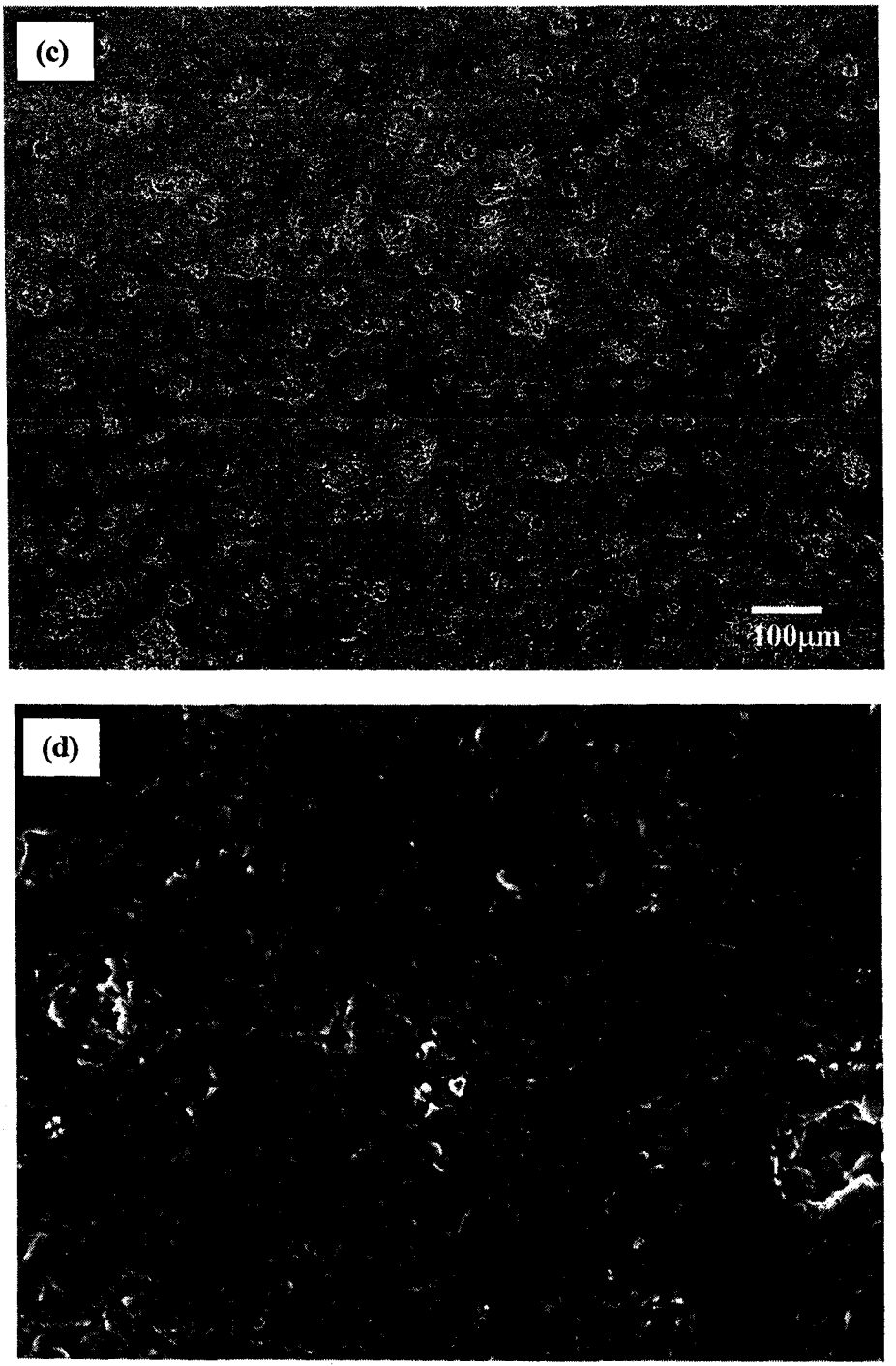

Fig. 6.5 to be continued

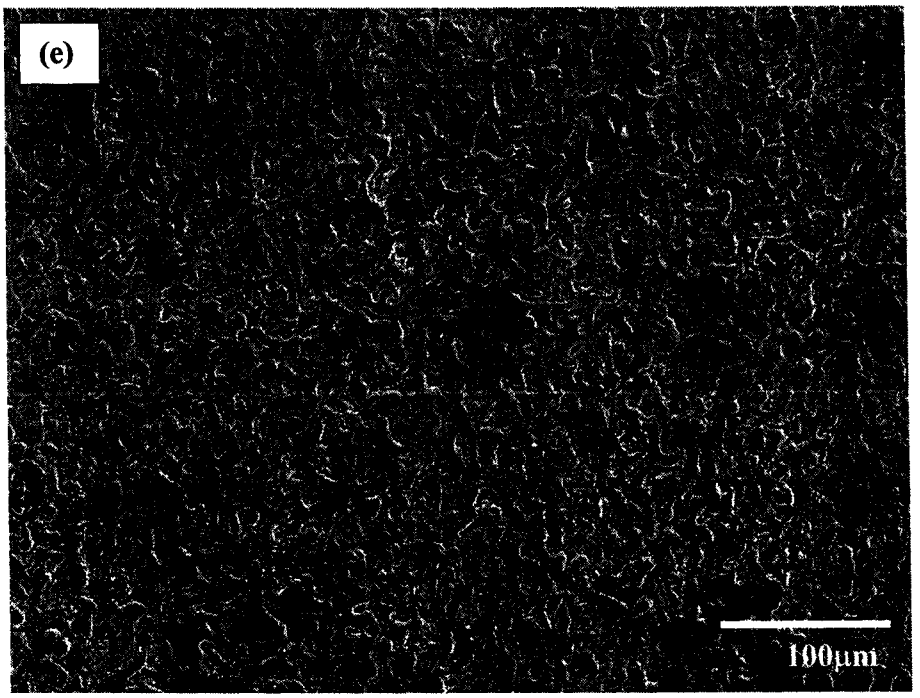

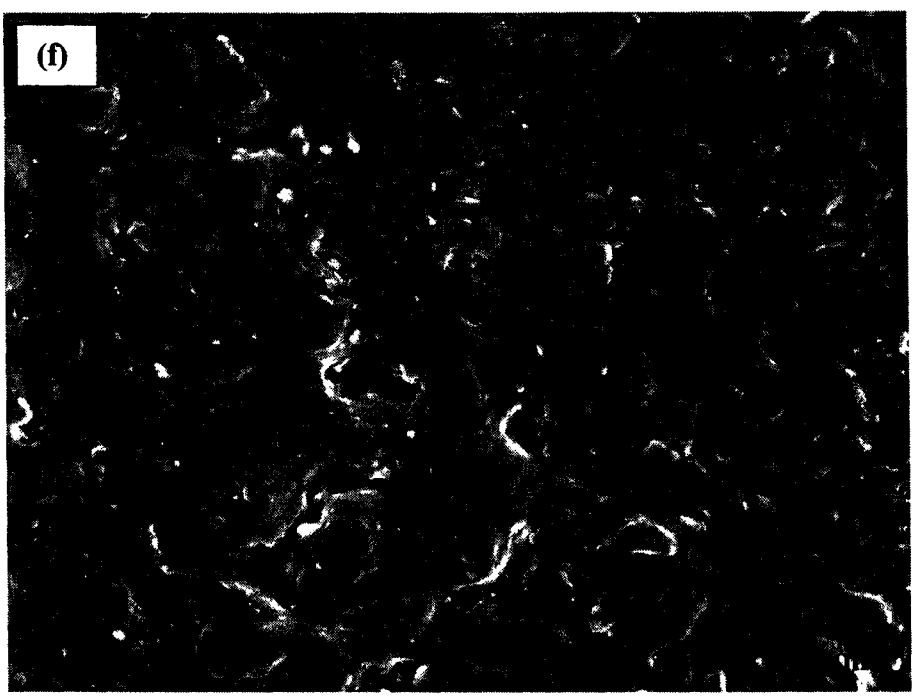

Fig. 6.5 to be continued

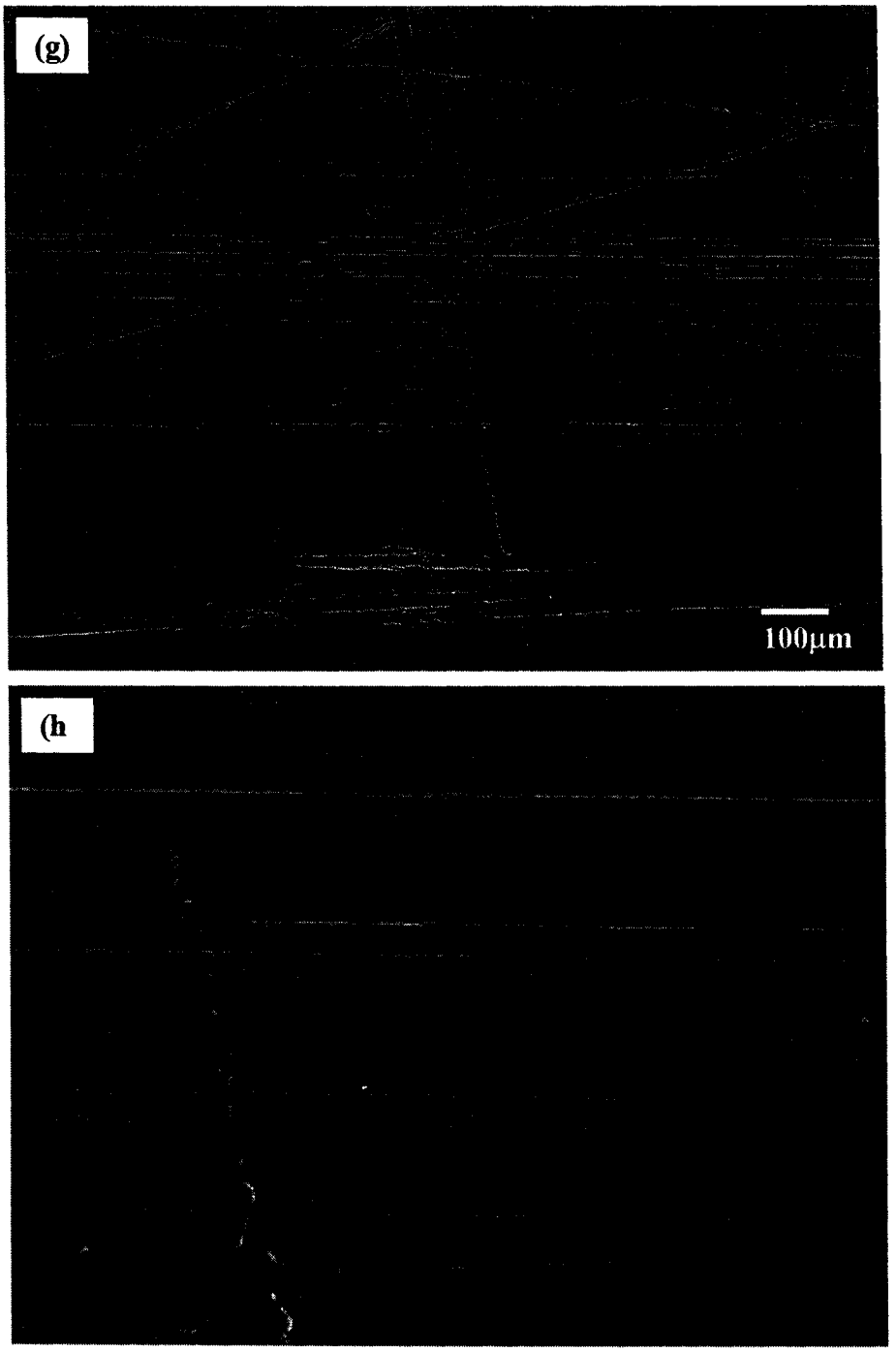

Fig. 6.5 SEM micrographs of the wear tracks for Al6061 and PEO/graphite composite coatings sliding against steel balls with 2N normal load under residual oil lubrication for 50m, (a) Z1, (c) Z2, (e) Z3,and (g) Al6061, and the corresponding high magnification micrographs of (b) Z1, (d) Z2, (f) Z3, and (h) Al6061

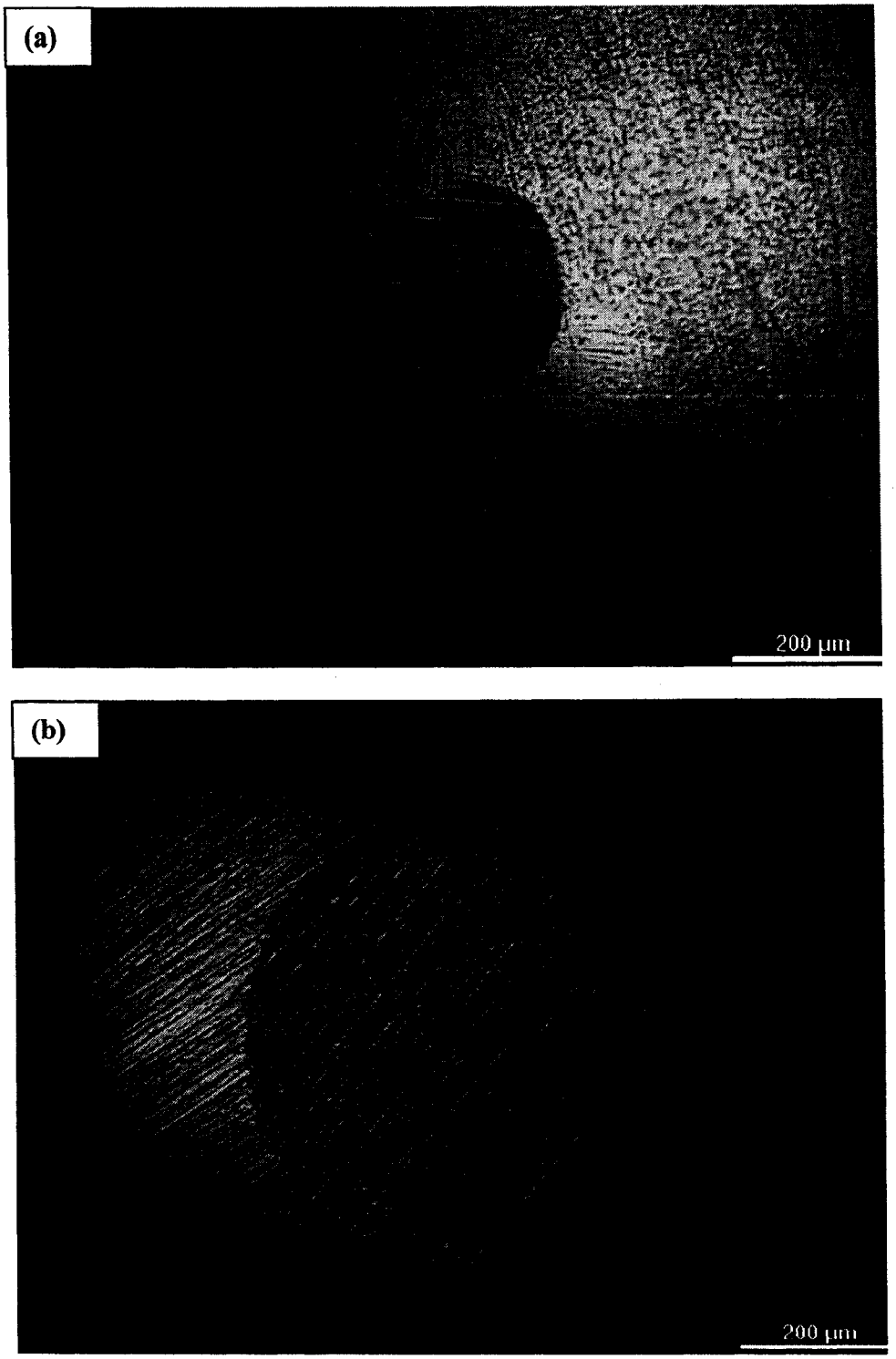

Fig. 6.6 to be continued

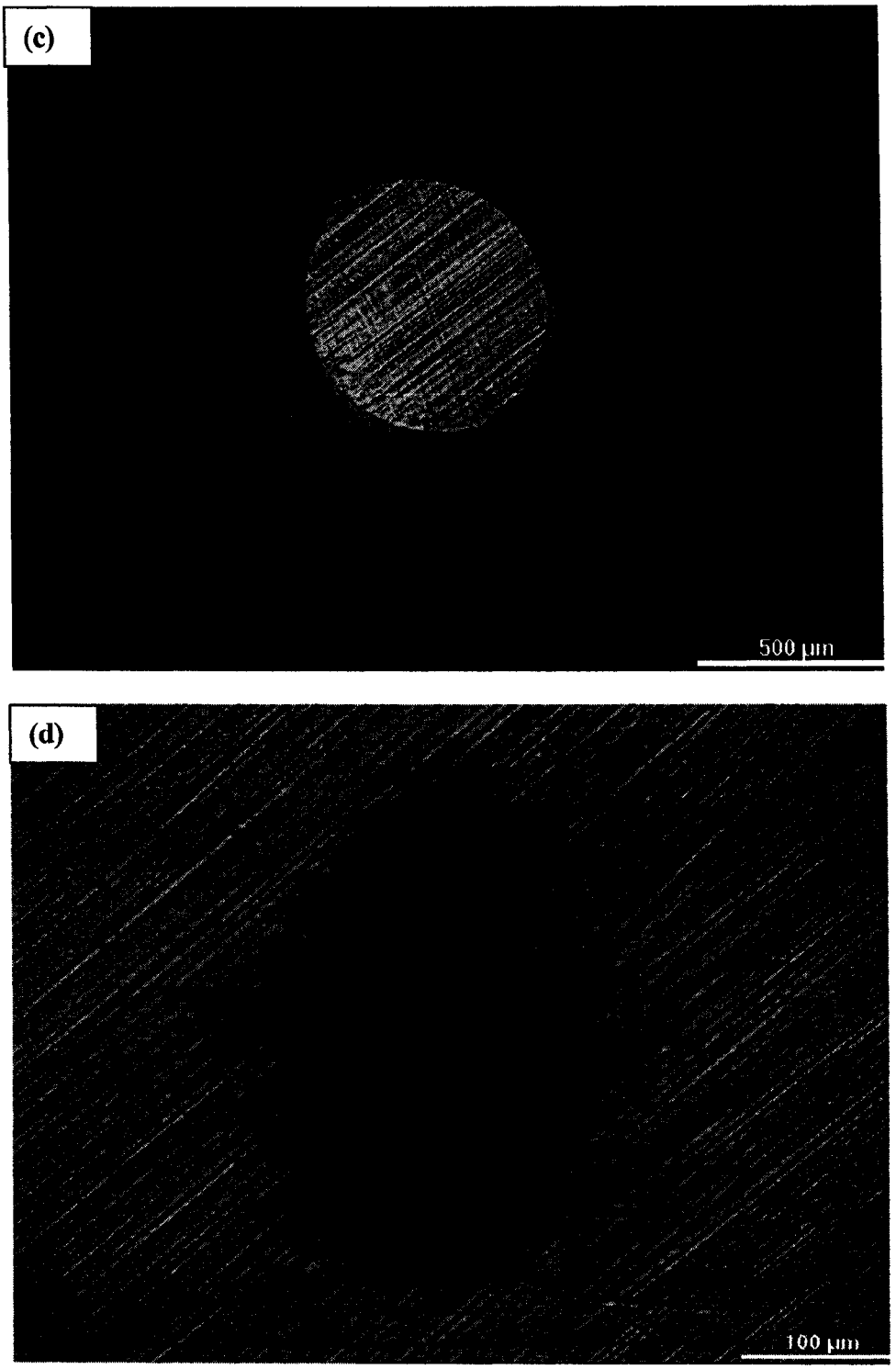

Fig. 6.6 Optical microscope photographs of the counter steel balls, sliding against PEO/graphite composite coatings (a) Z1, (b) Z2, and (c) Z3, and (d) Al6061 respectively, for 50m

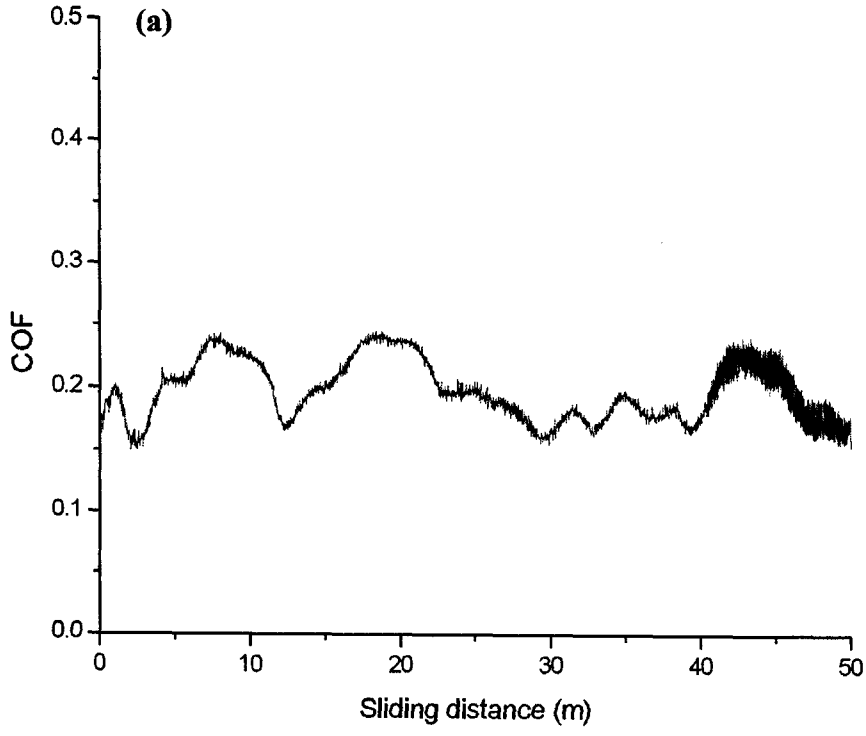

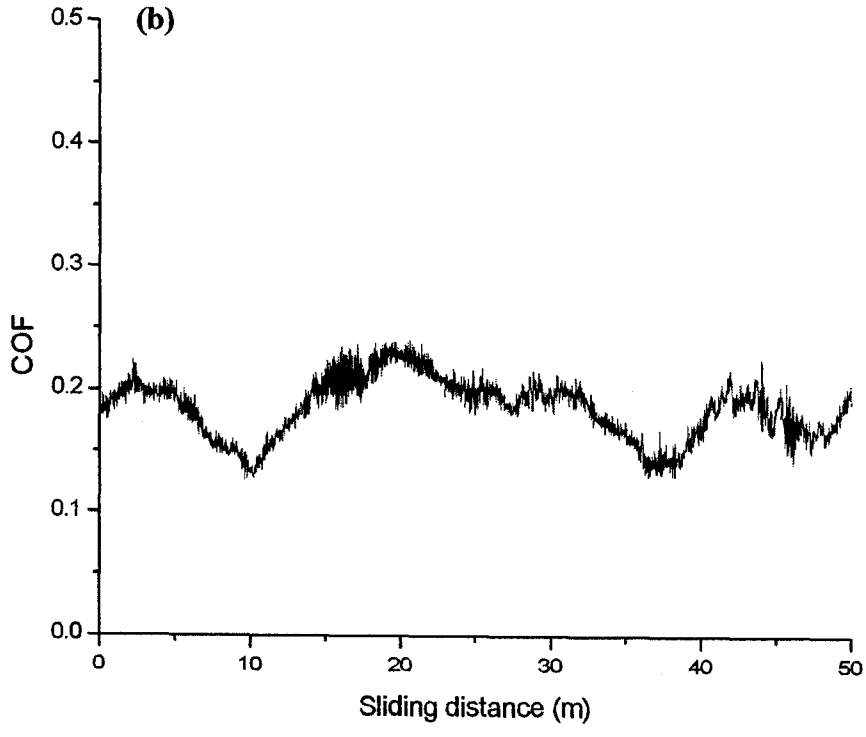

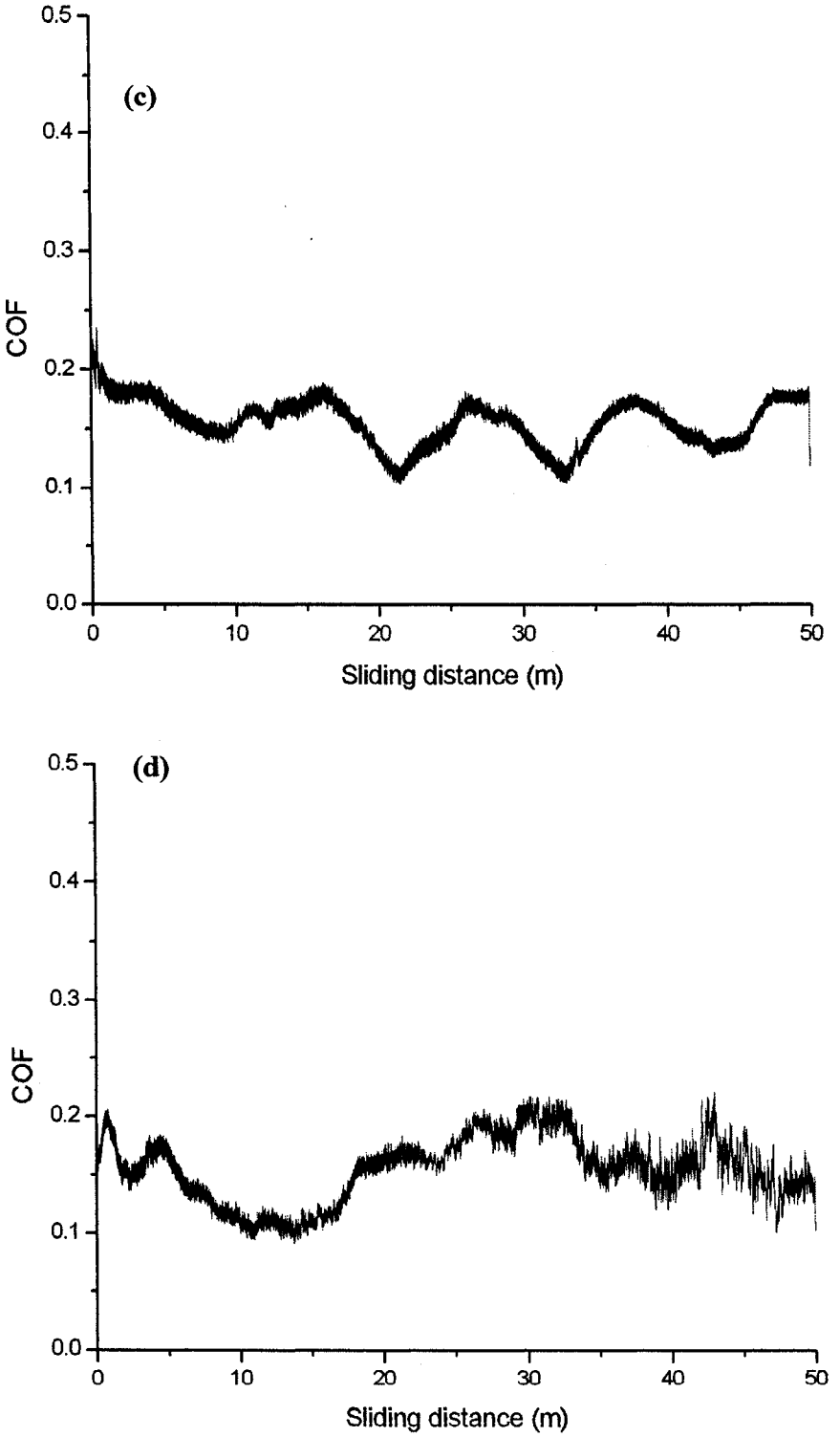

Fig. 6.7 COF curves for PEO/graphite composite coatings (a) Z1, (b) Z2, and (c) Z3, and (d) Al6061, sliding against steel balls for 50m individually under residual oil lubrication

Figs. 6.8 (a, c, e) show the low magnification SEM micrographs of wear tracks for coating Z1, Z2 and Z3, sliding against steel balls for 250m, individually. The corresponding high magnification micrographs are displayed in Figs. (b, d, f). The aggravated delamination occurs in the wear track of coating Z1, although no plowing or scratching is detected. The asperities of coating Z2 are partially worn away. For coating Z3, some projections are slightly polished. .

The optical microscopic photographs of the counterfaces are shown in Figs. 6.9 (a, b, c). Ploughing is clearly observed. Coating Z1 presents the best compatibility. Comparatively, the worn area of the counter pin sliding against coating Z2 is the largest.

The corresponding COF curves are shown in Figs. 6.10 (a, b, c). For coating Z1, the friction dramatically increase after sliding against steel ball for about 60m. The average values of COF curves for all coatings are listed in Table 6.5. Coating Z3 exhibits the lowest value, whilst coating Z1 presents the largest one.

Table 6.5 Average value of COF for PEO/graphite composite coating Z1, Z2 and Z3, sliding against steel balls for 250m

	Z1	Z2	Z3
COF	0.221	0.191	0.159

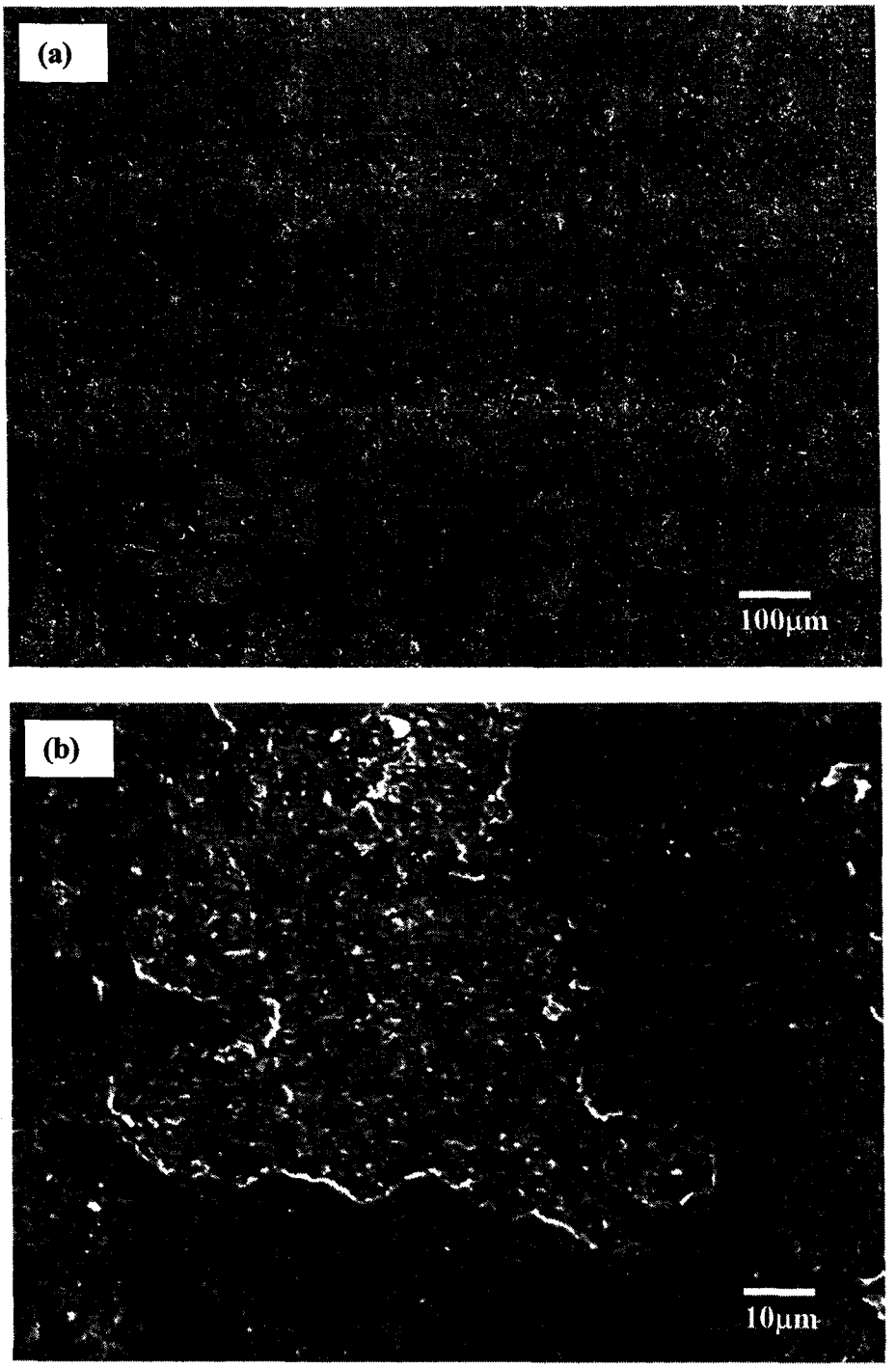

Fig. 6.8 to be continued

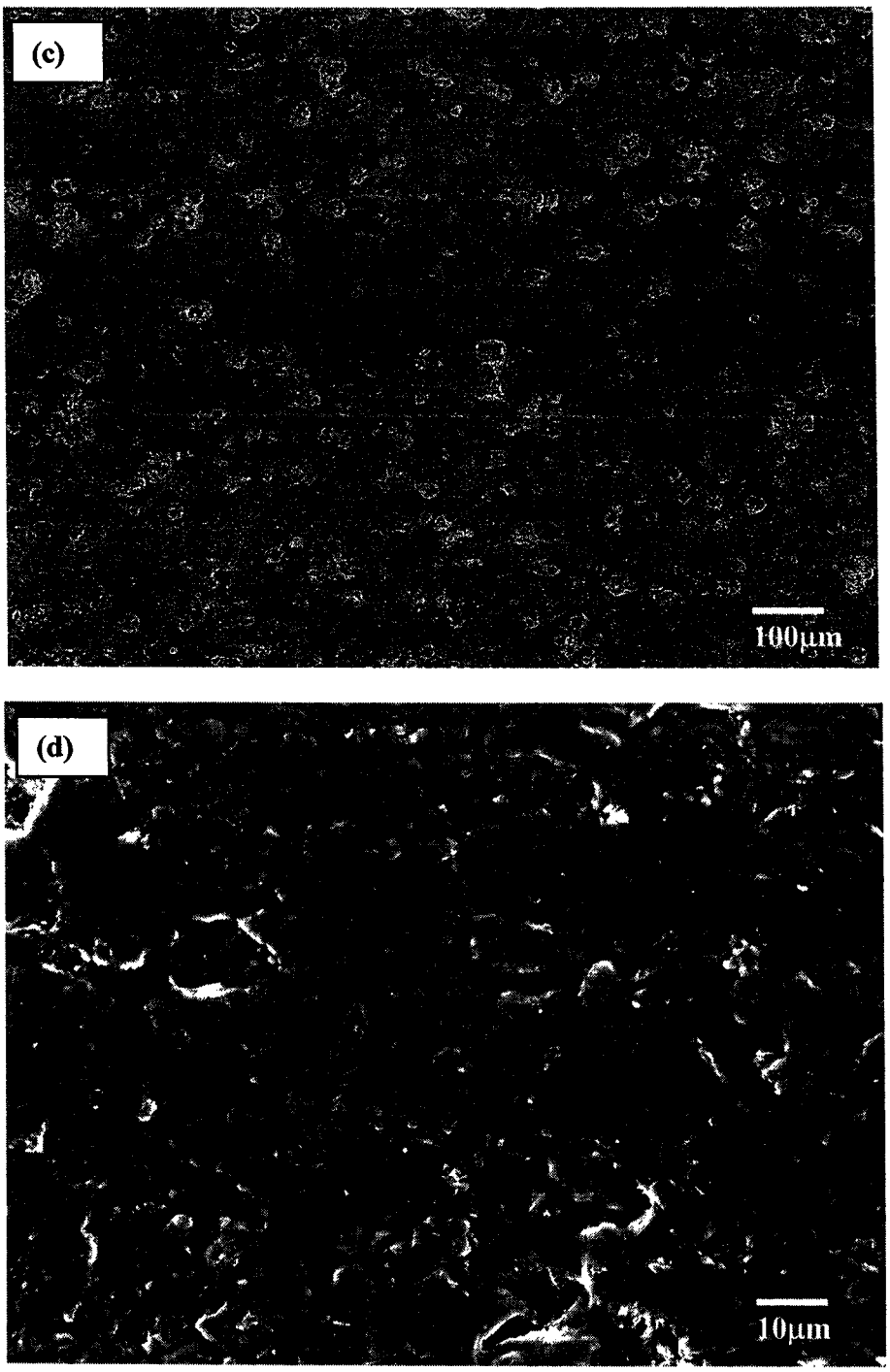

Fig. 6.8 to be continued

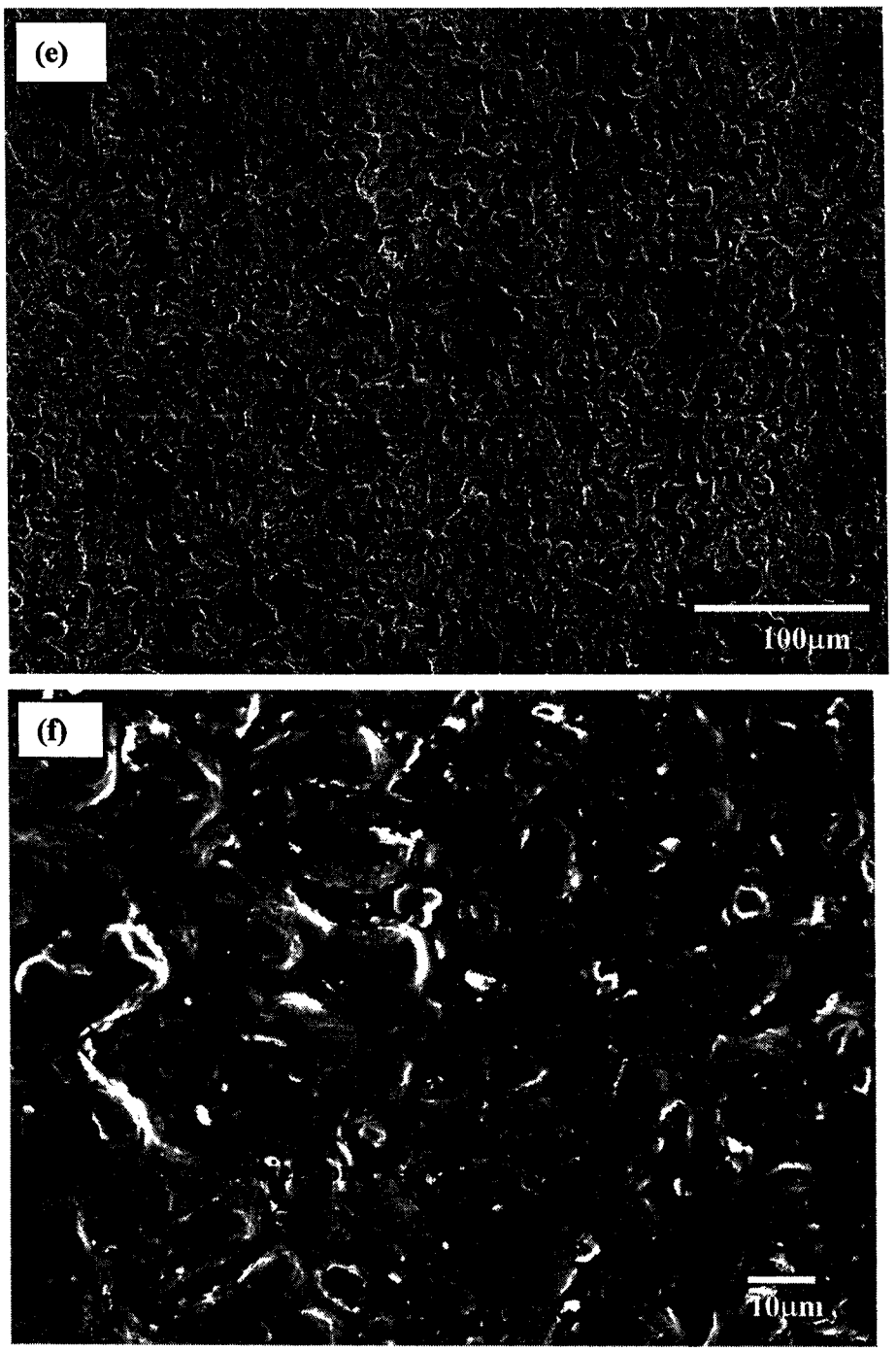

Fig. 6.8 SEM micrographs of the wear tracks for PEO/graphite composite coatings sliding against steel ball with 2N normal load under residual oil lubrication for 250m, (a) Z1, (c) Z2 and (e) Z3, and the corresponding high magnification micrographs of (b) Z1, (d) Z2, and (f) Z3

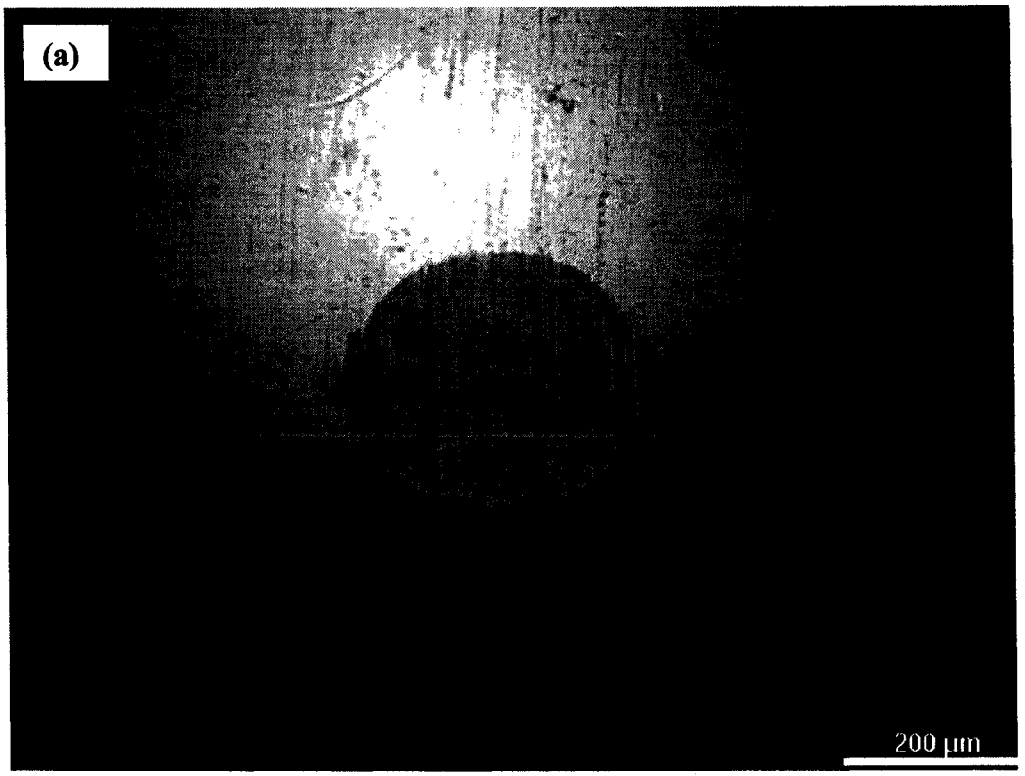

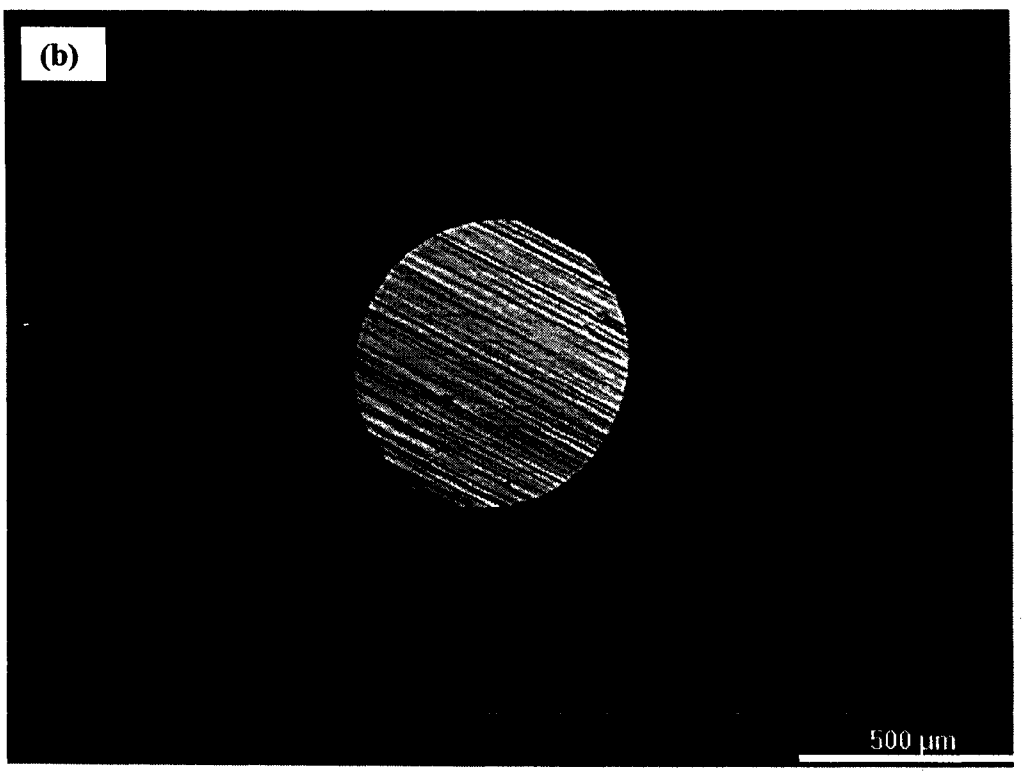

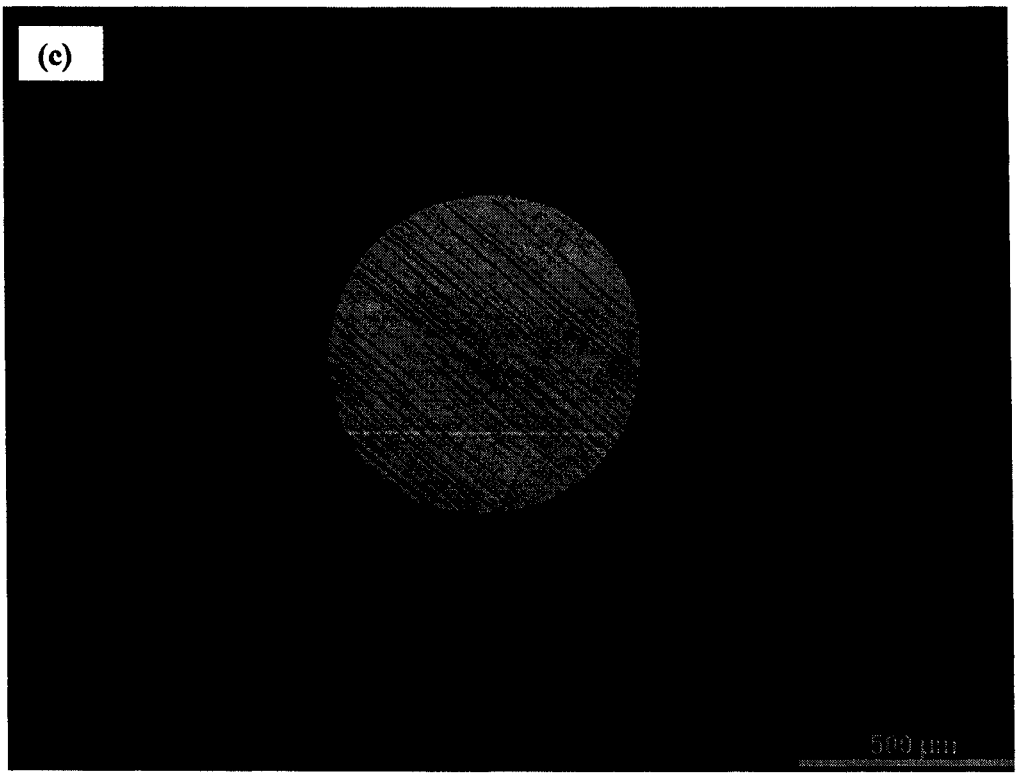

Fig. 6.9 Optical microscope photographs of the counter steel balls, sliding against PEO/graphite composite coatings (a) Z1, (b) Z2 and (c) Z3, for 250m, respectively

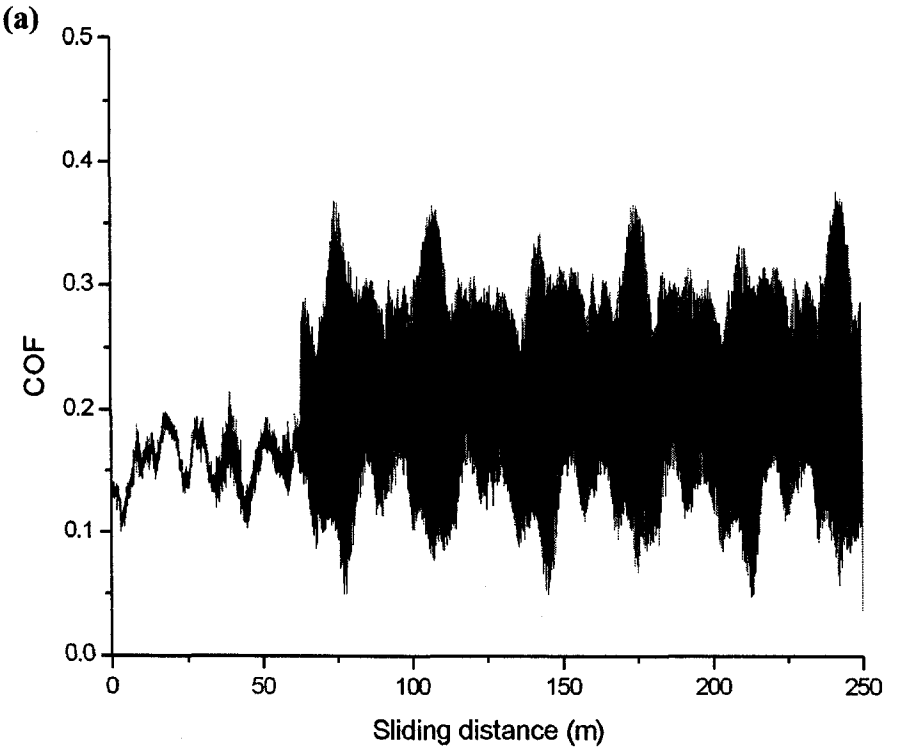

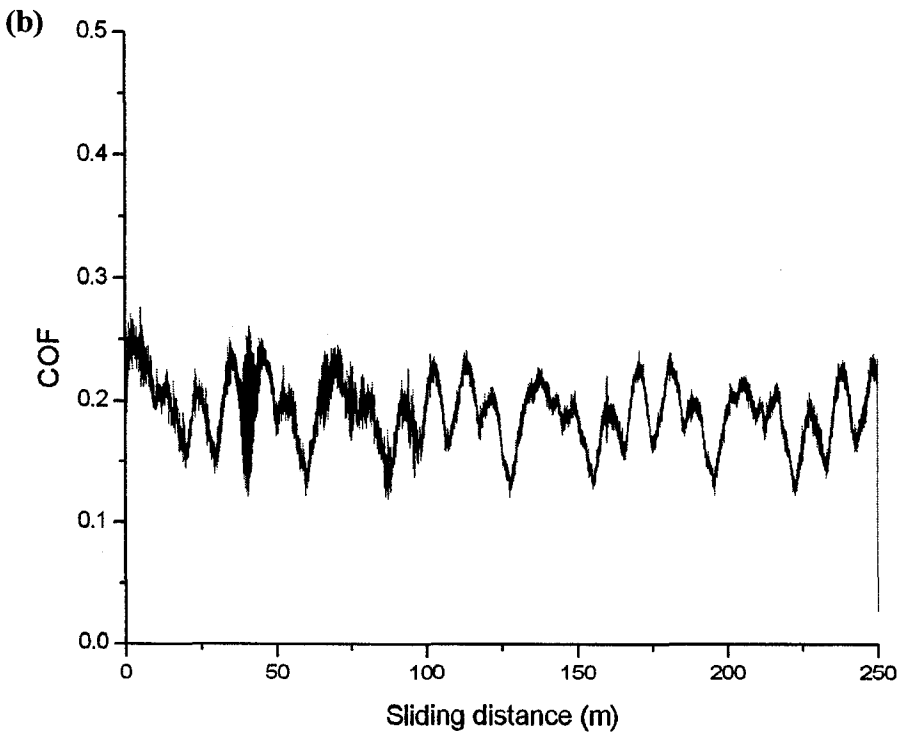

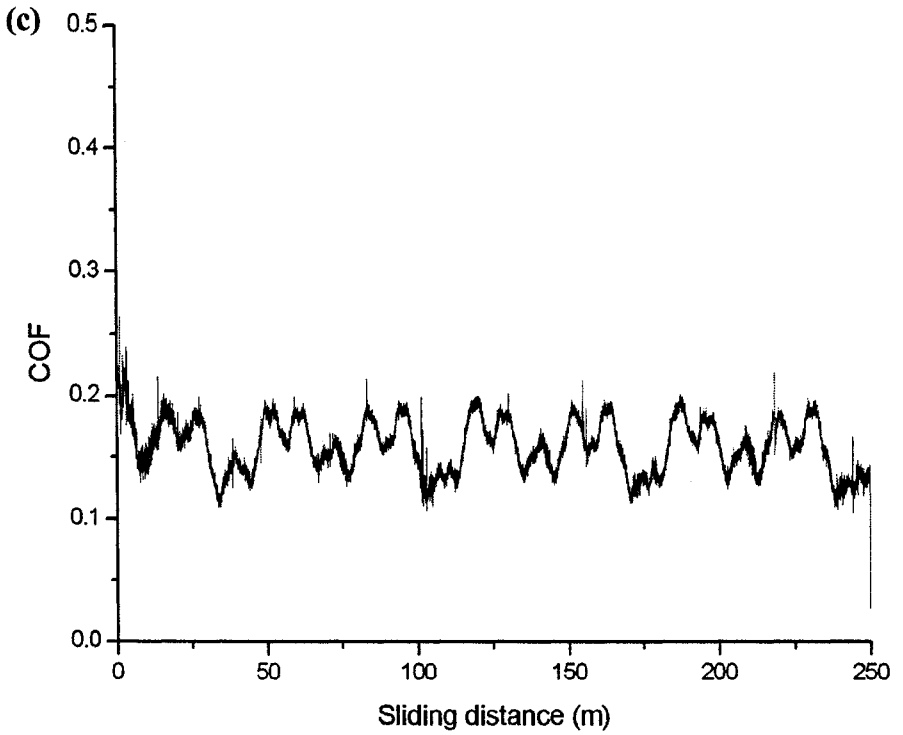

Fig. 6.10 COF curves for PEO/graphite composite coatings (a) Z1, (b) Z2 and (c) Z3, sliding against steel ball for 250m, respectively

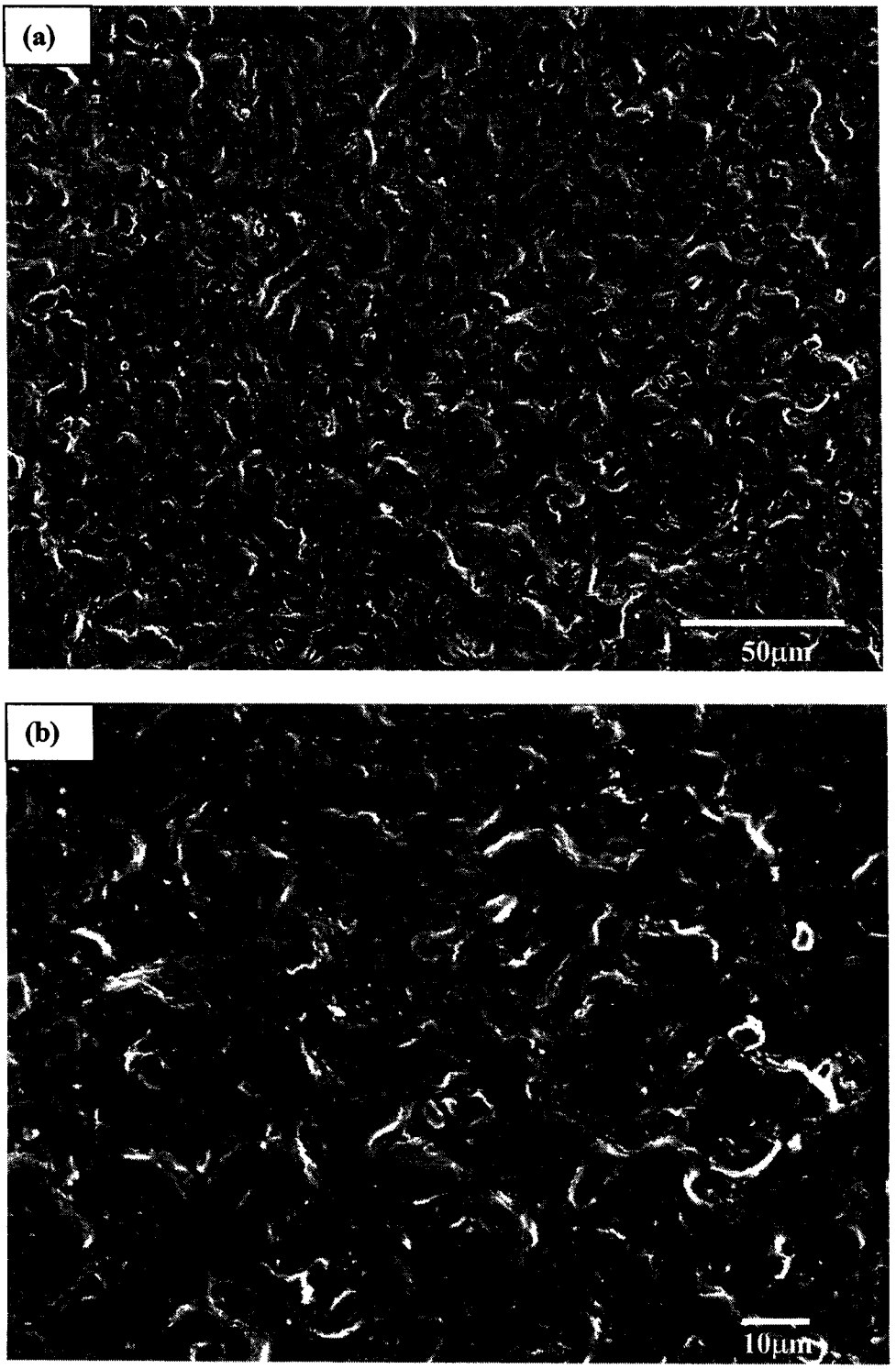

Fig. 6.11 to be continued

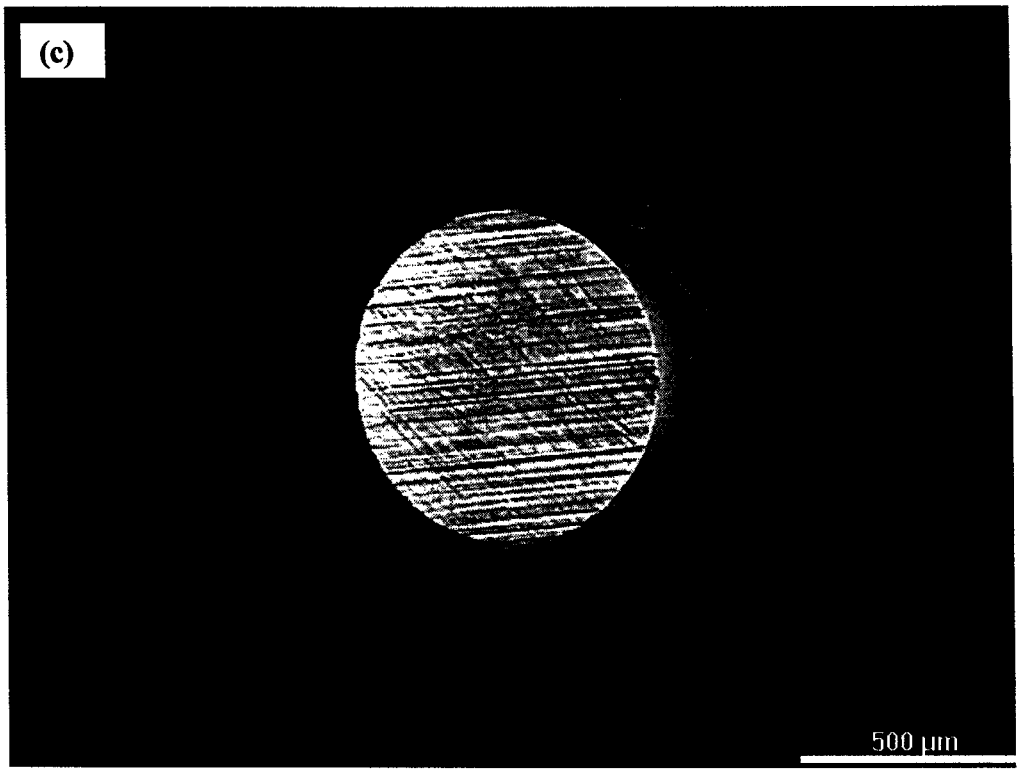

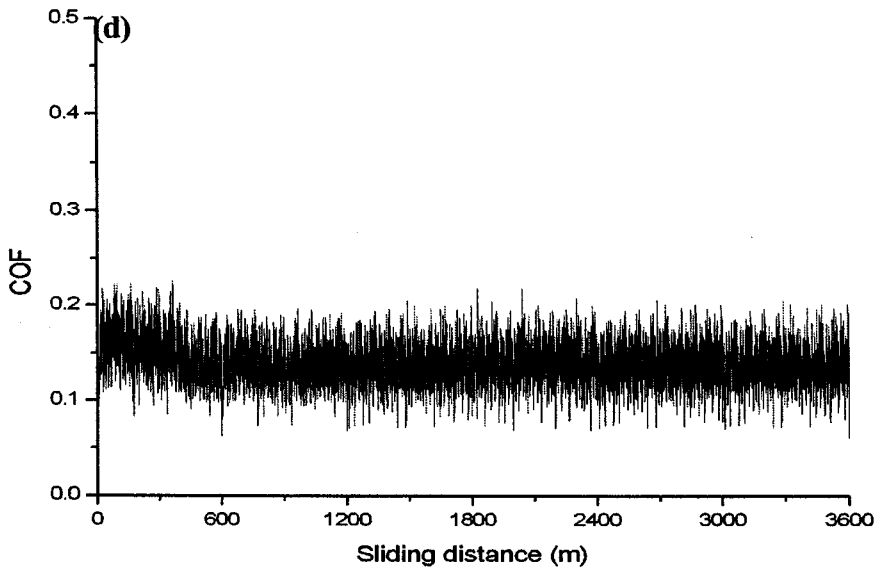

Fig. 6.11 SEM micrographs of the wear track for PEO/graphite composite coating Z3 sliding against steel ball with 2N normal load under residual oil lubrication for3600m, (a) low magnification, (b) high magnification, (c) optical microscope photographs of the counter steel ball, and (d) the corresponding COF curve

6.3 Tribological properties of PEO/graphite composite coatings on Al 6061 treated with DC power supply under oil immersion lubrication

Figs. 6.12 (a, b, c) showed the friction coefficient responses to the increase in sliding speed, represented by the sliding frequency from 2 Hz to 6 Hz, for Al6061, coating Z1 and Z3. In each individual curve, a lower friction coefficient was shown in the middle of every half cycle, where a higher sliding speed existed. Compared with the curves of each sample, the increased sliding frequency generally resulted in a low friction coefficient. A similar phenomenon was observed by other researchers [58].

It was also found that the coefficients of friction (C.O.F = 0.14-0.18) of the coating Z3 were slightly higher than those of the Al6061 (C.O.F = 0.11-0.19) and coating Z1 (0.1-0.16) at the low sliding speeds (i.e., 2 Hz and 4 Hz) in the immersed lubricant oil test condition. At the sliding speed of 6 Hz, the coating Z3 exhibited a similar friction coefficient (C.O.F = ~0.1) to that of the Al6061, whilst the coating Z1 still presented a lower COF of 0.08.

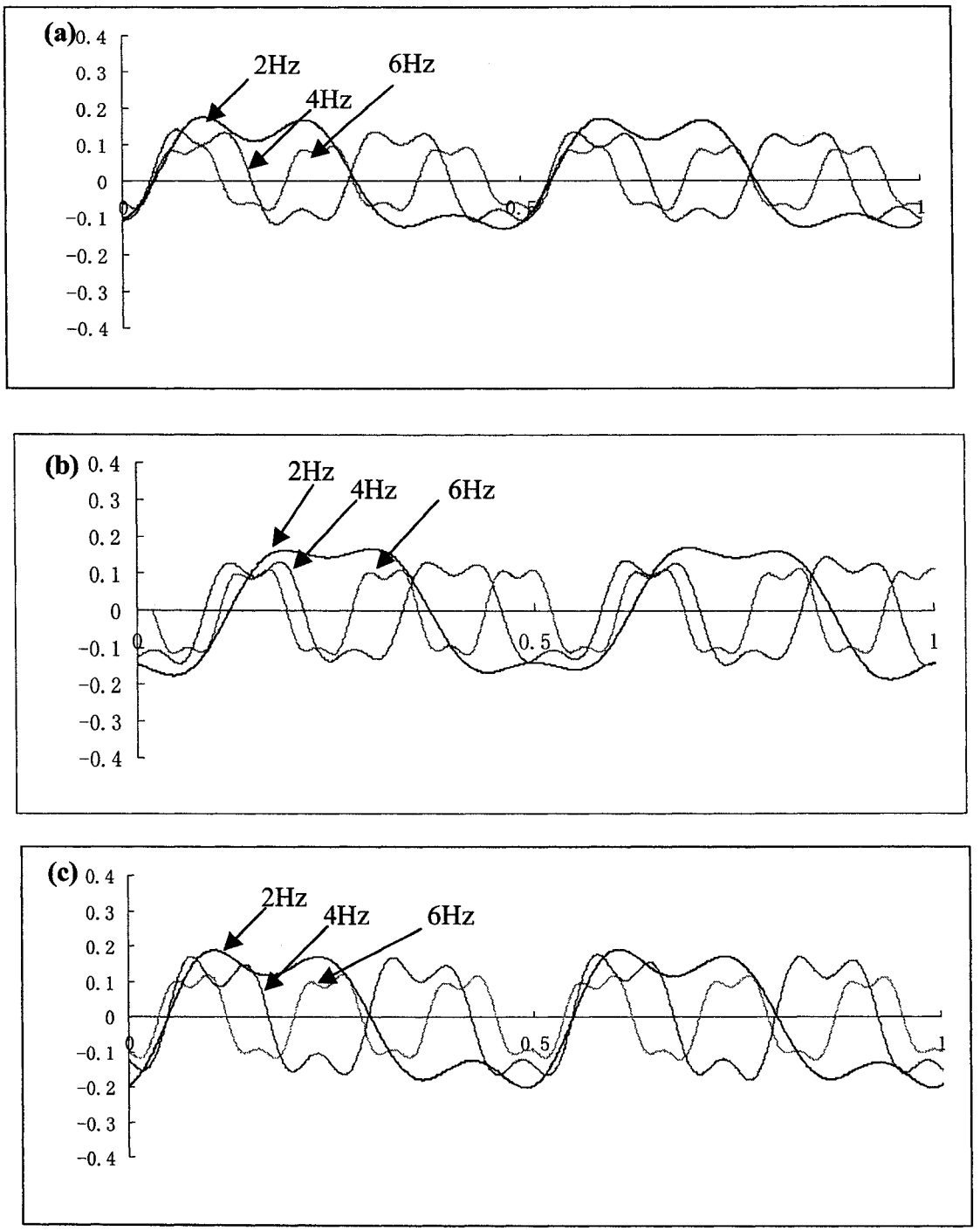

Figure 6.12 COF curves of coatings (a) Z1, (b) Z3, and (c) Al6061, sliding against Steel balls with a 1N normal load under oil immersion lubrication

6.4 Discussion

Since the silicon content in Al6061 is very low, an anodizing film firstly grows evenly at the whole substrate surface. In stage II, tiny sparse micro-discharges concentrate on the spots where the electrical field reaches the critical value, causing breakdown of the dielectric film and forming small pores on the smooth coating surface. At this stage, due to the short treatment time, the coating is too thin, only 0.33 μm for coating Z1, to provide enough load-bearing ability. Therefore, during the tribological sliding test under residual oil lubrication with a 2N normal load, the coating peeled off, possibly resulting from the large stress exerted to the soft Al matrix. Along with the increase of the sliding distance, the delamination became worse. Additionally, the smooth coating surface is not good for oil retaining, although there are a few of tiny round pinholes. Also, the coating surface with such a small roughness can not sustain graphite particles, which were easily flushed away from the surface. Thus coating Z1 presented the largest average COF. However, the low hardness of the coating was beneficial to a small couterface worn area, second only to that of the Al6061 substrate.

Strong and intense micro-discharges appear in stage III, forming large discharge channels distributed at the whole coating surface. Due to the high temperature generated by the discharges, the coating is melted and solidified by the electrolyte around the channels to shape into the dense curly projections. Both the thickness and hardness of the coating increase with the treatment time [16], contributing to a better wear resistance. Also, since

the rough surface was better for oil and graphite retaining, coating Z2 had a lower COF. However, owing to the increased roughness, the compatibility for steel became worse.

During the forth stage, due to the stronger discharges, the coating is fused by the high temperature, forming the larger curly projections, which provide hard contact surface sliding against the steel ball. However, the high hardness and large roughness of coating Z3 contributed to its worst compatibility for steel. But, the valleys lying among the projections are ideal for oil reservoir. Consequently, coating Z3 presented the low friction and the high wear resistance. Additionally, although the roughness of coating Z3 was higher than that of coating Z2, the worn areas of the counter pins for both coatings were almost same, which can also be attributed to the better lubrication.

With crosshatch pattern, used for oil retaining, the Al6061 sample had the similar roughness to that of the coating Z3. Under residual oil lubrication, the Al6061 sample and the coating Z3 presented almost the same COF. Due to the softness of the material, ploughing occurred during the sliding test, partially erasing the pattern. But the low hardness was beneficial to protect the counter pin.

Under the oil lubrication immersion condition, a pressurized oil film could be formed at a high surface sliding velocity to provide hydrodynamic lubrication. The direct solid-to-solid contact is avoided by this film. The effectiveness of such thick film lubrication depends directly on relative velocity and lubricant viscosity. At a relatively low surface sliding speed, hydrodynamic lubrication transits to a mixture of hydrodynamic and

boundary lubrication, where solid-to-solid contact occurs to some of the asperities. With the sliding speed decreasing further, complete boundary lubrication comes into being. Therefore, in every individual COF curve, at the two ends of each half cycle, where the sliding speed of the steel ball is lower than in the middle, boundary lubrication is dominant, causing a higher friction. Comparatively, in the middle of each half cycle, the high sliding speed is favorable for the formation of a localized oil film, leading to a reduction of friction. In the same way, for each sample, the friction decreases with the sliding frequency. At the sliding frequency of 6 Hz, the COF curves of all samples approached to an average value around 0.1.

Roughness also has a great effect on the lubrication. Large roughness is good for oil retaining but unfavorable to the formation of oil film. The degree of separation between the asperities of two sliding surface is often expressed in terms of the lambda ratio [63]:

$$\lambda = \frac{h_{min}}{(e_s + e_b)/2} \quad \text{(Eq. 6.1)}$$

where h_{min} is the minimum oil film thickness, increasing the sliding speed and decreasing with the normal load [64]. e_s and e_b are the average roughness of the respective surfaces. Therefore, under the oil lubrication immersion condition, for a given sliding frequencies where h_{min} is fixed, coating Z3 and Al6061, with the larger roughness around 0.6 μm, have lower ratios, indicating more direct asperity contacts. Consequently, the higher COF were exhibited.

6.5 Summary

With low content of Si in an Al6061 alloy, aluminum oxide film forms evenly on the whole substrate surface at the beginning of treatment. The roughness increases with the treatment time. The thin and smooth coating can not bear the high normal load (2N), causing scratches during the sliding test under residual oil lubrication. Also, the smooth surface, which is lack of oil retaining ability, contributes to the high friction. However, the low hardness and small roughness are good for counter pin protection. As the process continues, the hardness and roughness of the coating increase, which improves the load-bearing and oil retaining abilities of the coating. Thus, for a thicker coating, the higher wear resistance and lower friction are exhibited.

Under oil immersion lubrication, the sliding speed is crucial to the formation of oil film, which separates the direct asperity contact. For the same friction pairs, the higher sliding speed is good for forming a thicker oil film, which reduces the friction. Under the mixture of boundary lubrication and hydrodynamic lubrication, the rough surface reduces the efficiency of the oil film in the separation of asperity contact. Therefore, the thick coating, which shows better anti-wear properties than the thinner one under residual oil lubrication, exhibits the higher friction for the same sliding speed.

CHAPTER 7 SUMMARY

In this thesis, electrolyte jetting plasma process (EJPP) was used to produce thin plasma electrolyte oxidation (PEO) coatings on Al390 with a DC power and a pulsed bipolar DC power. PEO/graphite composite coatings on Al6061 were prepared using the DC power. With proper process parameters, compared with substrate samples, PEO coatings exhibit much better wear resistance and almost the same friction coefficients but only cause a little larger worn area of the counterpins. Three parts of studies are included in this thesis, and the corresponding research results are summarized as follows.

7.1 Effects of treatment time and electrolyte concentration on coating surface morphology and tribological properties

Al390 consists of aluminum matrix and embedded needle shape silicon particles. During the PEO process, the anodizing process only occurs at the aluminum matrix to form a thin and smooth aluminum oxide film. With the treatment time increasing, microdischarges firstly appear at the Si-Al boundaries due to the tip/corner effect of electrical field concentration and mainly concentrate on the silicon phase regions. At this stage, the smooth aluminum oxide region is too thin to have an enough load-bearing ability to resist the scratch during the sliding wear test. And the piling-up porous silicon phase rich regions are also inclined to be worn away. Furthermore, the smooth surface of the

aluminum oxide region can not provide the good oil retaining ability. Therefore, a high COF and low wear resistant are exhibited. However, the low hardness of the coating is beneficial to the counterface protection. Along with the increase of the treatment time, more microdischarges emerge at the aluminum oxide region. The micro pores resulted from the discharge channels, are in favor for oil retaining. Due to the increased coating thickness, the aluminum oxide region can bear the load. As a result, no obvious material removal is observed. Thus a high wear resistance and low friction are presented. Also, the aluminum oxide region starts to mix with the oxidized silicon phase region to form Si-Al-O compound due to the high temperature produced by the discharges. With the process continuing, the discharges contract to form stronger but less micro-arc discharges, resulting in large Si-Al-O compound projections scattered at the whole coating surface. The electrical resistance of the solution decreases with the electrolyte concentration. Also, the high electrolyte concentration supplies more Si and O, which accelerates the combination of Al-O in coatings with Si-O in the electrolyte to form the Al-Si-O compound. Compared with Al_2O_3, the Al-Si-O compound has a low electrical resistance and low breakdown voltage. Therefore, high electrolyte concentration promotes the microdischarge formation, resulting in a rougher coating surface.

The pores in the rougher surface can act as oil reservoirs, but it is difficult for the oil to exist at the top surface of the projections due to the large height distance between the peak and valley. Also, the hardness of the coating increases with the treatment time due to the phase transformation of Al_2O_3 from the soft $\gamma - Al_2O_3$ to the hard $\alpha - Al_2O_3$ [16].

Therefore, the coating presents high wear resistance, but also high friction and poor compatibility for steel.

7.2 Effect of pulsed bipolar DC on coating surface morphology and tribological properties

The sharp rising edge of each pulse current in the high frequency pulsed bipolar DC produces a high initial current peak, which promotes the formation of the perforate projections in the aluminum oxide region at the initial stages of the PEO process. The volcano-shape structure is beneficial to reducing friction and worn loss of the counter pin during the sliding test under residual oil lubrication, because the oil retained in the micro pore can exist at the top of the projections. Also, the high frequency pulse provides ability to control the duration time of the microdischarges, which is beneficial to the arc-extinguishing and reduces the thermal impact to the coating. However, as the treatment time increases further, the large imperforate projections are dominant. Although the rougher surface is good for oil retaining, the lack of the oil at the top of the projections weakens the lubrication effect, resulting in a higher friction. Furthermore, the increased hardness and roughness leads to a worse compatibility for steel.

7.3 Effect of different lubrication condition on friction

Due to the low content of Si, a dense and smooth anodizing film firstly forms on the whole substrate Al6061 surface. Then micro-discharges appear at some spots as a result of the increased electrical voltage field. Small micro pores form at the smooth aluminum oxide film. At this stage, the coating is too thin to bear the high normal load (2N) during the sliding test under residual oil lubrication, therefore, scratches are clearly observed in the wear track. Also, the poor oil retaining ability of the smooth film aggravates the friction. But the thin coating shows good compatibility for steel because of the low hardness and small roughness, resulting from the short treatment time. A rougher and thicker coating is obtained as the process goes on further. The coating surface is occupied by the large curly projections and the porosities. With the better oil retaining ability and the enhanced hardness, the friction decreases. However, the wear loss of the counter pin increases, attributing to the higher hardness and larger roughness. Nevertheless, different from the situation under residual oil lubrication, where the roughness is good for oil retaining, under the oil immersion lubrication, the roughness makes it difficult for the oil film to separate the direct asperity contact. Also, for the given friction pairs, the increased sliding surface speed promotes the formation of thick oil film, which is beneficial to reducing friction.

7.4 Future work

In order to improve the tribological properties and counterface compatibility of PEO coatings further, solid lubricants, which can be attached to the smooth and thin coating firmly, are in great need.

Additionally, more research needs to be conducted to reduce the roughness of the thick coatings by adjusting the process parameters.

REFERENCES

[1] ASM: "Properties and Selection: Nonferrous Alloys and Special-Purpose Materials," ASM Handbook, Vol. 2, ASM International, Materials Park, OH, (1990).

[2] Haizhi Ye, JMEPEG: "An Overview of the Development of Al-Si-Alloy Based Material for Engine Applications," 12 (2003), 288-297

[3] A.R. Riahi, T. Perry, A.T. Alpas, Materials Science and Engineering A, 343 (2003), 76-81.

[4] T.W. Clyne, An introductory overview of MMC systems, types and developments, Comprehensive Composite Materials, Vol. 3. Metal Matrix Composites, Elsevier, Amsterdam (2000), 1–26.

[5] T.W. Clyne, P.J. Withers, An Introduction to Metal Matrix Composites, Cambridge University Press, Cambridge, UK, (1993).

[6] A.E. Ostermann, Experiences with Nickel-Silicon Carbide Coatings in Cylinder Bores of Small Aluminum Engines, TP 790843, Society of Automotive Engineers, (1979).

[7] Y.C. Wang, S.C. Tung, Wear, 225-229 (1999), 1100-1108.

[8] J. W Cox, R.F. Bunshah, Handbook of Hard Coatings, William Andrew Publishing, (2001), 420-457.

[9] A. Edrisy, T. Perry, Y. T. Cheng, A. T. Alpas, Wear, 251 (2001), 1023-1033.

[10] Ronald A. Walsh, Electromechanical Design Handbook (3rd Edition), McGRAW-HILL, New York (2000), 13-15.

[11] E.I. Meletis, X. Nie, F.L. Wang, J.C. Jiang, Surface & Coatings Technology, 150 (2002), 246-256.

[12] X. Nie, C. Tsotsos, A. Wilson, A.L. Yerokhin, A. Leyland, A. Matthews, Surface & Coatings Technology, 139 (2001), 135-142.

[13] A.A. Voevodin, A.L. Yerokhin, V.V Lyubimov, M.S. Donley, J.S. Zabinski, Surface & Coatings Technology, 86-87 (1996), 516-521.

[14] X. Nie, E.I. Meletis, J.C. Jiang, A. Leyland, A.L. Yerokhin, A. Matthews, Surface & Coatings Technology, 149 (2002), 245-251.

[15] L.Rama Krishna, K.R.C. Somaraju, G. Sundararajan, Surface & Coatings Technology, 163-164 (2003), 484-490.

[16] G. Sundararajan, L. Rama Krishna, Surface & Coatings Technology, 167 (2003), 269-277.

[17] A.L. Yerokhin, V.V. Lyubimov, R.V. Ashitkov, Ceramics International, 24 (1998), 1-6.

[18] L.O. Snizhko, A.L. Yerokhin, A. Pikington, N.L. Gurevina, D.O. Misnyankin, A. Leyland, A. Matthews, Electrochimica Acta, 49 (2004), 2085-2095.

[19] L. Wang, X. Nie, Silicon effects on formation of EPO oxide coatings on aluminum alloys, Thin Solid Films, 494, (2006), 211-18,

[20] A. L. Yerokhin, X. Nie, A. Leyland, A. Matthews, S. J. Dowey, Surface & Coatings Technology, 122 (1999), 73-93.

[21] G. A. Markov, G. V. Markova, USSR Patent 526961, Bul. Inv. 32, (1976).

[22] A. V. Nikolaev, G.A. Markov, B.I. Peshchevitskij, Izv. SO AN SSSR. Ser. Khim. Nauk 5 (12) (1977) 32, in Russian.

[23] A. V. Nikolaev, G.A. Markov, B.I. Peshchevitskij, Izv. SO AN SSSR. Ser. Khim. Nauk 5 (12) (1977) 32, in Russian.

[24] L.A. Snezhko, G.V. Rozenboym, V.I. Tchernenko, Zashch. Tet., 17 (5) (1981), 618

[25] L.A. Snezhko, S.G. Pavlus, V.I. Tchernenko, Zashch. Met., 20 (4) (1984), 292.

[26] V.I. Tchernenko, L.A. Snezhko, C.B. Tchernova, Zashch., Met. 20 (3) (1984), 454.

[27] L.A. Snezhko, L.A. Beskrovnyj, Yu.M. Nevkrytyj, V.I. Tchernenko, Zashch. Met., 16 (3) (1980), 365.

[28] L.A. Snezhko, V.I. Tchernenko, Elektron. Obrab. Mater., (2) (1983), 25.

[29] L.A. Snezhko, V.I. Tchernenko, Elektron. Obrab. Mater., (2) (1983), 38.

[30] G.A. Markov, M.K. Mironova, O.G. Potapova, Izv. AN SSSR. Ser. Neorgan. Mater., 19 (7) (1983), 1110.

[31] A.A. Petrosyants, V.N. Malyshev, V.A. Fyedorov, G.A. Markov, Trenie Iznos, 5 (2) (1984), 350.

[32] V.N. Malyshev, S.I. Bulychev, G.A. Markov, V.A. Fyedorov, A.A. Petrosyants, V.V. Kudinov, M.H. Shorshorov, Fiz. Khim. Obrab. Mater., (1) (1985), 82.

[33] V.A. Fyedorov, V.V. Belozerov, N.D. Velikosel'skaya, S.I. Bulychev, Fiz. Khim. Obrab. Materialov, 4 (1988), 92.

[34] V.S. Rudnev, P.S. Gordienko, Preprint No. 3384-B87, Inst. Khimii DVO AN SSSR, Vladivostok, (1987).

[35] O.A. Khrisanfova, P.S. Gordienko, Preprint No. 2986-B89, Inst. Khimii DVO AN SSSR, Vladivostok, (1987).

[36] P.S. Gordienko, P.M. Nedozorov, L.M. Volkova, T.P. Yarovaya, O.A. Khrisanfova, Zashch. Met., 25 (1) (1989), 125.

[37] P. Kurze, W. Krysmann, G. Marx, Z. Wiss, Tech. Hochsch. Karl-Marx-Stadt, 24 (1982), 139.

[37] P. Kurze, W. Krysmann, G. Marx, Z. Wiss, Tech. Hochsch. Karl-Marx-Stadt, 24 (1982), 139.

[38] K.H. Dittrich, W. Krysmann, P. Kurze, H.G. Schneider, Cryst. Technol., 19 (1) (1984), 93.

[39] W. Krysmann, P. Kurze, K.H. Dittrich, H.G. Schneider, Cryst. Technol., 19 (7) (1984), 973.

[40] P. Kurze, J. Schreckenbach, T. Schwarz, W. Krysmann, Metalloberflaeche, 40 (12) (1986), 539.

[41] L.S. Saakian, A.P. Yefremov, L.Y. Ropyak, A.V. Apelfeld, Corrosion Control and Environment Protection. Informative Survey, VNIIOENG, Moscow, (6) (1986).

[42] V.A. Fyedorov, A.G. Kan. R.P. Maksutov, Surface Strengthening of Oil & Gas Trade Facilityies by Micro Acr Oxidation, VNIIOENG, Moscow, (6) (1989).

[43] G.A. Markov, B.S. Gizatullin, I.B. Rychazhkova, USSR Patent 926083, Bulletin of Inventions, 17, (1982).

[44] L.A. Snezhko, V.I. Techernenko, USSR Patent 973 583, Bulletin of Inventions 23, (1982).

[45] P. Kurze, W. Krysmann, G. Marx, K.H. Dittrich, DDR Patent DD-WP C25D/236988(5).

[46] A. L. Yerokhin, L. O. Snizhko, N. L. Gurevina, A. Leyland, A. Pilkington, A. Matthews, J. Phys. D: Applied Physics, 36 (2003) 2110-2120

[47] A.L. Yerokhin, L.O. Snizhko, N.L. Gurevina, A. Leyland, Surface and Coatings Technology 177-178 (2004), 779-783.

[48] S. Ikonopisov, A. Girginov, M. Machrova, Electrochim. Acta, 24 (1979), 451.

[50] N. Klein, Thin Solid Films, 50 (1978), 223.

[51] J.M. Albella, I. Montero, J.M. Martinez-Duart, Electrochimica Acta, 32 (1987), 255 (1984), 973.

[52] A. Hickling, M.D. Ingram, Trans. Faraday Soc., 60 (1964), 783.

[53] H.E. Wagner, R. Brandenburg, K.V. Kozlov, A. Sonnenfeld, P. Michel, J.F. Behnke, Vacuum, 71 (2003), 417.

[54] X. Nie, A. Leyland, H.W. Song, A.L. Yerokhin, S.J. Dowey, A. Matthews, Surface and Coatings Technology, 116-119 (1999), 1055-1060.

[55] A.L. Yerokhin, A.A. Voevodin, V.V. Lyubimov, J. Zabinski, M. Donley, Surface & Coatings Technology, 110 (1998), 140-146.

[56] A. Datta, J. D. Carpenter, R. D. Ott, P. J. Blau, SAE Technical paper series, 2002-01-0490.

[57] V.D. N Rao, H. A. Cikanek, B. A. Boyer, SAE paper, 970022, (1997)

[58] X. Nie, L. Wang, E. Konca, A.T. Alpas, Surface & Coatings Technology, 188-189 (2004), 207-213.

[59] X. Nie, A. Wilson, A. Leyland, A. Matthews, Surface & Coatings Technology, 131 (2000), 506-513.

[60] J.R. Davis, Surface Engineering for Corrosion and Wear Resistance, Woodhead Publishing, (2001).

[61] A.R.West, Basic solid state chemistry Chemistry, John Wiley & Sons, New York, (1999).

[62] A.L. Yerokhin, A. Shatrov, V. Samsonov, P. Shashkov, A. Pilkington, A. Leyland, A. Matthews, Surface & Coatings Technology, 199 (2005), 150-157.

[63] Tribology in Machine Design, Elsevier, (1990), P281.

[64] Standard Handbook of Machine Design (3rd Edition), Part V. Bearings and Lubrication, McGraw-Hill, New York (2004), 20.5.

LIST OF PUBLICATIONS

Publications during the master's program in University of Windsor:

1. X. Nie, P. Zhang, A.M. Weiner, Y.T. Cheng, Nanoscale wear and machining behavior of nanolayer interfaces, Nano Letters, 5 (10) (2005) 1992-1996

2. P. Zhang, L. Wang, X. Nie, Y.T. Cheng, Tribological Properties of Cr(N)/a-C(N) Coatings in Micro- and Nanoscales, Surface & Coatings Technology, in Press.

VITA AUCTORIS

NAME:	Peng Zhang
PLACE OF BIRTH:	Shanxi, China
YEAR OF BIRTH:	1979
EDUCATION:	Shanghai Jiaotong University, China
	1997-2001, B. Sc
	Shanghai Jiaotong University, China
	2001-2004, M. A. Sc
	University of Windsor, Canada
	2005-2006, M. A. Sc